



# Kent Academic Repository

**Kalinovsky, Yaroslav (2019) *Bulk Remediation of Organophosphorus Contaminants using Metal-Organic Framework Polymer Composites*. Doctor of Philosophy (PhD) thesis, University of Kent,.**

## Downloaded from

<https://kar.kent.ac.uk/73307/> The University of Kent's Academic Repository KAR

## The version of record is available from

## This document version

UNSPECIFIED

## DOI for this version

## Licence for this version

UNSPECIFIED

## Additional information

## Versions of research works

### Versions of Record

If this version is the version of record, it is the same as the published version available on the publisher's web site. Cite as the published version.

### Author Accepted Manuscripts

If this document is identified as the Author Accepted Manuscript it is the version after peer review but before type setting, copy editing or publisher branding. Cite as Surname, Initial. (Year) 'Title of article'. To be published in *Title of Journal*, Volume and issue numbers [peer-reviewed accepted version]. Available at: DOI or URL (Accessed: date).

### Enquiries

If you have questions about this document contact [ResearchSupport@kent.ac.uk](mailto:ResearchSupport@kent.ac.uk). Please include the URL of the record in KAR. If you believe that your, or a third party's rights have been compromised through this document please see our [Take Down policy](https://www.kent.ac.uk/guides/kar-the-kent-academic-repository#policies) (available from <https://www.kent.ac.uk/guides/kar-the-kent-academic-repository#policies>).

# **Bulk Remediation of Organophosphorus Contaminants using Metal-Organic Framework Polymer Composites**

Yaroslav Kalinovsky (2019)

## Preface

This thesis is submitted for the degree of Doctor of Philosophy at the University of Kent. The research described in this document was conducted under the supervision of Dr. Barry A. Blight and Simon J. Holder at the School of Physical Sciences, University of Kent, between September 2014 and September 2018. The research was funded by a joint studentship awarded by DSTL to Dr. Barry A. Blight and Simon J. Holder.

This work is to the best of my knowledge, original, except where references are made to previous work and where acknowledgements are made to the contributors. Parts of this thesis have been published in the following peer-reviewed journals:

Z. H. Fard, Y. Kalinovsky, D. M. Spasyuk, B. A. Blight and G. K. H. Shimizu, *Chem. Commun.*, 2016, **52**, 12865–12868.

R. J. Marshall, Y. Kalinovsky, S. L. Griffin, C. Wilson, B. A. Blight and R. S. Forgan, *J. Am. Chem. Soc.*, 2017, **139**, 6253–6260.

Y. Kalinovsky, N. J. Cooper, M. J. Main, S. J. Holder and B. A. Blight, *Dalton Trans.*, 2017, **46**, 15704–15709.

A reference to the publication and the contributors is made at the start of relevant chapters.

## Acknowledgements

I would like to thank a number of people for their help and support throughout the course of this doctorate, without whom the whole process would have been infinitely more difficult. First of all, I would like to thank my mentor Dr. Barry Blight for his supervision, for knowing when I've needed a push, some inspiration or just some reassurance. Without his brilliance and his guidance, this work would not have been possible. I would then like to thank my second supervisor, Dr. Simon Holder for his invaluable ideas and support, and for his assistance with the assembly of this thesis. Thank you also to my project partner, Alex Wright, with whom it has been an absolute pleasure to work with and develop our ideas over the last four years. Thank you to Dr. Ross Forgan along with Dr. Ross Marshall for introducing me to the synthetic aspects of MOF chemistry and for their work on the synthesis of a series of functionally versatile Zirconium MOFs. Thank you to Dr. George Shimizu and Dr. Zoreh Fard for their work on the synthesis of novel alkaline earth MOFs. Thank you to Dr. Helena Shepherd for her crystallographic expertise. Thank you to Dr. Jennifer Hiscock for her assistance with all my NMR problems. Thank you also to Dr. Ewan Clark for always being an indispensable source of knowledge. I would like to thank everyone at the School of Physical Sciences for maintaining such an inspiring work environment. Finally, I would like to thank Dr. Nicholas Cooper and Dr. Marcus Main for carrying out CWA testing, and DSTL for funding this doctorate.

I would then like to thank my Kent colleagues, both past and present, and in no particular order: Alex, Matt L, Jed, Francesco, JJ, Saeed, Barbora, Aaron, Andryj, Towseef, Kate, Liv, Ollie, Sam, Christine, Matt E and Christina. I am incredibly grateful for your friendship, assistance and support throughout my time at Kent, I shall be leaving with many fond memories.

I would like to thank Emma for her endless encouragement, reassurance and patience throughout the doctorate. You have motivated me to keep on track at all times.

Finally, I would like to thank my parents for always pushing me to succeed, and for never failing to provide me with the opportunity to do so.

## Abstract

Organophosphorus (OP) chemical warfare agents (CWAs) are a group of deadly compounds which inhibit the enzyme acetyl cholinesterase and disrupt the normal functioning of the nervous system. Events in Damascus, Syria (2013) and Salisbury, United Kingdom (2018), have highlighted the dangers that these noxious agents still pose to civilian and military personnel. CWA degradation measures often employ an excess of stoichiometric reagents and solution buffers. There is therefore a demand for catalytic systems which can combat the CWA threat in the absence of additional reagents.

This work reports the development of a catalytic material for the degradation of the deadly V-series CWAs. Zirconium metal-organic frameworks (MOFs) are identified as the most promising material for such an application. Methyl paraoxon in a mildly alkaline buffer is found to be a good simulant system for mimicking the hydrolysis of VX, with both substrates showing similar degradation rates in the presence of zirconium MOFs. Using this simulant system, MOF-808 is identified as the most potent and cost-effective hydrolysis catalyst. Initial studies on OP CWAs showed that MOF-808 (1.25 % catalyst loading vs. substrate) was able to hydrolyse VX in just water and in the absence of buffer. Additionally, MOF-808 was found to be capable of slowly hydrolysing VX in the presence of only ambient humidity.

Upon investigating the hydration of zirconium MOFs for enhancing hydrolysis catalysis, two additional studies were performed. Using solid-state photoluminescence (ssPL), two alkaline earth MOFs composed of the 2,4,6-tris(4-phosphonophenyl)pyridine ( $H_6L$ ) ligand were shown to exhibit reversible hydration-dependant emission. A strontium AE MOF ( $Sr_4(H_2L)_2(H_2O)_x$ ) displayed a red-shifted emission on exposure to increases in relative humidity (RH). A series of 4,4'-[1,4-phenylene-bis(ethyne-2,1-diyl)]-dibenzoate (peb) zirconium MOFs were also studied using ssPL. A dimethyl functionalisation on the peb linker resulted in solvatochromism. A tetrafluorinated peb linker displayed no hydration-dependent emission which prompted the examination of its super-hydrophobic properties. Finally, a benzothiazole functionalization of

the peb linker led to a RH dependent emission. These properties were all probed using ssPL, thus highlighting the utility of the technique.

Moving back to catalysis, acetate-modulated MOF-808, DUT-84 and UiO-66 were activated through hydration using microwave irradiation. This involved the removal of acetate modulator thus exposing more catalytic vacancies. Enhanced DMNP hydrolysis was observed in the presence of the activated counterpart of each MOF. A modest enhancement in VM hydrolysis was also observed, with both MOF-808 and DUT-84 being capable of degrading VM in the absence of a buffering agent.

MOF-808 was then incorporated into a high internal-phase emulsion polymer (pHIPE) to form a MOF-HIPE composite. The pHIPE polymer is capable of swelling in the presence of V-series agents to very high degrees ( $Q > 50$ ). The MOF-HIPE composite was shown to degrade the simulant DMNP with no reduction in activity compared to the MOF-808 powder. The composite, containing a 1.25 % catalyst loading relative to substrate, is shown to rapidly degrade VX in a H<sub>2</sub>O:THF medium. Finally, the MOF-HIPE is able to fully degrade neat VX over a 2 week period in the presence of only 50 RH % and a catalytic loading of just 0.15 %. A potent encapsulation and degradation material was developed for the effective remediating of V-series agents.

## Abbreviations

4-VBPP	4-vinylbenzyl piperidine
AcOH	acetic acid
AE	alkaline earth
Amine Lig	2-aminobiphenyl-4,4'-dicarboxylate
BET	Brunauer-Emmett-Teller
CWA	Chemical Warfare Agent
DCM	dichlormethane
DCNP	diethyl cyanophosphonate
DCP	diethyl chlorophosphate
DEF	N,N-Diethylformamide
DEMDP	diethyl dimethyldisphosphonate
DEP	diethyl phosphate
DESH	2-(N,N-diethylamino)ethanethiol
DIFP	diisopropyl fluorophosphonate
DMA	diethylacetamide
DMF	N,N-Dimethylformamide
DMMP	dimethyl methylphosphonate
DMNP	methyl paraoxon
DMP	dimethyl phosphonate

DMSO	dimethyl sulfoxide
EA-2192	S-[2-(Diisopropylamino)ethyl] hydrogen methylphosphonothioate
EMPA	ethyl methylphosphonate
ESPIT	excited state intramolecular proton transfer
EtOH	ethanol
GA	Tabun
GB	Sarin
GD	Soman
GF	Cyclosarin
H <sub>2</sub> BDC	1,4 benzenedicarboxylic acid
H <sub>2</sub> BiPy	bipyridine-5,5'-dicarboxylic acid
H <sub>2</sub> BPDC	biphenyl-4,4'-dicarboxylic acid
H <sub>2</sub> DEPPA	diethyl pyrophosphoric acid
H <sub>3</sub> BTC	1,3,5 benzenetricarboxylic acid
H <sub>6</sub> L	2,4,6-tris(4-phosphonophenyl)pyridine ligand
HBA	hydrogen-bond acceptor
HDEPA	diethyl phosphoric acid
HIPE	high internal-phase emulsion

IMPA	isopropyl methyl phosphonic acid
IP	internal phase
IPA	isopropyl alcohol
IR	infra-red
LCCT	ligand-to-cluster charge-transfer
LMCT	ligand-to-metal charge transfer
MAS	Magic Angle Spinning
MeCN	acetonitrile
MeOH	methanol
MLCT	metal-to-ligand charge transfer
MOF	metal-organic framework
MONPs	metal oxide nanoparticles
NEM	N-ethyl morpholine
NMR	nuclear magnetic resonance
OP	organophosphorus
peb	4,4'-[1,4-phenylene-bis(ethyne-2,1-diyl)]- dibenzoate
PEI	polyethyleneimine
PL	photoluminescence
ppm	parts per million

PSE	post-synthetic exchange
PSM	post-synthetic modification
PXRD	powder X-ray diffraction
Q	swelling degree
QY	quantum yield
RH	relative humidity
$S_0$	ground state
$S_1$	excited singlet state
SAP	super-absorbent polymer
SBU	secondary building block unit
SC-XRD	single-crystal X-ray diffraction
SEM	scanning electron microscopy
ssPL	solid-state photoluminescence
$T_1$	excited triplet state
TACN	1,4,7-triazacyclononane
TEA	triethylamine
TFA	trifluoroacetic acid
TGA	thermal gravimetric analysis
THF	tetrahydrofuran
TMEDA	tetramethylethylenediamine

TPP	triphenyl phosphine
TPPO	triphenyl phosphine oxide
UV	ultra-violet
VM	S-[2-(Diethylamino)ethyl] O-ethyl methylphosphonothioate
VX	[2-(Diisopropylamino)ethyl]-O-ethyl methylphosphonothioate
ZIF	zeolitic-imidazolate framework
Zr <sub>6</sub>	Zr <sub>6</sub> O <sub>4</sub> (OH) <sub>4</sub> <sup>12+</sup>
Φ <sub>F</sub>	quantum yield

# Contents

<b>Preface</b> .....	i
<b>Acknowledgements</b> .....	ii
<b>Abstract</b> .....	iii
<b>Abbreviations</b> .....	v
<b>Chapter 1. Introduction</b> .....	1
1.1 Chemical Warfare Agents .....	3
1.1.1 Organophosphorus Nerve Agents .....	5
1.1.2 Combative measures for Organophosphorus Nerve Agents .....	6
1.1.3 Recent Events and International Legislations .....	7
1.2 Systems for the Degradation of Organophosphorus Nerve Agents .....	9
1.2.1 Metal-Oxide Surfaces .....	10
1.2.2 Hydrogen Bond Donors and Metal Chelates as CWA Catalysts .....	13
1.3 Metal-Organic Frameworks .....	17
1.3.1 Assembly Strategies .....	18
1.3.2 Photoluminescence in MOFs .....	22
1.3.3 Ligand-Centred Emission in MOFs; Applications and Recent Examples .....	25
1.3.4 Hydration-Dependent Emission .....	28
1.4 Zirconium Metal-Organic Frameworks .....	34
1.4.1 Zirconium MOFs as Catalysts .....	37
1.4.2 Zirconium MOFs as OP CWA Catalysts .....	42
1.4.3 Dehydration of Zr <sub>6</sub> Nodes for Enhancing Hydrolysis .....	51
1.5 Zirconium MOF Composites for CWA degradation .....	54
1.6 Summary and Reflection .....	59
1.7 Thesis Objective .....	61
1.8 Bibliography .....	62
<b>Chapter 2. Screening of potential CWA simulants and catalysts</b> .....	72
2.1 Introduction .....	72
2.1.1 Simulant selection .....	73
2.1.2 Oxidative Hydrolysis .....	76
2.1.3 Hydrolysis .....	77
2.2 Experimental .....	79
Instrumentation .....	79
Synthesis of dimethyl-2-aminobiphenyl-4,4'-dicarboxylate (Amine Lig) .....	79
Synthesis of 2,2'-Bipyridine-5,5'-dicarboxylic acid (BiPy Lig) .....	81
Multi-step synthesis of tris(2',3',5',6'-tetramethylbiphenyl-4-carboxylic acid) (Boron Lig) .....	81
Synthesis of Cu(TMEDA)Cl <sub>2</sub> .....	84

Synthesis of DUT-52 .....	84
Synthesis of DUT-84 .....	85
Synthesis of UiO-67-BiPy-ML (Approximate Formula $ZrO_4(OH)_4(BiPy\ Lig)_{4.5}(BPDC)_{1.5}$ ) .....	86
Synthesis of UiO-67-NH <sub>2</sub> -ML (Approximate Formula $ZrO_4(OH)_4(Amine\ Lig)_3(BPDC)_3$ ) .....	87
Synthesis of MOF-808 .....	88
Synthesis and Characterization of Zr-Boron MOF .....	89
Procedure for the Oxidation of triphenyl phosphine with MONPs .....	90
Procedure for the Oxidation of Diethyl phosphite with MONPs .....	90
Procedure for the Degradation of Diethyl chlorophosphate with MONPs .....	91
Procedure for the Oxidation of Diethyl phosphite with Cu <sup>2+</sup> .....	91
Procedure for the Reaction condition assessment of Diethyl phosphite with Cu <sup>2+</sup> .....	91
Procedure for the Non-buffered hydrolysis of DMNP .....	92
Procedure for the Buffered hydrolysis of DMNP .....	92
Procedure for the Humidity Water Absorption assessment of MOF-808 .....	92
Procedure for the Neat Hydrolysis of GB (performed by DSTL) .....	92
Procedure for the Aqueous Hydrolysis of VX (performed by DSTL) .....	92
Procedure for the Hydrolysis of VX with stoichiometric H <sub>2</sub> O (performed by DSTL) .....	93
Procedure for the Neat Hydrolysis of VX (Performed by DSTL) .....	93
2.3 Oxidative Hydrolysis .....	94
2.3.1 Phosphine Oxidation .....	94
2.3.2 Autodegradation of Diethyl Chlorophosphate .....	96
2.3.3 Oxidative Hydrolysis of Diethyl phosphite .....	97
2.4 Hydrolysis .....	102
2.4.1 Choice and Synthesis of Zirconium MOF catalysts .....	102
2.4.2 Zirconium MOFs as hydrolysis catalysts for DMNP hydrolysis .....	105
2.5 Preliminary OP CWA degradation using Nominated Catalysts .....	110
2.5.1 Preliminary GB Degradation using Oxidation Catalysts .....	110
2.5.2 Preliminary VX Degradation using Hydrolysis Catalysts .....	111
2.6 Summary and Conclusion .....	117
2.7 Bibliography .....	119
<b>Chapter 3. Photoluminescence as a Probe for Screening the Functional Properties of MOFs</b> .....	123
3.1 Introduction .....	123
3.2 Experimental Methods .....	128
Emission Measurements .....	128
PXRD Measurements .....	129
Contact Angle Measurements .....	129

PL Measurements under N <sub>2</sub> and CO <sub>2</sub> environments.....	130
PL Measurements under H <sub>2</sub> S environment .....	130
Wet/Dry Cycling of MOF-1 (Ba) and MOF-2 (Sr).....	130
Synthesis of UiO-67-NH <sub>2</sub> -ML, UiO-67 BiPy-ML, DUT-52, DUT-84, MOF-808 and Boron MOF .....	130
Synthesis of 2,3,6-tris(4-phosphonophenyl)pyridine ligand (H6L) (Performed by Z. H. Fard) .....	131
Synthesis and characterization of MOF-1 (Ba) and MOF-2 (Sr) (Performed by Z. H. Fard) .....	131
Synthesis of L1, L2, L5, L6 and L7 ligands (Performed by R. J. Marshall) .....	131
Synthesis and characterization of Zr-L1, Zr-L2, Zr-L5, Zr-L6 and Zr-L7 (Performed by R. J. Marshall) .....	132
3.3 Solid State Photoluminescence of Zirconium MOF CWA Catalyst Candidates.....	134
3.4 Solid-State Photoluminescence in Alkaline Earth MOFs.....	136
3.4.1 Hydration .....	136
3.4.2 Detection Limit – A Humidity Study.....	140
3.4.2 Reversibility of Hydration .....	141
3.5 Solid State Photoluminescence in a series of Iso-Structural Zirconium MOFs.....	146
3.5.1 Hydration .....	146
3.5.2 Solvatochromism .....	156
3.6 Summary and Conclusion .....	160
3.7 References .....	162
<b>Chapter 4. Activation through Hydration of Zirconium MOF Nodes.....</b>	<b>165</b>
4.1 Introduction .....	165
4.2 Experimental methods.....	169
Instrumentation .....	169
MOF-808 Synthesis and Characterization.....	169
DUT-84 Synthesis and Characterization.....	170
UiO-66 Synthesis and Characterization .....	172
Benzoic acid modulated UiO-66 (Benzoic acid) Synthesis and Characterization.....	174
Boron MOF Synthesis and Characterization .....	175
DMNP and VM hydrolysis procedure.....	175
4.3 Results and Discussion .....	176
4.3.1 Synthesis of nMOFs.....	176
4.3.2 Microwave activation of MOF-808 and Optimisation .....	176
4.3.3 Microwave activation of Acetate-Modulated MOFs .....	179
4.3.4 Thermal Analysis of Activated MOFs .....	186
4.4 DMNP Hydrolysis Enhancement .....	190

4.5 Zirconium MOFs as Hydrolysis Catalysts for live CWA Hydrolysis .....	197
4.6 Conclusion .....	200
4.7 References .....	201
<b>Chapter 5. MOF/HIPE Composites for the Encapsulation and Degradation of VX .....</b>	<b>204</b>
5.1 Introduction .....	204
5.2 Experimental Methods.....	208
Instrumentation .....	208
<sup>1</sup> H MAS NMR Analysis .....	208
Synthesis of DUT-52 .....	208
Synthesis of MOF-808 .....	209
Synthesis of 4-vinylbenzyl piperidine.....	209
General procedure for HIPE Formation (Performed by Alexander J. Wright) .....	209
Swelling with methyl benzoate procedure (performed by Alexander J Wright) .....	211
Buffered DMNP hydrolysis procedure .....	211
DMNP hydrolysis throughout sections of MOF-HIPE.....	211
MOF-HIPE-S Hydrolysis Cycling .....	212
Non-Buffered DMNP hydrolysis procedure .....	212
VX hydrolysis procedure in the presence of Water/THF (performed by Nicholas J. Cooper) .....	213
Neat VX hydrolysis procedure (performed by Nicholas J. Cooper) .....	213
5.3 Results and Discussion .....	214
5.3.1 Swelling studies.....	214
5.3.2 Prototyping .....	215
5.3.2.1 DUT/HIPE .....	215
5.4 Working Prototypes .....	218
5.4.1 MOF-HIPE, a working prototype .....	218
5.4.2 MOF-HIPE-S, Enhancing Aqueous Compatibility.....	222
5.4.3 MOF-HIPE-VBPP-S; Heterogeneous Amine.....	224
5.5 HIPE Swelling Summary .....	230
5.6 Simulant Hydrolysis Summary .....	232
5.7 Encapsulation and Degradation of V-series Agent .....	237
5.8 Summary and Conclusion .....	242
5.9 References .....	244
<b>Chapter 6. Thesis Summary and Conclusion .....</b>	<b>246</b>
6.1 Thesis Summary .....	246
6.2. Thesis Conclusion .....	249
6.3 Future Work .....	251

<b>Chapter 7. Appendix</b> .....	253
7.1 Boron MOF Single Crystal Data (performed by Helena J. Shepherd) .....	253
7.2 ssPL Emission Spectra of L2-Me <sub>2</sub> and L7-Me <sub>2</sub> in the Presence of Various Solvents .....	254
7.3 Buffered DMNP hydrolysis in the presence of MOF-HIPE composites and THF/H <sub>2</sub> O.....	255
7.4 Buffered DMNP hydrolysis in the presence of MOF-HIPE composites and H <sub>2</sub> O .....	258
7.5 MOF-HIPE-S Hydrolysis Cycling .....	259

## Chapter 1. Introduction

This introductory chapter explores some of the background knowledge regarding Chemical Warfare Agents (CWAs) and the systems which exist for countering their existence. First, an overview is given to establish what a CWA is and a brief outline of the various CWAs which have existed through time. Focusing on OP (organophosphorus) CWAs, a summary is provided of the OP nerve agents which have been developed and utilised in the last century. The mode of action of these Nerve Agents is explained along with the current preventative and combative methods which exist for dealing with them in a military and civilian setting. The limitations of the current techniques is discussed. Finally, a compilation of recent events is provided to highlight the danger that CWAs still pose to humans.

The scientific literature is surveyed to identify the state of the art technologies which have been established for dealing with OP CWAs. An emphasis is made on the degradation of CWAs and three leading technologies are chosen and studied in more detail. First, metal oxide surfaces which possess highly intricate surface morphologies and exhibit a remarkable degree of surface reactivity.<sup>1-3</sup> Secondly, hydrogen bond and metal chelate catalysts which display a high degree of specificity for OP CWAs.<sup>4-6</sup> Third, Metal-Organic Frameworks (MOFs), a group of hybrid materials which demonstrate an almost biomimetic ability, comparable to that of a phosphotriesterase (PET) enzyme, to bind and degrade OP CWAs.<sup>7-9</sup> MOFs are recognized as showing the most promise as potential materials for the degradation of CWAs. A focus is then made on MOFs and an in-depth overview is provided on their utility along with the synthetic strategies which exist for assembling these frameworks. Zirconium MOFs receive special attention due to their outstanding chemical stability<sup>10</sup> and the numerous publications which discuss their application as potent hydrolysis catalysts for CWA degradation.<sup>11,12</sup> These publications are then compiled to identify the most suitable Zirconium MOF catalyst.

Due to their effectiveness at a low catalytic loading combined with fast degradation rates,<sup>9,13</sup> this review determined that MOFs were the most effective catalyst for the hydrolysis of OP

CWAs and CWA simulants. Hydrolysis was the shortlisted degradation method and so a natural interest was developed for the hydration of MOF catalysts. Due to the conjugated nature of MOF components,<sup>14,15</sup> a vast number of photo-luminescence studies have been undertaken including some which deal with hydration dependent fluorescence.<sup>16,17</sup> A general assessment of ligand based emission in MOFs is then undertaken along with an insight as to how functional properties can be derived from these emissive profiles. The focus is then shifted to hydration dependant fluorescence and how this can act as a probe for identifying numerous functional attributes.

Finally, the information in this introductory chapter is summarised and the most appropriate technology for CWA degradation is identified. A thesis objective is then presented which sets the tone for the following chapters.

## 1.1 Chemical Warfare Agents

CWA is a broad term which encompasses a range of chemical compounds, the primary function of these materials is to injure, incapacitate or kill other humans.<sup>18</sup> CWAs should not be confused with biological warfare which encompasses the use of viruses, bacteria and other biological toxins to inflict harm on organisms. CWAs can be split into several distinct categories based on their mode of action. This very short section will provide a brief outline of each category of CWAs.

Blistering agents, also referred to as vesicants, are a group of CWAs which severely irritate the skin, eyes and respiratory tract.<sup>19</sup> A group of compounds known as the Sulfur Mustards, sometimes also referred to as mustard gas, are a prime example of blistering agents (Figure 1.1). Skin exposure to sulphur mustard causes extreme chemical burns in the form of skin lesions which manifest themselves as large blisters. These large blisters can take a very long time to heal and easily become infected.<sup>20</sup> Upon inhalation of a vesicant, blistering of the respiratory tract can result in severe breathing difficulties. Additionally, mustard agents are capable of alkylating DNA, making them highly cytotoxic. The overwhelming number of physical ailments caused by blistering agents can easily incapacitate a person and if not immediately treated, can readily cause death. An enhanced group of vesicants known as the nitrogen mustards perform a similar function but have also found a use as chemotherapy agents.<sup>21,22</sup> Whilst protective clothing and respiratory equipment can be worn to minimize exposure to these agents, the immediate damage upon contact is irreversible. Blistering agents are therefore extremely dangerous compounds that are capable of incapacitating and killing humans.

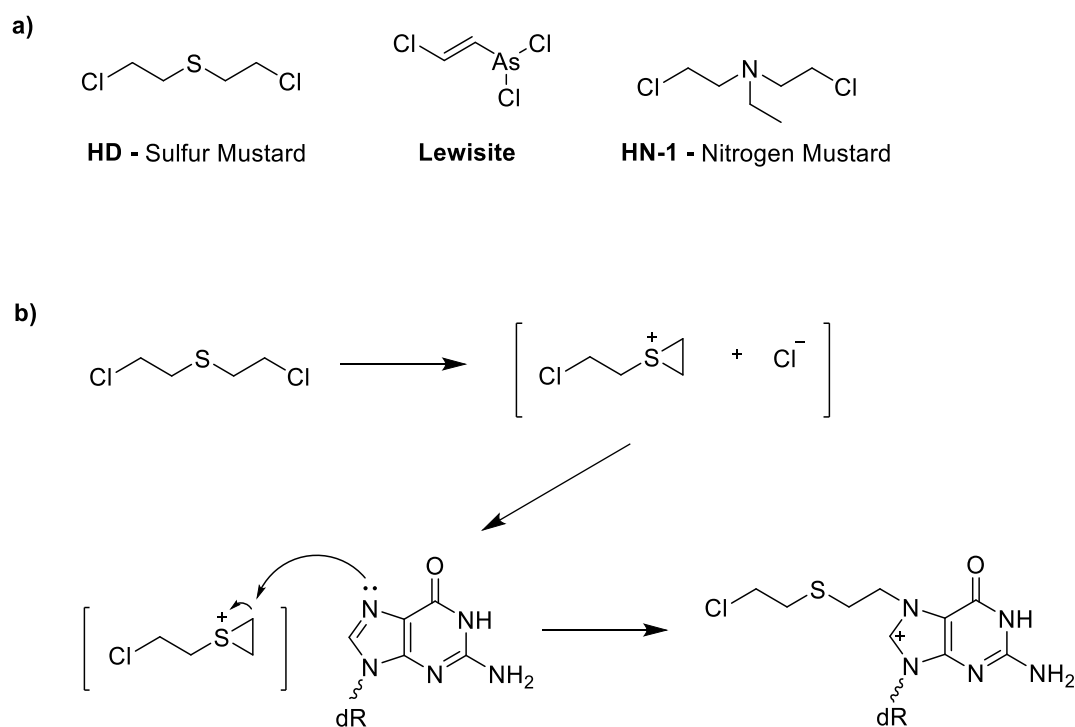


**Figure 1.1.** a) A structural representation of some common vesicants. b) Example mechanism of HD induced alkylation a 2-deoxyguanosine base: one chloroethyl side-chain undergoes intramolecular cyclization to form ethylsulfonium ring, the intermediate reacts rapidly with a nucleophilic group, such as the nitrogen of 2-deoxyguanosine, this is followed by the cyclization of the remaining chloroethyl side-chain which either reacts with another nucleophilic species. Reproduced from reference 23.

Blood agents are another group of CWAs which can prove fatal upon inhalation or ingestion.

(Figure 1.2) Blood agents are known as such because they inhibit the bodily function of consuming oxygen from the blood stream.<sup>24</sup> A classic example of a blood agent is hydrogen cyanide gas which can be readily absorbed into the blood stream upon inhalation. The cyanide ion is capable of binding to the ferrous heme-groups in cytochrome-c enzymes blocking the last steps of aerobic cellular respiration. Other examples of blood agents are cyanogen compounds along with phosgene and arsine.<sup>25</sup> Whilst blood agents can be readily countered by the use of respiratory equipment, the faint odour of these compounds can make them difficult to detect thus making it all too easy to be exposed to a lethal dose.



**Figure 1.2:** A structural representation of some common blood agents.

### 1.1.1 Organophosphorus Nerve Agents

Organophosphorus chemical warfare agents (OP CWAs) are a group of organophosphorus compounds, which inhibit the enzyme acetylcholinesterase.<sup>26</sup> Acetylcholinesterase is responsible for the breakdown of the neurotransmitter acetylcholine into acetic acid and choline.<sup>27</sup> The build-up of acetylcholine results in prolonged muscle contractions, which can produce symptoms such as hypotension, bronchoconstriction and a slowed heart-rate.<sup>28</sup> The combination of symptoms exhibited during exposure to a lethal dose of nerve agent can very quickly lead to respiratory failure and death due to the disruption of the normal functioning of the nervous system. Nerve agents can be introduced to the body dermally, by inhalation or in rare instances as a result of ingestion. The first series of Nerve Agents, the G-series were discovered serendipitously whilst surveying organophosphates, which at the time had been noted for their cholinergic properties,<sup>29</sup> as potential pesticides. In order of discovery and increasing toxicity, the G-series (Figure 1.3), includes Tabun (GA), Sarin (GB), Soman (GD) and Cyclosarin (GF).<sup>27,30</sup>

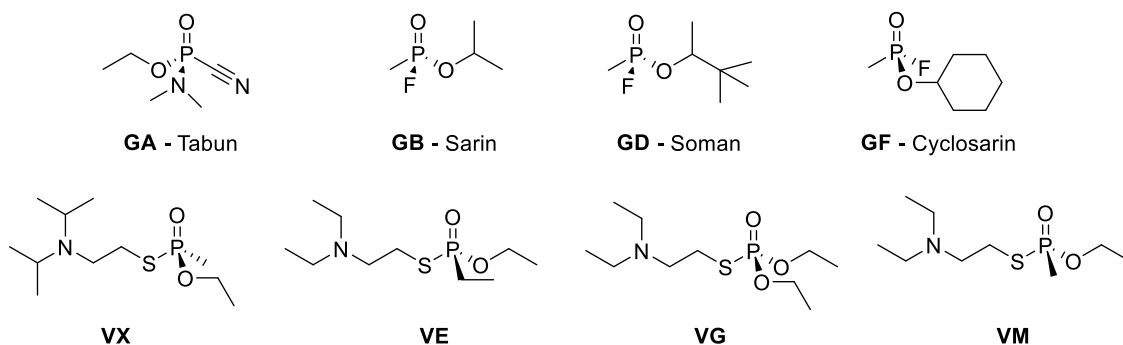


**Figure 1.3:** A structural, single enantiomer illustration of the G and V-series agents

The next series; the V-series, were discovered just over a decade later, again whilst investigating organophosphates as pesticides and insecticides. The V-series (Figure

1.3), consists of VX, VE, VG and VM; nerve agents in the V-series have a significantly higher toxicity than agents of the G-series.<sup>27,30</sup> Agents such as GB are more volatile by nature and are often deployed as a vapour or aerosol mist. The V-series agents have a much lower vapour pressure but can be used effectively as an area denial weapon due to their resilience in the environment combined with their high lethality upon contact with skin. The synthesis of nerve agents is non-stereoselective and so they exist as a racemate, however it should be noted that (-)-GB, (-)GA and (-)-VX are considerably more toxic than their (+) enantiomer counterparts.<sup>31</sup>

### 1.1.2 Combative measures for Organophosphorus Nerve Agents

The methods which are currently employed for bulk CWA degradation are stoichiometric in nature. A large excess of a reagent such as aqueous sodium hydroxide or bleach, along with a surfactant, is used to oxidise the OP CWA.<sup>32,33</sup> The diagram in Figure 1.4 illustrates the degradation pathway for the hydrolysis of G-series agent Sarin and the V-agent VX. G-series agents are typically hydrolysed by the severance of P-F bond (P-CN in the case of GA), thus producing HF and the isopropyl methyl phosphonic acid (IMPA) as a by-product. The P-F bond is relatively labile which results in Sarin having a short persistence in humid environments.<sup>34</sup> Fast hydrolysis can be achieved with the use of weakly acidic or basic solutions.<sup>33</sup>

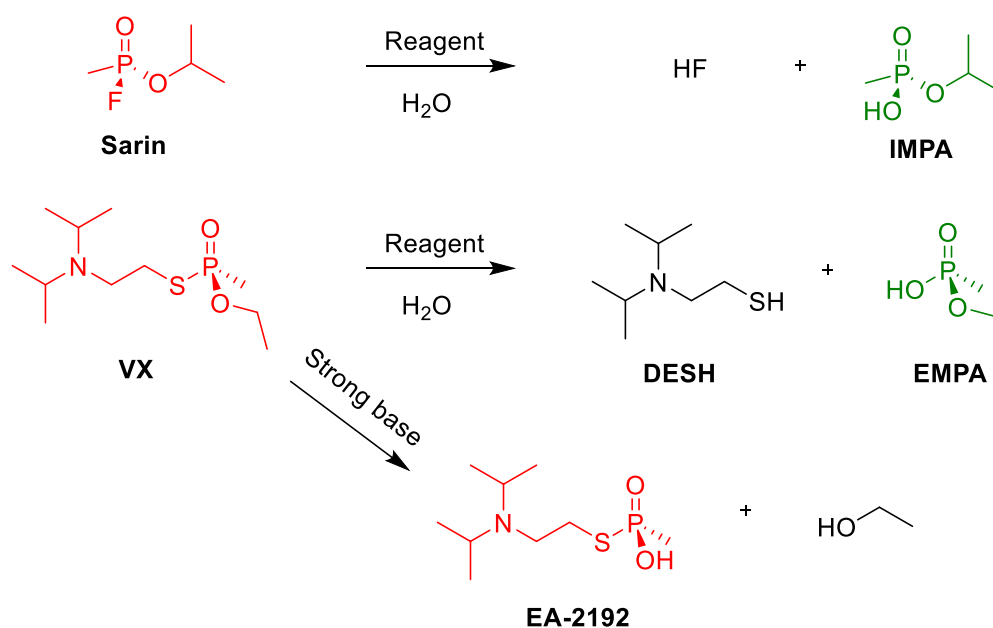


**Figure 1.4:** A schematic outlining the degradation pathways for Sarin and VX.

VX and other V-series agents can be degraded by the selective hydrolysis of the P-S to give the ethyl methyl phosphonic acid (EMPA) product.<sup>33</sup> V-agents are highly persistent under ambient conditions and as a result of this, are often deployed as area-denial weapons to prohibit infrastructure access.<sup>35</sup> Employing a highly alkaline reagent for V-agent can result in P-O bond hydrolysis occurring, this generates the EA-2192 (Figure 1.4) by-product which possesses a toxicity similar to that of the original V-agent.<sup>36</sup> When degrading V-series agents, it is therefore imperative to employ a mild enough reagent that results in selective P-S bond hydrolysis.

### **1.1.3 Recent Events and International Legislations**

A number of protocols and conventions exist to control the use, storage and manufacture of CWAs. The 1925 Geneva Protocol<sup>37</sup> is an international treaty which prohibits the use of chemical and biological weapons in warfare, there are so far 133 member nations. In 1993, the Chemical Weapons Convention<sup>38</sup> was established, this arms control treaty prohibits the development, production, stockpiling and use of CWAs. As of 2015, 191 nations have signed the treaty and have commenced/finished the destruction of their CWA stockpiles. US congress reports have stated that North Korea possess a significant quantity of chemical and biological weapons,<sup>39</sup> Sudan and Egypt have historically stockpiled and utilised CWAs and there have been no reports of these weapons being decommissioned.<sup>40</sup> Incidentally, North Korea, Sudan and Egypt are the only existing nations which have not yet acknowledged the treaty.

Some of the most documented and publicised incidents involving the use of nerve agents are the 1995 Tokyo subway sarin attack<sup>41</sup> and the more recent 2013 Ghouta chemical attack. In the Tokyo subway incident, plastic bags containing GB were pierced and abandoned on subway trains by domestic terrorists. The attack resulted in the death of 12 people, another 50 civilians were left in a critical condition and nearly 1,000 more displaying cholinergic symptoms. The Ghouta chemical attack<sup>42</sup> occurred in the 2013 Syrian civil war when the suburbs of Damascus, Syria were struck by rockets containing GB. According to several different sources, the death toll for this attack is estimated to be anywhere between 300 and

1,700 people with another 3,000 people exhibiting symptoms of exposure to the agent.<sup>43,44</sup>

The 1980-88 Iran-Iraq war<sup>45</sup> is however the most chilling example of the widespread use of chemical weapons. Tabun was readily deployed against Iranian troops resulting in an estimated 50,000 casualties; many thousands more troops and civilians were also afflicted by the long term effects of neurotoxicity.<sup>46</sup> These events highlight just how devastatingly effective nerve agents can be when they are used as a weapon against other human beings.

## 1.2 Systems for the Degradation of Organophosphorus Nerve Agents

Since the original inception of OP CWAs, there have been countless studies which have explored their detection, immobilization and degradation. This next section will aim to provide an overview of the current systems which exist for the catalytic degradation of OP CWAs. Several initial avenues are explored.

Nano-structured metal oxides are well established as oxidation catalysts in the literature. Cerium dioxide possesses a highly reversible redox potential for the redox of  $\text{Ce}^{3+}/\text{Ce}^{4+}$ ; this cycle is responsible for oxidative properties of the material.<sup>3,47</sup> Titanium dioxide is another material which has been shown to function as a potent photo-oxidation catalyst with absorption occurring in the visible UV region.<sup>48,49</sup> These materials have also been studied for their ability to degrade various CWA simulants along with OP CWAs. The oxidative properties of these metal oxides is intrinsically linked to their size and morphology. The following section will aim to provide a selective overview of the various metal oxides which have been reported as CWA degradation catalysts. Hydrogen-bonding catalysts<sup>50</sup> also display a high affinity for OP CWAs, while metal chelate complexes have displayed near biomimetic behaviour for their ability to degrade phospho-esters.<sup>5,6</sup> A selection of previously reported homogeneous catalysts will be reviewed (section 1.2.2) for their efficacy as OP CWA degradation catalysts.

Finally, zirconium MOFs have shown significant promise as OP CWA hydrolysis catalysts and will become the focus of this introductory chapter. The catalytic properties of Zr MOFs are derived from empty/defective coordination sites on the  $\text{Zr}_6\text{O}_4(\text{OH})_4^{12-}$  ( $\text{Zr}_6$ ) cluster which function as Lewis acids (LA).<sup>51</sup> Section 1.4 will explore the evolution of the zirconium MOF hydrolysis catalyst from UiO-66<sup>52</sup> to the optimisations that have led to the enhanced MOF-808<sup>8</sup> and NU-1000 catalysts.<sup>11</sup> Finally, Section 1.5 will then explore the various zirconium MOF composite materials which have been developed for CWA.

### 1.2.1 Metal-Oxide Surfaces

Metal oxide nanoparticles (MONPs) are well established in the literature as potent oxidation and oxidative hydrolysis catalysts.<sup>53–55</sup> The high reactivity is owed to their high surface area and their surface activity; reduction and oxidation (redox) reactions occur on this surface.

MONPs can function as heterogeneous catalysts thus giving them the advantage of being robust and easily recyclable for a high throughput conversion. A variety of different MONPs exist for oxidation catalysis. These MONPs can be transition metal oxides such as CuO and Al<sub>2</sub>O<sub>3</sub>,<sup>56–58</sup> Lanthanides such as CeO<sub>2</sub><sup>59–61</sup> or even composites of two metals such as Au-TiO<sub>2</sub>.<sup>62</sup> CeO<sub>2</sub> provides a good model for showcasing the oxidative and reductive processes which can occur through a catalytic cycle. Figure 1.5 shows a scheme for the disproportionation of H<sub>2</sub>O<sub>2</sub> into H<sub>2</sub>O and O<sub>2</sub>. This involves both the reduction (Ce<sup>4+</sup> to Ce<sup>3+</sup>) and oxidation (Ce<sup>3+</sup> to Ce<sup>4+</sup>) of the cerium, and therefore the regeneration of the catalyst.

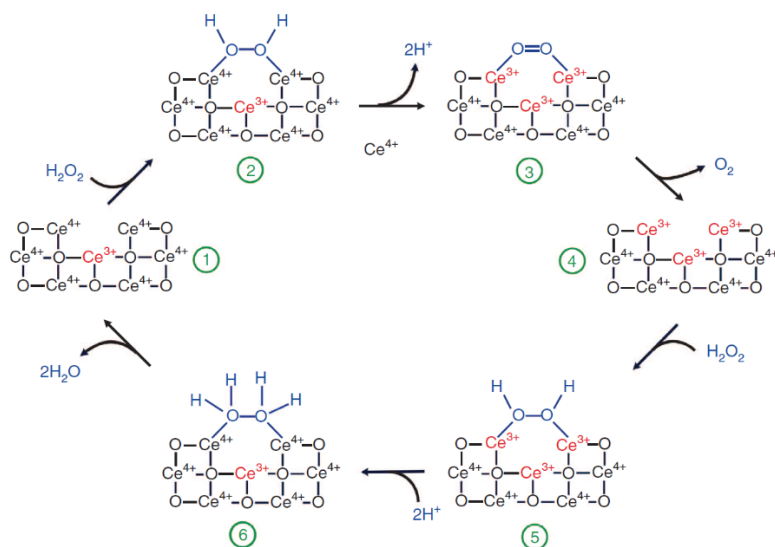


**Figure 1.5.** A reaction mechanism showing the complete disproportionation of hydrogen peroxide on the surface of a cerium MONP. Reproduced from reference 63.

The synthesis of MONPs can be modified to result in specific facets of the oxide structure being exposed on the surface, thus providing some control over the shape of the nanoparticle.

Mesoporous MONPs of various pore shapes and sizes,<sup>2</sup> as well as composite MONPs can be

synthesised,<sup>64</sup> a degree of control can therefore be had over the bulk structure of the nanoparticle. The size, shape and structure of MONPs is therefore highly tunable. Bulk metal oxides have stable structures and surfaces that are well-defined crystallographic planes, but it is these properties that can limit their usefulness. MONPs can on the other hand exhibit a higher density of surface edge and corner sites than larger particles due to their smaller volume. This is because the phases associated with these planes increase in stability when the particle decreases in size resulting in a decrease in surface energy at these planes. Ceria provides a good example of this phenomenon;<sup>65,66</sup> the most stable shape that a bulk ceria particle can take on is that of a truncated octahedron. In a truncated octahedron configuration, the (111) facets, or crystallographic planes, are the most stable and therefore the most abundant with the more reactive (001) facets making up a small proportion of the total surface area (See Figure 1.6 a)) A decrease in overall particle size will therefore increase the abundance of the (001) facet in relation to the (111) facet thus exposing a more reactive surface (Figure 1.6). This can be taken even further if the particle is synthesised to take on a cubic morphology where the majority of the surface consists of the (111) facet as opposed to the (001).<sup>67</sup>

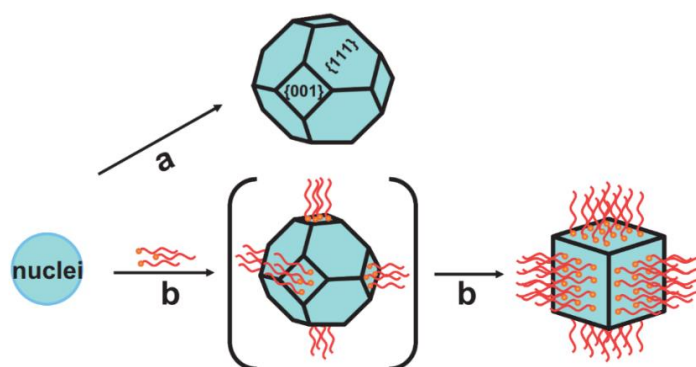


**Figure 1.6.** The shape control of ceria nanocrystals. a) A truncated octahedron in the case when no organic ligand molecules are used. b) At a low decanoic acid to ceria precursor ratio, the preferential interaction of the ligand molecules with the ceria (001) planes slows the growth of (001) faces relative to (111) faces, which leads to the formation of nanocubes. Figure reproduced from reference 67.

In terms of CWAs, there have been a significant number of publications relating to the use of MONPs as catalysts for the degradations of both CWAs and CWA simulants.<sup>62,68,69</sup> Recently, a variety of Ceria nanoparticles, each prepared using a different synthetic route were found to be effective for the stoichiometric degradation of the agents VX and GD.<sup>68</sup> Ceria samples prepared by a homogeneous hydrolysis method and by precipitation from a bicarbonate precursor were found to be the most effective. The catalytic loading was exceptionally high: a 50-fold excess of catalyst was present relative to substrate. Complete hydrolysis was achieved, however, in 10 minutes for both VX and GD thus making Ceria a suitable degradation agent. Similar results were achieved using mesoporous manganese oxide with the same catalytic loading relative to the substrate.<sup>70</sup> VX was fully hydrolysed in 8 minutes, GD was however only 50% hydrolysed in 16 minutes and the hydrolysis did not proceed much further, even after an hour.

Nano-tubular titania is yet another nanoscale catalyst which has been employed for the hydrolysis of VX, GD and HD.<sup>48</sup> A very large stoichiometric excess of catalyst was used for each study so the catalyst loading efficiency is questionable. Despite this, an impressive degradation half-life of 58 minutes was observed when VX was loaded onto a large excess of the dry titania. This half-life was enhanced further to only 24.7 minutes when an excess of water was used.

Metal oxides have been portrayed as effective materials for the degradation of neat nerve agents. Unfortunately, none of the above studies can be truly described as catalytic since a large stoichiometric excess of the metal oxide is used relative to the substrate, where in fact vacancies and defects in the metal oxide are often the site of reaction. Investigating whether any of these materials retain their efficacy at much lower concentrations would allow one to determine whether they can be employed for the neat, catalytic breakdown of CWAs.

### 1.2.2 Hydrogen Bond Donors and Metal Chelates as CWA Catalysts

This next section will explore some previously reported hydrogen bond and metal chelate systems. The systems which will be discussed have all been reported for the application of either CWA simulant or OP CWA degradation.

The P=O and P-O functionalities of OP CWAs can act as effective hydrogen bond acceptors (HBAs). Figure 1.7 below shows a proposed mechanism for the hydrolysis of the diethyl cyanophosphonate (DCNP) simulant using 1,3- Diindolylurea derivatives.<sup>4</sup> 1,3- Diindolylureas have been previously noted for their selectivity towards phosphate anions in polar solvent mixtures and in the solid state through HB interactions.<sup>71</sup> The carboxylate functionality on the urea provide an electron withdrawing effect on the nitrogen atoms which in turn creates a more polarised N-H bond, this makes the N-H protons particularly strong hydrogen bond donors (HBDs). The example below shows the P=O: oxygen acting as a HBA and forming a bifurcated hydrogen bond with the N-H protons; the P-O oxygen also acts as a HBA. The immobilisation of the DCNP simulant through hydrogen bonds draws the P=O electron density towards the HBD species thus destabilising the P-CN bond, which allows H<sub>2</sub>O to substitute the cyano species. Whilst several H-bond catalysts exist for CWA degradation, they all function in a similar fashion to the mechanism shown in Figure 1.7; the P=O: acts as a HBA and the binding of the substrate through H-bonds destabilises the P-S, P-F or P-CN bond and activates it for nucleophilic substitution by H<sub>2</sub>O. Studies using the simulants DCNP and DECP with these catalysts show modest enhancements in the rates of hydrolysis. Up to a 44% enhancement in the rate of DECP hydrolysis was observed in the presence of 0.001 equivalents of catalyst. Interestingly enough, a lower rate of hydrolysis was observed when 0.005 equivalents of catalyst was used in the studies.<sup>4</sup>

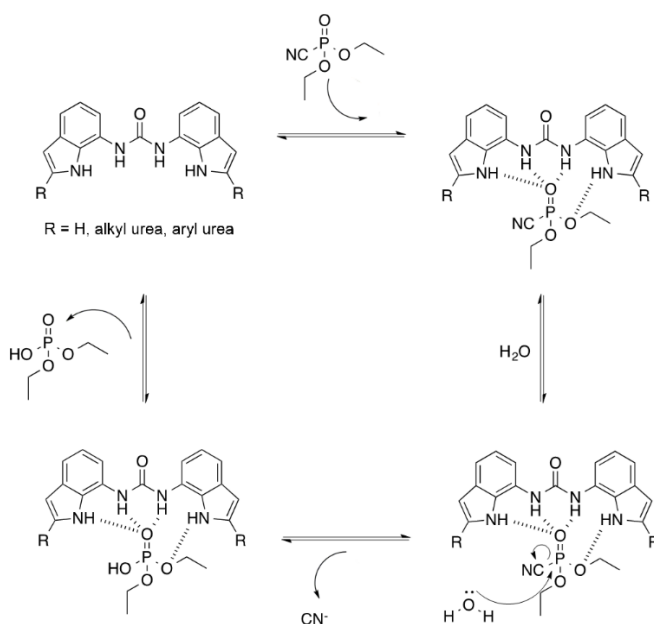


**Figure 1.7.** Proposed mechanism for the hydrolysis of DCNP simulant using 1,3-Diindolylureas which occurs through an associative  $S_N2$  pathway. Reproduced from Reference 4.

In terms of Lewis base mediated catalysis, a number of studies have employed nitrogenous bases to facilitate the hydrolysis. The most recent study describes swellable polymer composed of either polyallylamine or polyvinylamine monomer units.<sup>72</sup> These polymers were functionalised with either 4-aminopyridine, bipyridine or a  $Cu^{2+}$  bipyridine complex. These modified polymers were able to hydrolyse the simulant DIFP as well as the agents GD and VX. These studies were, however, conducted in buffer and an excess of  $H_2O$  and catalyst. Another study describes the use of a water-swelled polystyrene-based polymer where the monomers have been functionalised with trimethylammonium fluoride.<sup>73</sup> This particular polymer is able to selectively hydrolyse VX in the presence of water and a buffer. When six equivalents of VX to polymer catalyst were used, 180 hours were required for the complete hydrolysis of VX into EMPA. From a practical perspective, the timescale and the catalyst loading for the hydrolysis is too high.

All of the above studies were performed in aqueous solutions, with both of the polymer studies being carried out in buffer. Whilst the hydrogen-bond catalysts and the polymers are shown to be effective at low catalytic concentrations, their reliance on a large excess of  $H_2O$

makes them of questionable value. Investigating whether these materials are able to rely on atmospheric H<sub>2</sub>O for their degradation process would further elucidate their efficacy.

Metal complexes of the ligand 1,4,7-triazacyclononane (TACN) have been shown to enable the hydrolysis of phosphodiester. The TACN ligand is highly modifiable and can be readily functionalised to alter both reactivity and solubility. The main application of this is for the hydrolytic cleavage of the phosphodiester linkages in DNA and RNA. It should be noted that in RNA, this can occur through a self-cleaving process due the close proximity of two OH groups on the ribose sugar groups. Therefore, RNA has a higher susceptibility to base-catalysed hydrolysis, higher than that of DNA which is composed of deoxyribose groups.

The example in Figure 1.8 shows a binuclear Zinc TACN complex.<sup>5</sup> The complex consists of a ligand containing two TACN components bound by an alcohol, this ligand is coordinated to two Zn<sup>2+</sup> metal centres. The RNA analogue, 2-hydroxypropyl-4-nitrophenyl phosphate, is the substrate. The complex binds a hydroxyl ion from water deprotonation as well as each terminal phosphoryl oxygen atom. The deprotonation of the 2-hydroxypropyl group is then followed by the nucleophilic attack of the of the phosphorus centre and the elimination of the nitrophenol group. This whole study was conducted using DFT calculations and so no data is available to confirm how efficient the catalyst loading would be experimentally.

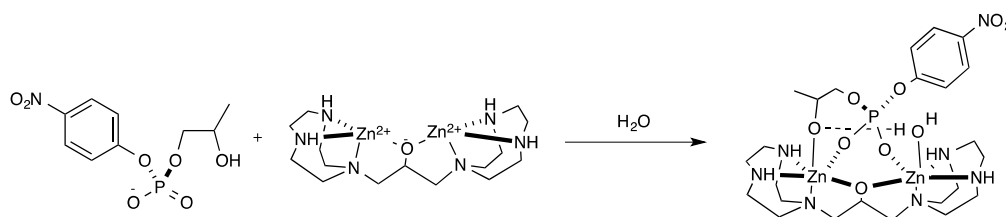


**Figure 1.8.** An illustrated example of a Binuclear Zinc TACN activating 2-hydroxypropyl-4-nitrophenyl phosphate for hydrolysis. Reproduced from reference 5.

Another study utilises the same substrate but a different catalyst. The catalyst this time is a Copper(II) complex consisting of a Cu<sup>2+</sup> centre and a TACN ligand functionalised with a single alkyl guanidine chain.<sup>6</sup> The dimerized structure can be seen in Figure 1.9. It should be noted

that upon exposure to  $\text{H}_2\text{O}_2$ , which is often produced endogenously,<sup>74</sup>  $\text{Cu}^{2+}$  species are capable of generating reactive oxygen species which are capable of oxidatively damaging RNA.<sup>75</sup> The TACN guanidine complex features a  $\text{Cu}^{2+}$  bound oxide which acts as the active nucleophilic species. However, the study employed 20 equivalents of complex to substrate. Due to the large excess of complex relative to the substrate, the hydrolysis of the substrate was modelled as a first-order process. A first order process has a reaction rate ( $\text{s}^{-1}$ ) which depends on the concentration of one reactant. Whilst a large enhanced hydrolysis first-order rate constant was observed for the  $\text{Cu}^{2+}$  catalyst over a control sample, no timescale was presented. It would therefore be interesting to see how either of the two complexes would function as potential catalysts for the degradation of CWAs or the simulant DMNP.

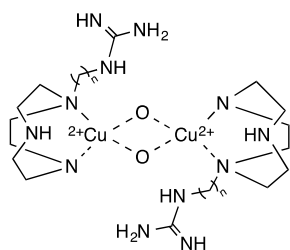


**Figure 1.9.** An illustration of a dimerized Copper TACN guanidine complex for the hydrolysis of 2-hydroxypropyl-4-nitrophenyl phosphate. Reproduced from reference 6.

Copper(II) chelates are yet another group of complexes that have been shown to hydrolyse GB and DIFP.<sup>76</sup> A copper(II) 1,3 diaminopropane complex was shown to hydrolyse 2 equivalents of GB with a half-life of 2 minutes. A Copper(II) tetramethylethylenediamine (TMEDA) complex was able to hydrolyse 1 equivalent of GB with a half-life of 1 minute. 1,8-dihydroxynaphthalene-3,6-disodiumsulfonate and 2,2'-Bipyridine were just some of the other ligands with reasonable half-lives. The reactions were, however, conducted in buffered aqueous media (pH 7-7.5), which hinders their applicability.

All of the studies which have been outlined have utilised a combination of high catalyst loading and a buffering agent to degrade the OP simulants/ CWAs. This limits their practical applicability and so a different material was sought out.

### 1.3 Metal-Organic Frameworks

Metal-organic Frameworks (MOFs) are a *relatively* new subset of highly porous materials which have found a number of potential applications in catalysis,<sup>8,51,77</sup> gas storage,<sup>78–80</sup> separation,<sup>81–83</sup> chemical sensing<sup>17,84,85</sup> and drug delivery.<sup>86,87</sup> The structure of a MOF consists of bridging multi-topic organic ligands coordinated to metal ions or clusters to form a high surface area three-dimensional network (Figure 1.10). MOFs are more commonly assembled using solvothermal synthetic procedures.<sup>88–90</sup> The extensive array of ligands as well as metal ions and clusters that can be employed for the formation of a MOF makes them highly designable, functionally diverse structures.

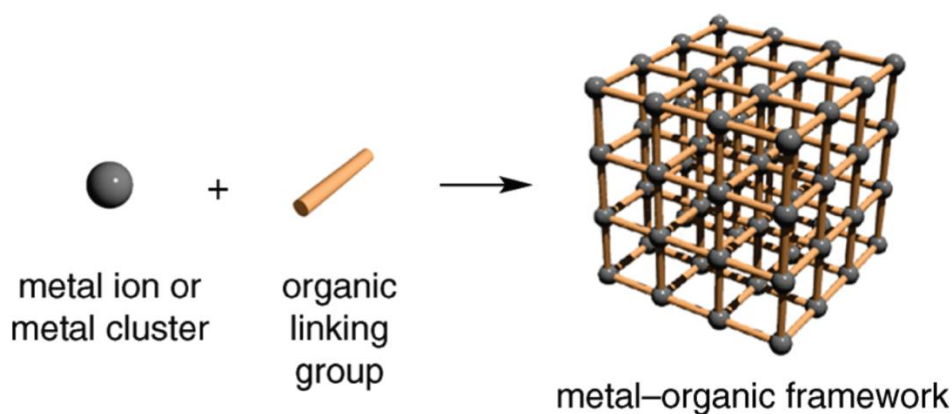


**Figure 1.10.** A simplified schematic illustrating the concept of a metal-organic framework.

Reproduced from Reference 66.

Over the last century, zeolites, a form of aluminosilicate microporous minerals, have been used for several purposes such as separation,<sup>91</sup> catalysis<sup>92</sup> and ion-exchange.<sup>93</sup> Although a number of both naturally occurring and synthetic zeolitic frameworks exist, the number of structures is still rather limited and the potential for rational design and functionalisation is quite narrow. The tunability of pore shape, size and surface functionality is where MOFs excel over zeolites. Despite all the potential that MOFs have had for rational design, the initial problem is related to their stability, as the majority of structures would collapse on the removal of a guest molecule species. MOF-5 (Figure 1.11) was the first developed framework

which maintained its crystallinity upon the removal of a guest solvent.<sup>94</sup> Brunauer-Emmett-Teller (BET) theory,<sup>95</sup> an assumption that gas adsorption occurs in multi-molecular layers, is often used when calculating the surface area of porous materials.<sup>96</sup> The physical volume of the MOF-5 framework is only 20% of the total volume of the crystal; a non-interpenetrating MOF-5 crystal has a BET surface area of around  $\sim 2900 \text{ m}^2/\text{g}$ .<sup>94</sup>

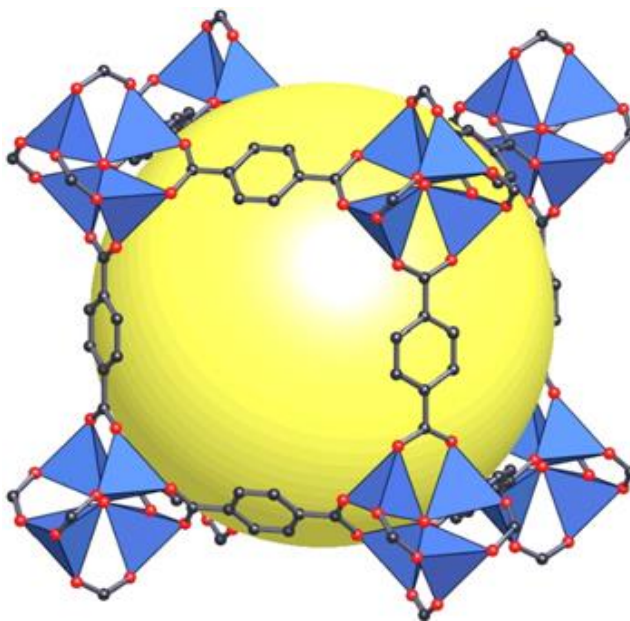


**Figure 1.11.** An illustration of MOF-5, the yellow sphere highlights the high internal void space. Reproduced from reference 97.

The high surface area, high degree of functionalisation and the solid nature of MOF-5 has inspired a whole generation of hybrid metal-organic materials. The next section will provide an outline of synthetic strategies for obtaining MOFs. The following sections will then focus on ligand-based photoluminescence in MOFs followed by the application of zirconium MOFs for catalysis and, subsequently, CWA degradation.

### 1.3.1 Assembly Strategies

There exist a variety of synthetic strategies for assembling metal organic frameworks. Metals salts act as a source of metal for forming the nodes, also known as the secondary building unit (SBU). Varying the metals will affect the overall geometry of the framework based upon the coordination environments of the metal anion/ metal cluster. Multi-topic organic ligands are

then used to bridge these SBUs. The majority of linkers are aromatic carboxylates such as 1,4-benzenedicarboxylic acid<sup>94,98</sup> or biphenyl-4,4'-dicarboxylic acid<sup>88,99</sup> which coordinate to the metal nodes through this functionality. Alternatively, phosphonates<sup>100,101</sup> and pyridines<sup>102,103</sup> can also be utilised as linkers. Imidazolate linkers (imidazole) and tetrahedrally coordinating anions form a group of materials known as zeolitic imidazolate frameworks (ZIFs).<sup>104–106</sup> ZIFs are isostructural to zeolites because they contain a bond angle similar to that of the Si-O-Si bond found in zeolites.<sup>107</sup> The choice of ligand is very important for influencing the pore shape and size. For instance, using a tritopic ligand<sup>108,109</sup> over a ditopic ligand<sup>88,94</sup> will produce a very different pore shape. Employing longer linkers over shorter linkers will increase the pore diameter but can also lead to interpenetration, a phenomenon where two frameworks become physically interconnected.<sup>110,111</sup> By using metals and linkers which possess additional coordination sites / functional groups, the resulting frameworks can be further modified after the initial assembly. This is known as post-synthetic modification (PSM) or post synthetic exchange (PSE).<sup>112–114</sup> The PSM and PSE process is useful for obtaining structures which would otherwise not be feasible if the MOF was grown in a single step (Figure 1.12).

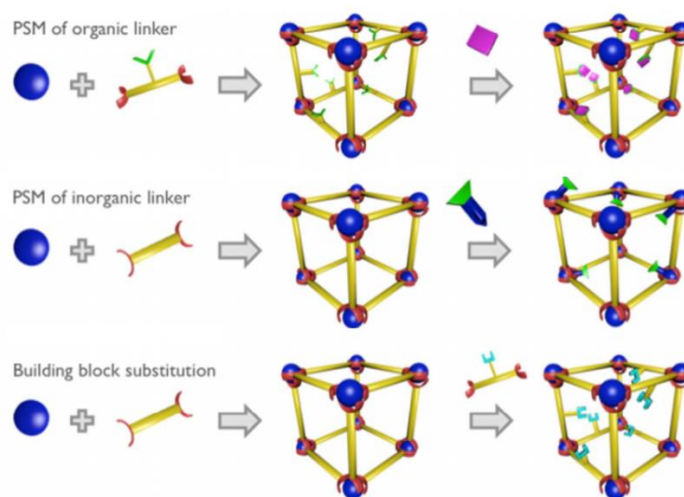


**Figure 1.12.** A schematic illustrating PSM. (Top) An illustration of ligand PSM. (Middle) An illustration of SBU PSM. (Bottom) An illustration of PSE of the organic linker through substitution. Figure reproduced from reference 87.

Solvothermal methods (Figure 1.13) encompass the majority of MOF assembly strategies.<sup>89,90</sup>

The procedure generally involves dissolving the chosen metal source (usually a metal salt) and linker in a high boiling point solvent and heating the mixture in a sealed hydrothermal vessel at elevated temperatures ( $> 100\text{ }^{\circ}\text{C}$ ) for a prolonged period of time ( $\geq 24$  hours). DMF is commonly used as the solvent because it effectively solubilises carboxylate linkers and possesses a high boiling point.<sup>115,116</sup> Other polar solvents such as dimethyl acetamide (DMA), diethyl formamide (DEF), MeOH and H<sub>2</sub>O can also be used. Bulkier solvents such as DEF can prevent framework interpenetration and mixtures of H<sub>2</sub>O/DMF can be used to solubilise particular metal salts.<sup>117,118</sup> There has been significant interest in developing greener synthetic methods and so there a growing number of reports which deal with frameworks which have assembled in just H<sub>2</sub>O,<sup>119,120</sup> by microwave irradiation,<sup>121,122</sup> and under continuous flow.<sup>123,124</sup>

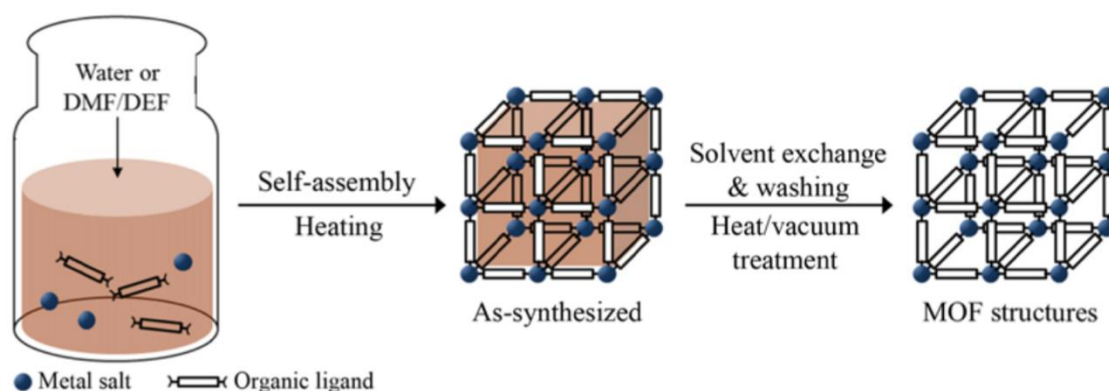


**Figure 1.13.** A graphical illustration of solvothermal MOF synthesis followed by the activation of the material. Figure reproduced from reference 125.

Molecules which form monotopic coordination interactions, such as benzoic acid or hydrochloric acid, are often added to MOF reaction mixtures. These molecules are known as modulators and they compete with the linker for metal coordination sites and effectively result in a controlled assembly.<sup>126–128</sup> The additional control imparted by the presence of modulators is an additional step towards rational MOF design. Modulators can lead to the enhancement of a number of properties such as crystallinity and porosity.<sup>127,129</sup> Varying modulator concentrations can also result in different topologies,<sup>130</sup> dimensionality<sup>131</sup> and

particle size.<sup>132</sup> Some modulators can also help to introduce defects into a structure by occupying coordination sites in favour of the linker.<sup>133</sup> Modulators are therefore important for fine-tuning structural properties in these hybrid structures.

Upon synthesising a framework using conventional solvothermal methods, the material is generally isolated through centrifugation or filtration. Upon isolating a solid powder, the material must then be 'activated'.<sup>134</sup> 'Activation' refers to evacuation of framework pores to remove any residual solvent used during synthesis. This is typically achieved by soaking the solid in a low-boiling solvent such as chloroform or acetone to exchange with any residual high boiling solvent.<sup>135</sup> The solvent-exchanged material is then subjected to a dynamic vacuum to purge the pores. Activation can also refer to the removal of any residual modulator or to any PSM/PSE which must be undertaken to achieve material functionality.<sup>136</sup>

Whilst conventional synthetic methods are hydrothermal/solvothermal, there are a number of alternative strategies which exist for assembling frameworks. Microwave synthesis can be used for the high throughput of reactions due to much shorter reaction times.<sup>122,137,138</sup> Some greener alternatives involve mechanochemical methods (Figure 1.14)<sup>139–141</sup> including liquid-assisted grinding<sup>142,143</sup> which aim to minimise the use of solvents, however, there appears to be a distinct lack of literature reports regarding the synthesis of novel MOFs using these techniques.

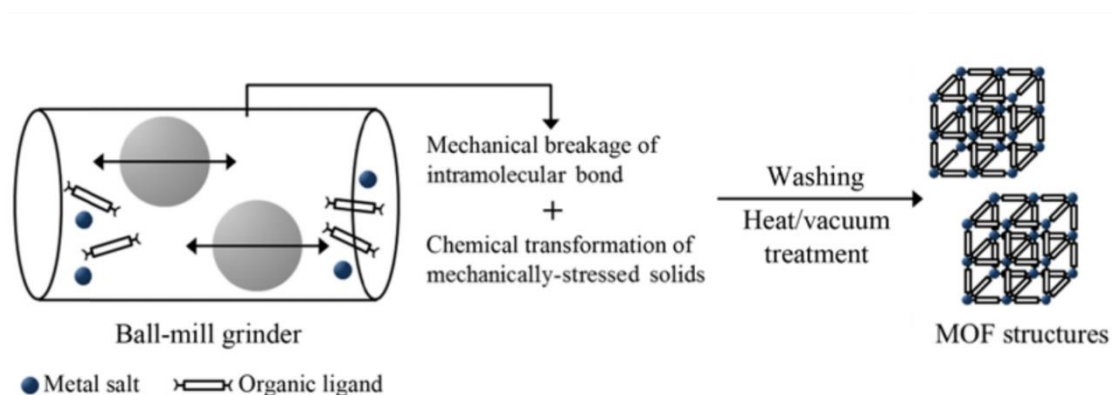


**Figure 1.14.** A graphical illustration of mechanochemical MOF synthesis followed by the activation of the material. Figure reproduced from reference 125.

Finally, when synthesising novel materials, it is essential to characterize them. MOFs are generally highly ordered structures so are structurally characterised using single crystal X-ray diffraction and bulk phase purity is often confirmed using powder X-ray diffraction.<sup>144,145</sup> Unfortunately, obtaining single crystals is not always easy and an empirical approach is often employed where ligand/metal concentrations, heating/cooling rates and modulators are all varied in the hope of obtaining large enough crystals. Aside from X-ray analysis, frameworks are typically analysed using porosimetry to characterise their pore size, surface area and gas sorption properties.<sup>146,147</sup> TGA is also routinely employed to assess the stability of frameworks as well as the presence of any residual solvents and modulators.<sup>148,149</sup> Finally, digestion of frameworks using strong acids yields them to analysis with solution-phase NMR spectroscopy, which can be useful for determining the ratios of the various substituents that compose each framework.<sup>136,150,151</sup>

### 1.3.2 Photoluminescence in MOFs

Photoluminescence is the emission of energy in the form of light after the initial photo-excitation of a material. In terms of MOFs, there are four main origins of photoluminescence (Figure 1.15): 1) ligand-based emission derived from conjugated organic linkers;<sup>152,153</sup> 2) metal-centred emission that typically arises from the electronic transitions in lanthanide metal based SBUs;<sup>154,155</sup> 3) charge-transfer luminescence involving excited state charge transfer via metal-to-ligand charge transfer (MLCT)<sup>156,157</sup> or ligand-to-metal charge transfer (LMCT) transitions;<sup>156,157</sup> 4) guest-induced emission can occur from the incorporation of a photoluminescent guest species into a framework capable of influencing the emission process. This section will focus on ligand-centred emission along with the MLCT and LMCT processes.

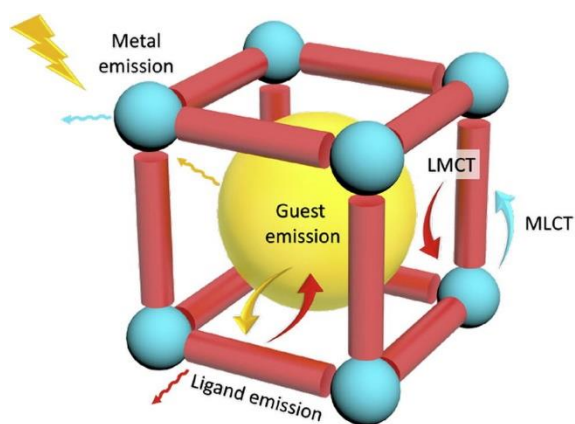


**Figure 1.15:** An illustration of the origins of emission in MOFs. Reproduced from reference 158.

The majority of MOFs are assembled using aromatic linkers which provide rigidity to the framework structure.<sup>158</sup> The  $\pi$ -conjugated nature of these organic linkers results in the framework exhibiting fluorescent / phosphorescent properties (Figure 1.16).<sup>14</sup> Fluorescence is the result of an electron returning from the excited singlet state ( $S_1$ ) to the ground state ( $S_0$ ). Phosphorescence is several orders of magnitude slower than fluorescence and occurs when an electron returns from the excited triplet state ( $T_1$ ) back to the ground state ( $S_0$ ), this occurs through an intersystem crossing process which involves the reversion of an electron spin state.<sup>159</sup> Relaxation of the electron in either state releases energy in the form of a photon.

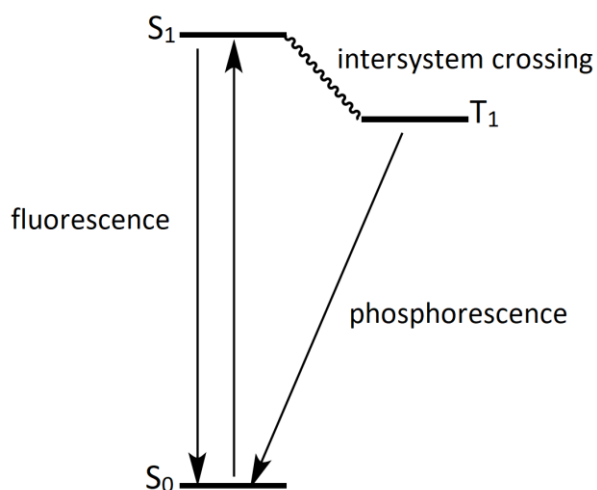


**Figure 1.16.** A simplified Jablonski diagram illustrating fluorescence and phosphorescence.

In conjugated organic linkers, the majority of excitations occur through  $\pi \rightarrow \pi^*$  and  $n \rightarrow \pi^*$  electronic transitions with  $n \rightarrow \pi^*$  transitions harbouring a lower energy requirement. These

transitions generally occur in the near-UV and visible region of the spectrum, with absorption occurring in the 200-400 nm for  $\pi \rightarrow \pi^*$  transitions and the 400-700 nm region for  $n \rightarrow \pi^*$  transitions. The fluorescence of materials can be characterized by recording the emission spectra of materials after excitation at their optimum excitation wavelength ( $\lambda_{ex}$ ), thus determining the maximum wavelength of emission ( $\lambda_{max}$ ). The efficiency of this process can be elucidated by obtaining the quantum yield ( $\Phi_F$ ).<sup>160</sup>  $\Phi_F$  is a measure of the number photons absorbed vs. the number of photons emitted and determined using the following formula:

$$\Phi_F = \frac{\# \text{ Photons emitted}}{\# \text{ Photons absorbed}}$$

The incorporation of a linker into a framework structure often alters the fluorescent properties of the linker. The rigidity provided by the cage structure can lead to the reduction of non-radiative relaxation processes by restricting ligands rotation and vibration, this can result in increased quantum yields and fluorescent intensities.<sup>14</sup> As a result, the  $\lambda_{max}$  and  $\Phi_F$  of the linker molecule will be different to the resulting framework. An example of this can be demonstrated with the simple 1,3,5 benzenetricarboxylate (BTC) linker for which  $\lambda_{max} = 370$  nm ( $\lambda_{ex} = 334$  nm). Incorporating the linker into the  $Zn_3(BTC)_2(DMF)_3(H_2O)_3 \cdot (DMF)(H_2O)$  results in a  $\lambda_{max} = 410$  nm ( $\lambda_{ex} = 341$  nm), in the case of  $Zr_6O_4(OH)_4(BTC)_2(AcOH)_6$ , a  $\lambda_{max} = 446$  nm ( $\lambda_{ex} = 370$  nm) is achieved.<sup>161</sup> This shift in  $\lambda_{max}$  is derived from the mixing of ligand and metal orbitals which alters the emission energy. This phenomenon can be best described as metal perturbed ligand emission and occurs in the vast majority of frameworks. An example of  $\Phi_F$  increases in MOFs relative to their substituent linker are shown in  $\{[Cd_2(bdpb)_2(H_2O)] \cdot 18 DMF\}_n$  MOF composed of the (S)-4,4'-bis(4-carboxyphenyl)-2,2'-bis(diphenylphosphinoyl)-1,1'-binaphthyl (bdpb) linker.<sup>162</sup> The  $\Phi_F$  of the bdpb linker increases from 33 % to 42 % upon incorporation into the cadmium framework.

### 1.3.3 Ligand-Centred Emission in MOFs; Applications and Recent Examples

MOFs can display ligand-centred emission due to the conjugated backbone of the ligands which are used to assemble the framework. Photoluminescent MOFs have shown a number of promising applications in heterogeneous solid-state sensing,<sup>85,163</sup> biomedical imaging,<sup>15,164</sup> drug delivery<sup>14,86</sup> and white light emission.<sup>155,165</sup>

White light emission devices are very important due to their applications in flat panel displays and in the field of lighting. Lanthanide MOFs are generally used for this application due to the intensity of the emission arising from Ln<sup>3+</sup> metals.<sup>155,166,167</sup> However, ideal white-light emitters would avoid the use of such rare-earth metals. Recently, there have been a handful of examples of rare-earth metal free MOFs as potential white-light emitting devices. A semi-conducting 1,4,5,8-naphthalenetetracarboxylate (H<sub>4</sub>ntc) linker was incorporated into a strontium MOF ([Sr(ntc)(H<sub>2</sub>O)<sub>2</sub>]·H<sub>2</sub>O).<sup>165</sup> The MOF was then applied over a layer of inorganic semiconductors and then coated with graphene oxide, this resulted in an electroluminescent white-light which originated from the MOF. Unfortunately, a poor  $\Phi_F$  of only 1.2 % was achieved. Another recent example was the synthesis of an aluminium based MOF using the 9,10-bis(p-benzoate)anthracene (DBA) form Al(OH)(DBA).<sup>168</sup> Al(OH)(DBA) was then loaded with the Rhodamine B to yield RhB@Al-DBA. The MOF-Dye composite results in a dual blue and yellow emission with the framework structure preventing the aggregation induced quenching of the dye. A  $\Phi_F$  of 12.2 % was reported for the emission in this study. Finally, the most recent study reports on a 5-azidoisophthalic acid (N<sub>3</sub>ipa-H<sub>2</sub>) which was used to assemble a zinc MOF ([Zn(N<sub>3</sub>ipa)(Py)<sub>2</sub>]·2H<sub>2</sub>O).<sup>169</sup> The framework showed emission in three different regions, with  $\pi \rightarrow \pi^*$  and  $n \rightarrow \pi^*$  transitions resulting in emission at 384 and 468 nm. A charge transfer from the metal-bound pyridine to the N<sub>3</sub>ipa ligand resulted in a third emission at 570 nm (Figure 1.17). This is a notable example as it involves a single-component framework capable of producing white light with a high  $\Phi_F$  of 32.5 %. Rare-earth-free MOFs for white light emitting devices may still be in their infancy but have shown potential for further development.

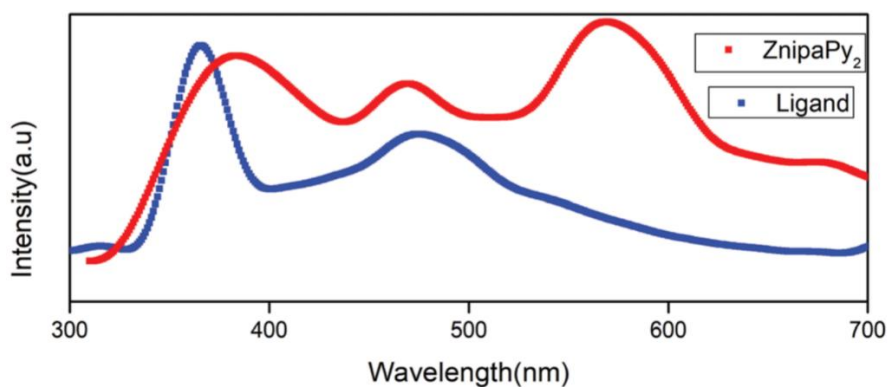


**Figure 1.17.** Solid-state photoluminescence spectra of the free  $N_3ipa$  ligand (blue) and the  $[Zn(N_3ipa)(Py)_2] \cdot 2H_2O$  MOF (red). The MOF shows 3 broad emission profiles which cover the entirety of the visible light spectrum. Reproduced from reference 169.

The application of photoluminescent MOFs in a biomedical setting is another area of interest.<sup>14,86,164</sup> The combination of imaging techniques such as MRI with fluorescence has led to the development of multimodal imaging which can have increased sensitivity and spatial resolution.<sup>170</sup> Rare-earth metals feature in the majority of MOFs which have been reported for use in biomedical imaging.<sup>171–173</sup> Recently however, a zirconium MOF constructed from the porphyrin ligand (5, 10, 15, 20–Tetrakis (4-carboxyl)-21H, 23H-porphine), was grown on a  $Fe_3O_4$  core.<sup>164</sup> The resulting composite demonstrated fluorescence due to the presence of the porphyrin functionality but also exhibited enhanced  $T_2$ -weighted MRI (magnetic resonance imaging) properties as a result of the iron core. The composite material was successfully used for the dual-modality PL / MR imaging of tumour bearing mice (Figure 1.18). A number of alternative imaging materials have been reported which involved the use of MOFs as carriers of fluorescent dyes such as Rhodamine-B<sup>86,174</sup> and Indocyanine green<sup>175</sup> for fluorescent imaging, however, the origin of this emission cannot truly be considered ligand based.

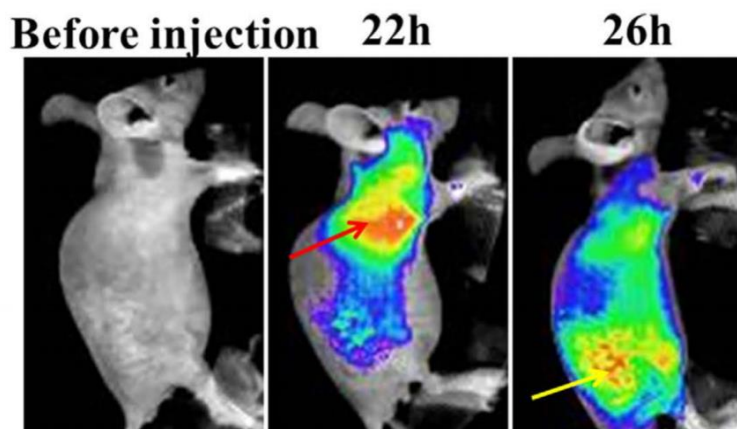


**Figure 1.18.** Fluorescent imaging ( $\lambda_{\text{ex}} = 550\text{nm}$ ,  $\lambda_{\text{em}} = 660\text{nm}$ ) of tumor-bearing mice before and after intravenous injection of  $\text{Fe}_3\text{O}_4@\text{C}@\text{PMOF}$  ( $20 \text{ mg kg}^{-1}$ ). The liver region was marked by red dot line and the yellow lines referred to tumor region. Reproduced from reference 164.

In terms of photoluminescent MOFs, sensing is the most widely reported application.<sup>17,85,163,176</sup>

MOFs offer a number of advantages as solid-state sensors due in part to their solid nature, the size exclusion ability of their pores, as well as the ability to concentrate analytes in the porous structure. A plethora of MOF sensing studies have been conducted where the emission has originated from the linker. An example of ion sensing can be seen in a 2,4,6-tris(4-pyridyl)pyridine (pytpy) copper MOF ( $\text{Cu}(\text{pytpy})](\text{NO}_3) \cdot (\text{CH}_3\text{OH})$ )<sup>16</sup> where the replacement of the nitrate counterion with  $\text{Cl}^-$ ,  $\text{Br}^-$ ,  $\text{N}_3^-$ ,  $\text{SCN}^-$  or  $\text{I}^-$  leads to an anion-dependent shift in emission maxima. The colour change was also visually detectable by then naked eye (Figure 1.19). pH sensing is yet another possibility, UiO-66- $\text{NH}_2$  showed an exponential increase in emission intensity from pH 1 to 9 due to deprotonation of the amine linker.<sup>177</sup> Sensing of small organic molecules is another widely reported application. 4,4'-(2,2-diphenylethene-1,1-diyl)dibenzoate (HDPEB) was used to form the zinc  $\text{Zn}_4\text{O}(\text{HDPEB})_3 \cdot 2\text{DEF} \cdot 4\text{H}_2\text{O}$  which was capable of red-shifted and blue-shifted solvent-dependent emission based on the conformation of the dangling phenyl rings.<sup>178</sup> The solvatochromic detection of small liquid analytes is also made possible using a zirconium MOF constructed from a 4,4'-((2,5-dimethyl-1,4-phenylene)bis(ethyne-2,1-

diyl))dibenzoic acid linker, the rotation of the central dimethyl pendant results in red-shifted emission maxima with increased solvent dipole moment.<sup>84</sup>



**Figure 1.19.** Images showing the colour change in MOF Cu(pytpy)](NO<sub>3</sub>)·(CH<sub>3</sub>OH) as result of anion-exchange. Reproduced from reference 16.

Gas phase sensing of vapours<sup>176</sup> and gases<sup>179</sup> is one of the many other possibilities with the help of luminescent MOFs. Finally, hydration dependent fluorescence has been reported in a number of frameworks where the emission originates from the organic linker. The next section will explore these studies in greater detail.

### 1.3.4 Hydration-Dependent Emission

The detection of water, both in the liquid and gas phase, has many important applications in processes which involve food processing, pharmaceutical manufacturing and environmental surveying. MOFs which exhibit a hydration-dependant emission at an appropriate concentration or relative humidity can be utilised as water sensors. This next section shall review a number of such MOF sensor systems which display ligand-centred emission.

Ferrando-Soria et al. reported one of the first MOF materials capable of exhibiting a hydration dependant emission in the form of an increased emission intensity.<sup>85</sup> The authors reported a

hybrid, manganese-copper framework composed of the N,N'-1,3-phenylenebis(oxamate) (mpba) linker and a N,N'-dimethyl-4,4'-bipyridinium/methyl viologen (MV) counterion, the resulting framework possessed the structural formula  $MV[Mn_2Cu_3(mpba)_3(H_2O)_3] \cdot 20H_2O$ . The resulting framework exhibited selective gas sorption ability for  $CO_2$  in a  $CO_2$ - $CH_4$  mixture and a paramagnetic to ferromagnetic phase transition ( $T_c = 19.0$  K). Upon dispersion in toluene, the dehydrated framework also exhibited luminescent behaviour arising from the MV counterion with two emission bands being observed:  $\lambda_{max} = 330$  nm ( $\lambda_{ex} = 225$  nm) and  $\lambda_{max} = 586$  nm ( $\lambda_{ex} = 400$  nm); the 330 nm band resulting from the MV cation and the 586 nm band being attributed to the interaction of the MV cation with the copper nodes ( $Cu^{II}$ - $MV^{2+}$ ). Upon addition of known amounts of water to the dispersion of the anhydrous framework in toluene, the 586 nm emission band gradually blue shifts to 544 nm upon increased hydration (Figure 1.20). The hydration of the Cu nodes results in small changes in the  $Cu^{II}$ - $MV^{2+}$  interaction distance. This is further validated by the lack of change in the 330 nm emission band upon hydration of the framework. This work is demonstrative of a MOF hydration-dependent emission which occurs in solution. However, since the emission originates from the  $MV^{2+}$  counter-ion, it is not linker based.

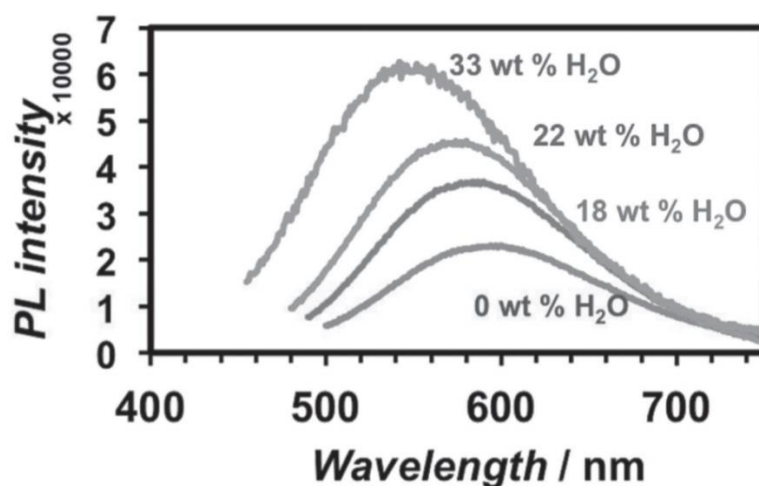


**Figure 1.20.** Emission spectra of anhydrous  $MV[Mn_2Cu_3(mpba)_3(H_2O)_3]$  at different water loadings ( $\lambda_{ex} = 400$  nm). A blue shifted emission is observed upon hydration. Reproduced from reference 85.

Douvali et al. provided the first report of a MOF capable of detecting trace quantities (0.05–5 % v/v) of water in organic solvents.<sup>163</sup> 2,5-dihydroxy-terephthalate (dhtp) was used to construct the alkaline earth magnesium MOF [(Mg(dhtp)(H<sub>2</sub>O)<sub>2</sub>)]·DMA (AEMOF-1). Upon removal of the DMA guest species from AEMOF-1·DMA to form AEMOF-1', the framework was found to exhibit a weak emission at  $\lambda_{\text{max}}$  of 530 nm with a smaller shoulder at 610 nm ( $\lambda_{\text{ex}}$  = 360 nm), both of which originate from the excited-state intramolecular proton transfer (ESIPT) on the bridging ligand. The  $\Phi_{\text{F}}$  of these emission bands was a modest 1.89 % and was said to be self-quenched due to the close proximity of the dhtp linker in the dense AEMOF-1' structure (BET surface area = 11 m<sup>2</sup> g<sup>-1</sup>). Upon hydration of AEMOF-1', the authors noted that the emission profile changed to just one emission band ( $\lambda_{\text{max}}$  = 536 nm) and an enhanced  $\Phi_{\text{F}}$  of 12.6 %. This prompted the authors to investigate the utility of AEMOF-1' as a moisture sensor in organic solvents (THF, MeOH, EtOH and CH<sub>3</sub>CN). The dry AEMOF-1' was suspended in dry THF, fluorescence analysis revealed a  $\lambda_{\text{max}}$  = 455 nm ( $\lambda_{\text{ex}}$  = 350 nm). Subsequent additions of water caused a gradual shift towards a  $\lambda_{\text{max}}$  of 530 nm in a 5 % v/v solution of H<sub>2</sub>O in THF. The smallest change was observed in H<sub>2</sub>O/THF solution of just 0.05 % v/v (Figure 1.21), this is in contrast to the free dhtp ligand which only produced a measureable emission change above 1.0 % v/v H<sub>2</sub>O. A similar, yet not as drastic emission response was observed when the AEMOF-1' was exposed to different quantities of H<sub>2</sub>O in EtOH, this highlights the selectivity of the framework, even in polar-protic solvents. This work is highly notable as being the first example of a suitably sensitive turn-on sensor for the detection of water in organic solvents. The luminescence-based determination method is also considerably faster and easier than traditional methods such as the Karl Fischer titration, a method which relies on specialised equipment and training.<sup>180</sup>

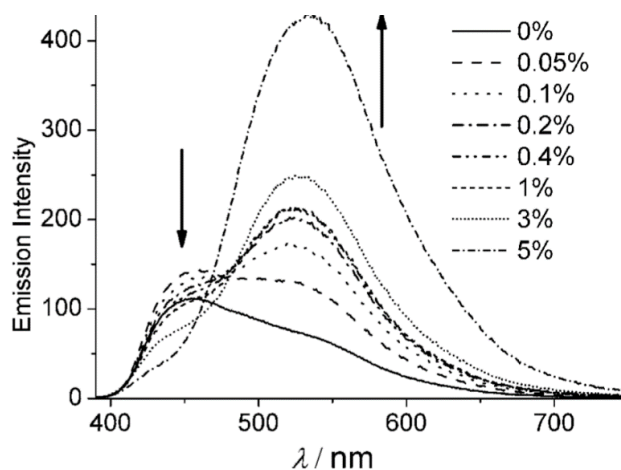


**Figure 1.21.** Emission spectra of a stirred suspension of AEMOF-1' in THF upon addition of aliquots of water (0.05-5 % v/v), ( $\lambda_{\text{ex}} = 400 \text{ nm}$ ). Figure reproduced from reference 163.

Following on, Yu et al. offered the first demonstration of a MOF which was capable of producing an emission change based on an increase in relative humidity.<sup>181</sup> 1-benzimidazolyl-3,5-bis(4-pyridyl)benzene (bzipyb) was used in the assembly of the copper  $\text{Cu}_2(\text{bzipyb})_2\text{I}_2$  framework. When the authors allowed the  $\text{Cu}_2(\text{bzipyb})_2\text{I}_2$  to stand at room temperature, a gradual colour change from yellow to deep red brown was observed. Single-crystal X-ray structure analysis of the frameworks revealed identical structures with the only difference being the presence of hydrogen bonding interactions between the copper cluster and guest  $\text{H}_2\text{O}$  species ( $4\text{H}_2\text{O} \subset \text{Cu}_2(\text{bzipyb})_2\text{I}_2$ ). This prompted the authors to expose the sample to a range of relative humidities (5, 33, 43, 57 and 78 RH %). The solid-state fluorescence spectra of the MOF were then recorded at the varied RH (Figure 1.22). A quenching effect of the emission maximum at 607 nm ( $\lambda_{\text{ex}} = 418 \text{ nm}$ ) was observed, with a greater RH resulting in a faster and greater degree of quenching. This work offered the first demonstration of a humidity-dependent emission in MOFs and whilst the response was that of a turn-off sensor, the

hydration could be visualised colorimetrically with the naked-eye.

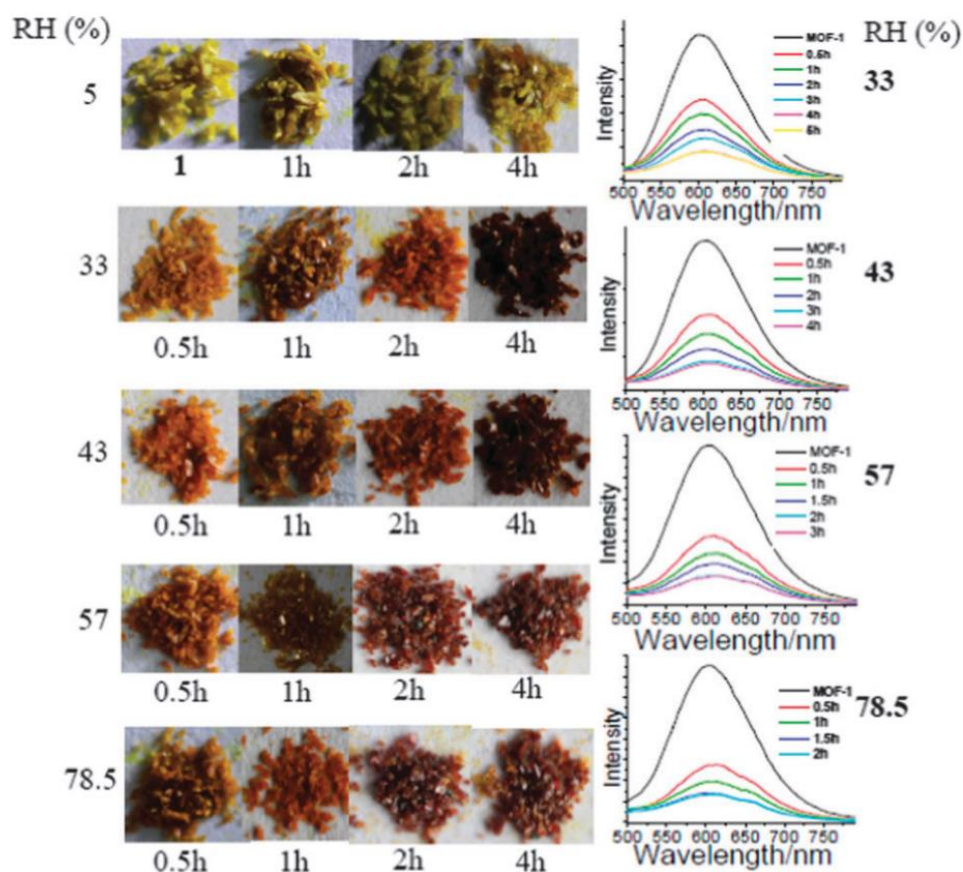


**Figure 1.22.** (left) Photographs showing the color change of the bulk crystal samples of  $\text{Cu}_2(\text{bziptyb})_2\text{I}_2$  in different atmospheres with different RH. The single crystal nature was kept during the color change process. (right) The corresponding solid-state emission spectra ( $\lambda_{\text{ex}} = 418 \text{ nm}$ ) of  $\text{Cu}_2(\text{bziptyb})_2\text{I}_2$  in different atmospheres with different RH (33–78.5%). Reproduced from reference 181.

Finally, the most recent example of MOF facilitated water sensing was reported by Chen et al.<sup>17</sup> The authors synthesised a zinc framework which was composed of a 5-(2-(5-fluoro-2-hydroxyphenyl)-4,5-bis(4-fluorophenyl)-1H-imidazol-1-yl)isophthalate linker (hpi2cf) with the general formula  $\text{Zn}(\text{hpi2cf})(\text{DMF})(\text{H}_2\text{O})$ . The hpi2cf linker exhibits a characteristic excited state intramolecular proton transfer (ESIPT). The overall framework displayed a highly reversible blue-shifted hydration-dependant emission which could be trivially reversed by gentle heating (70 °C) or through subjection to a stream of dry nitrogen gas (Figure 1.23). The change in

emission was derived from a single crystal to single crystal transformation which, upon dehydration, facilitated keto-enol tautomerism in the hpi2cf linker, thus inducing a higher energy enol emission through ES IPT. The framework could detect trace water in organic solvents (THF) at concentrations as low as a 0.05 % v/v solution of H<sub>2</sub>O in THF, the blue-shifted emission could also be induced by a 1 RH %. This makes the material the most sensitive MOF hydration sensor to date.

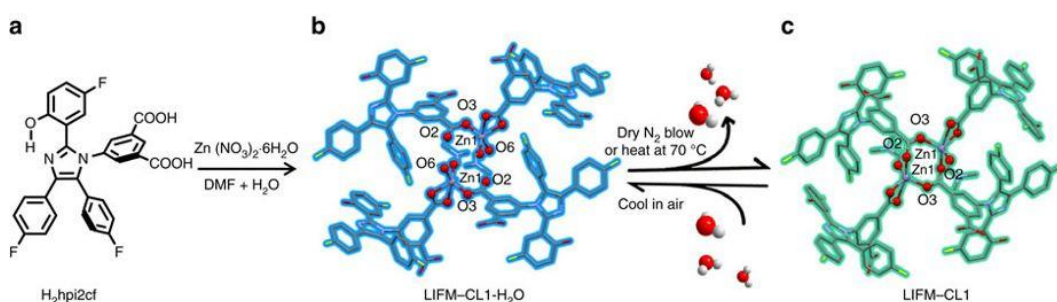


**Figure 1.23.** Structural illustration of: (a) hpi2cf ligand, (b) hydrated Zn(hpi2cf)(DMF)(H<sub>2</sub>O) (blue) and (c) dehydrated Zn(hpi2cf)(DMF) (cyan), showing coordination environmental change around Zn centres. Figure reproduced from reference 17.

Hydration-dependent emission in MOFs remains a widely under-reported phenomenon. Due to the conjugated nature of substituent MOF linkers and the propensity for metal nodes/clusters to become hydrated, there are likely many previously reported frameworks that exhibit some form of structural perturbation upon exposure to water. These subtle structural changes upon hydration could very well display hydration-dependant luminescence.

## 1.4 Zirconium Metal-Organic Frameworks

Although many existing MOFs remain intact upon the evacuation of their pores, stability remains an issue. The stability of MOFs relies heavily upon the ligand-metal interactions. Nucleophilic species such as H<sub>2</sub>O and conjugate base pairs can readily displace coordinated ligands; a slightly humid environment can be enough to result in the collapse of a framework. Recently, zirconium-based MOFs originating from zirconium salts (ZrCl<sub>4</sub> and ZrOCl<sub>2</sub>) have attracted attention due in part to their robustness. This stability is derived from the high oxidation state (+4) of the zirconium metal which increases the electrostatic interaction between the metal nodes and the linkers.<sup>10</sup> General synthetic strategies for assembling zirconium MOFs are very similar to the methods outlined in the previous section with the majority of these frameworks being synthesised solvothermally.<sup>88,182</sup> There are some reports of alternative methods such as microwave synthesis<sup>121</sup> and mechanochemical grinding.<sup>139</sup>

At the heart of a zirconium-based MOF is the zirconium-oxo cluster, often denoted as the Zr<sub>6</sub> node (Figure 1.24). The Zr<sub>6</sub> cluster has the general formula Zr<sub>6</sub>O<sub>4</sub>(OH)<sub>4</sub><sup>12+</sup>. This cluster is extremely stable towards temperature and hydration and remains intact upon amorphization of a zirconium framework.<sup>98</sup> This cluster possesses a maximum coordination environment of 12. This generally means that ideal zirconate MOFs are 12-connected; each node forms 12 coordination interactions with the chosen linkers. Zirconate MOFs that are not composed of the Zr<sub>6</sub> cluster, such as the MIL-140 series,<sup>183</sup> will not feature in this section.

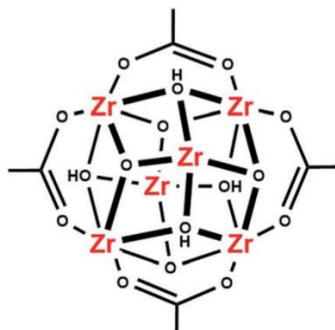


**Figure 1.24.** A structural representation of the Zr<sub>6</sub>O<sub>4</sub>(OH)<sub>4</sub> node featuring four node-bound carboxylates. Reproduced from reference 184.

The archetypal zirconium MOF is UiO-66 (Figure 1.25), first synthesised at the University of Oslo in 2008.<sup>98</sup> UiO-66 includes 1,4 benzenedicarboxylate (BDC) linkers, with each  $Zr_6$  node forming 12 carboxylate linkages and taking on the general formula  $Zr_6O_4(OH)_4(BDC)_6$  and possessing a pore diameter of 6 Å. UiO-66 is synthesised from  $ZrCl_4$  and BDC in DMF using solvothermal conditions; HCl, acetic acid or benzoic acid are often used as modulators.<sup>88</sup> Varying the modulators and their concentration can be used to induce both missing linker and cluster defects which affect the porosity and stability of the material.<sup>127,185,186</sup> UiO-66 is also highly stable in aqueous medium. Previous investigations into green chemistry have shown that the framework can be synthesised hydrothermally<sup>187</sup> and using liquid water-assisted grinding.<sup>139</sup> The thin film deposition of this framework is also possible through gas phase synthesis, thus realising applications in sensing and electronics.<sup>188</sup>

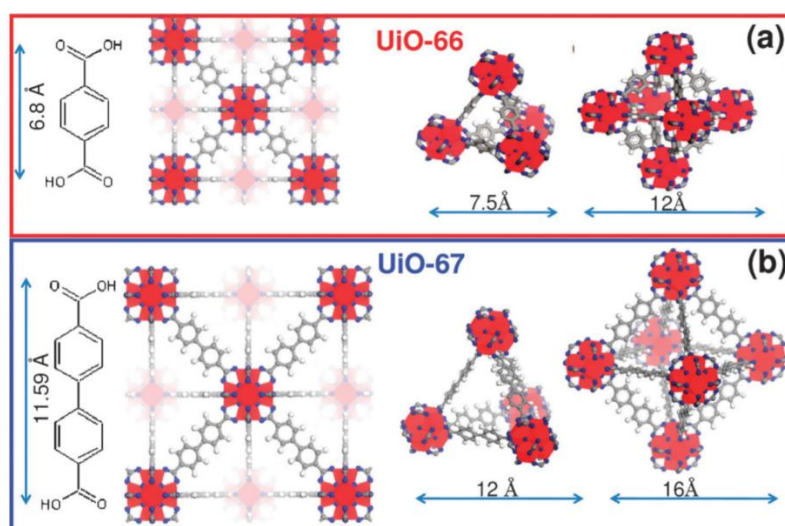


**Figure 1.25.** A structural representation of a) UiO-66 and b) UiO-67. From left to right: a comparison of the linker dimensions, structure and cage dimensions. Reproduced from reference 189.

Isostructural variants of UiO-66 exist which possess alternative functionalities on the BDC pendant such as 2-aminoterephthalate acid, 2-hydroxyterephthalate and 2,3,5,6-tetrafluoro-1,4-benzenedicarboxylate. Utilising the longer biphenyl-4,4'-dicarboxylate (BPDC) linker results in the framework known as UiO-67 (Figure 1.25). This framework is iso-reticular to UiO-66 and

differs only in pore diameter.<sup>98</sup> Again, substituting the BPDC linker for the likes of 2,2'-bipyridine-5,5'-dicarboxylate (BiPy) and 2-aminobiphenyl-4,4'-dicarboxylate results in a topology which is iso-structural to that of UiO-67.<sup>88</sup>

Carefully pairing a suitable linker with an appropriate modulator concentration can be used to synthesise zirconium MOFs with a variety of connectivities which differ from the ideal of 12. For example, employing a tritopic ligand such as 1,3,5 benzene tricarboxylate, 1,3,5-tris(4-carboxyphenyl)benzene or even 4,4',4''-s-triazine-2,4,6-triyl-tribenzoate, will result in a 6-connected framework (MOF-808).<sup>190</sup> The remaining six vacancies on the  $Zr_6$  cluster are occupied by the monotopic modulators. A more notable example is with the tetrakis(4-carboxyphenyl)porphyrin (TCPP) linker, using dichloroacetic acid modulator which results in the eight-connected PCN-222/MOF-545 framework. Modulating the synthesis with acetic acid leads to the 12-connected PCN-223 framework. Finally changing the modulator to benzoic acid will lead to PCN-224, a 6-connected zirconate MOF.<sup>182</sup> PCN-222, 223 and 224 could also be accessed simply through varying the concentration of triethylamine (TEA) modulator (Figure 1.26).<sup>130</sup>

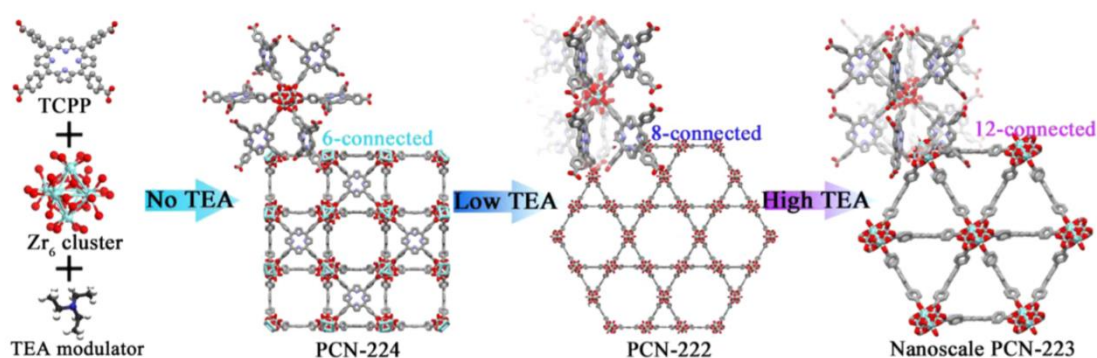


**Figure 1.26.** A graphical outline of the strategies employed to access PCN-222 (8-connected), PCN-223 (12-connected) and PCN-224 (6-connected) from the TCPP. The outline illustrates how varying the synthetic modulator can be used to achieve different node connectivity. Figure reproduced from reference 130.

Zirconium MOFs can undergo a number of post-synthetic modifications and this can be broken down into a variety of strategies. Covalent modifications of linker functionalities is a popular approach. For instance the amine functionality in UiO-66-NH<sub>2</sub> can be modified to form imines, amides and aziridines using a range of reagents.<sup>191</sup> Direct functionalization of the linker backbone is also possible through hydroxylation<sup>192</sup> and halogenation<sup>193</sup> of the ligand. Both processes have been previously reported for zirconium frameworks. Frameworks such as UiO-67-BiPy possess a bipyridyl functionality and can be modified through post-synthetic metalation using metal salts such as CuCl<sub>2</sub>, PtCl<sub>2</sub> and even PdCl<sub>2</sub> to yield immobilized heterogeneous catalysts.<sup>194</sup> Alternatively, the Zr<sub>6</sub> cluster can be metalated, with previous work showing the incorporation of AuMe(PMe<sub>3</sub>)<sup>195</sup> and LiO<sup>t</sup>Bu<sup>196</sup> onto the node. Finally, post-synthetic surface functionalization can be achieved by functionalizing frameworks with moieties and reagents which are too large to pass into the MOF pores.<sup>197</sup>

Due to their robustness and due to the Lewis acidity of uncoordinated Zr<sub>6</sub> nodes, zirconium MOFs have found a number of applications as heterogeneous catalysts.<sup>51</sup> The following section will explore their general utility as catalysts followed by their application as Lewis acid catalysts for the hydrolysis of CWAs.

#### **1.4.1 Zirconium MOFs as Catalysts**

Due to their robustness and stability in a vast array of chemical media, zirconium MOFs have shown great promise as heterogeneous catalysts. Predominant reports of catalysis have usually involved zirconium MOFs in which the catalytically active components are functionalised linkers,<sup>198,199</sup> metal-ligated linkers<sup>200</sup> or metal clusters.<sup>201</sup> The schematic below (Figure 1.27) illustrates the design strategies that exist for functionalizing zirconium frameworks for applications in catalysis. This section will focus on catalysis which is derived from the Lewis acidic zirconium-oxo cluster.

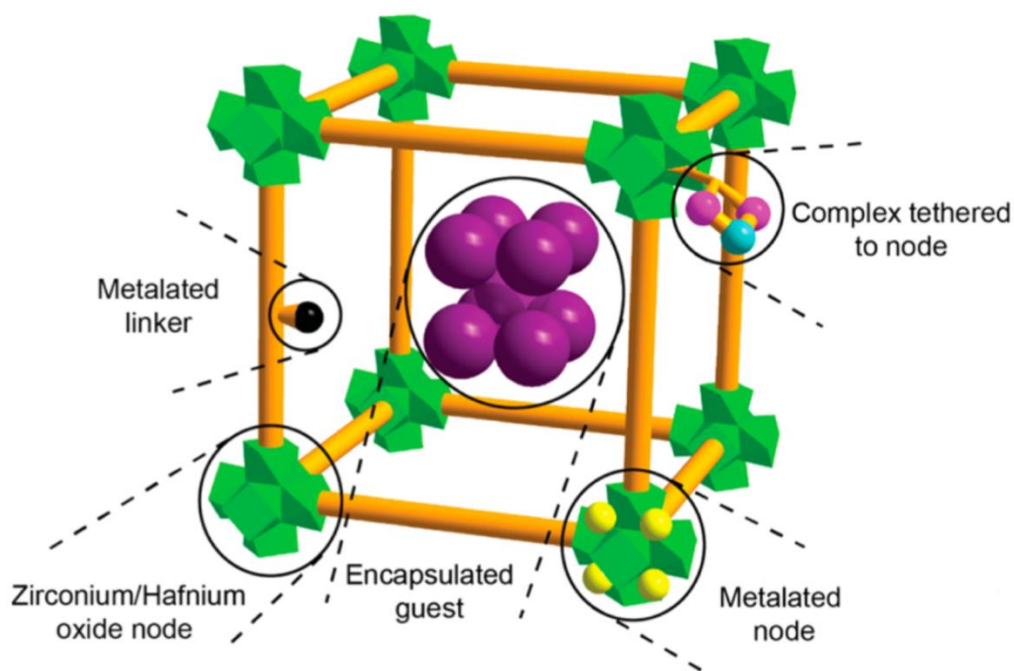


**Figure 1.27.** An illustration of the locations of catalytically active sites on  $Zr_6$  based MOFs.

Reproduced from reference 202.

One of the earliest examples of  $Zr_6$  node-facilitated catalysis was reported by Vermoortele et. al.<sup>128</sup> and features UiO-66. The synthesis of UiO-66-10 was modulated with 10 equivalents of trifluoroacetic acid (TFA) relative to  $ZrCl_4$ , this yielded a number of linker defects. The modulator was removed through thermal activation resulting in an average of two coordination vacancies per  $Zr_6$  cluster (Figure 1.28). A 15 mol % catalyst loading was then used for the cyclization of citronellal to isopulegol in toluene. This was followed by the Meerwein–Ponndorf–Verley reduction of 4-*tert*-butylcyclohexanone with isopropyl alcohol for which a 10 mol % catalyst loading was used. It should be noted that modulating the synthesis of UiO-66-10<sub>HCl</sub> with 1 equivalent of HCl alongside 10 equivalents of TFA doubled the amount of citronellal which was converted over 10 hours when compared to a UiO-66-10 framework which was modulated with only TFA. HCl partially inhibits the hydrolysis of the  $ZrCl_4$  salt and mildly suppresses the deprotonation of the 1,4-benzene dicarboxylic acid linker. This facilitates a slower and more controlled growth which leads to a more crystalline framework. It should also be noted that UiO-66 which was synthesised without the presence of TFA modulator and

activated, showed a fraction of the catalytic activity compared to UiO-66-10<sub>HCl</sub>. This highlights the necessity of the coordination vacancies formed by modulation with TFA.

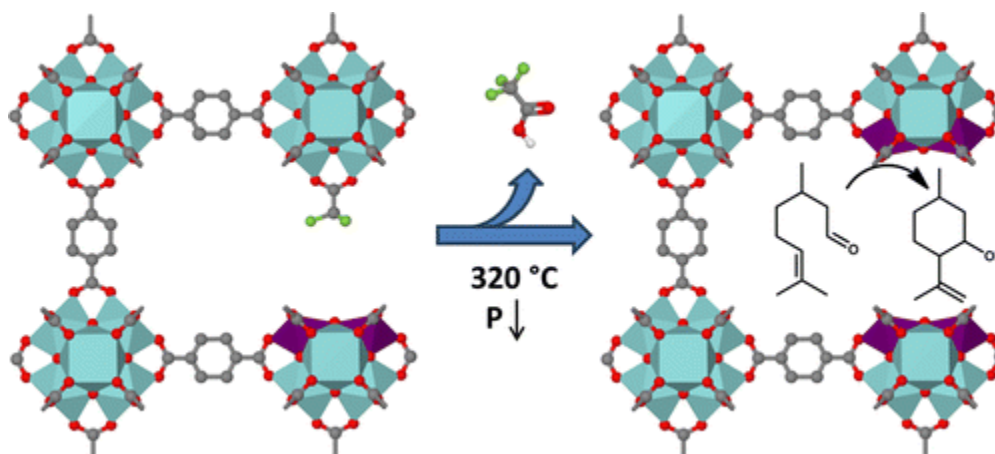


**Figure 1.28:** A graphical illustration of the creation of missing linker defects how they facilitate catalysis. Reproduced from reference 128.

A series of zirconium MOFs were also tested for the catalytic (1 mol % catalyst loading) regioselective epoxide ring opening of styrene oxide in the presence of iso-propyl alcohol to form the primary alcohol 2-isopropoxy-2-phenylethan-1-ol. The series of MOFs consisted of several variants of UiO-66, the eight-connected MOF NU-1000 and the 6-connected framework MOF-808. The number of missing linkers in each MOF and the corresponding conversion % of styrene oxide is shown below.

MOF Catalyst	Number of Missing Linkers (per Zr <sub>6</sub> cluster)	Relative reaction rate	Styrene oxide conversion (%)
<b>UiO-66</b>	1.75	1	40
<b>UiO-67 (HCl)</b>	1.75	0.9	34
<b>UiO-67 (Benzoic Acid)</b>	0	~0	4
<b>NU-1000</b>	4	1.3	90
<b>MOF-808</b>	6	2.0	100

**Table 1.1.** Estimated missing linkers in UiO-type MOFs as determined by potentiometric acid-base titration, relative initial reaction rate and conversion of styrene oxide after 24 h.

Reproduced from reference 51.

As can be seen from Table 1.1, the study concluded a quantitative relation between the number of missing linkers and the catalytic activity of each framework for the ring opening reaction. It should be noted that the entry titled UiO-67 (Benzoic Acid), was modulated with benzoic acid, this particular synthesis results in the minimal number of defects and provides minimal conversion of styrene oxide over the reaction period. UiO-67 (Benzoic Acid) is employed as useful experimental control for showcasing the necessity of the Lewis acidic coordination vacancies for enabling the ring opening conversion.

More recently, the 6-connected MOF-808 was noted for its remarkable activity towards peptide bond hydrolysis.<sup>77</sup> The dipeptide Glycyl-glycine (Gly-Gly) was the substrate of choice. A 100 mol % loading of MOF-808 was used along with a phosphate buffer (pD 7.4) at 60 °C. Near full hydrolysis of Gly-Gly to Gly was observed after a 4 hour period. A mechanism is proposed for the peptide hydrolysis: the amine nitrogen and amide oxygen coordinate to two  $Zr^{4+}$  centers on the  $Zr_6$  node, the coordination polarizes the peptide bond which makes it more susceptible to nucleophilic attack from water.

Lower/Higher pD and a lower temperature both resulted in a smaller amount of Gly-Gly conversion. A 20-fold increase of Gly-Gly relative to MOF-808 was then used and a substantial amount of hydrolysis was observed, albeit at a slower rate, this shows that MOF-808 is truly catalytic. The authors then repeated their Gly-Gly and MOF-808 hydrolysis procedure in the presence of several aliphatic mono-, di- and tri- carboxylic acids, a lower conversion was observed of Gly-Gly to the Gly product. Shorter aliphatic acids resulted in greater inhibition than their longer counterparts and a di-acid would generally result in a doubly large inhibition in comparison to a mono-acid. The Gly-Gly therefore competes with other moieties carboxylate moieties for the oxophilic coordination vacancies on the  $Zr_6$  nodes. Finally, using MOF-808, the authors tested a number of Gly-X dipeptides which differed in size, hydrophobicity index and which possessed alternative functionalities. The hydrolysis of the

Gly-X dipeptides generally decreased as the size of the side chain increased, the following size trend was observed: Gly-Gly > Gly-Ala > Gly-Asp > Gly-Asn > Gly-Lys  $\approx$  Gly-Arg (Figure 1.29).

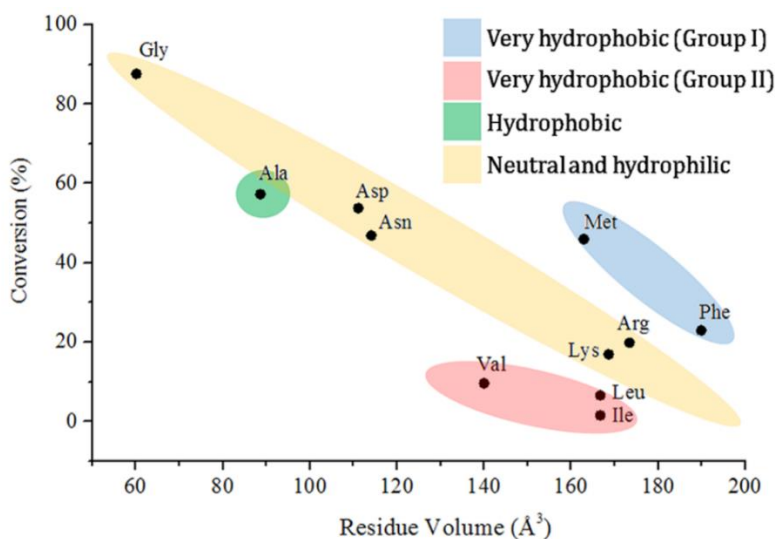


**Figure 1.29.** A graph showing the conversion of 2.0  $\mu\text{mol}$  Gly-X dipeptides in the presence of 2.0  $\mu\text{mol}$  MOF-808 at pD 7.4 and 60  $^{\circ}\text{C}$  as a function of the residual volume of amino acid X. Reproduced from reference 77.

The steric bulk of the dipeptide therefore affects the access of the amide C=O group to the  $\text{Zr}_6$  nodes. Dipeptides with more hydrophobic residues (Val, Leu, Ile) were also shown to react slower, which was postulated to result from less favourable inter-molecular interactions with the 1,3,5-benzenetricarboxylate linker in MOF-808, thus hindering the diffusion of the substrate through the MOF pores. The above study highlights the utility of zirconate MOFs as heterogeneous catalysts. The research also showcases the steric effect of substrate to node access along with how guest electron pair donating species can inhibit catalysis by competitively binding the active coordination vacancies.

Finally, there is a significant collection of studies regarding the hydrolysis of of the nerve agent simulant DMNP, and consequently organophosphorus CWAs. Numerous zirconium MOFs have been employed for this phospho-ester hydrolysis, ranging from UiO-66, UiO-67-NMe<sub>2</sub>, MOF-

808 and NU-1000. This work is discussed chronologically and in great detail in the following section.

### 1.4.2 Zirconium MOFs as OP CWA Catalysts

As discussed in the previous section, zirconate frameworks possessing coordination vacancies have been employed as heterogeneous Lewis acid catalysts. This section will discuss the development of their application for the hydrolysis of CWAs along with their simulants. All studies which involve the zirconium MOF facilitated hydrolysis of CWAs were initially carried out on the nerve agent simulant, DMNP. This procedure employs the use of N-ethylmorpholine (NEM) buffer. The methodology was likely developed from an initial study involving the hydrolytic cleavage of O,O-diethyl O-(4-nitrophenyl) phosphate (DENP) in the presence of 4-(2-hydroxyethyl)piperazine-1-ethanesulfonic acid (HEPES) buffer and the chromium MOF MIL-101.<sup>203</sup> It should also be noted that salts of 4-nitrophenyl phosphate are also commonly employed in biological settings to assess the effectiveness of phosphoesterases. The zirconium node facilitated hydrolysis mechanism of DMNP, as determined by electronic structure calculations,<sup>204</sup> is shown in Figure 1.30. The first reported example of nerve agent simulant hydrolysis was reported in 2014 by Katz et al.<sup>7</sup> The study described the hydrolysis of the DMNP simulant in aqueous N-ethylmorpholine solution which has now been widely adopted as a standard procedure for screening potential OP CWA catalysts. The authors employed UiO-66 as a hydrolysis catalyst and they described the topology of the  $Zr_6$  oxo-cluster as being biomimetic of the PET enzyme which is comprised of an alkoxide bridged  $Zn^{II}$  centre surrounded by nitrogen donors (Figure 1.31). For phosphoester hydrolysis, one  $Zn^{II}$  centre binds and activates the P=O group, while the other  $Zn^{II}$  centre transfers an  $OH^-$  to enable the cleavage of an –OR group.

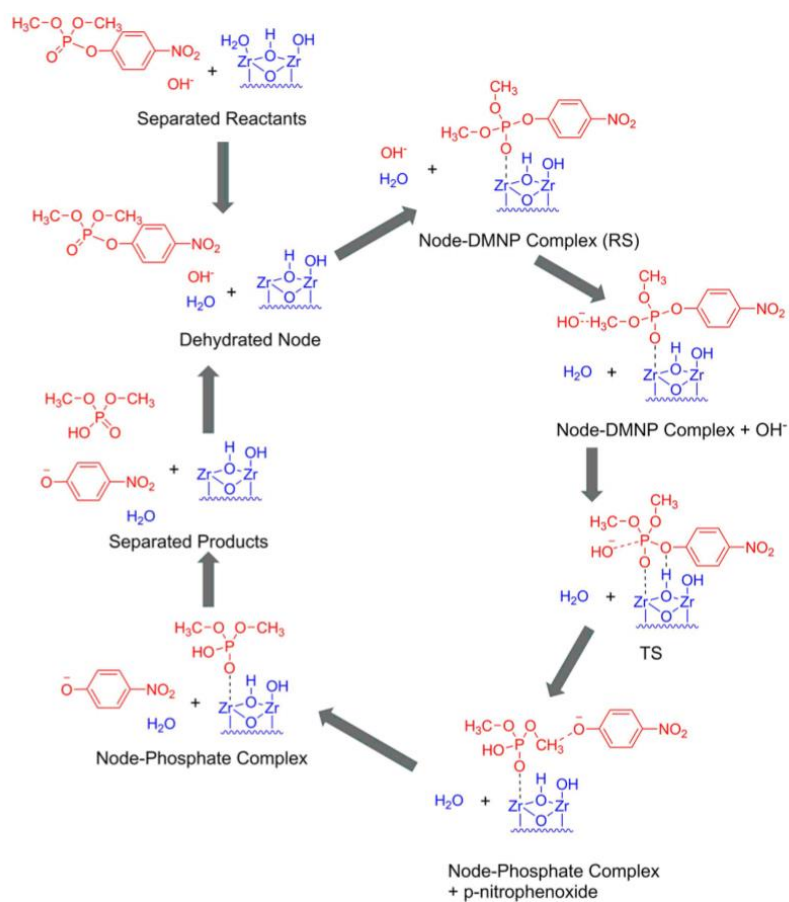


**Figure 1.30.** The catalytic cycle of DMNP on a NU-1000 node. Reproduced from reference 204.

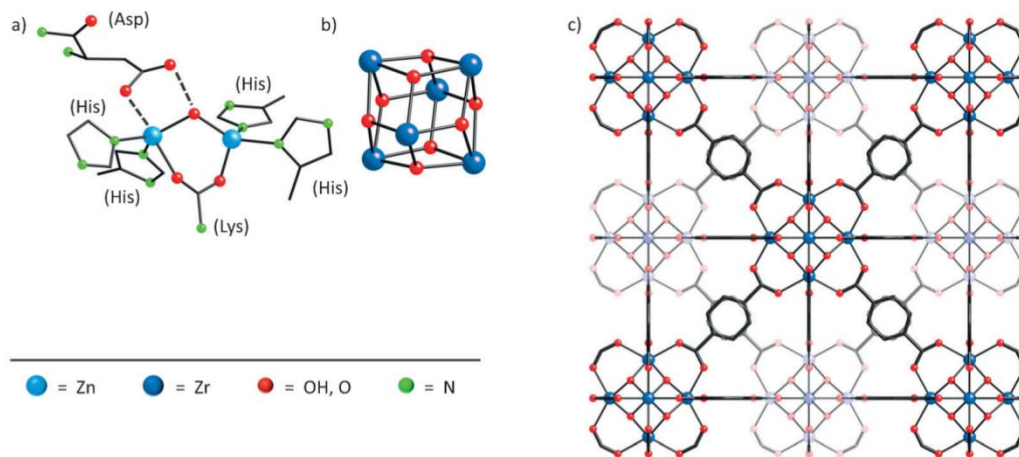


**Figure 1.31.** a) schematic drawing of the structure of the active site of phosphotriesterase. b) The Zr<sub>6</sub> cluster. c) The 3D structure of UiO-66. Reproduced from 52.

However, zirconium MOFs offer several advantages over PET enzymes; zirconium MOFs are stable over a wide pH and temperature range<sup>10</sup> and function as heterogeneous catalysts. The high stability and solid nature of zirconium MOF catalysts enhances their field applicability in the context of CWA degradation (filters/textiles/composites).<sup>7</sup> For the catalytic testing, DMNP and p-nitrophenyl diphenyl phosphate (PNPDPP) were both subjected to a methanolysis reaction in the presence of UiO-66 (6 mol %). Near full methanolysis was observed for DMNP (~ 90 %) and PNPDPP (~ 85 %) after 3 hours.

Under hydrolysis reaction conditions, UiO-66 (6 mol %) was able to fully convert DMNP to dimethyl phosphonate in the presence of aqueous NEM buffer over 3 hours at room temperature. Unsurprisingly, a faster hydrolysis was observed when the reaction temperature was raised to 60 °C. The authors were keen to note that an individual molecule of DMNP (11 x 4.5 Å) is too large to access the 6 Å large pore apertures of UiO-66 and that the observed hydrolysis was restricted to the MOF surface (6 mol % catalyst loading, 0.045 mol % accessible surface sites). Finally, to demonstrate that the MOF facilitated catalysis was heterogeneous, the authors removed the UiO-66 from a DMNP reaction mixture mid-reaction, after which point no further hydrolysis was observed. This first work regarding MOF catalysed CWA simulant hydrolysis was highly demonstrative but there was no mention of coordination vacancies, nor was the work confirmed on CWAs.

A follow up project was pursued by Katz et al.<sup>184</sup> to investigate how alternative functionalities on the 1,4 benzene dicarboxylic acid linker affected the hydrolysis of the DMNP simulant. Using identical hydrolysis conditions (DMNP in aqueous NEM buffer) and a 6 mol % catalyst loading, UiO-66-(OH)<sub>2</sub>, UiO-66-NO<sub>2</sub>, UiO-66-NH<sub>2</sub>, UiO-67, UiO-67-NH<sub>2</sub> and UiO-67-NMe<sub>2</sub> were all tested as hydrolysis catalysts. No significant improvement in DMNP half-life was observed in the presence of UiO-66-(OH)<sub>2</sub> and UiO-66-NO<sub>2</sub> when compared to un-functionalised UiO-66, as shown in Figure 1.32. The electron-withdrawing nitro group of UiO-66-NO<sub>2</sub> provides no electronic effect on the rate-limiting step and the electron-donating OH group of UiO-66-(OH)<sub>2</sub>

results in a slight steric inhibition of the rate limiting step. However, a 20-fold increase in initial rate ( $\text{mM s}^{-1}$ ) was observed for UiO-66-NH<sub>2</sub> when compared to UiO-66 (Figure 1.32). The authors suggested that this remarkable enhancement was a result of the Brønsted basicity of the proximal 2-aminoterephthalate linker.

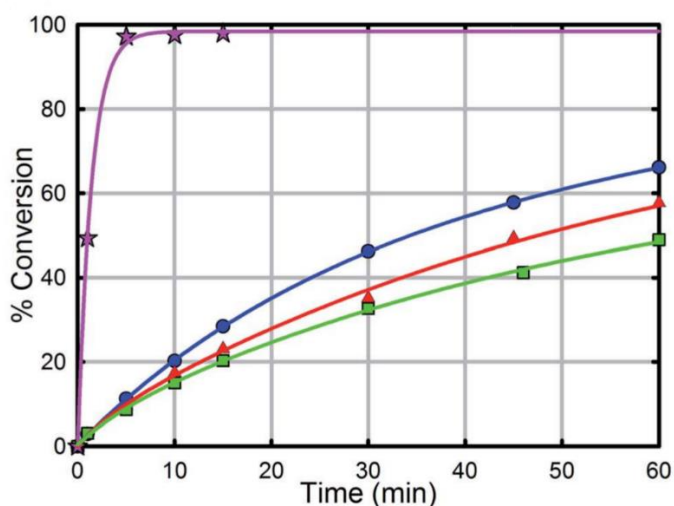


**Figure 1.32.** Hydrolysis rate of UiO-66 (blue circles), UiO-66-NO<sub>2</sub> (red triangles), UiO-66-(OH)<sub>2</sub> (green squares), and UiO-66-NH<sub>2</sub> (pinkstars). Reproduced from reference 184.

UiO-67 was also found to outperform UiO-66 due to less steric crowding between nodes provided by the longer biphenyl-4,4'-dicarboxylic acid linker. However, only a 1.2-fold increase was observed in initial rate in the presence of UiO-67-NH<sub>2</sub> and UiO-67-NMe<sub>2</sub> relative to UiO-67, which is in contrast to the 20-fold enhancement between UiO-66 and UiO-66-NH<sub>2</sub>. Decreasing the catalyst loading by 50 % (from 6 % to 3 %) resulted in a 3.2-fold rate increase when comparing UiO-67 to UiO-67-NH<sub>2</sub> and UiO-67-NMe<sub>2</sub>. This prompted the authors to suggest that there was second rate-limiting step present in the catalytic cycle.

Following on, Mondloch et al reported the use of the eight-connected NU-1000 MOF composed of the tetratopic 1,3,6,8(p-benzoate) (TBAPy) inker as a catalyst for DMNP hydrolysis.<sup>11</sup> Identical reaction conditions were used along with a 6 mol % catalyst loading. A significant reduction in half-life was observed for NU-1000 in comparison to UiO-66 (15 mins vs

45 mins). This enhancement was the result of two factors. One, NU-1000 possesses a maximum pore diameter of 31 Å which allows the DMNP substrate to permeate the entirety of the internal framework. Two, the tetratopic nature of the TBAPy linker results in the formation of an eight-connected framework vs. that of the 12-connected UiO-66. The lower connectivity results in improved access to the Lewis acidic Zr<sup>IV</sup> sites due to a less than maximal occupancy of the 12 coordination sites on the Zr<sub>6</sub> node. A tenfold enhancement in DMNP hydrolysis half-life was then achieved by thermally activating the NU-1000 framework Zr<sub>6</sub>(μ<sub>3</sub>-O)<sub>4</sub>(μ<sub>3</sub>-OH)<sub>4</sub>(H<sub>2</sub>O)<sub>4</sub>(OH)<sub>4</sub>(TBAPy)<sub>2</sub> and removing the terminal aqua ligands. Using density functional theory (DFT) quantum chemical calculations, DMNP was found to interact directly with the Lewis acidic Zr<sup>IV</sup> sites in dehydrated NU-1000 (Figure 1.33).

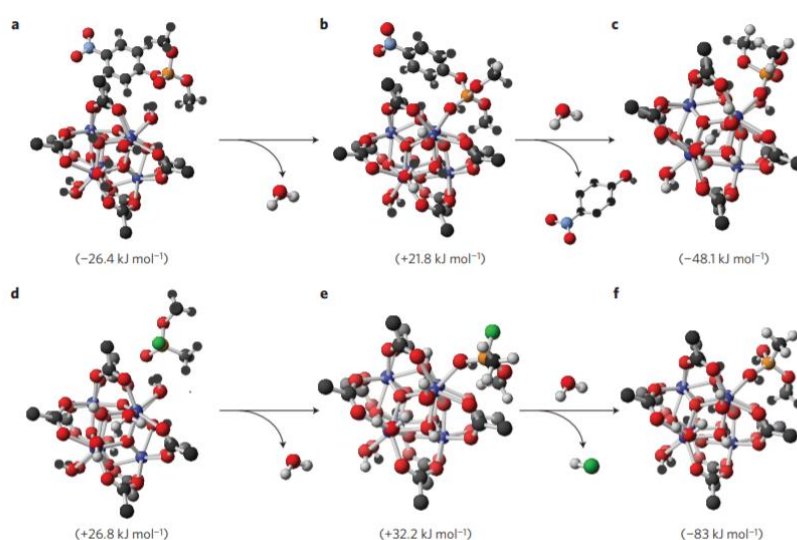


**Figure 1.33.** Association and reaction energies predicted by DFT. a–f, Key  $\Delta G^{\circ}_{\text{assoc}}$  (a,d) and  $\Delta G^{\circ}_{\text{rxn}}$  (b,c,e,f) values for the interaction of DMNP and GD analogue with the node of NU-1000. a, DMNP binding. b, DMNP replacing a H<sub>2</sub>O molecule. c, Hydrolysis of DMNP. d, GD analogue binding. e, GD analogue replacing a H<sub>2</sub>O molecule. f, Hydrolysis of GD. Colour code: Zr (blue); O (red); C (black); H (white); P (orange); N (light blue); F (green); S (yellow). Reproduced from reference 11.

With regular NU-1000, DMNP formed hydrogen bonding interactions with Zr<sub>6</sub> node-ligated water along with the hydroxyl moieties which composed the nodes. In addition to hydrogen bonding interactions, DMNP also formed  $\pi$ - $\pi$  stacking interactions with the TBAPy<sup>4+</sup> linker. The direct interaction of DMNP with the Zr<sup>IV</sup> sites in dehydrated NU-1000 is a more favourable interaction with the hydrolysed product being 48 kJ mol<sup>-1</sup> downhill in free energy relative to the separated reactants. Finally, the authors reported the hydrolysis of the nerve agent GD. Using a buffered solution of NEM and NU-1000 (6 mol % catalyst loading), GD was hydrolysed with a half-life of just 3 minutes. This was the first example in a series of studies where the hydrolysis of DMNP was shown to correspond with the hydrolysis of an OP CWA.

Based on observations that a lower connectivity in Zr-MOFs results in more accessible catalytic sites Moon et al<sup>184</sup> reported their findings on the use of 6-connected MOF-808 as a hydrolysis catalyst. Using MOF-808 (6 mol %) along with an aqueous NEM buffer, DMNP was hydrolysed with a half-life of less than 0.5 minutes. Reducing the catalyst concentration further to a 1.25 mol % loading also resulted in a half of 0.5 minutes. This was the fastest reported half-life to date and thus highlighted how an increase in the number of coordination vacancies resulted in significantly enhanced catalysis. It should be noted that the synthesis of MOF-808 was modulated with formic acid thus resulting in an as-synthesised Zr<sub>6</sub>( $\mu_3$ -O)<sub>4</sub>( $\mu_3$ -OH)<sub>4</sub>(HCOO)<sub>6</sub>(BTC)<sub>2</sub> framework. The framework was then activated by heating in fresh solvent to substitute the formate ions with six labile water ligands, thus resulting in Zr<sub>6</sub>( $\mu_3$ -O)<sub>4</sub>( $\mu_3$ -OH)<sub>4</sub>(H<sub>2</sub>O)<sub>6</sub>(OH)<sub>6</sub>(BTC)<sub>2</sub>.

Moon et al then went on to report the first example of the zirconium MOF facilitated hydrolysis of the V series agent, VX.<sup>12</sup> UiO-67-NH<sub>2</sub> and UiO-67-NMe<sub>2</sub> were both used (6 mol %) as degradation catalysts for the hydrolysis of VX in NEM buffer. Remarkably, a VX half-life of 6 minutes was achieved in the presence of UiO-67-NH<sub>2</sub> and a half-life of 1.5 minutes was achieved with UiO-67-NMe<sub>2</sub>. The superior activity of UiO-67-NMe<sub>2</sub> was derived from the greater Brønsted basicity of the dimethyl-amine functionalised linker. The same degradation

procedure was repeated, but this time in the absence of NEM buffer, a VX half-life of 7 minutes was observed in the presence of UiO-67-NMe<sub>2</sub> (Figure 1.34). It is also worth noting that in all cases the hydrolysis of VX was selective. The ethyl-methyl phosphoric acid (EMPA) product was always formed instead of the harmful EA-2192 (Figure 1.4). The zirconate nodes therefore displayed selectivity for P-S bond cleavage over that of the P-O bond in VX.

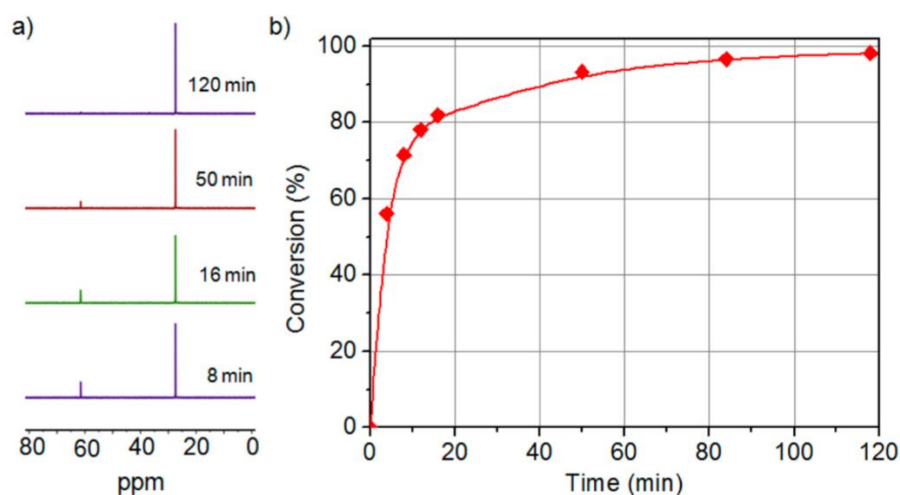


**Figure 1.34.** <sup>31</sup>P NMR spectra in the absence of buffer indicating (a) the progress of hydrolysis of 14.7 μmol of VX (62.5 ppm) to EMPA (27.5 ppm) with 1.1 μmol of UiO-67-NMe<sub>2</sub> at room temperature and (b) the percent conversion of VX to EMPA in the presence of UiO-67-NMe<sub>2</sub> in water. Reproduced from reference 12.

All of the studies outlined so far in this section were conducted by members of the Farha and the Hupp groups.<sup>8,11,12,52,184</sup> Due to the consistency of their methodology, a direct comparison may be drawn between all of the OP hydrolysis tests conducted by these groups (Table 1.2). MOF-808 resulted in the shortest half-life for DMNP hydrolysis, even at a much smaller catalytic loading. At the time, UiO-67-NMe<sub>2</sub> was the only zirconium framework that had been tested on VX in the absence of buffer. Due to the lower formula weight of MOF-808, cheaper linker (1,3,5-benzene tricarboxylate vs. 2-(dimethylamino)-[1,1'-biphenyl]-4,4'-dicarboxylate) and improved DMNP hydrolysis, it was of great interest to see whether MOF-808 could show the same affinity for degrading VX in the absence of buffer.

MOF (6 mol % loading)	Substrate	T <sub>1/2</sub> (min)	Reference
UiO-66	DMNP	35	52
UiO-66-(OH) <sub>2</sub>	DMNP	60	184
UiO-66-NO <sub>2</sub>	DMNP	45	184
UiO-66-NH <sub>2</sub>	DMNP	1	184
UiO-67	DMNP	4.5	184
UiO-67-NH <sub>2</sub>	DMNP	2	184
UiO-67-NMe <sub>2</sub>	DMNP	2	184
NU-1000	DMNP	15	11
NU-1000 dehydrated	DMNP	1.5	11
MOF-808	DMNP	<0.5	8
MOF-808 (1.25 mol % loading)	DMNP	0.5	8
NU-1000	GD	3	11
UiO-67-NH <sub>2</sub>	VX	6	12
UiO-67-NMe <sub>2</sub>	VX	1.8	12
UiO-67-NMe <sub>2</sub>	VX (no buffer)	7	12

**Table 1.2.** A table summarising the half-lives of various OP CWA substrates in the presence of a range zirconium MOF catalysts.

Finally, de Koning et al.<sup>9</sup> report on a highly comprehensive study which allows for a direct comparison between a several MOF hydrolysis systems (Table 1.3). UiO-66-NH<sub>2</sub>, MOF-808, NU-1000 and PCN-777 were all tested for their ability to degrade the DMNP simulant along with the CWAs tabun, soman and VX, in buffer and without. The study confirmed that VX was self-buffering due to the fact that hydrolysis occurred in the presence of all of the MOFs which were tested when no NEM buffer was used. UiO-66-NH<sub>2</sub> resulted in the shortest VX non-buffered half-life (UiO-66-NH<sub>2</sub> t<sub>1/2</sub> 5 mins vs. MOF-808 t<sub>1/2</sub> 6.3 mins), which is likely due to the proximal amine linker of UiO-66-NH<sub>2</sub> aiding the initial hydrolysis when no DESH by-product is yet present. Interestingly, when N-alkylated VX (VX-Me<sup>+</sup>) was employed, no catalytic hydrolysis was observed due to the lack of basicity present on the amine. Partial hydrolysis of tabun was observed during non-buffered hydrolysis experiments in the presence of all frameworks, this can be ascribed to the assistance by the basic dimethyl-amine group of tabun. Finally, when looking at the non-buffered hydrolysis of soman, no hydrolysis was observed in the presence of any frameworks, this is quite simply explained by the lack of any basic functionalities being present in the reaction mixture.

conditions		NEM			MQ		
agent	MOF	$k$ , min <sup>-1</sup>	$t_{1/2}$ , min	conv <sup>a</sup> , %	$k$ , min <sup>-1</sup>	$t_{1/2}$ , min	conv <sup>a</sup> , %
<b>POX</b>	NU-1000	0.27	2.6	100	n.d.	n.d.	n.d.
	MOF-808	0.19	3.6	100	n.d.	n.d.	n.d.
	PCN-777	0.19	3.6	100	n.d.	n.d.	n.d.
	UiO-66-NH <sub>2</sub>	0.02	35	75 <sup>a</sup>	0.007	99	21
<b>GD</b>	NU-1000	n.d.	<1	100	n.d.	n.d.	<2
	MOF-808	n.d.	<1	100	n.d.	n.d.	<2
	PCN-777	n.d.	<1	100	n.d.	n.d.	<2
	UiO-66-NH <sub>2</sub>	n.d.	<1	100	n.d.	n.d.	<2
<b>VX</b>	NU-1000	0.13	5.3	100	0.081	8.7	77
	MOF-808	n.d.	<0.5	100	0.11	6.3	73
	PCN-777	n.d.	<0.5	100	0.04	17.3	34
	UiO-66-NH <sub>2</sub>	0.32	2.2	100	0.14	5	85
<b>GA</b>	NU-1000	n.d.	<1	100	0.0072	97	23
	MOF-808	n.d.	<1	100	0.0074	94	24
	PCN-777	n.d.	<1	100	0.019	37	37
	UiO-66-NH <sub>2</sub>	n.d.	<1	100	0.018	39	33

<sup>a</sup>Conversion within the experimental time frame.

**Table 1.3.** Summary of Kinetic Data and Maximum Conversions (after 40 min) Obtained in the Degradation Reactions of POX (paraoxon), GD, VX, and GA in NEM Buffer (pH 10) and Water, by the MOFs NU-1000, MOF-808, PCN-777, and UiO-66-NH<sub>2</sub> (pH 2.8– 4.4). Reproduced from reference 9.

To summarise, this section has explored the evolution of the zirconium MOF for the enhancement of its application for OP hydrolysis. The findings have determined that pore diameter, proximal basicity, and most importantly, the abundance of coordination vacancies/defects, all play a role in facilitating a more effective hydrolysis. Upon evaluating the results, it would appear that MOF-808 has proven to be the most effective catalyst for OP CWA hydrolysis. This is because it possesses the most enhanced  $t_{1/2}$  for DMNP hydrolysis along with

NU-1000. MOF-808 also rivals UiO-67-NMe<sub>2</sub> for the unbuffered hydrolysis of VX. MOF-808 does offer several advantages over rival zirconium MOFs. First, it is composed of a very simple 1,3,5 benzene tricarboxylate linker, which is cheaper and easier to synthesise than the linker composing UiO-67-NMe<sub>2</sub> and NU-1000. Second, due to the simplicity of the linker and the 6-connected nature of MOF-808, the framework possesses a significantly lower molecular weight, thus making it more efficient for practical applications. MOF-808 has therefore been identified as the most desirable catalyst for any future applications in OP CWA applications.

### 1.4.3 Dehydration of Zr<sub>6</sub> Nodes for Enhancing Hydrolysis

There have been a number of reports regarding the dehydration of Zr<sub>6</sub> nodes for the enhancement of OP hydrolysis. The first study was reported by Mondloch et al.<sup>11</sup> and involved the thermal dehydration of the NU-1000 framework to form NU-1000-dehyd (Figure 1.35). The dehydrated framework was found to exhibit a 10-fold increase in activity for the hydrolysis of the DMNP simulant. This study was further backed by DFT studies conducted by the authors which show that the DMNP simulant binds more favourably with the vacant, dehydrated node of NU-1000-dehyd, as opposed to forming hydrogen bonding interactions with node ligated H<sub>2</sub>O and OH in regular NU-1000. These results are further confirmed by additional DFT studies performed by Chen et al.<sup>204</sup> regarding the transition states of DMNP on NU-1000 and NU-1000-dehyd during the catalytic cycle. There is therefore good agreement between simulation and experimental data. However, when the authors chose to assess the ability of NU-1000 for the degradation of GD, they opted to test regular NU-1000 and not NU-1000-dehyd, thus leaving this optimisation unconfirmed on a live OP CWA.

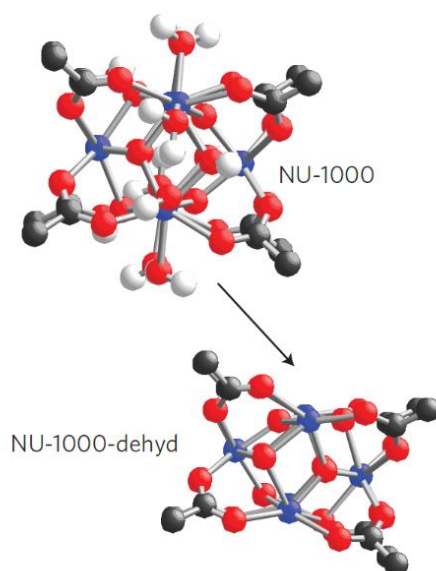


**Figure 1.35.** Molecular representation of the dehydration of the NU-1000 node. Reproduced from reference 11.

Katz et al.<sup>205</sup> then performed an extensive study to investigate the positive effect of decreasing  $[\text{OH}^-]$  on increasing the rate of DMNP hydrolysis in the presence of UiO-66 and NEM buffer. Different pH NEM buffers were used (10.2-8.3) and a pH of 8.6 resulted in the fastest initial rate for DMNP hydrolysis, with a drastic drop in initial rate being observed above pH 9.0. The authors suggest that at a higher pH, node ligated water molecules are converted to hydroxyl ligands which are less readily displaced by the DMNP (Figure 1.36). The displacement of coordinated  $\text{OH}^-$  becomes the rate limiting step at higher pH. To reinforce this, UiO-66 was thermally activated to yield UiO-66-dehyd. A tenfold rate enhancement was then observed for UiO-66-dehyd over that of regular UiO-66 for the hydrolysis of DMNP in NEM buffer. This observation supports the study performed by Mondloch et al., but both of these studies were only performed on DMNP.

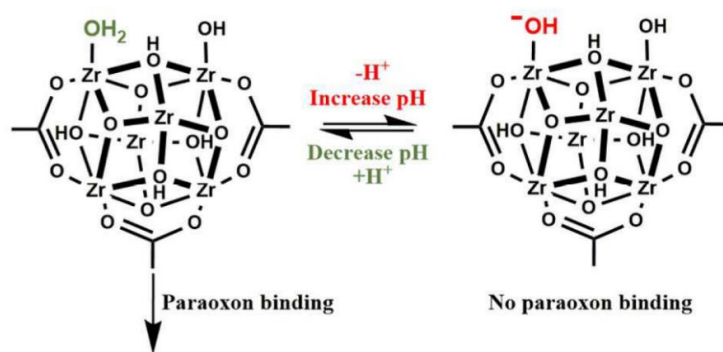


**Figure 1.36.** (left) presumed composition of a defective UiO-66 cluster in the absence of one BDC linker. The open  $Zr^{IV}$  sites are occupied by terminal hydroxide and aqua ligands. (right) at high pH values, the aqua ligand converts to a substitution resistant hydroxide. Reproduced from reference 205.

In contrast, Moon et al.<sup>8</sup> reported the use of a ‘hydrated’ MOF-808 for the hydrolysis of DMNP. The preparation of this framework involved the aqueous activation of  $Zr_6(\mu_3-O)_4(\mu_3-OH)_4(HCOO)_6(BTC)_2$  to remove the formate modulator occupying the  $Zr^{IV}$  vacancies, thus yielding  $Zr_6(\mu_3-O)_4(\mu_3-OH)_4(H_2O)_6(OH)_6(BTC)_2$ . Unfortunately, no hydrolytic comparison was made between the as-synthesised and activated framework. MOF-808 remains one of the most active degradation materials to date for the hydrolysis of CWAs but there have been no reports of any further enhancements through dehydration.

Taking the above studies into consideration, ‘hydration’ of zirconate MOFs under hydrothermal conditions can be useful for removing synthetic modulator, thus making coordination vacancies available. Furthermore, thermal activation can then be used to ‘dehydrate’ a hydrated, modulator free node. The dehydration further enhances the catalytic ability of the framework by allowing DMNP to interact directly with the coordinatively unsaturated metal. However, for the ultimate confirmation of the dehydration facilitated enhancement, a future study needs to be conducted on live OP CWAs, and not just the DMNP simulant.

## 1.5 Zirconium MOF Composites for CWA degradation

Due to the reported success of zirconium frameworks as potent hydrolysis catalysts for the degradation of OP CWAs and their simulants, their functional utility has been highlighted for the combating of the treat CWAs still pose. There is a growing need for sorbents, filters and textiles with self-detoxifying properties which can be deployed for clean ups and in protective equipment. As a result of this, a number of composite materials have been reported which have incorporated well reported CWA degradation catalysts for this very purpose. This next section will review a number of composite materials which have utilised zirconate MOFs as active degradation catalysts for protection against CWAs.

The earliest example of a MOF composite was described by López-Maya et al.<sup>206</sup> UiO-66 was first activated at 300 °C and then treated with LiOtBu to yield UiO-66@LiOtBu ( $[\text{Zr}_6\text{O}_6(\text{bdc})_6] \cdot (\text{LiOtBu})_{0.3}$ ). The MOF was then heterogeneously sprayed onto the surface of a silk fibroin fabric (Figure 1.37). Diisopropylfluorophosphate (DIFP), a structural simulant of sarin was then used to probe the effectiveness of the composite material. A stoichiometric catalyst loading was employed for this hydrolysis, but it should be noted that the DIFP simulant was administered neat on to the fabric.

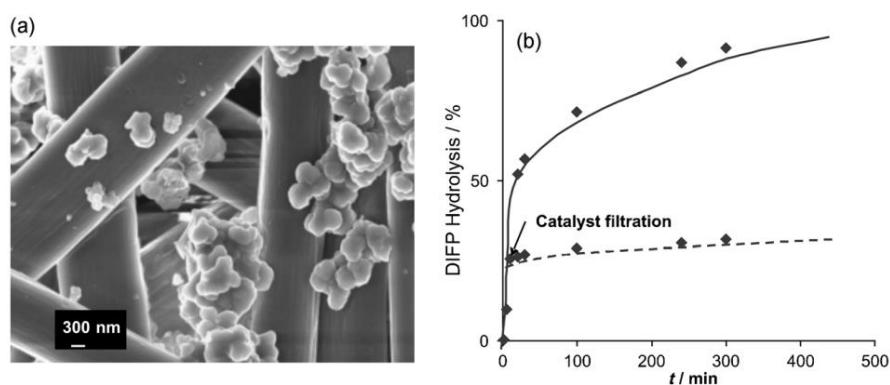


**Figure 1.37.** a) VP-SEM (VP = variable pressure) images of silk@[UiO-66@LiOtBu] composite. Hydrolytic degradation profile of b) DIFP catalyzed by silk@[UiO-66@LiOtBu] composite at room temperature. The dotted lines indicate the effect of removing the [UiO66@LiOtBu] by filtration to demonstrate the heterogeneity of the catalytic process. Reproduced from reference 206.

Near-full hydrolysis of DIFP into diisopropyl phosphonate (> 95 %) was observed after 6 hours (Figure 1.37). It should be noted that when the reaction was repeated but the MOF-textile was removed after a short period of time, very little hydrolysis was observed after this point, confirming the heterogeneity of the process. Unfortunately, the authors did not perform any studies with DMNP so no comparisons can be made to previously reported experiments which utilised this simulant. Also, the results were not confirmed on live CWAs, but the similarity between the structures of the DIFP simulant and Sarin make it quite a compelling example, at least for G-series agents. It is also heavily implied that the hydrolytic properties of the material are derived from stoichiometric loading of alkoxide moieties onto the  $Zr_6$  nodes. Whether the material is truly catalytic is therefore questionable.

Following on from this study, Zhao et al. reported the growth of UiO-66, UiO-66-NH<sub>2</sub> and UiO-67 on the surface of electrospun polymeric nanofibers of polyamide-6 (PA-6).<sup>207</sup> This was achieved by coating the PA-6 with a thin layer (5nm) of TiO<sub>2</sub> using atomic layer deposition. The frameworks were then grown on the TiO<sub>2</sub> surface which functioned as a nucleation point for the MOF films. HCl was used as modulator for more growth and an incubation temperature of 85°C was used (Figure 1.38). The hydrolysis of DMNP in aqueous NEM buffer was then probed in the presence of the three MOF-fiber composites. The powdered form of UiO-66, UiO-66-NH<sub>2</sub> and UiO-67 were also tested alongside the composites. The fiber-composites of UiO-66 and UiO-66-NH<sub>2</sub> both exhibited a significantly poorer performance than their powdered counterparts, likely due to the catalysis being restricted to the surface of these smaller frameworks. However, the performance of the UiO-67-fiber composite was near identical to powdered UiO-67 with a DMNP half-life of 9 minutes being observed. The composites were then tested for their ability to degrade the nerve agent Soman. A composite loading containing a catalyst loading of approximately 20 % (relative to substrate) was used in the presence of aqueous NEM buffer. A very short Soman half-life (< 5 mins) was recorded in the presence of all of the composites with the UiO-67-fiber exhibiting the largest degree of hydrolysis over the

course of the reaction. This study was showing the first example of a MOF composite able to degrade live OP CWAs. However, the degradation still relied on the presence of a liquid buffering agent to facilitate the hydrolysis which is not ideal for practical applications.

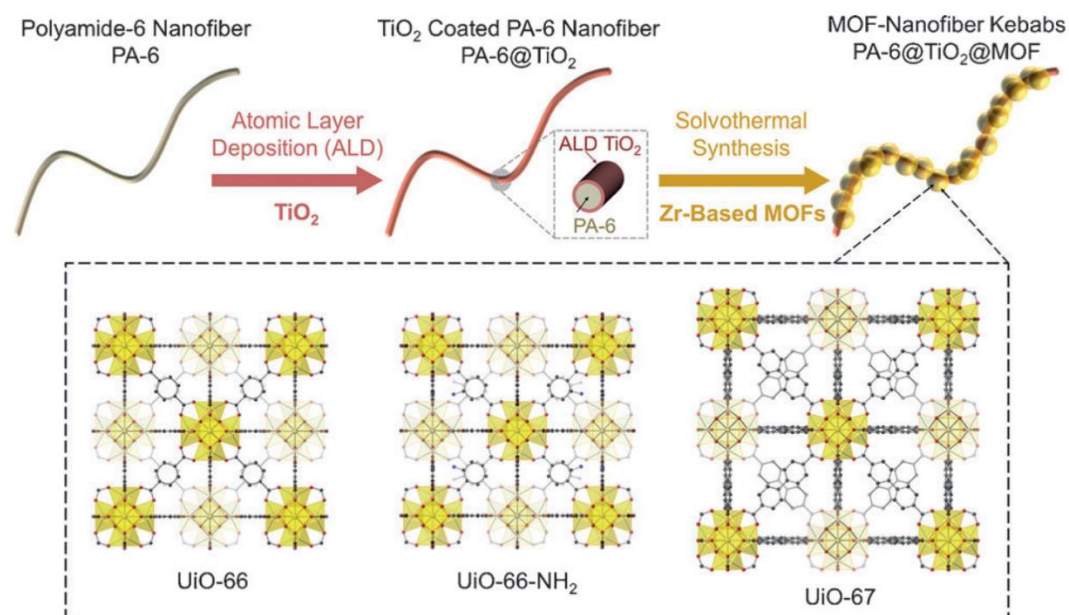


**Figure 1.38.** Synthetic procedure for Zr-based MOF–nanofiber kebab structures on polyamide-6 nanofibers. Reproduced from reference 207.

Soon after, Moon et al. reported the synthesis of a composite material featuring the MOF NU-1000 embedded in a polyethyleneimine (PEI) membrane (NU-1000/PEI).<sup>208</sup> The PEI functions as a heterogeneous buffer for OP hydrolysis. The authors synthesised three NU-1000/PEI composites, each containing a different MW of PEI, NU-1000/PEI MW2500, NU-1000/PEI MW25000 and NU-1000/PEI MW250000. Using standard DMNP hydrolysis conditions, NU-1000/PEI MW2500, powdered NU-1000 and PEI MW2500 were all tested for their ability to degrade DMNP in aqueous NEM buffer. Both the NU-1000/PEI MW2500 composite and powdered NU-1000 performed very well with DMNP half-lives of < 7.5 mins, negligible hydrolysis was observed in the presence of just PEI MW2500. Moving on, PEI, NU-1000/PEI MW2500, NU-1000/PEI MW25000 and NU-1000/PEI MW250000 were then tested as degradation materials for the hydrolysis of DMNP, but this time in the absence of a solution

buffer, the number of moles of amine were kept consistent in each material. Full DMNP hydrolysis was observed with NU-1000/PEI MW2500, NU-1000/PEI MW25000 but not NU-1000/PEI MW250000. This can be attributed to the relatively lower pH of the polymer solution with high molecular weight PEI in water; NU-1000/PEI MW2500 (pH 9.2), NU-1000/PEI MW25000 (pH 8.8) and NU-1000/PEI MW250000 (pH 7.7). NU-1000/PEI MW2500 and NU-1000/PEI MW25000 were then screened for their ability to degrade Soman and VX in water and in the absence of a buffer. Interestingly, NU-1000/PEI MW25000 outperformed NU-1000/PEI MW2500 for the hydrolysis of VX due to a lower pH of 8.8 vs 9.2 (Figure 1.39). The hydrolysis of VX entails the protonation of a tertiary amine ( $pK_a$  8.6) which is more thermodynamically favourable at a lower pH. This was in contrast to the hydrolysis of Tabun which occurred faster in the presence of the more basic NU-1000/PEI MW2500. This study was highly demonstrative as it was the first example of MOF composite material which was able to function in the absence of a solution buffer, however a large stoichiometric excess of water was still required.

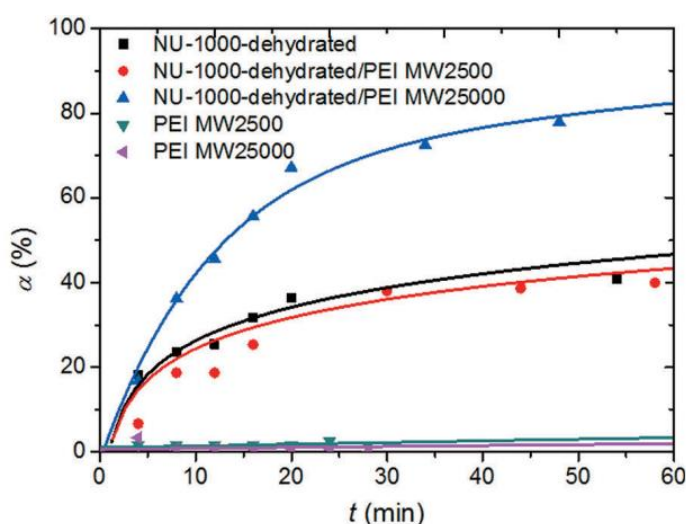


**Figure 1.39.** Hydrolysis profiles of VX in the presence of catalyst and/or different molecular weight PEI. Solid lines are used as a guide reproduced from reference 208.

Finally, the most recent example of a zirconium MOF composite for OP degradation was reported by Liang et al. The authors reported flexible, free-stranding  $ZrO_2$  nanofiber mats

which were obtained via sol-gel electrospinning followed by calcination.<sup>209</sup> UiO-66, UiO-67 and UiO-66-NH<sub>2</sub> were then all individually grown on the nanofiber surface at 150°C, in the solution state (Figure 1.40). The hydrolysis of DMNP was then monitored in the presence of MOF-fiber-composites, the performance was compared to the corresponding UiO-66, UiO-67 and UiO-66-NH<sub>2</sub> powders. The hydrolysis of DMNP was performed in the presence of NEM buffer.

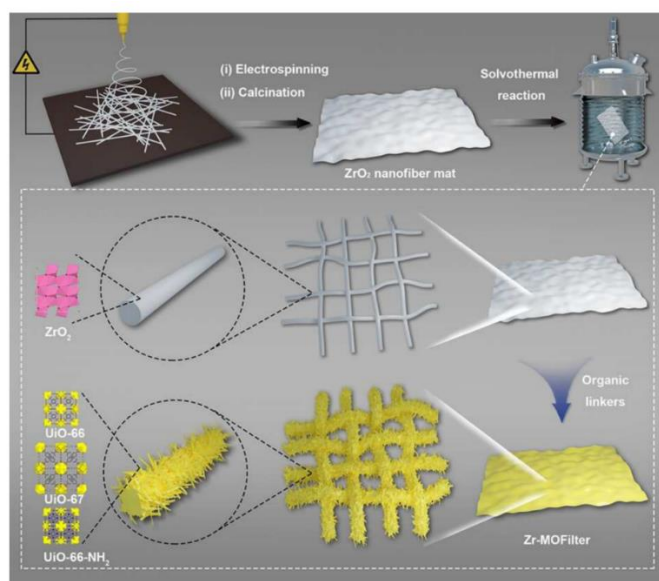


**Figure 1.40.** Synthetic procedure for the flexible ZrO<sub>2</sub> MOF filters. Reproduced from reference 209.

A notable reduction in DMNP half-life was observed in the presence of the MOF composites when compared to their corresponding MOF powders:  $t_{1/2}$  13.3 mins vs. 22.7 mins for UiO-66,  $t_{1/2}$  6.7 mins vs. 9.7 mins for UiO-67 and  $t_{1/2}$  2.4 mins vs. 6.5 mins for UiO-66-NH<sub>2</sub>. A negligible amount of hydrolysis occurred in the presence of just the nanofiber. The enhancement in hydrolysis is derived from the superior dispersion of the MOF catalysts provided by the nanofiber framework. Whilst a novel approach was taken towards synthesising a composite for CWA hydrolysis, the hydrolysis was still conducted in the solution state and relied on the presence of an aqueous buffer. The reliance upon additional solvent and buffer limits the practical applicability of the MOF-fiber composite as a filter.

## 1.6 Summary and Reflection

To summarise, this introductory review chapter has provided an outline of several areas regarding the remediation of OP CWAs, along with an in-depth introduction to MOFs and ligand-based emission in such materials. A number of G and V-series agents were summarised along with common methods which exist for decontaminating them. An outline was also provided of previous events which highlight the threat that CWAs still pose on humankind. Moving on, several previously reported catalytic degradation systems were explored for the degradation of OP CWAs. First, the review looked at nano-structured metal oxides such as  $\text{CeO}_2$  and  $\text{TiO}_2$  which had been reported for combating OP CWAs, it was found that the entirety of studies described the use of a large stoichiometric excess of metal oxide relative to the substrates which were tested. The review then explored hydrogen bond/ metal chelate complexes, these materials have also been reported as degradation materials of OP simulants/CWA. However, they were also hindered by high catalyst loading and the necessitated an aqueous buffer.

The subject of the introduction was then shifted to MOFs. The review looked at some of the applications and strategies which exist for assembling MOFs. The review then explored some of the applications of photoluminescent MOFs which exhibit ligand-based emission with a focus on hydration-dependant emission for water sensing. Ligand-based emission was chosen to draw attention away from rare earth/lanthanide metal frameworks which are commonly reported for the majority of photoluminescent applications. Following on, the review focused on zirconium MOFs and the numerous reports of their utility as heterogeneous catalysts. A plethora of studies were reviewed which involved the catalytic zirconium MOF facilitated hydrolysis of the OP CWA simulant DMNP along with G and V-series agents. For the hydrolysis of DMNP, the studies all employed buffer, however the catalyst loading was kept low (1.25 – 5 %). The hydrolysis of V-series agents was also found to occur in the absence of buffer, in the presence of only water and a catalytic quantity of zirconate MOF, thus making it the most

effective catalytic OP CWA degradation material available. MOF-808, a zirconium MOF with a six-connected structure, was found to be the most effective catalyst for both CWA simulant and OP CWA hydrolysis. The effectiveness was due to a higher abundance of catalytic sites on the  $Zr_6$  nodes of MOF-808.

Finally, the introduction explored some of the previously reported composite materials which have incorporated zirconium MOFs for the hydrolysis of CWAs. The leading material was found to be a composite composed of PEI/NU-1000, with the PEI polymer matrix facilitating the buffer-free hydrolysis of the DMNP simulant along with VX. The incorporation of a heterogeneous amine was noted as an effective method for enhancing the hydrolytic performance of a composite material.

Zirconium MOFs possessing coordination vacancies/defects, MOF-808 in particular, are potent heterogeneous catalysts for the hydrolysis of OP CWAs. MOF-808 is capable of hydrolysing the nerve agent VX in the absence of a buffering reagent. MOF-808 is therefore a suitable candidate for incorporation into composite materials such as filters, textiles or encapsulation agents, for combatting CWAs. In these composites, MOF-808 could function as an effective catalyst whilst negating the necessity for any additional reagents, this would enhance the practical applicability of the material to real life scenarios.

## 1.7 Thesis Objective

The thesis objective is to develop a material capable of swelling/encapsulating and degrading neat V-series agent. The degradation should be scalable to the Litre scale. The material will likely exist as a composite and will be composed of two parts. First, a super-absorbent polymer (SAP) sponge capable of swelling to high degrees ( $Q < 40$ ) with neat CWA. Secondly, the composite will house a catalyst which will be embedded in the polymer matrix which should be capable of degrading neat CWA. The degradation should be catalytic and should take place in the absence of any solvent or buffer. For hydrolysis, the degradation fuel should be  $H_2O$  that should be exclusively facilitated by the presence of atmospheric humidity. The research and development of the SAP shall be conducted by Alexander J Wright.

The research and development of the OP CWA degradation catalyst shall be conducted by the author of this thesis. This will involve screening several catalyst systems on OP CWA simulants. Once several catalytic candidates have been identified, the materials will be tested on live OP CWAs such as VX and VM. Any successful materials will be nominated for testing on neat CWAs. Further modifications will be explored in an attempt to optimise the degradation capacity of the catalytic material. The aim is not necessarily fast degradation. In the end, the material should be able to facilitate the complete breakdown of the OP CWAs and at a significantly enhanced rate compared to the ambient degradation of the material and in the absence of any excess reagents.

## 1.8 Bibliography

- 1 Y. Ma, W. Gao, Z. Zhang, S. Zhang, Z. Tian, Y. Liu, J. C. Ho and Y. Qu, *Surf. Sci. Rep.*, 2018, **73**, 1–36.
- 2 P. Ji, J. Zhang, F. Chen and M. Anpo, *J. Phys. Chem. C*, 2008, **112**, 17809–17813.
- 3 P. Janoš, J. Henych, O. Pelant, V. Pilařová, L. Vrtoch, M. Kormunda, K. Mazanec and V. Štengl, *J. Hazard. Mater.*, 2016, **304**, 259–268.
- 4 A. Barba-Bon, A. M. Costero, M. Parra, S. Gil, R. Martínez-Máñez, F. Sancenón, P. A. Gale and J. R. Hiscock, *Chem. Eur. J.*, 2013, **19**, 1586–1590.
- 5 H. Gao, Z. Ke, N. J. DeYonker, J. Wang, H. Xu, Z.-W. Mao, D. L. Phillips and C. Zhao, *J. Am. Chem. Soc.*, 2011, **133**, 2904–2915.
- 6 L. Tjioe, T. Joshi, C. M. Forsyth, B. Moubaraki, K. S. Murray, J. Brugger, B. Graham and L. Spiccia, *Inorg. Chem.*, 2012, **51**, 939–953.
- 7 M. J. Katz, J. E. Mondloch, R. K. Totten, J. K. Park, S. T. Nguyen, O. K. Farha and J. T. Hupp, *Angew. Chem. Int. Ed.*, 2014, **53**, 497–501.
- 8 S.-Y. Moon, Y. Liu, J. T. Hupp and O. K. Farha, *Angew. Chem. Int. Ed.*, 2015, **54**, 6795–6799.
- 9 M. C. de Koning, M. van Grol and T. Breijaert, *Inorg. Chem.*, 2017, **56**, 11804–11809.
- 10 M. Bosch, M. Zhang and H.-C. Zhou, *Adv. Chem.*, 2014, **2014**, 1–8.
- 11 J. E. Mondloch, M. J. Katz, W. C. Isley III, P. Ghosh, P. Liao, W. Bury, G. W. Wagner, M. G. Hall, J. B. DeCoste, G. W. Peterson, R. Q. Snurr, C. J. Cramer, J. T. Hupp and O. K. Farha, *Nat. Mater.*, 2015, **14**, 512–516.
- 12 S.-Y. Moon, G. W. Wagner, J. E. Mondloch, G. W. Peterson, J. B. DeCoste, J. T. Hupp and O. K. Farha, *Inorg. Chem.*, 2015, **54**, 10829–10833.
- 13 M. J. Katz, S.-Y. Moon, J. E. Mondloch, M. H. Beyzavi, C. J. Stephenson, J. T. Hupp and O. K. Farha, *Chem. Sci.*, 2015, **6**, 2286–2291.
- 14 Y. Cui, Y. Yue, G. Qian and B. Chen, *Chem. Rev.*, 2012, **112**, 1126–1162.
- 15 D. Liu, K. Lu, C. Poon and W. Lin, *Inorg. Chem.*, 2014, **53**, 1916–24.
- 16 Y.-Q. Chen, G.-R. Li, Z. Chang, Y.-K. Qu, Y.-H. Zhang and X.-H. Bu, *Chem. Sci.*, 2013, **4**, 3678–3682.
- 17 L. Chen, J.-W. Ye, H.-P. Wang, M. Pan, S.-Y. Yin, Z.-W. Wei, L.-Y. Zhang, K. Wu, Y.-N. Fan and C.-Y. Su, *Nat. Commun.*, 2017, **8**, 15985.
- 18 D. A. Giannakoudakis and T. J. Bandosz, in *Detoxification of Chemical Warfare Agents*, Springer International Publishing, Cham, 2018, pp. 1–3.
- 19 *J. R. Army Med. Corps*, 2002, **148**, 358–70.
- 20 H. Q. Le and S. J. Knudsen, *Emerg. Med. J.*, 2006, **23**, 296–9.

- 21 B. Saha, N. Choudhury, S. Seal, B. Ruidas and P. De, *Biomacromolecules*, 2019, **20**, 546–557.
- 22 Y. Chen, Y. Jia, W. Song and L. Zhang, *Front. Pharmacol.*, 2018, **9**, 1453.
- 23 M. P. Shakarjian, D. E. Heck, J. P. Gray, P. J. Sinko, M. K. Gordon, R. P. Casillas, N. D. Heindel, D. R. Gerecke, D. L. Laskin and J. D. Laskin, *Toxicol. Sci.*, 2010, **114**, 5–19.
- 24 K. Ganesan, S. K. Raza and R. Vijayaraghavan, *J. Pharm. Bioallied Sci.*, 2010, **2**, 166–78.
- 25 R. C. Gupta, *Handbook of toxicology of chemical warfare agents*, Elsevier/Academic Press, 2009, pp. 172-174
- 26 F. R. Sidell and J. Borak, *Ann. Emerg. Med.*, 1992, **21**, 865–871.
- 27 S. W. Wiener and R. S. Hoffman, *J. Intensive Care Med.*, 2004, **19**, 22–37.
- 28 C. H. Gunderson, C. R. Lehmann, F. R. Sidell and B. Jabbari, *Neurology*, 1992, **42**, 946–50.
- 29 G. A. Petroianu, *Pharmazie*, 2010, **65**, 776–80.
- 30 C. P. Holstege, M. Kirk and F. R. Sidell, *Crit. Care Clin.*, 1997, **13**, 923–942.
- 31 H. P. Benschop and L. P. A. De Jong, *Acc. Chem. Res.*, 1988, **21**, 368–374.
- 32 G. W. Wagner, *Main Gr. Chem.*, 2010, **9**, 257–263.
- 33 Y.-C. Yang, *Acc. Chem. Res.*, 1998, **32**, 109–115.
- 34 F. Spellman, *Handbook of Environmental Engineering*, CRC Press, 2015, pp. 577-581
- 35 S. Talmage, A. Watson, V. Hauschild, N. Munro and J. King, *Curr. Org. Chem.*, 2007, **11**, 285–298.
- 36 E. Ghanem, Y. Li, C. Xu and F. M. Raushel, *Biochemistry*, 2007, **46**, 9032–9040.
- 37 1925 Geneva Protocol – UNODA, <https://www.un.org/disarmament/wmd/bio/1925-geneva-protocol/>, (accessed 3 September 2018).
- 38 Z. Moshaver, *Int. Aff.*, 1994, **70**, 590–591.
- 39 Military and Security Developments Involving the Democratic People’s Republic of Korea 2017, <https://fas.org/irp/world/dprk/dod-2017.pdf>, (accessed 12 March 2019).
- 40 Chemical and Biological Weapons in the Middle East - Carnegie Endowment for International Peace, <https://carnegieendowment.org/2002/04/16/chemical-and-biological-weapons-in-middle-east-pub-11745>, (accessed 19 February 2019).
- 41 R. Beaton, A. Stergachis, M. Oberle, E. Bridges, M. Nemuth and T. Thomas, *Traumatology*, 2005, **11**, 103–119.
- 42 R. Pita, J. Domingo, R. Pita and J. Domingo, *Toxics*, 2014, **2**, 391–402.
- 43 Government Assessment of the Syrian Government’s Use of Chemical Weapons on August 21, 2013 | whitehouse.gov, <https://obamawhitehouse.archives.gov/the-press-office/2013/08/30/government-assessment-syrian-government-s-use-chemical-weapons-august-21>, (accessed 8 February 2019).

- 44 Syria: reported chemical weapons use - Joint Intelligence Committee letter - GOV.UK, <https://www.gov.uk/government/publications/syria-reported-chemical-weapons-use-joint-intelligence-committee-letter>, (accessed 8 February 2019).
- 45 T. L. McNaugher, *Int. Secur.*, 1990, **15**, 5-34.
- 46 F. Hashemian, K. Khoshnood, M. M. Desai, F. Falahati, S. Kasl and S. Southwick, *JAMA*, 2006, **296**, 560-566.
- 47 P. Kuran, P. Janos, M. Kormunda, V. Stengl, T. M. Grygar, M. Dosek, M. Stastny, J. Ederer, V. Pilarova and L. Vrtoch, *J. RARE EARTHS*, 2014, **32**, 360-370.
- 48 G. W. Wagner, Q. Chen and Y. Wu, *J. Phys. Chem. C*, 2008, **112**, 11901–11906.
- 49 J. Henych, V. Štengl, M. Slušná, T. Matys Grygar, P. Janoš, P. Kuráň and M. Štastný, *Appl. Surf. Sci.*, 2015, **344**, 9–16.
- 50 A. Barba-Bon, A. M. Costero, M. Parra, S. Gil, R. Martínez-Máñez, F. Sancenón, P. A. Gale and J. R. Hiscock, *Chem. Eur. J.*, 2013, **19**, 1586–1590.
- 51 Y. Liu, R. C. Klet, J. T. Hupp and O. Farha, *Chem. Commun.*, 2016, **52**, 7806–7809.
- 52 M. J. Katz, J. E. Mondloch, R. K. Totten, J. K. Park, S. T. Nguyen, O. K. Farha and J. T. Hupp, *Angew. Chem. Int. Ed.*, **126**, 507–511.
- 53 R. D. L. Smith, M. S. Prevot, R. D. Fagan, Z. Zhang, P. A. Sedach, M. K. J. Siu, S. Trudel and C. P. Berlinguette, *Science*, 2013, **340**, 60–63.
- 54 J. P. Dunn, H. G. Stenger and I. E. Wachs, *J. Catal.*, 1999, **181**, 233–243.
- 55 S. C. Kim, *J. Hazard. Mater.*, 2002, **91**, 285–99.
- 56 F. Yu, F. Li, B. Zhang, H. Li and L. Sun, *ACS Catal.*, 2015, **5**, 627–630.
- 57 H. C. Genuino, S. Dharmarathna, E. C. Njagi, M. C. Mei and S. L. Suib, *J. Phys. Chem. C*, 2012, **116**, 12066–12078.
- 58 S. M. Saqer, D. I. Kondarides and X. E. Verykios, *Appl. Catal. B Environ.*, 2011, **103**, 275–286.
- 59 S. D. Senanayake, D. Stacchiola and J. A. Rodriguez, *Acc. Chem. Res.*, 2013, **46**, 1702–1711.
- 60 E. Aneggi, C. de Leitenburg, J. Llorca and A. Trovarelli, *Catal. Today*, 2012, **197**, 119–126.
- 61 A. Bueno-López, *Appl. Catal. B Environ.*, 2014, **146**, 1–11.
- 62 Ş. Neaţu, B. Cojocar, V. I. Pârvulescu, V. Şomoghi, M. Alvaro and H. Garcia, *J. Mater. Chem.*, 2010, **20**, 4050-4054.
- 63 I. Celardo, J. Z. Pedersen, E. Traversa and L. Ghibelli, *Nanoscale*, 2011, **3**, 1411-1420.
- 64 G. I. Almerindo, P. Bueno, L. M. Nicolazi, E. H. Wanderlind, P. Sangaletti, S. M. Landi, L. A. Sena, B. S. Archanjo, C. A. Achete, H. D. Fiedler and F. Nome, *J. Phys. Chem. C*, 2016, **120**, 22323–22329.
- 65 D. Zhang, X. Du, L. Shi and R. Gao, *Dalton. Trans.*, 2012, **41**, 14455-14475.

- 66 X. Wang, Z. Jiang, B. Zheng, Z. Xie and L. Zheng, *CrystEngComm*, 2012, **14**, 7579-7582.
- 67 J. Zhang, S. Ohara, M. Umetsu, T. Naka, Y. Hatakeyama and T. Adschiri, *Adv. Mater.*, 2007, **19**, 203–206.
- 68 P. Janoš, J. Henych, O. Pelant, V. Pilařová, L. Vrtoch, M. Kormunda, K. Mazanec and V. Štengl, *J. Hazard. Mater.*, 2016, **304**, 259–268.
- 69 J. P. Kumar, P. V. R. K. Ramacharyulu, G. K. Prasad, A. R. Srivastava and B. Singh, *J. Porous Mater.*, 2015, **22**, 91–100.
- 70 V. Štengl, D. Králová, F. Opluštil and T. Němec, *Microporous Mesoporous Mater.*, 2012, **156**, 224–232.
- 71 C. Caltagirone, P. A. Gale, J. R. Hiscock, S. J. Brooks, M. B. Hursthouse and M. E. Light, *Chem. Commun.*, 2008, **0**, 3007-3009.
- 72 L. Bromberg, W. R. Creasy, D. J. McGarvey, E. Wilusz and T. A. Hatton, *ACS Appl. Mater. Interfaces*, 2015, **7**, 22001–22011.
- 73 D. Marciano, M. Goldvaser, I. Columbus and Y. Zafrani, *J. Org. Chem.*, 2011, **76**, 8549–8553.
- 74 T. M. Florence, *J. Inorg. Biochem.*, 1984, **22**, 221–230.
- 75 Q. Kong and C.-L. G. Lin, *Cell. Mol. Life Sci.*, 2010, **67**, 1817–29.
- 76 R. C. Courtney, R. L. Gustafson, S. J. Westerback, H. Hyytiainen, S. C. Chaberek and A. E. Martell, *J. Am. Chem. Soc.*, 1957, **79**, 3030–3036.
- 77 H. G. T. Ly, G. Fu, A. Kondinski, B. Bueken, D. De Vos and T. N. Parac-Vogt, *J. Am. Chem. Soc.*, 2018, **140**, 6325–6335.
- 78 Y. Liao, L. Zhang, M. H. Weston, W. Morris, J. T. Hupp and O. K. Farha, *Chem. Commun.*, 2017, **53**, 9376–9379.
- 79 D. Alezi, Y. Belmabkhout, M. Suyetin, P. M. Bhatt, Ł. J. Weseliński, V. Solovyeva, K. Adil, I. Spanopoulos, P. N. Trikalitis, A.-H. Emwas and M. Eddaoudi, *J. Am. Chem. Soc.*, 2015, **137**, 13308–13318.
- 80 D. DeSantis, J. A. Mason, B. D. James, C. Houchins, J. R. Long and M. Veenstra, *Energy & Fuels*, 2017, **31**, 2024–2032.
- 81 J. Fu, S. Das, G. Xing, T. Ben, V. Valtchev and S. Qiu, *J. Am. Chem. Soc.*, 2016, **138**, 7673–7680.
- 82 K. J. Hartlieb, J. M. Holcroft, P. Z. Moghadam, N. A. Vermeulen, M. M. Algaradah, M. S. Nassar, Y. Y. Botros, R. Q. Snurr and J. F. Stoddart, *J. Am. Chem. Soc.*, 2016, **138**, 2292–2301.
- 83 F. Luo, C. Yan, L. Dang, R. Krishna, W. Zhou, H. Wu, X. Dong, Y. Han, T.-L. Hu, M. O’Keeffe, L. Wang, M. Luo, R.-B. Lin and B. Chen, *J. Am. Chem. Soc.*, 2016, **138**, 5678–5684.

- 84 R. J. Marshall, Y. Kalinovsky, S. L. Griffin, C. Wilson, B. A. Blight and R. S. Forgan, *J. Am. Chem. Soc.*, 2017, **139**, 6253–6260.
- 85 J. Ferrando-Soria, H. Khajavi, P. Serra-Crespo, J. Gascon, F. Kapteijn, M. Julve, F. Lloret, J. Pasán, C. Ruiz-Pérez, Y. Journaux and E. Pardo, *Adv. Mater.*, 2012, **24**, 5625–5629.
- 86 X. Gao, Y. Wang, G. Ji, R. Cui and Z. Liu, *CrystEngComm*, 2018, **20**, 1087–1093.
- 87 S. Wuttke, M. Lismont, A. Escudero, B. Rungtaweeworanit and W. J. Parak, *Biomaterials*, 2017, **123**, 172–183.
- 88 M. J. Katz, Z. J. Brown, Y. J. Colón, P. W. Siu, K. A. Scheidt, R. Q. Snurr, J. T. Hupp and O. K. Farha, *Chem. Commun.*, 2013, **49**, 9449.
- 89 M. Miyamoto, K. Hori, T. Goshima, N. Takaya, Y. Oumi and S. Uemiya, *Eur. J. Inorg. Chem.*, 2017, 2094–2099.
- 90 S. Biswas and P. Van Der Voort, *Eur. J. Inorg. Chem.*, 2013, 2154–2160.
- 91 N. Kosinov, J. Gascon, F. Kapteijn and E. J. M. Hensen, *J. Memb. Sci.*, 2016, **499**, 65–79.
- 92 J. Zhang, L. Wang, Y. Shao, Y. Wang, B. C. Gates and F.-S. Xiao, *Angew. Chem. Int. Ed.*, 2017, **129**, 9879–9883.
- 93 Z. Xu, I. Michos, X. Wang, R. Yang, X. Gu and J. Dong, *Chem. Commun.*, 2014, **50**, 2416.
- 94 M. Eddaoudi, J. Kim, N. Rosi, D. Vodak, J. Wachter, M. O’Keeffe and O. M. Yaghi, *Science*, 2002, **295**, 469–72.
- 95 S. Brunauer, P. H. Emmett and E. Teller, *J. Am. Chem. Soc.*, 1938, **60**, 309–319.
- 96 K. S. W. and R. Q. Snurr, *J. Am. Chem. Soc.*, 2007, **129**, 8552–8556.
- 97 S. S. Kaye, A. Dailly, O. M. Yaghi and J. R. Long, *J. Am. Chem. Soc.*, 2007, **129**, 14176–14177.
- 98 J. H. Cavka, S. Jakobsen, U. Olsbye, N. Guillou, C. Lamberti, S. Bordiga and K. P. Lillerud, *J. Am. Chem. Soc.*, 2008, **130**, 13850–13851.
- 99 O. G. Nik, X. Y. Chen and S. Kaliaguine, *J. Memb. Sci.*, 2012, **413–414**, 48–61.
- 100 Z. H. Fard, Y. Kalinovsky, D. M. Spasyuk, B. A. Blight and G. K. H. Shimizu, *Chem. Commun*, 2016, **52**, 12865–12868.
- 101 M. Taddei, F. Costantino, A. Ienco, A. Comotti, P. V. Dau and S. M. Cohen, *Chem. Commun.*, 2013, **49**, 1315.
- 102 L. Li, G. J. Clarkson, D. J. Evans, M. R. Lees, S. S. Turner and P. Scott, *Chem. Commun.*, 2011, **47**, 12646–12648.
- 103 Y. Takashima, S. Furukawa and S. Kitagawa, *CrystEngComm*, 2011, **13**, 3360–3363.
- 104 E. Haldoupis, T. Watanabe, S. Nair and D. S. Sholl, *ChemPhysChem*, 2012, **13**, 3449–3452.
- 105 S. A. Moggach, T. D. Bennett and A. K. Cheetham, *Angew. Chem. Int. Ed.*, 2009, **48**, 7087–7089.

- 106 B. Assfour, S. Leoni and G. Seifert, *J. Phys. Chem. C*, 2010, **114**, 13381–13384.
- 107 V. M. Aceituno Melgar, J. Kim and M. R. Othman, *J. Ind. Eng. Chem.*, 2015, **28**, 1–15.
- 108 M. R. Lohe, M. Rose and S. Kaskel, *Chem. Commun.*, 2009, **0**, 6056–6058.
- 109 W. Liang, H. Chevreau, F. Ragon, P. D. Southon, V. K. Peterson and D. M. D'Alessandro, *CrystEngComm*, 2014, **16**, 6530–6533.
- 110 B. Liu, Q. Yang, C. Xue, C. Zhong and B. Smit, *Phys. Chem. Chem. Phys.*, 2008, **10**, 3244–3249.
- 111 B. Kesanli, Y. Cui, M. R. Smith, E. W. Bittner, B. C. Bockrath and W. Lin, *Angew. Chem. Int. Ed.*, 2005, **117**, 74–77.
- 112 R. J. Marshall and R. S. Forgan, *Eur. J. Inorg. Chem.*, 2016, 4310–4331.
- 113 D. Sun, W. Liu, M. Qiu, Y. Zhang and Z. Li, *Chem. Commun.*, 2015, **51**, 2056–2059.
- 114 J. D. Evans, C. J. Sumbly and C. J. Doonan, *Chem. Soc. Rev.*, 2014, **43**, 5933–5951.
- 115 N. Stock and S. Biswas, *Chem. Rev.*, 2012, **112**, 933–969.
- 116 H.-C. Zhou, J. R. Long and O. M. Yaghi, *Chem. Rev.*, 2012, **112**, 673–674.
- 117 T. K. Prasad and M. P. Suh, *Chem. Eur. J.*, 2012, **18**, 8673–8680.
- 118 H.-L. Jiang, T. A. Makal and H.-C. Zhou, *Coord. Chem. Rev.*, 2013, **257**, 2232–2249.
- 119 G. Zahn, H. A. Schulze, J. Lippke, S. König, U. Sazama, M. Fröba and P. Behrens, *Microporous Mesoporous Mater.*, 2015, **203**, 186–194.
- 120 M. Sánchez-Sánchez, N. Getachew, K. Díaz, M. Díaz-García, Y. Chebude and I. Díaz, *Green Chem.*, 2015, **17**, 1500–1509.
- 121 M. Taddei, P. V. Dau, S. M. Cohen, M. Ranocchiari, J. A. van Bokhoven, F. Costantino, S. Sabatini and R. Vivani, *Dalton. Trans.*, 2015, **44**, 14019–14026.
- 122 J. Klinowski, F. A. Almeida Paz, P. Silva and J. Rocha, *Dalton. Trans.*, 2011, **40**, 321–330.
- 123 P. A. Bayliss, I. A. Ibarra, E. Pérez, S. Yang, C. C. Tang, M. Poliakoff and M. Schröder, *Green Chem.*, 2014, **16**, 3796–3802.
- 124 M. Rubio-Martinez, M. P. Batten, A. Polyzos, K.-C. Carey, J. I. Mardel, K.-S. Lim and M. R. Hill, *Sci. Rep.*, 2015, **4**, 5443.
- 125 Y.-R. Lee, J. Kim and W.-S. Ahn, *Korean J. Chem. Eng.*, 2013, **30**, 1667–1680.
- 126 T. Li, D.-L. Chen, J. E. Sullivan, M. T. Kozlowski, J. K. Johnson and N. L. Rosi, *Chem. Sci.*, 2013, **4**, 1746–1755.
- 127 C. Atzori, G. C. Shearer, L. Maschio, B. Civalleri, F. Bonino, C. Lamberti, S. Svelle, K. P. Lillerud and S. Bordiga, *J. Phys. Chem. C*, 2017, **121**, 9312–9324.
- 128 F. Vermoortele, B. Bueken, G. Le Bars, B. Van de Voorde, M. Vandichel, K. Houthoofd, A. Vimont, M. Daturi, M. Waroquier, V. Van Speybroeck, C. Kirschhock and D. E. De Vos, *J. Am. Chem. Soc.*, 2013, **135**, 11465–11468.
- 129 R. J. Marshall, C. L. Hobday, C. F. Murphie, S. L. Griffin, C. A. Morrison, S. A. Moggach

- and R. S. Forgan, *J. Mater. Chem. A*, 2016, **4**, 6955–6963.
- 130 J. Yang, X. Chen, Y. Li, Q. Zhuang, P. Liu and J. Gu, *Chem. Mater.*, 2017, **29**, 4580–4589.
- 131 V. Bon, I. Senkovska, M. S. Weiss and S. Kaskel, *CrystEngComm*, 2013, **15**, 9572–9577.
- 132 R. Nayuk, D. Zacher, R. Schweins, C. Wiktor, R. A. Fischer, G. Van Tendeloo and K. Huber, *J. Phys. Chem. C*, 2012, **116**, 6127–6135.
- 133 G. C. Shearer, S. Chavan, S. Bordiga, S. Svelle, U. Olsbye and K. P. Lillerud, *Chem. Mater.*, 2016, **28**, 3749–3761.
- 134 J. E. Mondloch, O. Karagiari, O. K. Farha and J. T. Hupp, *CrystEngComm*, 2013, **15**, 9258–9264.
- 135 A. M. Ploskonka and J. B. DeCoste, *ACS Appl. Mater. Interfaces*, 2017, **9**, 21579–21585.
- 136 Y. Kalinovsky, N. J. Cooper, M. J. Main, S. J. Holder and B. A. Blight, *Dalton. Trans.*, 2017, **46**, 15704–15709.
- 137 G. H. Albuquerque and G. S. Herman, *Cryst. Growth Des.*, 2017, **17**, 156–162.
- 138 Z. N. and R. I. Masel, *J. Am. Chem. Soc.*, 2006, **128**, 12394–12395
- 139 K. Užarević, T. C. Wang, S.-Y. Moon, A. M. Fidelli, J. T. Hupp, O. K. Farha and T. Friščić, *Chem. Commun.*, 2016, **52**, 2133–2136.
- 140 T. Friščić, in *Encyclopedia of Inorganic and Bioinorganic Chemistry*, John Wiley & Sons, Ltd, Chichester, UK, 2014, pp. 1–19.
- 141 M. Klimakow, P. Klobes, A. F. Thünemann, K. Rademann and F. Emmerling, *Chem. Mater.*, 2010, **22**, 5216–5221.
- 142 T. Friščić, D. G. Reid, I. Halasz, R. S. Stein, R. E. Dinnebier and M. J. Duer, *Angew. Chem. Int. Ed.*, 2010, **49**, 712–715.
- 143 Y. Chen, H. Wu, Z. Liu, X. Sun, Q. Xia and Z. Li, *Ind. Eng. Chem. Res.*, 2018, **57**, 703–709.
- 144 A. J. Howarth, A. W. Peters, N. A. Vermeulen, T. C. Wang, J. T. Hupp and O. K. Farha, *Chem. Mater.*, 2017, **29**, 26–39.
- 145 J. G. Vitillo, C. Atzori, B. Civalieri, N. Barbero, C. Barolo and F. Bonino, in *Hybrid Organic-Inorganic Interfaces*, Wiley-VCH Verlag GmbH & Co. KGaA, Weinheim, Germany, 2017, pp. 459–495.
- 146 K. Seki and W. Mori, *J. Phys. Chem. B*, 2002, **106**, 1380–1385
- 147 G. Giakisikli and A. N. Anthemidis, *Anal. Chim. Acta*, 2013, **789**, 1–16.
- 148 S. Devautour-Vinot, G. Maurin, F. Henn, C. Serre, T. Devic and G. Férey, *Chem. Commun.*, 2009, **0**, 2733–2735.
- 149 N. Sahiner, K. Sel, O. F. Ozturk, S. Demirci and G. Terzi, *Appl. Surf. Sci.*, 2014, **314**, 663–669.
- 150 X. Yu and S. M. Cohen, *Chem. Commun.*, 2015, **51**, 9880–9883.
- 151 A. D. Burrows and L. L. Keenan, *CrystEngComm*, 2012, **14**, 4112–4114.

- 152 C. A. Bauer, T. V. Timofeeva, T. B. Settersten, B. D. Patterson, V. H. Liu, B. A. Simmons and M. D. Allendorf, *J. Am. Chem. Soc.*, 2007, **129**, 7136–7144.
- 153 J. D. Furman, A. Y. Warner, S. J. Teat, A. A. Mikhailovsky and A. K. Cheetham, *Chem. Mater.*, 2010, **22**, 2255–2260.
- 154 Y. Cui, B. Chen and G. Qian, *Coord. Chem. Rev.*, 2014, **273–274**, 76–86.
- 155 X. Rao, Q. Huang, X. Yang, Y. Cui, Y. Yang, C. Wu, B. Chen and G. Qian, *J. Mater. Chem.*, 2012, **22**, 3210–3214.
- 156 D. Sun, Y. Gao, J. Fu, X. Zeng, Z. Chen and Z. Li, *Chem. Commun.*, 2015, **51**, 2645–2648.
- 157 J.-H. Wang, M. Li and D. Li, *Chem. Sci.*, 2013, **4**, 1793–1801.
- 158 Y. Zhang, S. Yuan, G. Day, X. Wang, X. Yang and H.-C. Zhou, *Coord. Chem. Rev.*, 2018, **354**, 28–45.
- 159 A. Adamson, *A Textbook of Physical Chemistry.*, Elsevier Science, 1979, pp. 789–848.
- 160 in *IUPAC Compendium of Chemical Terminology*, IUPAC, Research Triangle Park, NC.
- 161 Q. Fang, G. Zhu, M. Xue, J. Sun, F. Sun and S. Qiu, *Inorg. Chem.*, 2006, **45**, 3582–3587.
- 162 W. W. Lestari, H. C. Streit, P. Lönnecke, C. Wickleder and E. Hey-Hawkins, *Dalton. Trans.*, 2014, **43**, 8188–8195.
- 163 A. Douvali, A. C. Tsipis, S. V. Eliseeva, S. Petoud, G. S. Papaefstathiou, C. D. Malliakas, I. Papadas, G. S. Armatas, I. Margiolaki, M. G. Kanatzidis, T. Lazarides and M. J. Manos, *Angew. Chem. Int. Ed.*, 2015, **127**, 1671–1676.
- 164 H. Zhang, Y.-H. Li, Y. Chen, M.-M. Wang, X.-S. Wang and X.-B. Yin, *Sci. Rep.*, 2017, **7**, 44153.
- 165 G. Haider, M. Usman, T.-P. Chen, P. Perumal, K.-L. Lu and Y.-F. Chen, *ACS Nano*, 2016, **10**, 8366–8375.
- 166 Y. Zhou and B. Yan, *Nanoscale*, 2015, **7**, 4063–4069.
- 167 Q. Tang, S. Liu, Y. Liu, D. He, J. Miao, X. Wang, Y. Ji and Z. Zheng, *Inorg. Chem.*, 2014, **53**, 289–293.
- 168 Z. Wang, Z. Wang, B. Lin, X. Hu, Y. Wei, C. Zhang, B. An, C. Wang and W. Lin, *ACS Appl. Mater. Interfaces*, 2017, **9**, 35253–35259.
- 169 T. Mondal, S. Mondal, S. Bose, D. Sengupta, U. K. Ghorai and S. K. Saha, *J. Mater. Chem. C*, 2018, **6**, 614–621.
- 170 L. Martí-Bonmatí, R. Sopena, P. Bartumeus and P. Sopena, *Contrast Media Mol. Imaging*, 2010, **5**, 180–189.
- 171 A. Foucault-Collet, K. A. Gogick, S. Villette, A. Pallier, G. Collet, C. Kieda, T. Li, S. J. Geib, N. L. Rosi and S. Petoud, *Proc. Natl. Acad. Sci. U. S. A.*, 2013, **110**, 17199–204.
- 172 D. F. Sava Gallis, L. E. S. Rohwer, M. A. Rodriguez, M. C. Barnhart-Dailey, K. S. Butler, T. S. Luk, J. A. Timlin and K. W. Chapman, *ACS Appl. Mater. Interfaces*, 2017, **9**, 22268–

- 22277.
- 173 J. Della Rocca, D. Liu and W. Lin, *Acc. Chem. Res.*, 2011, **44**, 957–968.
- 174 H. Chen, J. Wang, D. Shan, J. Chen, S. Zhang and X. Lu, *Anal. Chem.*, 2018, **90**, 7056–7063.
- 175 W. Cai, H. Gao, C. Chu, X. Wang, J. Wang, P. Zhang, G. Lin, W. Li, G. Liu and X. Chen, *ACS Appl. Mater. Interfaces*, 2017, **9**, 2040–2051.
- 176 Y. Yu, J.-P. Ma, C.-W. Zhao, J. Yang, X.-M. Zhang, Q.-K. Liu and Y.-B. Dong, *Inorg. Chem.*, 2015, **54**, 11590–11592.
- 177 J. Aguilera-Sigalat and D. Bradshaw, *Chem. Commun.*, 2014, **50**, 4711–4713.
- 178 M. Zhang, G. Feng, Z. Song, Y.-P. Zhou, H.-Y. Chao, D. Yuan, T. T. Y. Tan, Z. Guo, Z. Hu, B. Z. Tang, B. Liu and D. Zhao, *J. Am. Chem. Soc.*, 2014, **136**, 7241–7244.
- 179 R.-B. Lin, F. Li, S.-Y. Liu, X.-L. Qi, J.-P. Zhang and X.-M. Chen, *Angew. Chem. Int. Ed.*, 2013, **52**, 13429–13433.
- 180 Y. Y. Liang, *Anal. Chem.*, 1990, **62**, 2504–2506.
- 181 Y. Yu, X.-M. Zhang, J.-P. Ma, Q.-K. Liu, P. Wang and Y.-B. Dong, *Chem. Commun.*, 2014, **50**, 1444–1446.
- 182 S. Wang, C. M. McGuirk, M. B. Ross, S. Wang, P. Chen, H. Xing, Y. Liu and C. A. Mirkin, *J. Am. Chem. Soc.*, 2017, **139**, 9827–9830.
- 183 V. Guillermin, F. Ragon, M. Dan-Hardi, T. Devic, M. Vishnuvarthan, B. Campo, A. Vimont, G. Clet, Q. Yang, G. Maurin, G. Férey, A. Vittadini, S. Gross and C. Serre, *Angew. Chem. Int. Ed.*, 2012, **51**, 9267–9271.
- 184 M. J. Katz, S.-Y. Moon, J. E. Mondloch, M. H. Beyzavi, C. J. Stephenson, J. T. Hupp and O. K. Farha, *Chem. Sci.*, 2015, **6**, 2286–2291.
- 185 M. J. Cliffe, W. Wan, X. Zou, P. A. Chater, A. K. Kleppe, M. G. Tucker, H. Wilhelm, N. P. Funnell, F.-X. Coudert and A. L. Goodwin, *Nat. Commun.*, 2014, **5**, 4176.
- 186 G. C. Shearer, J. G. Vitillo, S. Bordiga, S. Svelle, U. Olsbye and K. P. Lillerud, *Chem. Mater.*, 2016, **28**, 7190–7193.
- 187 Z. Hu, Y. Peng, Z. Kang, Y. Qian and D. Zhao, *Inorg. Chem.*, 2015, **54**, 4862–4868.
- 188 K. B. Lausund and O. Nilsen, *Nat. Commun.*, 2016, **7**, 13578.
- 189 S. Chavan, J. G. Vitillo, D. Gianolio, O. Zavorotynska, B. Civalieri, S. Jakobsen, M. H. Nilsen, L. Valenzano, C. Lamberti, K. P. Lillerud and S. Bordiga, *Phys. Chem. Chem. Phys.*, 2012, **14**, 1614–1626.
- 190 H. Furukawa, F. Gándara, Y.-B. Zhang, J. Jiang, W. L. Queen, M. R. Hudson and O. M. Yaghi, *J. Am. Chem. Soc.*, 2014, **136**, 4369–4381.
- 191 Y. Luan, Y. Qi, H. Gao, R. S. Andriamitantsoa, N. Zheng and G. Wang, *J. Mater. Chem. A*, 2015, **3**, 17320–17331.

- 192 B. Gui, X. Meng, Y. Chen, J. Tian, G. Liu, C. Shen, M. Zeller, D. Yuan and C. Wang, *Chem. Mater.*, 2015, **27**, 6426–6431.
- 193 J. B. DeCoste, M. A. Browe, G. W. Wagner, J. A. Rossin and G. W. Peterson, *Chem. Commun.*, 2015, **51**, 12474–12477.
- 194 M. I. Gonzalez, E. D. Bloch, J. A. Mason, S. J. Teat and J. R. Long, *Inorg. Chem.*, 2015, **54**, 2995–3005.
- 195 I. L. Malaestean, M. Speldrich, A. Ellern, S. G. Baca and P. Kögerler, *Dalton. Trans.*, 2011, **40**, 331–333.
- 196 R. Gil-San-Millan, E. López-Maya, M. Hall, N. M. Padial, G. W. Peterson, J. B. DeCoste, L. M. Rodríguez-Albelo, J. E. Oltra, E. Barea and J. A. R. Navarro, *ACS Appl. Mater. Interfaces*, 2017, **9**, 23967–23973.
- 197 C. He, K. Lu, D. Liu and W. Lin, *J. Am. Chem. Soc.*, 2014, **136**, 5181–5184.
- 198 S. A. Burgess, A. Kassie, S. A. Baranowski, K. J. Fritzsching, K. Schmidt-Rohr, C. M. Brown and C. R. Wade, *J. Am. Chem. Soc.*, 2016, **138**, 1780–1783.
- 199 C. Wang, Z. Xie, K. E. deKrafft and W. Lin, *J. Am. Chem. Soc.*, 2011, **133**, 13445–13454.
- 200 T. Zhang, K. Manna and W. Lin, *J. Am. Chem. Soc.*, 2016, **138**, 3241–3249.
- 201 S. Yuan, Y.-P. Chen, J. Qin, W. Lu, X. Wang, Q. Zhang, M. Bosch, T.-F. Liu, X. Lian and H.-C. Zhou, *Angew. Chem. Int. Ed.*, 2015, **54**, 14696–14700.
- 202 M. Rimoldi, A. J. Howarth, M. R. DeStefano, L. Lin, S. Goswami, P. Li, J. T. Hupp and O. K. Farha, *ACS Catal.*, 2017, **7**, 997–1014.
- 203 S. Wang, L. Bromberg, H. Schreuder-Gibson and T. A. Hatton, *ACS Appl. Mater. Interfaces*, 2013, **5**, 1269–1278.
- 204 H. Chen, P. Liao, M. L. Mendonca and R. Q. Snurr, *J. Phys. Chem. C*, 2018, **122**, 12362–12368.
- 205 M. J. Katz, R. C. Klet, S.-Y. Moon, J. E. Mondloch, J. T. Hupp and O. K. Farha, *ACS Catal.*, 2015, **5**, 4637–4642.
- 206 E. López-Maya, C. Montoro, L. M. Rodríguez-Albelo, S. D. Aznar Cervantes, A. A. Lozano-Pérez, J. L. Cenís, E. Barea and J. A. R. Navarro, *Angew. Chem. Int. Ed.*, 2015, **54**, 6790–6794.
- 207 J. Zhao, D. T. Lee, R. W. Yaga, M. G. Hall, H. F. Barton, I. R. Woodward, C. J. Oldham, H. J. Walls, G. W. Peterson and G. N. Parsons, *Angew. Chem. Int. Ed.*, 2016, **55**, 13224–13228.
- 208 S.-Y. Moon, E. Prousaloglou, G. W. Peterson, J. B. DeCoste, M. G. Hall, A. J. Howarth, J. T. Hupp and O. K. Farha, *Chem. Eur. J.*, 2016, **22**, 14864–14868.
- 209 H. Liang, A. Yao, X. Jiao, C. Li and D. Chen, *ACS Appl. Mater. Interfaces*, 2018, **10**, 20396–20403.

## Chapter 2. Screening of potential CWA simulants and catalysts

All hydrolysis experiments involving the agents GB and VX were completed by N. Cooper and M. Main at DSTL. Single-crystal X-ray analysis of Boron MOF was performed by H. Shepherd at the University of Kent. All other work described in this chapter was carried out by the author of this thesis.

### 2.1 Introduction

Chemical warfare agents (CWAs) are inherently highly toxic. Consequently, the possession, processing and manufacture of CWAs and their precursors is highly regulated. Due to highly strict regulations and the super-toxicity of CWAs,<sup>1,2</sup> it is not safe nor legal to handle these compounds in a standard laboratory environment. This presents an obvious problem when it comes to studying their properties. The solution is to use simulant compounds,<sup>3</sup> molecules which mimic a desired aspect of the CWA such as their reactivity or their solubility without the toxicity. It is important to select the correct simulant for the correct study but to also be aware of the certain limitations which exist for each simulant. Whilst some simulants are able to accurately mimic a selected property, it is vital that a study which begins with simulants should be concluded on live CWAs to truly confirm an effect. Tests on live CWAs are of course dangerous, costly and can only be carried out in specialised licensed laboratories. Simulants are therefore a safer, quicker and cheaper method for screening, identifying and nominating materials for testing on live CWAs.<sup>4-7</sup>

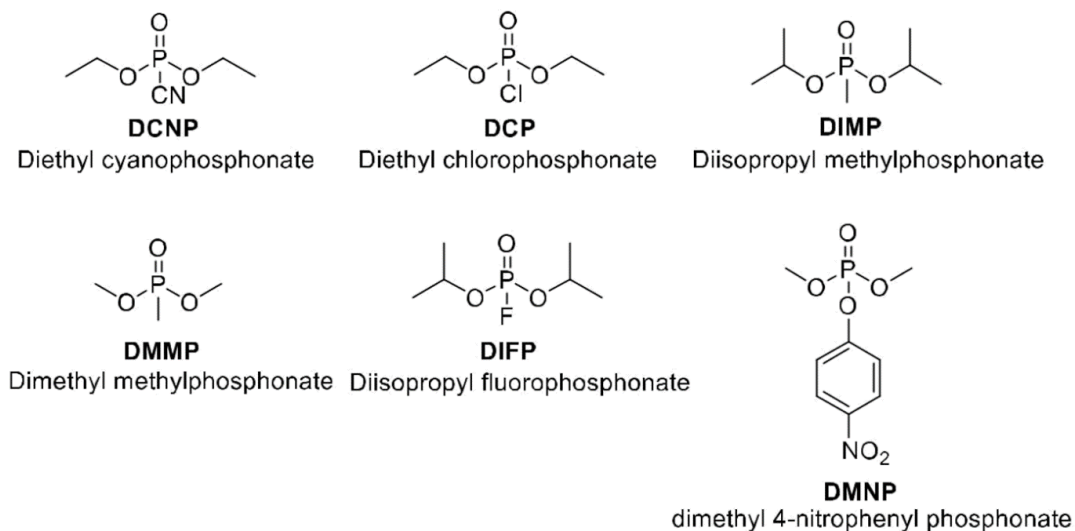
This chapter shall describe the search for a simulant system to mimic the hydrolysis of V-series agents. For hydrolysis, the degradation fuel should be H<sub>2</sub>O which should be exclusively facilitated by the presence of atmospheric humidity. For oxidation the degradation should be able to rely entirely on atmospheric oxygen. For enhanced efficiency, the catalyst should have a high turn-over frequency (TOF) with a catalytic loading not exceeding 5 mol %. The catalyst should also be compatible with the SAP and should not be hindered by being immobilised in the polymer membrane. Two initial avenues were explored for degradation, oxidative

hydrolysis and hydrolysis. First, the oxidation of phosphines and phosphites was studied. For oxidative hydrolysis, a number of commercial metal-oxide nanoparticles (MONPs) were selected to test as potential phosphine oxidation catalysts. A number of Cu(II) species were also screened for the oxidative hydrolysis of phosphites.<sup>8,9</sup> For hydrolysis, methyl-paraoxon (DMNP) was chosen based on results reported in the literature.<sup>6,10,11</sup> DMNP is a pesticide which in the presence of a basic aqueous buffer, undergoes hydrolysis that mimicks the hydrolysis of V-series agent VX. Whilst the use of a buffer was not ideal from the perspective of catalytic hydrolysis, DMNP would still serve as an effective simulant system for identifying catalytic candidates. Inspired by Farha's work on the hydrolysis of DMNP using the zirconium metal-organic framework (MOF) UiO-66,<sup>4</sup> a range of novel and previously reported zirconium MOF catalysts were screened as potential degradants. MOF-808,<sup>12,13,14</sup> a zirconium MOF with a Zr<sub>6</sub> node connectivity of 6 instead of the maximum of 12, proved to be the most effective catalyst. MOF-808 was then selected for testing on VX in aqueous solution and in the absence of any buffer. Finally, MOF-808 was screened for the hydrolysis of neat VX in the presence of only ambient humidity (40 RH %) to showcase the effectiveness of the catalyst.

### **2.1.1 Simulant selection**

A variety of simulants have been covered in the literature as replacements to model the CWAs. The natural problem with simulants is that they do not fully replicate the chemistry of the real CWAs.<sup>15,16</sup> Degradation is not the only activity studied which relates to CWAs. Alternative features such as the detection,<sup>17</sup> adsorption<sup>18</sup> and encapsulation<sup>19</sup> of these compounds has also been investigated. Therein lies the problem that because of the number of different features that are often explored, different chemical and physical aspects<sup>15,16</sup> of these toxins need to be examined. It is therefore difficult to find and use a 'one fits all' type simulant and so different properties of the CWAs need to be modelled by different simulants. Consequently, very careful consideration has to be given as to the choice of simulant for each particular study to ensure that the most realistic results are obtained. However, to ultimately obtain the most

accurate results, studies involving CWAs will inevitably have to be carried out on live agents. A number of compounds have been employed in the literature as simulants for various CWAs. Scheme 2.1 shows some of the more common simulants encountered in the literature.



**Scheme 2.1:** A scheme showing the structures of the various simulants discussed in this section.

DCNP is a mimic of the nerve agent Tabun.<sup>20</sup> It is used to simulate the hydrolysis of the P-C≡N bond in Tabun,<sup>21</sup> it is also used to develop sensors for the detection of Tabun. DCNP remains stable in the absence of a degradation reagent, allowing screening reactions to be conducted under a variety of conditions. Sadly, the hydrolysis product of DCNP is hydrogen cyanide and DCNP itself is cholinergic thus making it a dangerous simulant to work with. DCP is another CWA simulant.<sup>22</sup> The P-Cl bond in its structure is meant to partially mimic the P-F bond found in Sarin, Soman and Cyclosarin. However, as shown later in this chapter, near full hydrolysis of DCP is observed after 24 hours under ambient humidity, pressure and temperature. The fast, ambient degradation makes it difficult to properly screen catalysts which do not rapidly degrade the substrate. Depending on the nature of the investigation, this can become a nuisance, especially when instantaneous hydrolysis is not the aim. The instability of DCP combined with its toxicity can therefore make it troublesome simulant to work with.<sup>23–25</sup>

DMMP is mainly used to simulate the detection<sup>26,27</sup> and encapsulation<sup>22</sup> of Sarin. In terms of degradation, it has been previously used to simulate the cleavage of the P-S bond in VX which yields the hydrolysis product ethyl methyl phosphonate (EMPA), the P-O bond hydrolysis in DMMP is supposed to mimic this degradation. The hydrolysis of DMMP has, however, proven to be more difficult. Harsher, more alkaline, conditions are required to sever the P-O bond in DMMP than that of the P-S bond in VX.<sup>28</sup> Whilst a catalyst that is capable of hydrolysing DMMP is a promising candidate for the degradation of VX, milder catalysts which may only be effective against VX may be overlooked.

DIMP is another simulant, which finds its main use as a detection analogue,<sup>23-25</sup> it primarily mimics Sarin due to the similarity of the P-O-isopropyl functionality although it has also been used to model the recognition of other G-agents. DIMP appears to be of little value as a degradation simulant with only one publication relating to its use as a degradation simulant<sup>29</sup>; the lability of the P-O bonds make DIMP unsuitable for modelling the P-F bonds in the G-series.

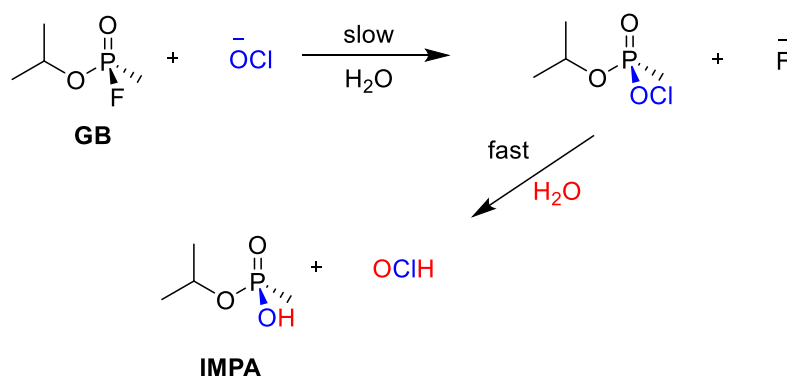
DIFP is a simulant for investigating both the capture<sup>30,31</sup> and degradation of the G-agents; the hydrolysis product of both DIFP and Sarin is HF. Unfortunately, the structural similarity between DIFP and the G-agents results in DIFP possessing a similar, yet relatively milder toxicity. DIFP also produces HF which presents a significant safety risk. This high toxicity makes DIFP a dangerous compound to work with yet it remains one of the most precise simulants for investigating CWA hydrolysis and sensing.

DMNP<sup>15,32,33</sup> is probably the most versatile degradation simulant. It has been used in a lot of studies mimicking the hydrolysis of the G and V-series. The hydrolysis of the P-O bond in DMNP to yield 4-nitrophenol emulates the hydrolysis of the P-F and P-S bonds in the G and V-series. In fact, direct kinetic comparisons exist in the literature between the degradation of OP CWAs and DMNP<sup>11,33</sup> in the presence of certain catalysts.

### 2.1.2 Oxidative Hydrolysis

Oxidative hydrolysis is one of the viable degradation pathways for degrading OP CWAs.

Stoichiometric oxidation procedures for the degradation of nerve agents consist of utilising aqueous solutions of sodium hypochlorite (bleach).<sup>34</sup> For VX, this occurs through the oxidative chlorination of the sulfur atom for which, in the presence of water, results in the hydrolytic cleavage of the P-S bond. A 20-fold stoichiometric excess of hydrogen peroxide at slightly alkaline pH is another previously reported procedure for the degradation of VX.<sup>35</sup> For the P-F bond containing G-series agents, the hypochlorite ion in bleach is able to directly displace the fluoride of the P-F bond, this is followed by the cleavage of the O-Cl bond in the presence of water to yield the corresponding phosphonate.<sup>36</sup> An example degradation scheme is shown for GB in Scheme 2.2.



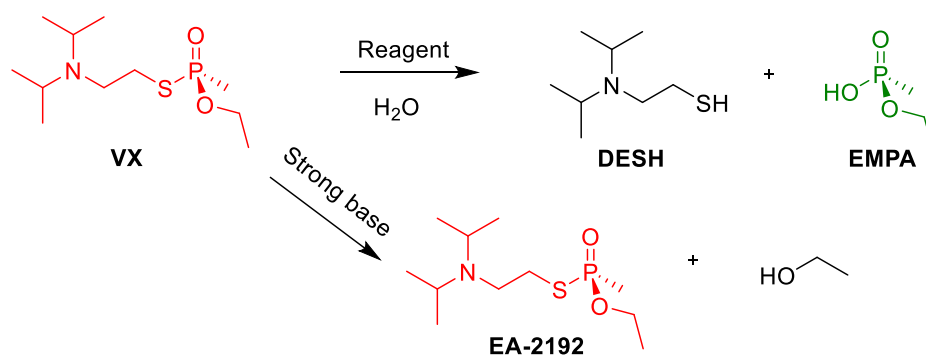
**Scheme 2.2:** A schematic outlining the degradation pathway for GB in the presence of a hypochlorite ion to form the non-toxic IMPA product.

Whilst these procedures may be effective at degrading the OP CWAs, the use of excessive reagent is undesirable for bulk decontamination. However, there were numerous reports of various metal oxide surface materials being utilised for the degradation of V and G series agents. Ceria ( $\text{CeO}_2$ ) nanoparticles were reported to fully degrade VX and GB in 10 minutes,<sup>37</sup> although, a large excess of the catalyst (50 weight equivalents) was used when performing this study. Nano-tubular titania ( $\text{TiO}_2$ ) is yet another metal oxide material which has been previously utilised for the degradation of VX and GD.<sup>38</sup> A half-life of 58 minutes was observed

for when the agents were subjected to a large excess of nano-tubular titania. All of the studies involving metal oxides involved a large excess of catalyst. It was therefore of great interest to see whether employing catalytic quantities of metal oxides would still result in efficient degradation. Upon initially surveying the literature, no nerve agent 'oxidation' simulants were identified. Triphenyl phosphine and diethyl phosphite, both phosphorus species in the +3 oxidation state, were chosen as potential oxidation simulants. It should be noted that the phosphorus atom in all OP CWAs is in the +5 oxidation state. As a starting point, commercial metal oxide nano-particles (MONPs) were chosen for initial screening as potential oxidative hydrolysis catalysts.  $\text{CeO}_2$ <sup>37</sup> and  $\text{TiO}_2$  MONPs<sup>38</sup> were chosen due to previous reports of their ability to degrade OP nerve agents.  $\text{CuO}$ <sup>39,40</sup> and  $\text{ZnO}$ <sup>41,42</sup> have been previously noted as oxidation catalysts in the literature, nanoparticles of these metal oxides were therefore also nominated for screening as OP degradation catalysts.

### 2.1.3 Hydrolysis

Hydrolysis is another attractive degradation pathway which is applicable to the neutralization of CWAs. Stoichiometric hydrolysis procedures for live CWAs involve the deployment of concentrated basic solutions such as conc. aqueous NaOH along with a surfactant to miscibilise and hydrolyse the CWA.<sup>35</sup> This procedure works to sever the P-F bond in Sarin and the P-S bond in VX, however, utilising a strong base can also hydrolyse the P-O bond which results in a degradation product (EA-2192) of similar toxicity (Scheme 2.3) as opposed to the non-toxic diisopropylaminoethanethiol (DESH) and ethyl methylphosphonic acid (EMPA) by-products.



**Scheme 2.3:** A schematic outlining the hydrolysis degradation pathways for VX.

The ideal catalyst would therefore be milder to avoid the formation of this by-product. The hydrolysis of DMNP requires the presence of a buffering agent to counteract the pH change caused by the accumulation of the p-nitrophenol by-product. Despite the necessity of using a buffer, direct comparisons have been drawn between the hydrolysis of V-series agents in aqueous medium and the hydrolysis of DMNP in buffer.<sup>11</sup> For this reason, a system was chosen where DMNP in N-ethyl morpholine (NEM) buffer is employed to screen for potential hydrolysis catalysts.

As discussed in Chapter 1, zirconium MOFs have shown a lot of promise as phosphoester hydrolysis catalysts.<sup>43-45</sup> The catalytic properties are derived from Lewis acidic Zr<sup>4+</sup> sites located in the Zr<sub>6</sub> cluster secondary building unit (SBU) of Zr MOFs.<sup>33</sup> Zirconium MOFs with missing linker defects or with a connectivity less than the maximum of 12, have been shown to possess enhanced catalytic properties due to the higher prevalence of uncoordinated Zr<sup>4+</sup> sites.<sup>43</sup> It was therefore decided that a number of previously reported Zr MOF hydrolysis catalysts would be synthesised, along with Zr MOFs which were believed to possess all the qualities of an effective catalyst.

## 2.2 Experimental

The following list is a compilation of all the reactants and starting materials utilised in this chapter. Biphenyl-4,4'-dicarboxylic acid 97% Sigma Aldrich, dimethyl biphenyl-4,4'-dicarboxylate 99% purity Sigma Aldrich, 5,5 dimethyl-,2,2' bipyridyl 98% Sigma Aldrich, 1, 2, 4, 5 tetramethylbenzene 98% Sigma Aldrich, 1.6M n-BuLi in hexane Sigma Aldrich, boron trifluoride diethyl etherate 48% BF3 Acros Organics, ZrCl<sub>4</sub> 99.5% Sigma Aldrich, Cu(II)Cl<sub>2</sub> 98% Riedel-de Haen, 2,6 naphthalenedicarboxylic acid 99% Fluorochem, 1,3,5 benzenetricarboxylic acid 95% Sigma Aldrich, methyl paraoxon pestanal grade Sigma Aldrich, diethyl phosphite 98% Acros Organics, triphenyl phosphine 98% Sigma Aldrich, diethyl chlorophosphate 95% Fisher, tetramethylethylenediamine 99% Sigma Aldrich, benzoic acid 99.5% Sigma Aldrich, Cu(II)O (>50 nm particle size) Sigma Aldrich, Ce(IV)O<sub>2</sub> (>25 nm particle size) Sigma Aldrich, Zn(II)O (>50 nm particle size) Sigma Aldrich and Ti(IV)O<sub>2</sub> (1:1 Anatase/Rutile mix <100 nm particle size) Sigma Aldrich.

### Instrumentation

<sup>1</sup>H, <sup>13</sup>C and <sup>31</sup>P NMR spectroscopy was conducted at 298 K using a JEOL 400 MHz spectrometer with an auto-sampler. PXRD patterns were collected on a silicon zero-background sample holder (a sample holder which presents no diffraction peaks) on a Rigaku Miniflex 600 desktop XRD using a Copper K- $\alpha$  (1.5406 Å) source. Measurements were taken in the 3 – 45 ° 2 $\theta$  range with a step size of 0.02 ° 2 $\theta$  and a scan speed of 1 ° 2 $\theta$  min<sup>-1</sup>.

### Synthesis of dimethyl-2-aminobiphenyl-4,4'-dicarboxylate (Amine Lig)

Dimethyl-2-nitrobiphenyl-4,4'-dicarboxylate was synthesised using a previously reported procedure.<sup>46</sup> Dimethyl biphenyl-4,4'-dicarboxylate (12 g, 44.4 mmol) was added to conc. H<sub>2</sub>SO<sub>4</sub>, the mixture was allowed to stir until all of the solid had dissolved, a thick yellow solution formed. The solution was then cooled to below 10 °C. HNO<sub>3</sub> 68 % (2.73 ml, 4.10 g, 44.4 mmol) was then mixed with H<sub>2</sub>SO<sub>4</sub>, this mixture was then added dropwise to the stirring solution which was continuously cooled to ensure that the temperature

remained below 10 °C. After all of the HNO<sub>3</sub>/H<sub>2</sub>SO<sub>4</sub> mixture was added, the solution was left stirring for one hour ensuring that the temperature did not rise above 20 °C. The reaction mixture was then poured onto crushed ice which caused a white solid to precipitate out, this white solid was filtered and washed with water and then recrystallized from hot IPA to yield off white crystals of 2-nitrobiphenyl-4,4'-dicarboxylate (9.10 g, 28.9 mmol). **Yield** 9.10 g (65 %) <sup>1</sup>H NMR (399.78 MHz, DMSO): δ 3.89 (s, 3H, CH<sub>3</sub>), δ 3.94 (s, 3H, CH<sub>3</sub>), δ 7.54 (d, 2H, ArH), δ 7.74 (d, 1H, ArH), δ 8.05 (d, 2H, ArH), δ 8.28 (d, 1H, ArH), δ 8.49 (d, 1H, ArH).

Dimethyl 2-aminobiphenyl-4,4'-dicarboxylate was synthesised using a previously reported procedure.<sup>47</sup> To a 1 litre round bottom flask was added dimethyl-2-nitrobiphenyl-4,4'-dicarboxylate (9.10 g, 28.9 mmol) which was dissolved in THF (400 ml), Pd/C 5% (3.03 g) was then added to the solution which was left stirring. The vessel was sealed, degassed and flushed with nitrogen several times. A 10-inch balloon was then filled with H<sub>2</sub> and then fed into the vessel and allowed to deflate. A total of 5 H<sub>2</sub> balloons were deflated into the reaction vessel over the course of 72 hours. The reaction mixture was then filtered through celite to remove Pd/C to give a pale yellow solution. The THF was then evaporated under reduced pressure to give a yellow solid which was recrystallized from hot ethanol to yield pale yellow crystals of dimethyl 2-aminobiphenyl-4,4'-dicarboxylate (6.64 g, 23.3 mmol).

**Yield** 6.64 g (80.6 %) <sup>1</sup>H NMR (399.78 MHz, DMSO): δ 3.83 (s, 3H, CH<sub>3</sub>), δ 3.88 (s, 3H, CH<sub>3</sub>), δ 5.25 (br s, 2H, NH<sub>2</sub>), 7.14 (d, 1H, ArH), δ 7.22 (d, 1H, ArH), δ 7.43 (s, 1H, ArH), δ 7.61 (d, 2H, ArH), δ 8.03 (d, 2H, ArH).

Dimethyl 2-aminobiphenyl-4,4'-dicarboxylate (1.00 g, 3.5 mmol) was dissolved in THF. KOH (0.59 g, 10.5 mmol) in H<sub>2</sub>O (5 ml) was then added to the solution. The solution was refluxed at 90 °C for 48 hours. After 24 hours, the THF was evaporated in vacuo. A solution of HCl (12 ml, 2 M) was then added to the resulting solid. The solid was then filtered, washed with water and

methanol and then vacuum dried to yield the product 2-aminobiphenyl-4,4'-dicarboxylate (0.79 g, 3.1mmol).

**Yield** 0.79 g (88.5 %)  $^1\text{H}$  NMR (399.78 MHz, DMSO):  $\delta$  5.23 (br s, 2H,  $\text{NH}_2$ ), 7.11 (d, 1H,  $\text{ArH}$ ),  $\delta$  7.21 (d, 1H,  $\text{ArH}$ ),  $\delta$  7.41 (s, 1H,  $\text{ArH}$ ),  $\delta$  7.58 (d, 2H,  $\text{ArH}$ ),  $\delta$  8.02 (d, 2H,  $\text{ArH}$ ).

$^{13}\text{C}$  NMR (100.53 MHz, DMSO):  $\delta$  116.4 (s, 1C),  $\delta$  117.5 (s, 1C),  $\delta$  128.5 (s, 1C),  $\delta$  128.8 (s, 2C),  $\delta$  129.5 (s, 1C),  $\delta$  129.9 (s, 2C),  $\delta$  130.3 (s, 1C),  $\delta$  131.0 (s, 1C),  $\delta$  143.4 (s, 1C),  $\delta$  145.4 (s, 1C),  $\delta$  167.2 (s, 1C),  $\delta$  167.6 (s, 1C).

### **Synthesis of 2,2'-Bipyridine-5,5'-dicarboxylic acid (BiPy Lig)**

5,5 dimethyl-,2,2' bipyridyl (0.5 g, 2.7 mmol) was dissolved in conc.  $\text{H}_2\text{SO}_4$  (12.5 ml, 18 M).

Potassium dichromate (2.4 g, 8.2 mmol) was then added slowly to the stirring solution over the course of 30 minutes. The temperature rose to 60 °C and was monitored to ensure that it did not rise above 80 °C. The reaction was then allowed to ambiently cool to 30 °C. The reaction mixture was poured over 100 ml of ice at which point a green precipitate was observed. The mixture was filtered, washed with water and acetone and then vacuum dried to yield the product 2,2'-Bipyridine-5,5'-dicarboxylic acid (0.602 g, 2.46 mmol).

**Yield** 0.602 g (91.0 % yield)  $^1\text{H}$  NMR (399.78 MHz, DMSO +  $\text{D}_2\text{SO}_4$ ):  $\delta$  8.59 (d, 2H,  $\text{ArH}$ ), 8.63 (d, 2H,  $\text{ArH}$ ), 9.14 (s, 2H,  $\text{ArH}$ ).

$^{13}\text{C}$  NMR (100.53 MHz, DMSO +  $\text{D}_2\text{SO}_4$ ):  $\delta$  123.8 (s, 2C),  $\delta$  129.3 (s, 2C),  $\delta$  141.7 (s, 2C),  $\delta$  149.6 (s, 2C),  $\delta$  154.2 (s, 2C),  $\delta$  166.0 (s, 2C),

### **Multi-step synthesis of tris(2',3',5',6'-tetramethylbiphenyl-4-carboxylic acid) (Boron Lig)**

#### *Synthesis of 1,4-Dibromodurene*

1,4-Dibromodurene was synthesised using a previously reported method.<sup>48</sup> 1,2,4,5-

Tetramethylbenzene (10 g, 74.6 mmol) was dissolved in DCM (400 ml), iodine (0.394 g, 1.56 mmol) was then added to the solution. The solution was degassed. A degassed solution of bromine (9 ml, 175.6 mmol) in DCM (20 ml) was then added dropwise whilst keeping the

reaction in the dark and under an atmosphere of  $N_2$ . The reaction was left stirring overnight and then quenched with 5 M NaOH (20 ml). The organic phase was extracted with DCM and washed with water followed by drying over anhydrous  $MgSO_4$ . The solution was concentrated under reduced pressure and recrystallized from DCM to obtain the product 1,4-dibromodurene (9.8 g, 33.5 mmol)

**Yield** 9.80 g (44.9 %)  $^1H$  NMR (399.78 MHz, DMSO):  $\delta$  2.49 (s, 12H,  $CH_3$ ).

#### *Synthesis of tris-(4-bromoduryl)borane*

Tris-(4-bromoduryl)borane was synthesised following a published procedure.<sup>49</sup> 1,4-Dibromodurene (5 g, 17.15 mmol) was dissolved in dry diethyl ether (150 ml). The solution was cooled to  $-78$  °C and a solution of 1.6 M n-BuLi in hexane (10.63 ml, 17 mmol) was then added dropwise to the reaction. After full addition, the solution was allowed to slowly warm to room temperature at which point it was left stirring for 30 minutes. The mixture was then again cooled to  $-78$  °C and a solution of Boron trifluoride diethyl etherate (0.7 ml, 5.6 mmol) was then added dropwise. After full addition, the solution was allowed to slowly warm to room temperature and then left stirring for 24 hours. Water was then added to the reaction and the resulting mixture was extracted with  $Et_2O$ . The organic extract was then washed with brine followed by drying over anhydrous  $MgSO_4$ . The solution was concentrated under reduced pressure and the resulting off white solid was partitioned in a 50:50  $Et_2O$ /MeOH solution. The resulting mixture was shaken vigorously, the insoluble solid was then filtered and washed with MeOH followed by vacuum drying to yield the white powder of tris-(4-bromoduryl)borane (2.84 g, 4.38 mmol)

**Yield** 2.84 g (78.2 % yield)  $^1H$  NMR (399.78 MHz, DMSO):  $\delta$  2.00 (s, 18H,  $CH_3$ ),  $\delta$  2.34 (s, 18H,  $CH_3$ ).

#### *Synthesis of tris(2',3',5',6'-tetramethylbiphenyl-4-methoxycarbonyl)borane.*

Tris(2',3',5',6'-tetramethylbiphenyl-4-methoxycarbonyl)borane was synthesised following a published procedure.<sup>50</sup> Tris-(4-bromoduryl)borane (200 mg, 0.3 mmol), 4-

methoxycarbonylphenylboronic acid (278 mg, 1.54 mmol) and Pd(PPh<sub>3</sub>)<sub>4</sub> (18 mg, 0.015 mmol) were dissolved in 5 ml THF and sealed in a 35 ml microwave reaction vessel. This was followed by the addition of a 1 M solution of NaCO<sub>3</sub> (2 ml) to the solution, the contents of the microwave vessel were then degassed. Vessel was placed in a microwave reactor and heated at 150 °C using dynamic power cycling for 30 minutes. The resulting solution was cooled to room temperature and 15 ml ethyl acetate was added. The reaction mixture was washed with H<sub>2</sub>O, the organic layer was dried with MgSO<sub>4</sub> and concentrated under reduced pressure. The concentrate was then purified using a silica column and DCM as the eluent to yield tris(2',3',5',6'-tetramethylbiphenyl-4-methoxycarbonyl)borane (0.172 g, 0.2 mmol).

**Yield** 0.172 g (67.2 % yield) <sup>1</sup>H NMR (399.78 MHz, DMSO): δ 1.84 (s, 18H, CH<sub>3</sub>), δ 2.07 (s, 18H, CH<sub>3</sub>), δ 3.96 (s, 9H, CH<sub>3</sub>), δ 7.24 (d, 6H, ArH), δ 8.11 (d, 6H, ArH).

*Synthesis of tris(2',3',5',6'-tetramethylbiphenyl-4-carboxylic acid) borane.*

Tris(2',3',5',6'-tetramethylbiphenyl-4-methoxycarbonyl)borane (150 mg, 0.17 mmol), LiOH (15 mg, 6 mmol) dissolved in a 10 ml 50:50 mixture of THF and Water. The solution was left stirring at room temperature for 48 hours. The solution was reduced under reduced pressure to remove THF and acidified with 2 M HCl resulting in a white precipitate, the white precipitate was then filtered and washed with water to yield tris(2',3',5',6'-tetramethylbiphenyl-4-carboxylic acid) borane (112 mg, 0.145 mmol).

**Yield** 0.112 g (85.3 % yield) <sup>1</sup>H NMR (399.78 MHz, DMSO): δ 1.72 (s, 18H, CH<sub>3</sub>), δ 1.98 (s, 18H, CH<sub>3</sub>), δ 7.16 (d, 6H, ArH), 7.97 (d, 6H, ArH).

<sup>13</sup>C NMR (100.53 MHz, DMSO): δ 18.2 (s, 6C), δ 20.4 (s, 6C), δ 129.4 (s, 3C), δ 129.9 (s, 3C), δ 130.1 (s, 3C), δ 131.1 (s, 6C), δ 135.8 (s, 6C), δ 142.6 (s, 3C), δ 147.7 (s, 3C), δ 149.1 (s, 3C), δ 167.7 (s, 3C).

### Synthesis of Cu(TMEDA)Cl<sub>2</sub>

Cu(TMEDA)Cl<sub>2</sub> was synthesised using a previously reported procedure.<sup>51</sup> Cu(II)Cl<sub>2</sub> (2.00g, 14.8 mmol) was added to a stirring solution of acetonitrile (60 ml): tetramethylethylenediamine (1.72 g, 2.2 ml, 14.8 mmol) was then added to the solution which was left stirring at room temperature for 20 hours. The resulting turquoise solid was filtered, washed with cold acetonitrile and vacuum dried to yield the product, Cu(TMEDA)Cl<sub>2</sub> (2.36 g, 5.08 mmol). The PXRD of the bulk product was then compared to the simulated pattern for Cu(TMEDA)Cl<sub>2</sub> (Figure 2.1).

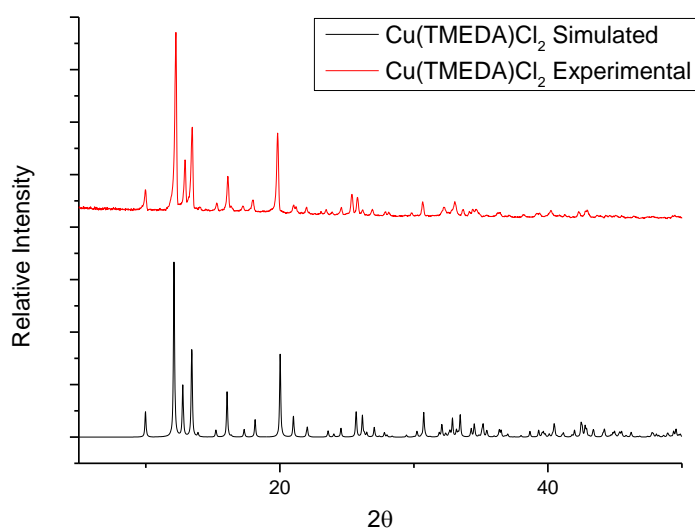


**Figure 2.1:** A PXRD overlay showing a simulated pattern for Cu(TMEDA)Cl<sub>2</sub> obtained from reference 51 and a PXRD of the as-synthesised material.

### Synthesis of DUT-52

DUT-52 was synthesised using a previously reported procedure.<sup>52</sup> 2,6 naphthalenedicarboxylic acid (216 mg, 1 mmol) and ZrCl<sub>4</sub> (230 mg, 1.03 mmol) were added to DMF (20 ml) and the mixture was sonicated for 5 minutes. Acetic acid (3ml, 47 mmol) was then added as a modulator. The solution was sonicated for a further 10 minutes. The reaction mixture was sealed in a 100 ml screw cap vial and heated in an oven at 120 °C for 24 hours. After 24 hours, a white precipitate was visible at the bottom of the vial. The vial was allowed to cool to room

temperature over a period of 1 hour and the white solid was washed with DMF 3 times. The DMF was then decanted and the solid was washed 3 times with ethanol, the solid was then filtered and vacuum dried to yield a fine white crystalline powder. The bulk phase of the as-synthesised DUT-52 was confirmed by PXRD by comparing against a simulated pattern. (Figure 2.2).

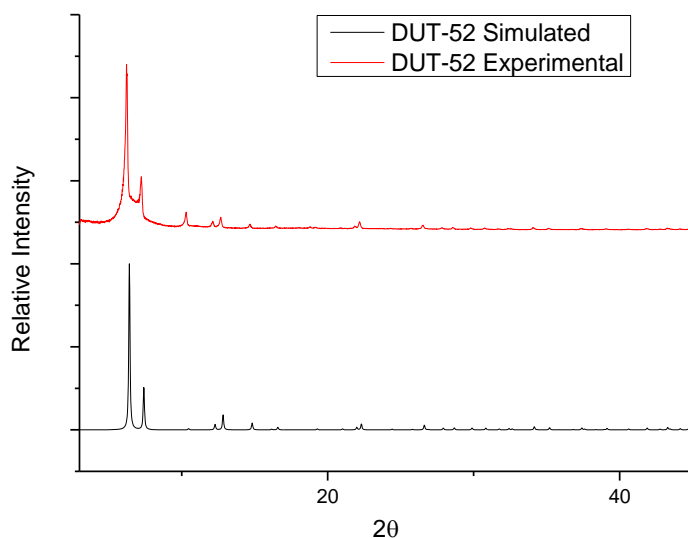


**Figure 2.2:** A PXRD overlay showing a simulated pattern for DUT-52 obtained from reference 52 and a PXRD of the as-synthesised material.

### Synthesis of DUT-84

DUT-84 was synthesised using a previously reported procedure.<sup>52</sup> 2,6-naphthalenedicarboxylic acid (500 mg, 2.78 mmol) and  $ZrCl_4$  (570 mg, 3.05 mmol) were added to DMF (120 ml). The mixture was sonicated for 10 minutes. Acetic acid (50 ml, 794 mmol) was then added to the solution which was sonicated for a further 10 minutes. The solution was sealed in a 250 ml screw top vial and heated in an oven at 120 °C for 24 hours. After 24 hours, a white precipitate was visible at the bottom of the vial. The vial was allowed to cool to room temperature over the course of an hour and the white solid was washed with DMF 3 times. The DMF was then decanted and the solid was washed 3 times with ethanol, the solid was then filtered and vacuum dried to yield a fine white crystalline powder. The bulk phase of the as-synthesised

DUT-84 was confirmed by PXRD by comparing against a simulated pattern of DUT-84 (Figure 2.3).

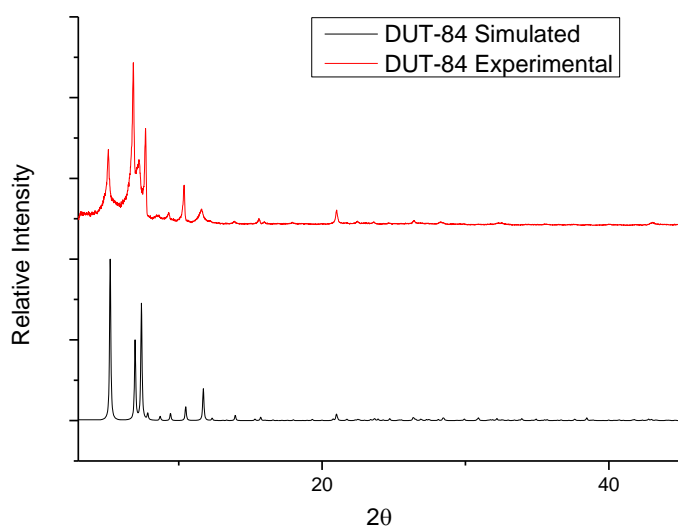


**Figure 2.3:** A PXRD overlay showing a simulated pattern for DUT-84 obtained from reference 52 and a PXRD of the as-synthesised material.

#### **Synthesis of UiO-67-BiPy-ML (Approximate Formula $ZrO_4(OH)_4(BiPy\ Lig)_4.5(BPDC)_{1.5}$ )**

UiO-67-BiPy-ML was synthesised using a previously reported procedure.<sup>53</sup>  $ZrCl_4$  (329 mg, 1.41 mmol) was dissolved in 50 ml DMF and sonicated for 10 minutes. 2,2'-Bipyridine-4,4'-dicarboxylic acid (256 mg, 1.05 mmol), Biphenyl-4,4'-dicarboxylic acid (85 mg, 0.35 mmol) and glacial acetic acid (2.7 ml, 42.5 mmol) were then added to the solution which was sonicated for a further 10 minutes. The suspension was then sealed in a 100 ml screw top vial and heated at 120 °C for 24 hours. The vessel was then allowed to ambiently cool to room temperature over the course of 1 hour. The resulting white solid was filtered from the supernatant, washed with DMF and acetone and then vacuum dried to yield a solid white powder. The bulk phase of the as-synthesised UiO-67-BiPy-ML was confirmed by PXRD by comparing against a simulated pattern of iso-structural UiO-67 (Figure 2.4).

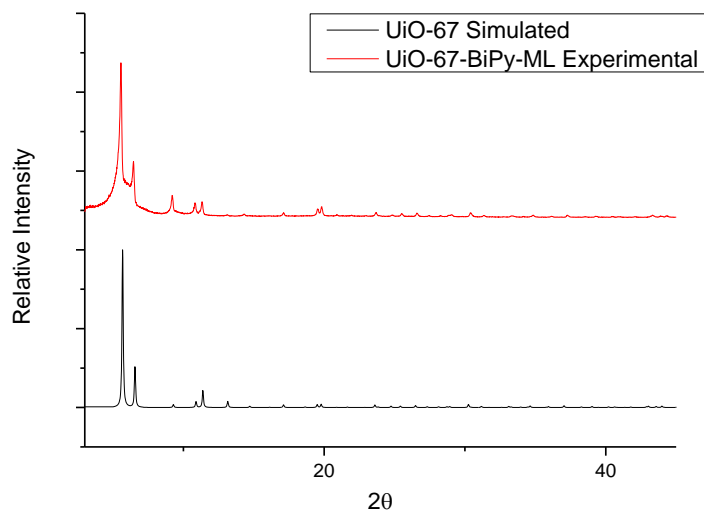


**Figure 2.4:** A PXRD overlay showing a simulated pattern for UiO-67 (iso-structural to UiO-67-BiPy-ML) obtained from reference 54 and a PXRD of the as-synthesised UiO-67-BiPy-ML.

#### **Synthesis of UiO-67-NH<sub>2</sub>-ML (Approximate Formula ZrO<sub>4</sub>(OH)<sub>4</sub>(Amine Lig)<sub>3</sub>(BPDC)<sub>3</sub>)**

UiO-67-NH<sub>2</sub>-ML was synthesised using a modified procedure to the one outlined by S. M Chavan et al.<sup>55</sup> ZrCl<sub>4</sub> (250 mg, 1.07 mmol) was dissolved in 50 ml DMF and sonicated for 10 minutes. Biphenyl-4,4'-dicarboxylic acid (129 mg, 0.53 mmol), dimethyl-2-aminobiphenyl-4,4'-dicarboxylate (137 mg, 0.53 mmol), conc. HCl (0.1 ml) and Benzoic acid (1.3 g, 10.7 mmol) were all added to the resulting solution and sonicated for a further 10 minutes. The suspension was sealed in a 250 ml screw top vial and heated at 100 °C for 48 hours. The vessel was then allowed to ambiently cool to room temperature over the course of 1 hour. The resulting white solid was filtered from the supernatant, washed with DMF and acetone and then vacuum dried to yield a solid white powder. The bulk phase of the as-synthesised UiO-67-NH<sub>2</sub>-ML was confirmed by PXRD by comparing against a simulated pattern of iso-structural UiO-67 (Figure 2.5).

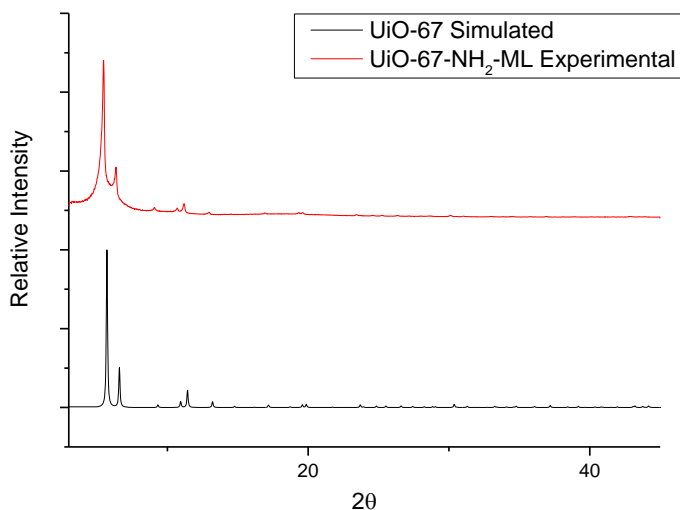


**Figure 2.5:** A PXRD overlay showing a simulated pattern for UiO-67 (iso-structural to UiO-67-NH<sub>2</sub>-ML) obtained from reference 54 and a PXRD of the as-synthesised UiO-67-NH<sub>2</sub>-ML.

### Synthesis of MOF-808

MOF-808 was synthesised using a previously reported procedure.<sup>14</sup> ZrCl<sub>4</sub>, (1281 mg, 5.5 mmol) was dissolved in DMF (60 ml) and sonicated for 10 minutes. 1,3,5 benzenetricarboxylic acid (1115 mg 5.5 mol) was then added and the solution was sonicated for a further 10 minutes. Finally, acetic acid (31 ml, 54 mmol) was added to the solution which was sonicated for another 10 minutes. The solution was sealed in a 250 ml screw top vessel and placed in a preheated oven where it was heated at 130 °C for 24 hours. The vial was removed from the oven and allowed to ambiently cool to room temperature over the course of an hour. A white solid was observed. The resulting white solid was filtered from the supernatant, washed with DMF and acetone and then vacuum dried to yield a solid white powder. The bulk phase of the as-synthesised MOF-808 was confirmed by PXRD by comparing against a simulated pattern of MOF-808 (Figure 2.6).

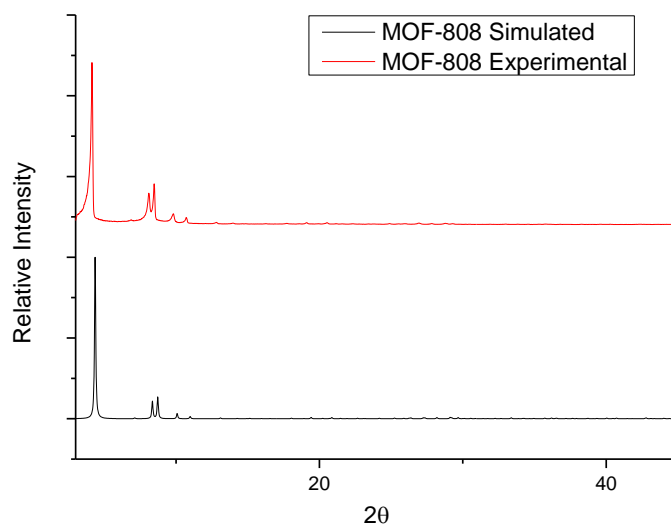


**Figure 2.6:** A PXRD overlay showing a simulated pattern for MOF-808 obtained from reference 14 and a PXRD of the as-synthesised material.

### Synthesis and Characterization of Zr-Boron MOF

Tris(2',3',5',6'-tetramethylbiphenyl-4-methoxycarbonyl)borane (137 mg, 0.155 mmol) and  $ZrCl_4$  (116 mg, 1 mmol) were added to acetic acid (2.8 ml, 49 mmol) and dissolved in 5ml DMF. The solution was sonicated for 10 minutes and then sealed in a 50 ml hydrothermal reaction vessel and heated at 135 °C for 24 hours. The vessel was then allowed to ambiently cool to room temperature over the course of an hour. The resulting white solid was filtered from the supernatant, washed with DMF and acetone and then vacuum dried to yield the bulk material as a solid white powder. The bulk crystalline phase of the material was analysed using PXRD (Figure 2.7).

Single crystals were obtained by using an incubation time of 24 hours at 135 °C, this was followed by cooling to 80 °C at a rate of 0.5 °C per hour, after 80 °C a cooling sequence of 1.0 °C per hour was used until 25 °C was reached. The solvothermal reaction vessel was also treated with a hydrophobic siliconizing reagent (Sigmacote®) before commencing the reaction. Single-crystal analysis was then performed by Dr. Helena Shepherd. A suitable crystal of Zr-Boron MOF was selected and mounted on a glass fiber with inert oil on a 'Bruker APEX-II CCD'

diffractometer at the ALS station 11.3.1. The crystal was kept at 100 K during data collection. Using Olex2, the structure was solved with the XS structure solution program using Direct Methods (Appendix Section 7.1).

The bulk phase of Zr-Boron MOF was then confirmed using PXRD by comparing against simulated data obtained from single-crystal X-ray analysis (Figure 2.7).

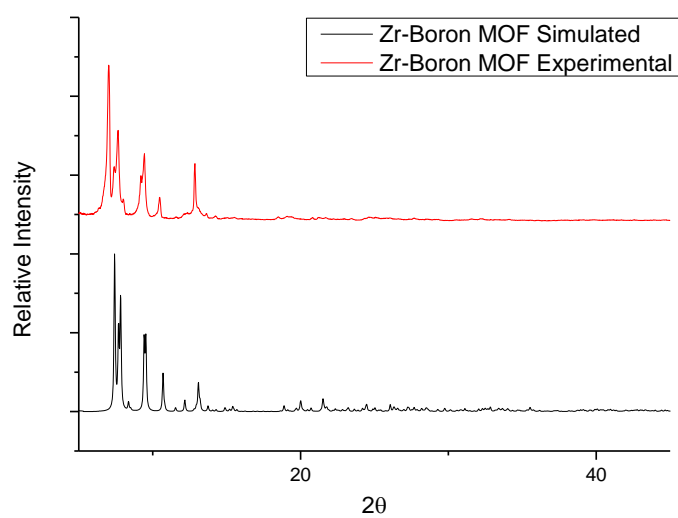


**Figure 2.7:** A PXRD overlay showing a simulated pattern for Zr-Boron MOF and a PXRD of the as-synthesised material.

#### **Procedure for the Oxidation of triphenyl phosphine with MONPs**

TPP (0.4 g, 1.59 mmol) was dissolved in MeOH (15 ml), MONPs (0.159 mmol) were then added to the solution. The reaction was left to stir for 48 hours at room temperature and atmospheric pressure. The reaction mixture was then analysed using proton coupled  $^{31}\text{P}$  NMR (161.83 MHz) in  $\text{CDCl}_3$ .

#### **Procedure for the Oxidation of Diethyl phosphite with MONPs**

DEP (0.5 ml, 3.9 mmol) was added to THF (0.32 ml, 3.9 mmol). MONPs (0.39 mmol) were then added to the solution. The reaction mixture was left stirring for 48 hours at room temperature

under atmospheric pressure. The reaction mixture was then analysed using proton coupled  $^{31}\text{P}$  NMR (161.83 MHz) in  $\text{CDCl}_3$ .

#### **Procedure for the Degradation of Diethyl chlorophosphate with MONPs**

MONPs (0.35 mmol) were added to DCP (0.5 ml, 3.5 mmol). The reaction mixture was left stirring for 24 hours at room temperature under atmospheric pressure. The reaction mixture was then analysed using proton coupled  $^{31}\text{P}$  NMR (161.83 MHz) in  $\text{CDCl}_3$ .

#### **Procedure for the Oxidation of Diethyl phosphite with $\text{Cu}^{2+}$**

$\text{Cu(II)Cl}_2$  or  $\text{Cu(TMEDA)Cl}_2$  (0.39 mmol) was added to DEP (0.5 ml, 3.9 mmol) The reaction mixture was left stirring for 24 hours at room temperature under atmospheric pressure. The reaction mixture was then analysed using proton coupled  $^{31}\text{P}$  NMR (161.83 MHz) in  $\text{CDCl}_3$ .

#### **Procedure for the Reaction condition assessment of Diethyl phosphite with $\text{Cu}^{2+}$**

Several conditions were altered for the condition assessment with  $\text{Cu(II)Cl}_2$ . For the air and moisture free measurements, glassware was oven dried and degassed and the reaction was carried out under a  $\text{N}_2$  atmosphere.

For the air-free measurements, the reaction was degassed and carried out under a  $\text{N}_2$  atmosphere, a stoichiometric quantity of water was also added to the reaction mixture.

For the  $\text{O}_2$  measurements, the glassware was oven dried and degassed and the reaction was carried out under an  $\text{O}_2$  atmosphere with the help of a balloon.

All condition assessment reactions were carried out for 24 hours. For the kinetic measurements, aliquots were collected as the reaction progressed, the aliquots were then analysed using proton coupled  $^{31}\text{P}$  NMR (161.83 MHz) in  $\text{CDCl}_3$ .

#### **Procedure for the Non-buffered hydrolysis of DMNP**

DMNP (13  $\mu$ L, 0.06 mmol) and Zr-MOF Catalyst (1mg) were added to an NMR tube, along with 0.6 ml of 50:50 D<sub>2</sub>O/H<sub>2</sub>O. The tubes were then analysed using <sup>31</sup>P NMR (161.83 MHz) after 2 days and 7 days.

#### **Procedure for the Buffered hydrolysis of DMNP**

An NMR tube was charged with DMNP, 20  $\mu$ L (0.09 mmol). The MOF catalyst (0.11  $\mu$ mol, 1.25 mol %) was then added to the tube. 0.1 ml of D<sub>2</sub>O along with 0.5 ml of 0.15 M *N*-ethyl morpholine aqueous buffer was then added to the tube. The contents of the tube were then analysed using <sup>31</sup>P NMR (161.83 MHz) after 3 hours.

#### **Procedure for the Humidity Water Absorption assessment of MOF-808**

Samples of MOF-808 were vacuum dried at 70 °C for 72 hours and their weight was then recorded. The samples were then immediately exposed to two different environments, one with a relative humidity (RH) of 30 % and another of 65 %. The weight change of each sample was then closely monitored using a 4 d.p scale with the help of a time lapse camera.

#### **Procedure for the Neat Hydrolysis of GB (performed by DSTL)**

A vial was charged with with GB (0.5 ml, 3.6 mmol) and either TiO<sub>2</sub> or Cu(TMEDA)Cl<sub>2</sub> (0.36 mmol, 10 mol%). The reaction was then left for 24 hours at room temperature under atmospheric pressure. After 24 hours, an aliquot was taken from each reaction mixture and analysed using <sup>31</sup>P NMR (161.83 MHz).

#### **Procedure for the Aqueous Hydrolysis of VX (performed by DSTL)**

An NMR tube was charged with VX (40 mg, 0.15 mmol), MOF-808 (0.18  $\mu$ mol, 1.25 mol %) was then added along with 0.7 ml D<sub>2</sub>O. The NMR tube was then cycled in an autosampler and analysed using <sup>31</sup>P NMR (161.83 MHz), the first data point was obtained within 10 minutes. For the blank, a similar tube was prepared but no MOF-808 was used.

**Procedure for the Hydrolysis of VX with stoichiometric H<sub>2</sub>O (performed by DSTL)**

A vial was charged with VX (110 mg, 0.41 mmol), MOF-808 (0.49 μmol, 1.25 mol %) was then added along with H<sub>2</sub>O (8 μL, 0.41 mmol). The reaction was then left to react at room temperature and ambient humidity. Aliquots were taken after 5 minutes, 30 minutes, 2.5 hours, 24 hours and 7 days. The aliquots were analysed using LC-MS.

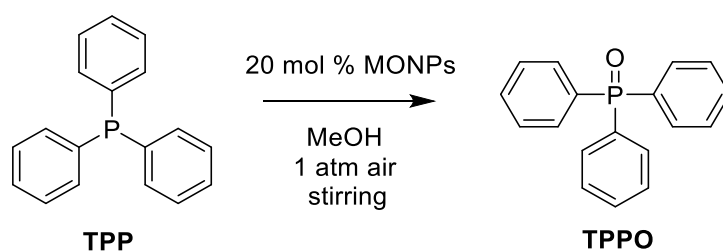
**Procedure for the Neat Hydrolysis of VX (Performed by DSTL)**

A vial was charged with VX (110 mg, 0.41 mmol), MOF-808 (0.49 μmol, 1.25 mol %) was then added. The reaction was then left to react at room temperature and ambient humidity. Aliquots were taken after 24 hours, 48 hours and 7 days. The aliquots were analysed using LC-MS.

## 2.3 Oxidative Hydrolysis

### 2.3.1 Phosphine Oxidation

This next section will look at initial attempts to identify a suitable oxidation catalyst for the oxidation of phosphines and phosphites. Oxidation was chosen as the most ideal reaction pathway to degrade the simulants. Specifically, the ideal catalyst would function as an aerobic oxidation catalyst, able to rely solely on atmospheric O<sub>2</sub> to fuel the oxidation. No suitable oxidation simulants were found in the literature. Simple phosphines and phosphites were therefore selected and an attempt was made to oxidise them using some high surface metal-oxide nano particles (MONPs). The first phosphorus species to be tested was triphenyl phosphine (TPP). TPP is a relatively stable compound with the phosphorus in the +3 oxidation state and a lone pair of electrons on the phosphorus. The initial aim was to convert TPP into triphenyl phosphine oxide (TPPO) using a range of commercial MONPs. These MONPs were chosen based on previous reports of metal-oxide facilitated oxidation catalysis.<sup>39,42,56,57</sup> The MONPs were used as purchased. TPP was dissolved in MeOH and MONPs were added to the reaction mixture, the reaction was left stirring at room temperature and open to air, an aliquot was taken after 24 hours from the reaction mixture and analysed using <sup>31</sup>P [H] NMR. Scheme 2.4 illustrates the conditions employed for the oxidation.



**Scheme 2.4:** A reaction scheme outlining the conditions employed for the aerobic oxidation of TPP to TPPO in the presence of various MONPs catalysts.

TiO<sub>2</sub> MONPs proved to be most effective with around 55 % oxidation occurring over 24 hours (Figure 2.8). This study was repeated in the absence of light and no oxidation was observed thus suggesting photo-activated oxidation in the presence of the anatase and rutile phases

which exist in the TiO<sub>2</sub> MONPs. CuO MONPs resulted in 20 % oxidation after 24 hours. CeO<sub>2</sub> and ZnO showed very little activity (Table 2.1). Both the CuO and TiO<sub>2</sub> MONP facilitated oxidation of TPP to TPPO likely occurs through an intramolecular singlet oxygen oxidation mechanism which was previously reported for TPP.<sup>58</sup> TiO<sub>2</sub><sup>59</sup> and CuO<sup>60</sup> MONPs have also been previously noted for their ability to generate singlet oxygen from molecular O<sub>2</sub>, the suggested reactive oxygen species in this reaction. Employing TiO<sub>2</sub> as a catalyst to fulfil the ultimate aim of this project would likely not be feasible. This is because TiO<sub>2</sub> is a photo-oxidation catalyst which requires UV light near 387 nm.<sup>61</sup> Whilst this range may lie in the visible light spectrum, embedding a photocatalyst in a polymer composite would possibly restrict the photo-oxidation to just the catalysts embedded on the polymer surface.

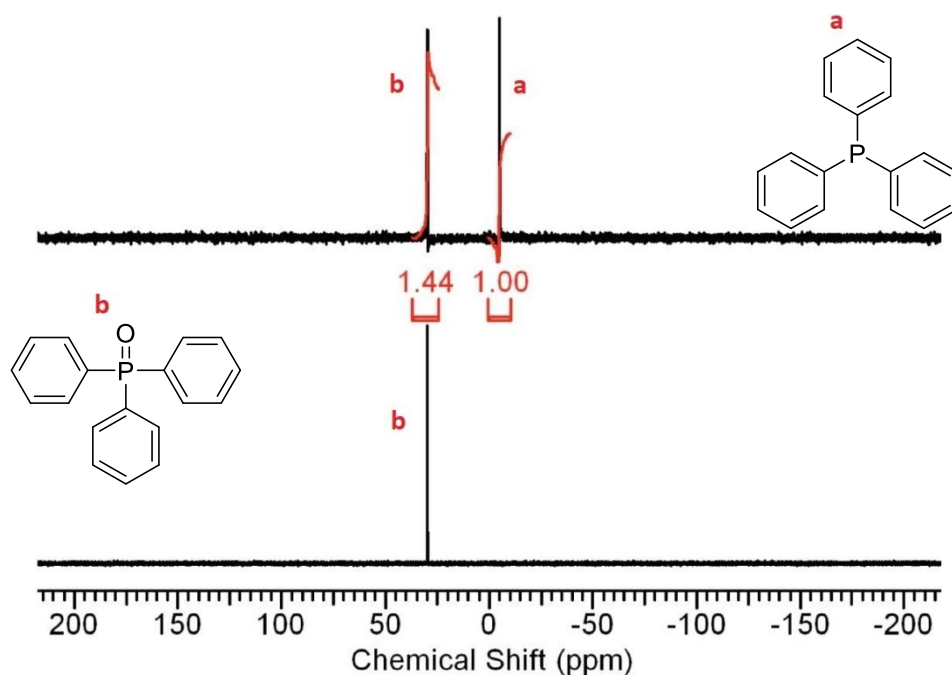


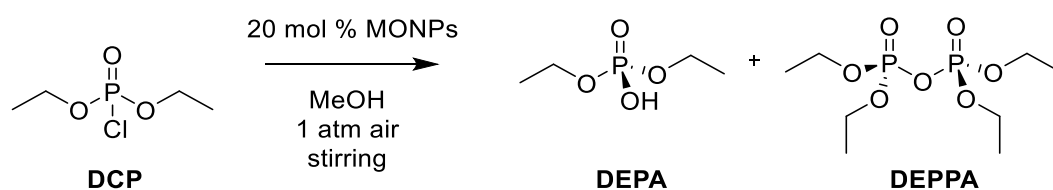
**Figure 2.8:** A <sup>31</sup>P [H] NMR overlay in CDCl<sub>3</sub>. Top spectrum shows TPP after 24 hours in the presence of TiO<sub>2</sub>. Bottom spectrum is pure TPPO.

Catalyst	Time	% TPP oxidized to TPPO
Blank	24 hrs	0 %
Ti(IV)O <sub>2</sub>	24 hrs	55 %
Ce(IV)O <sub>2</sub>	24 hrs	0 %
Cu(II)O	24 hrs	20 %
Zn(II)O	24 hrs	0 %
Ti(IV)O <sub>2</sub> (no light)	24 hrs	0 %

**Table 2.1:** A table showing the various MONPs catalysts which were screened as oxidation catalysts for the degradation of TPP to TPPO. The % of TPP which was oxidised to TPPO is shown alongside each catalyst.

### 2.3.2 Autodegradation of Diethyl Chlorophosphate

Due to numerous reports in the literature of DCP being employed as an OP CWA simulant,<sup>22,23</sup> it was the next simulant to feature in this study. The hydrolysis of the P-Cl bond functions to mimic the hydrolysis of the P-F bond in the nerve agent Sarin. DCP readily decomposes to diethyl phosphoric acid (DEPA) and diethyl pyrophosphoric acid (DEPPA) under atmospheric pressure and temperature. Zn(II)O, Ce(IV)O<sub>2</sub>, Cu(II)O and Ti(IV)O<sub>2</sub> were all screened as potential oxidative hydrolysis catalysts for the degradation of DCP. The MONPs were suspended in mixture of DCP and MeOH and left stirring at room temperature and open to air, an aliquot was taken after 24 hours from the reaction mixture and analysed using <sup>31</sup>P [H] NMR. Scheme 2.5 illustrates the reaction conditions employed for the oxidative hydrolysis.



**Scheme 2.5:** A reaction scheme outlining the conditions employed for the degradation of DCP to DEPA and DEPPA in the presence of various MONPs catalysts.

Zn(II)O, Ce(IV)O<sub>2</sub>, Cu(II)O and Ti(IV)O<sub>2</sub> all proved ineffective at accelerating the degradation. After 24 hours, no net increase in degradation was observed in the presence of the MONPs when compared to the background hydrolysis. The kinetic plot below (Figure 2.9) shows the zeroth order decomposition of DCP in the presence of ambient humidity and pressure. 70% Hydrolysis is achieved after 24 hours in the absence of any catalyst, this is in contrast to G and V-series agents which remain prevalent in the environment. The difference in ambient degradation between DCP and OP CWAs makes it a poor choice of degradation simulant. It was decided that a simulant which possessed a higher ambient stability would be required.

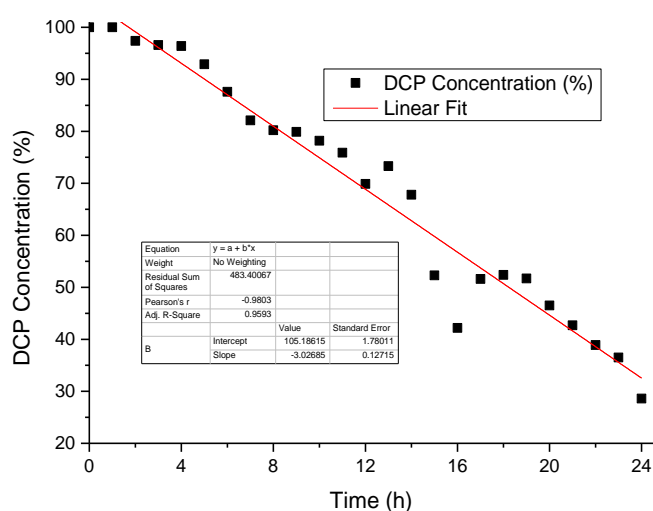
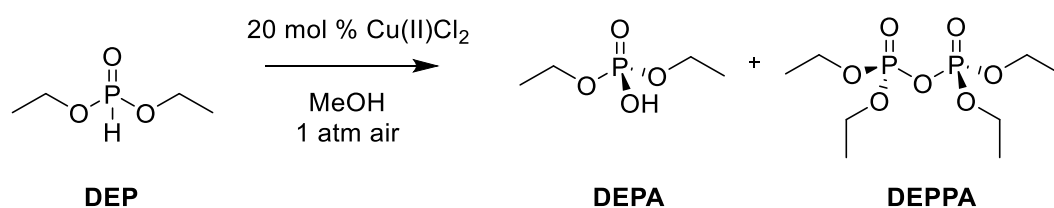


**Figure 2.9:** A degradation plot showing the ambient hydrolysis of DCP over time at room temperature and ambient humidity.

### 2.3.3 Oxidative Hydrolysis of Diethyl phosphite

Diethyl phosphite (DEP) is a P(III) phosphorus species containing a labile P-H bond, it is however still stable under prolonged exposure to air and ambient humidity and thus an improvement over DCP. The previous selection of 4 commercial MONPs; Zn(II)O, Ce(IV)O<sub>2</sub>, Cu(II)O and Ti(IV)O<sub>2</sub>, were all screened for the degradation of DEP. The MONPs were suspended in mixture of DEP and MeOH and left stirring at room temperature and open to air, an aliquot was taken after 24 hours from the reaction mixture and analysed using <sup>31</sup>P [H] NMR.

No degradation was observed over the course of 24 hours in the presence of any of the MONPs. A shift was made from MONPs to look at some simple homogeneous oxidation catalysts. A previously reported study utilised a variety of Cu(II) chelate complexes for the oxidative hydrolysis of G-series agents.<sup>9</sup> Cu(TMEDA)Cl<sub>2</sub> proved to be the most effective material at hydrolysing Sarin in buffered aqueous media with a  $t_{1/2}$  of 0.5 mins. Inspired by these results, Cu(TMEDA)Cl<sub>2</sub> was synthesised. A number of degradation tests were conducted using Cu(II)Cl<sub>2</sub> and Cu(TMEDA)Cl<sub>2</sub> as potential homogeneous catalysts for the oxidation of DEP. The Cu(II) catalyst was dissolved in mixture of DEP and MeOH and left stirring at room temperature and open to air, an aliquot was taken after 24 hours from the reaction mixture and analysed using <sup>31</sup>P [H] NMR. The conditions employed for this screening are outlined in Scheme 2.6.



**Scheme 2.6:** A reaction scheme outlining the conditions employed for the oxidative hydrolysis of DEP to DEPA and DEPPA in the presence of various Cu<sup>2+</sup> catalysts.

Remarkably, near full degradation was observed over the course of 24 hours in the presence of Cu(II)Cl<sub>2</sub> (Figure 2.10). Diethyl phosphoric acid (DEPA) ( $\delta$  0.82<sup>62</sup>) was formed as a degradation product along with a small quantity of diethyl pyrophosphoric acid (DEPPA) ( $\delta$  - 13.12<sup>8</sup>). Full degradation was also achieved in the presence of Cu(TMEDA)Cl<sub>2</sub>. Interestingly, only the DEPPA product was observed at the end of the reaction period. This observation is in keeping with a previously reported study<sup>8</sup> where the use of a Cu(II) catalyst with a bulky amine resulted in the oxidation of phosphites to their pyrophosphate counterpart. A kinetic analysis of DEP degradation was performed in the presence of Cu(II)Cl<sub>2</sub> using the same conditions. Figure 2.11 shows the zeroth order decomposition of DEP with a  $t_{1/2}$  of 8 hours and with almost 90 % hydrolysis occurring after 20 hours. Due to the zeroth order nature of the oxidation, it is

likely that the rate limiting step of the reaction is the saturation of the Cu(II)Cl<sub>2</sub> catalyst, or the diffusion of atmospheric oxygen to the catalytic sites. This prompted an investigation into the conditions which were facilitating the degradation.

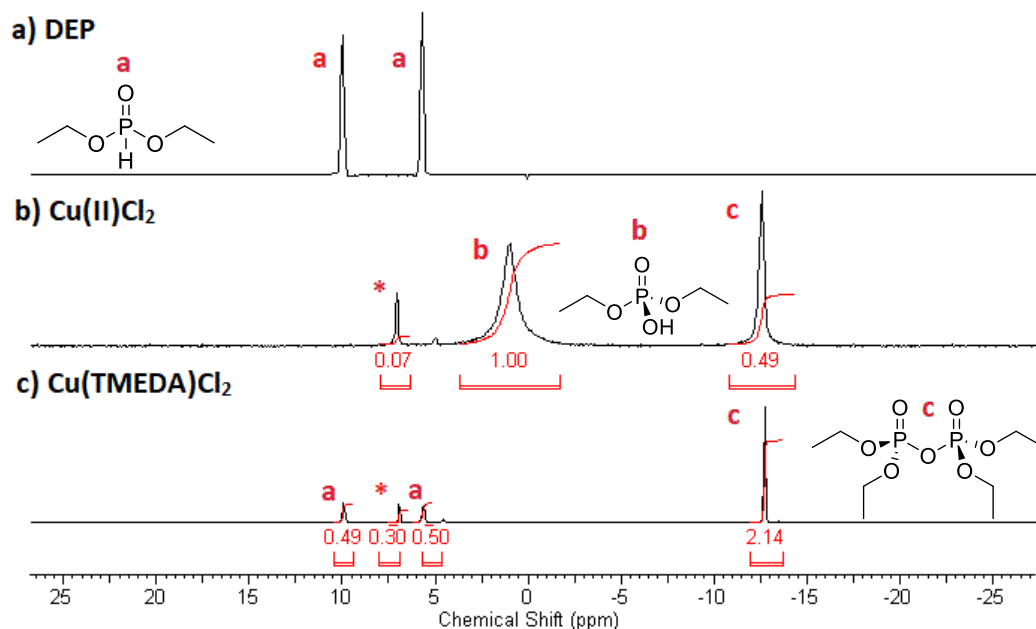


**Figure 2.10:** A <sup>31</sup>P NMR overlay in CDCl<sub>3</sub>. a) a spectrum of fresh DEP, two peaks are present due to P-H coupling. b) a spectrum of DEP after 24 hours in the presence Cu(II)Cl<sub>2</sub> b) a spectrum of DEP after 24 hours in the presence of Cu(TMEDA)Cl<sub>2</sub>. (\*) is believed to be tetraethyl hypophosphate.

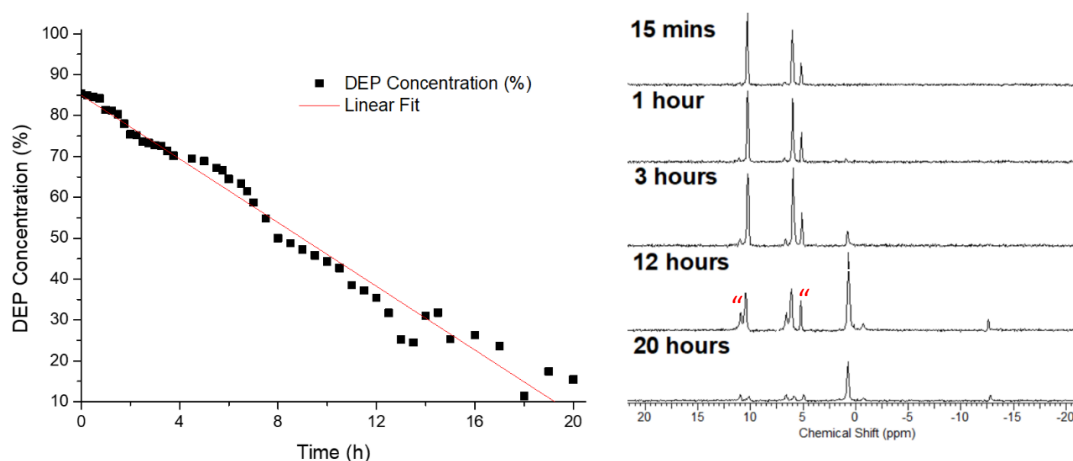


**Figure 2.11:** (left) A plot showing the oxidation of DEP over time in the presence of Cu(II)Cl<sub>2</sub>. (right) A <sup>31</sup>P NMR overlay in CDCl<sub>3</sub> of DEP in the presence Cu(II)Cl<sub>2</sub> at different times throughout the reaction period. (") represents unknown peaks.

An assessment of reaction conditions was performed on Cu(II)Cl<sub>2</sub> to verify its function as a catalyst. Table 2.2 and Figure 2.12 highlight the different distribution of products generated based on the various reaction conditions employed with the same Cu(II)Cl<sub>2</sub> catalyst. The reaction that was free of air and H<sub>2</sub>O did not proceed very far, the above spectrum shows that the majority of the DEP has remained unreacted. The reaction that contained H<sub>2</sub>O but no O<sub>2</sub>, proceeded slightly but again, a large quantity of the DEP remained unreacted, it should be noted that no DEPPA was formed in the presence of water. Finally, the reaction that contained no H<sub>2</sub>O but an O<sub>2</sub> atmosphere proceeded almost to completion in 24 hours with the secondary product, DEPPA, being formed. This condition assessment highlights the Cu(II)Cl<sub>2</sub> mediated breakdown of DEP into diethyl phosphoric acid is an aerobic process, in this respect, Cu(II)Cl<sub>2</sub> functions as an oxidation catalyst for the oxidation of DEP to DEPA and DEPPA. Different ratios of DEPA and DEPPA are achieved depending based on the water content of the reaction. The DEPPA likely exists in equilibrium with DEPA, the absence of H<sub>2</sub>O partially drives this equilibrium to the formation of the pyrophosphate through the condensation of two DEPA molecules.

Catalyst	Conditions	Time	% DEP oxidised to DEPA/DEPPA	% DEPPA
Blank	Air, Water, MeOH	24 hrs	0 %	0 %
Cu(II)Cl <sub>2</sub>	Air, Water, MeOH	24 hrs	95.5 %	0 %
Cu(TMEDA)Cl <sub>2</sub>	Air, Water, MeOH	24 hrs	62.2 %	62.2 %
Cu(II)Cl <sub>2</sub>	No Air, No Water	24 hrs	10 %	1.6 %
Cu(II)Cl <sub>2</sub>	No Air, Water	24 hrs	17.8 %	0 %
Cu(II)Cl <sub>2</sub>	O <sub>2</sub> , No Water	24 hrs	76.0 %	20.0%

**Table 2.2:** A table showing the Cu(II) catalysts which were screened as oxidative hydrolysis catalysts for the degradation of DEP under various conditions which are listed alongside each catalyst. The % of DEP which was degraded to DEPA/DEPPA is shown alongside each catalyst.

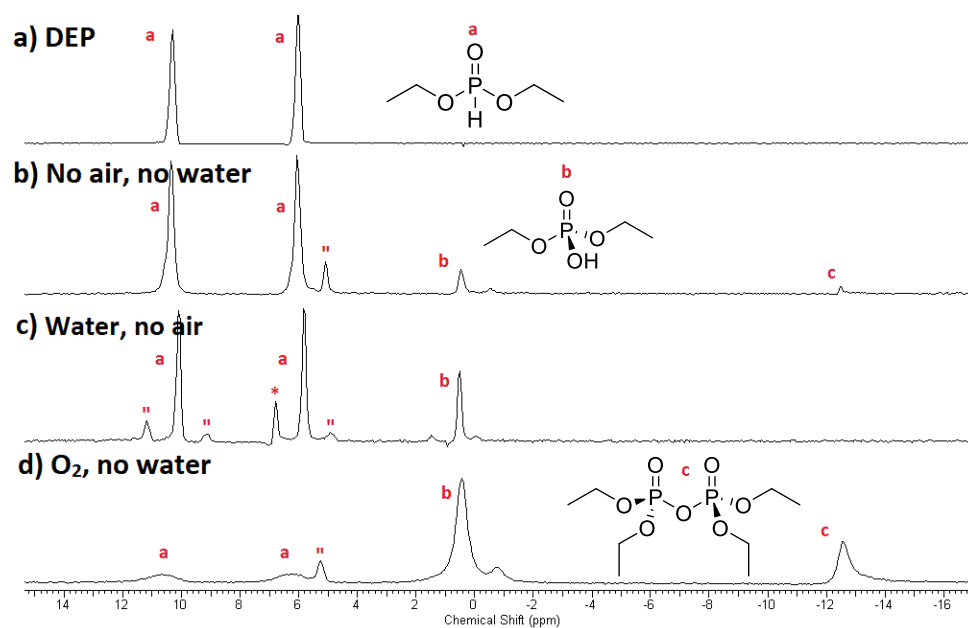


**Figure 2.12:** A  $^{31}\text{P}$  NMR overlay in  $\text{CDCl}_3$ . Peaks labelled a are DEP, peaks labelled b are DEPA and peaks labelled c are DEPPA a) spectrum shows fresh DEP, two peaks are present due to P-H coupling. b) a spectrum of DEP after 24 hours in the presence  $\text{Cu(II)Cl}_2$  and in the absence of air and water. c) a spectrum of DEP after 24 hours in the presence  $\text{Cu(II)Cl}_2$  and water but no air. d) a spectrum of DEP after 24 hours in the presence  $\text{Cu(II)Cl}_2$  and  $\text{O}_2$  but no water. (") represents unknown peaks.

Based on the limited number of oxidation studies that were performed, the oxidative hydrolysis simulant systems did not appear to mimic the degradation of OP CWAs due to the phosphorus atoms being in the 3+ oxidation states. Also, oxidation using a photo-catalyst such as  $\text{TiO}_2$  would reduce the degradation efficiency significantly, because the catalysis would be restricted to just the catalyst embedded on the surface of the polymer. Based on the huge quantity of publications relating to  $\text{CeO}_2$  as an oxidation catalyst,<sup>63-65</sup> the oxidative prowess of  $\text{CeO}_2$  cannot be questioned. Unfortunately, the vast majority of catalysis is conducted at elevated temperatures to facilitate the  $\text{Ce}^{3+}/\text{Ce}^{4+}$  redox cycle. Elevated temperatures are beyond the scope of the composite encapsulation and degradation material that is the ultimate aim of this thesis. However, the performance of the  $\text{Cu}^{2+}$  species as oxidative hydrolysis catalysts for the degradation of neat G-series agents, was of some interest. Some preliminary GB degradation tests are shown in section 2.5.1.

## 2.4 Hydrolysis

### 2.4.1 Choice and Synthesis of Zirconium MOF catalysts

UiO-66 is probably the most well-known zirconium MOF and has been previously used in hydrolysis studies,<sup>4,5</sup> however the small pore apertures (6 Å)<sup>66</sup> created by the short 1,4 benzene dicarboxylates restrict the reactivity to the catalyst surface. UiO-67, a larger framework containing biphenyl-4,4'-dicarboxylate (BDPC) and iso-reticular to the smaller UiO-66, possesses a marginally wider pore size, ranging from 8 to 10.5 Å.<sup>67</sup> UiO-67-NH<sub>2</sub>, a MOF consisting of the 2-aminobiphenyl-4,4'-dicarboxylate (Amine Lig) linker, was previously shown to effectively hydrolyse DMNP and VX. The amine functionality is believed to act as a Bronsted base and regulate the pH proximal to the active nodes and thus increases the effective basicity around the node. Two iso-structural mixed ligand (ML) derivatives of the UiO-67 series were nominated for testing (Figure 2.13), UiO-67-NH<sub>2</sub>-ML and UiO-67-BiPy-ML.

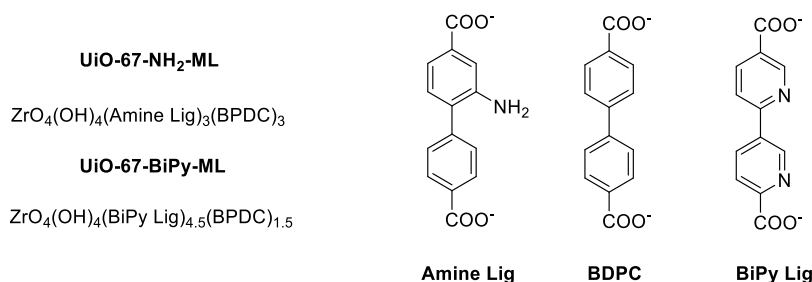


**Figure 2.13:** A formula unit representation of UiO-67-NH<sub>2</sub> and UiO-67-BiPy, along with an illustration of the structural linkers.

UiO-67-NH<sub>2</sub>-ML is composed of the 2-aminobiphenyl-4,4'-dicarboxylate and BDPC and was synthesised solvothermally in DMF using benzoic acid as a modulator. UiO-67-BiPy-ML, a framework composed of a 2,2'-Bipyridine-5,5'-dicarboxylate and BDPC ligand was also synthesised solvothermally in DMF but was modulated with acetic acid. Both of these syntheses were conducted using previously reported methodologies.<sup>53,55</sup> Mixed ligand variants of UiO-67-NH<sub>2</sub> have been shown to possess increased ambient stability over time when compared to a counterpart composed of only the single amine linker.<sup>55,68</sup>

MOF-808 (Figure 2.14) is a Zr MOF composed of the tritopic 1,3,5-benzene tricarboxylate (BTC) linker.<sup>12</sup> MOF-808 was synthesised using a previously reported procedure which involved solvothermal synthesis in DMF and modulation with acetic acid.<sup>14</sup> MOF-808 possesses a linker connectivity of 6 as opposed to the ideal number of 12. This means that each Zr<sub>6</sub> SBU possesses 6 sites which are not occupied by the linker thus vastly increasing the number of catalytic sites present in the material.<sup>69</sup>

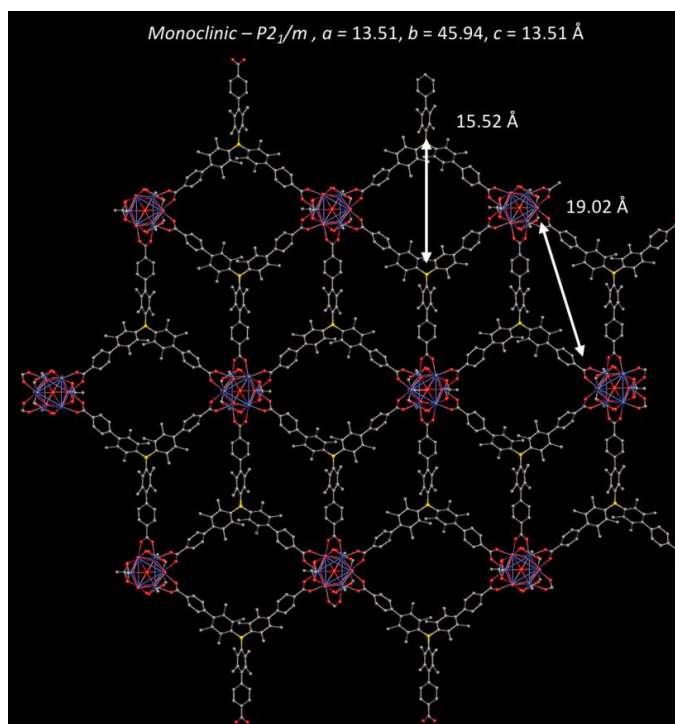
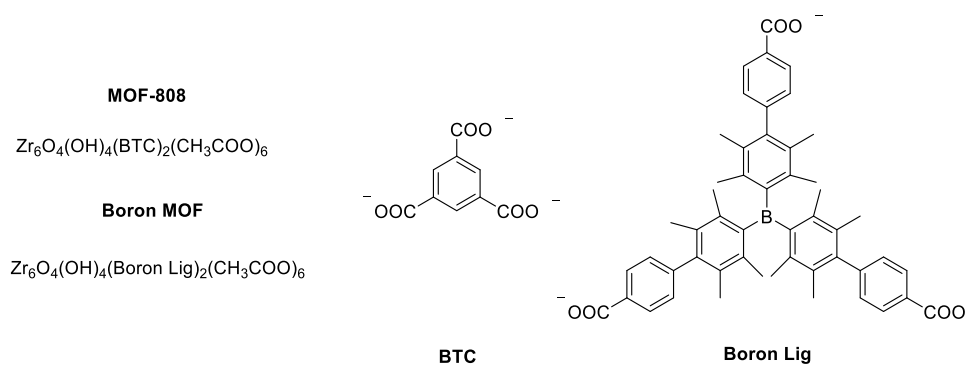


**Figure 2.14:** Top, a formula unit representation of MOF-808 and Boron MOF, along with an illustration of the structural linkers. Bottom, a graphical representation of the Boron MOF structure, the size of the two different types of pore apertures is shown (as calculated using Mercury).

An issue with MOF-808 was thought to be its rather small pore diameter of 10.5 Å, this potentially leaves very little space for DMNP (11 x 4.5 Å) to access the internal catalytic sites and therefore restricts the majority of the hydrolysis to the surface. An additional 6-connected Zr MOF was synthesised, one which would possess a larger pore diameter yet is still be composed of a tritopic ligand. The previously reported Tris(2',3',5',6'-tetramethylbiphenyl-4-carboxylic acid)borane linker precursor was synthesised.<sup>50</sup> The ligand contains a boron centre. The increased electron-withdrawing effect provided by this linker on the Zr<sub>6</sub> SBU would act to increase the Lewis acidity of the uncoordinated Zr<sup>4+</sup> nodes. After synthesising the borane linker, a novel 6-connected Zr MOF was assembled using the same procedure that was employed for the formation of MOF-808. Single crystals were also obtained using a slightly modified procedure with slower heating and cooling sequences. Figure 2.14 shows an illustration of the obtained crystal structure which reveals a maximum pore diameter of 19.02 Å (as calculated using Mercury), significantly larger than that of MOF-808 (10.5 Å).

Finally, the less studied DUT series of Zr MOFs were investigated.<sup>52</sup> The DUT series are composed of the ditopic 2,6-naphthalenedicarboxylate linker (Figure 2.15). The DUT variants differ in their connectivity based on the quantity of modulator employed during the synthesis.

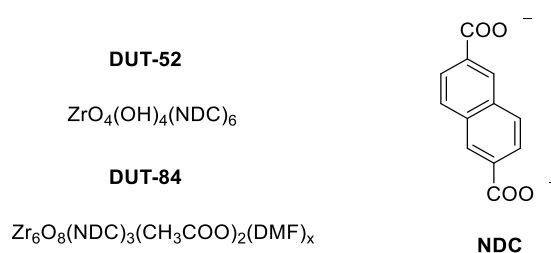


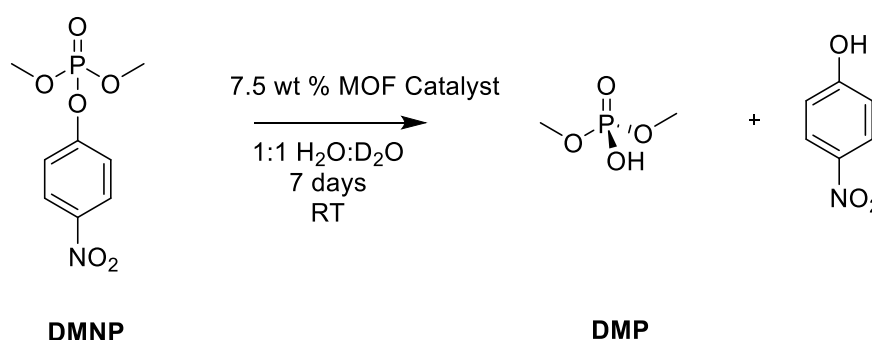
**Figure 2.15:** A formula unit representation of DUT-52 and DUT-84, along with an illustration of the structural linker.

DUT-52 and DUT-84 were both synthesised using the original author's methodology. In brief, this involved a solvothermal reaction in DMF which was modulated with acetic acid. The DUT-52 variant possesses a ligand connectivity close to the ideal value of 12 and was modulated with 47 equivalents of acetic acid. The lack of empty coordination sites and the small aperture

size provided by the naphthalene linker was thought to make this a poor catalyst. However, DUT-84 utilises 273 equivalents of acetic acid modulator relative to the naphthalene linker, this large excess results in a 6-connected network with a 2-D structure composed of double layers. It was hypothesised that the large prevalence of  $Zr^{4+}$  coordination vacancies would increase the catalyst density, the 2D structure would also allow easier access to the nodes.

#### 2.4.2 Zirconium MOFs as hydrolysis catalysts for DMNP hydrolysis

Having synthesised a range of potential Zr MOF catalysts, a number of hydrolysis screening studies were performed on the CWA simulant DMNP. The majority of studies to date involving MOF facilitated hydrolysis of DMNP have utilised NEM buffer to maintain a higher pH.<sup>4,11,33</sup> A higher-than-neutral pH, more specifically 8.3 – 8.8 pH,<sup>70</sup> reportedly increases the exchange rate between zirconium node bound water molecules and the OP substrate, this exchange is necessary for facilitating hydrolysis.<sup>71</sup> As the ultimate aim is to degrade neat VX in the absence of any stoichiometric reagents, the study was initiated by conducting the experiments in the absence of any buffering agent to see if any catalysts would persevere under less ideal circumstances. Scheme 2.7 illustrates the conditions that were employed for testing the catalysts.



**Scheme 2.7:** A reaction scheme outlining the conditions employed for the non-buffered hydrolysis of DMNP to DMP in the presence of a range of Zr MOF catalysts over 7 days.

Each reaction was conducted at room temperature (298 K) in an NMR tube, in a mixture of H<sub>2</sub>O/D<sub>2</sub>O and in the presence of 7.5 wt % MOF catalyst. The MOFs were not activated prior to

catalysis. The reaction mixtures were analysed using  $^{31}\text{P}$  {H} NMR spectroscopy. No hydrolysis was observed within the first 2 days of the study. This is unsurprising considering that no buffer was employed. The  $^{31}\text{P}$  {H} NMR overlay in Figure 2.16 shows the reaction after 7 days in the presence of the MOF-808 catalyst. No degradation of the DMNP control was observed after 7 days (DMNP – 7d). Unfortunately, no hydrolysis was observed for Boron MOF, DUT-52, DUT-84, UiO-67-NH<sub>2</sub>-ML and UiO-67-BiPy-ML after 7 days (Table 2.3). However, partial hydrolysis was obtained using MOF-808, 30% of the substrate was converted to the dimethyl phosphonate hydrolysis product after 7 days. This is remarkable considering that no buffering agent was present. A possible explanation for this is the much higher prevalence of Zr<sup>4+</sup> sites in MOF-808 that are unoccupied by the BTC linker, a direct result of MOF-808's 6-connected topology.<sup>69</sup> However, this does not explain why no hydrolysis was observed for Boron MOF or DUT-84, both of which also possess a 6-connected structure.

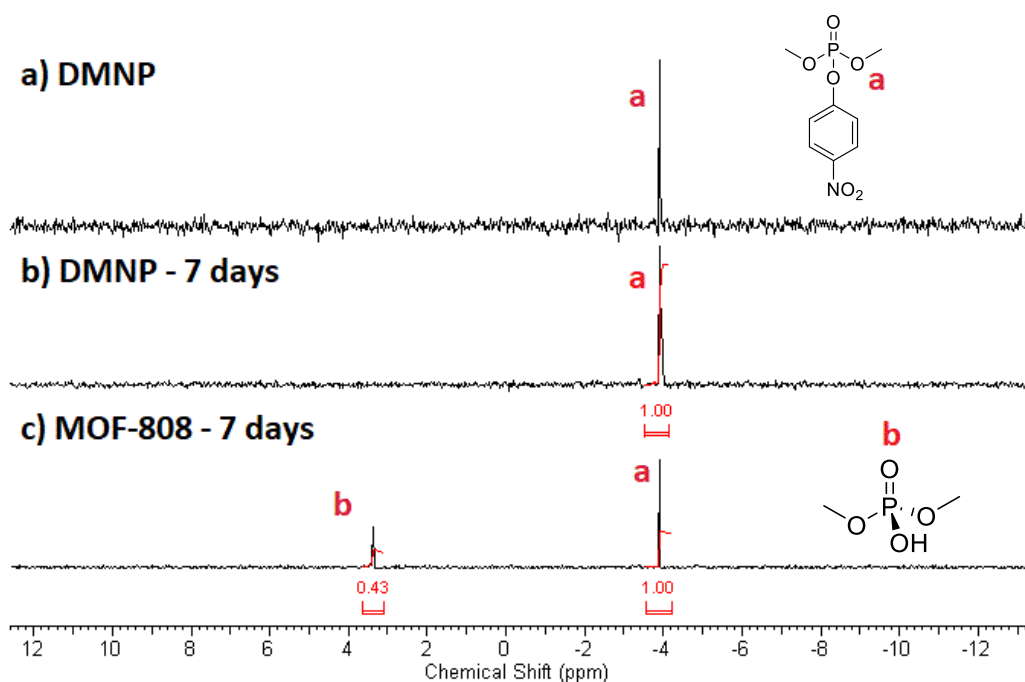
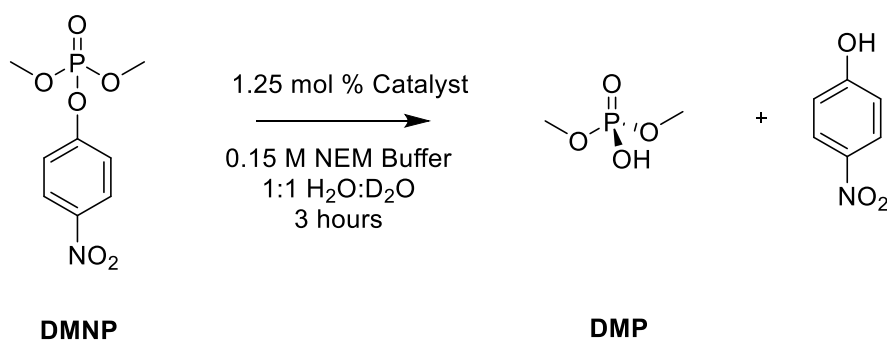


**Figure 2.16:** A  $^{31}\text{P}$  {H} NMR overlay. a) The top spectrum shows fresh DMNP in D<sub>2</sub>O. b) A spectrum of DMNP in D<sub>2</sub>O after 7 days. c) A spectrum of DMNP in D<sub>2</sub>O and in the presence of MOF-808, after 7 days under the conditions outlined in Scheme 2.7.

Catalyst	Conditions	% DMNP Hydrolysed to DMP
Blank	No buffer, 7 days	0 %
UiO-67-NH <sub>2</sub> -ML	No buffer, 7 days	0 %
UiO-67-BiPy-ML	No buffer, 7 days	0 %
Boron MOF	No buffer, 7 days	0 %
MOF-808	No buffer, 7 days	30 %
DUT-52	No buffer, 7 days	0 %
DUT-84	No buffer, 7 days	0 %

**Table 2.3:** A table showing the MOF catalysts which were screened as hydrolysis catalysts for the degradation of DMNP in the absence of buffer over the course of 7 days. The % of DMNP which was hydrolysed to DMP is shown alongside each catalyst. Each measurement was performed once.

To further probe the hydrolysis of DMNP in the presence of our MOF catalysts, an aqueous N-ethyl morpholine (NEM) buffer was employed. Scheme 2.8 outlines the conditions which were employed for our buffered hydrolysis screening procedure. DMNP was added to a mixture containing 1.25 mol % MOF catalyst in 0.15 M NEM buffer. Each reaction was allowed to proceed at room temperature (298 K) for 3 hours before being analysed using <sup>31</sup>P {H} NMR spectroscopy.



**Scheme 2.8:** A reaction scheme outlining the conditions employed for the buffered aqueous hydrolysis of DMNP to DMP in the presence of a range of Zr MOF catalysts over 3 hours.

DUT-52, UiO-67-NH<sub>2</sub>-ML and UiO-67-BiPy-ML all performed at a similar level with only ~10% hydrolysis being observed over the course of 3 hours (Table 2.4). The common factor amongst

these 3 MOFs is that they all possess a near ideal 12-connected structure, this means that there is a significantly lower frequency of catalytic nodes which are accessible to the substrate. It would also appear that the presence of a weakly basic linker in UiO-67-NH<sub>2</sub>-ML and UiO-67-BiPy-ML makes little difference in improving hydrolysis when a basic amine buffer is employed. There is of course disparity between the UiO-67-NH<sub>2</sub>-ML results obtained in this study and between previously published results for UiO-67-NH<sub>2</sub>. Literature studies involving the use of UiO-67-NH<sub>2</sub> to degrade DMNP in aqueous NEM buffer produced a DMNP  $t_{1/2}$  of just 2 minutes.<sup>11</sup> For the study in this chapter, a mixed ligand approach was used to synthesise the UiO-67-NH<sub>2</sub>-ML along with acetic acid and benzoic acid as a modulator. This approach was used to increase the ambient stability of UiO-67-NH<sub>2</sub>-ML over time.<sup>68</sup> Literature studies that have utilised UiO-67-NH<sub>2</sub> as a hydrolysis catalyst for DMNP degradation have used an alternative approach to form their catalyst. A single linker approach was used and HCl was employed as a modulator, HCl modulated Zr MOFs generally exhibit a more defective structure (i.e more catalytic vacancies) and a larger surface area. These properties would enhance the catalytic properties of UiO-67-NH<sub>2</sub> by improving access to uncoordinated nodes, at the expense of long-term storage stability.

The largest degree of hydrolysis is observed in the presence of MOF-808 with 78% of the total DMNP being converted to DMP over the course of 3 hours (Figure 2.17). This can be ascribed to the significantly higher population of Zr<sup>4+</sup> sites which are unoccupied by the linker.<sup>69</sup> However, just as before, DUT-84 and Boron MOF significantly underperformed when compared to MOF-808 as well as the other 12-connected MOFs. For the case of DUT-84, the 2D structure can potentially decrease specificity for the substrate. However, in chapter 4 a facile activation method is presented for enhancing the catalytic capability of DUT-84. In chapter 4, a likely explanation is also offered for the surprising underperformance of Boron MOF. After screening the above 6 MOFs as potential degradants for DMNP hydrolysis, MOF-808 unanimously outperformed the other Zr MOFs in all tests. Satisfied with the ease of

obtaining the trimesic acid linker combined with the trivial synthetic conditions required for the formation of MOF-808, the framework was promoted for testing on live OP CWAs.

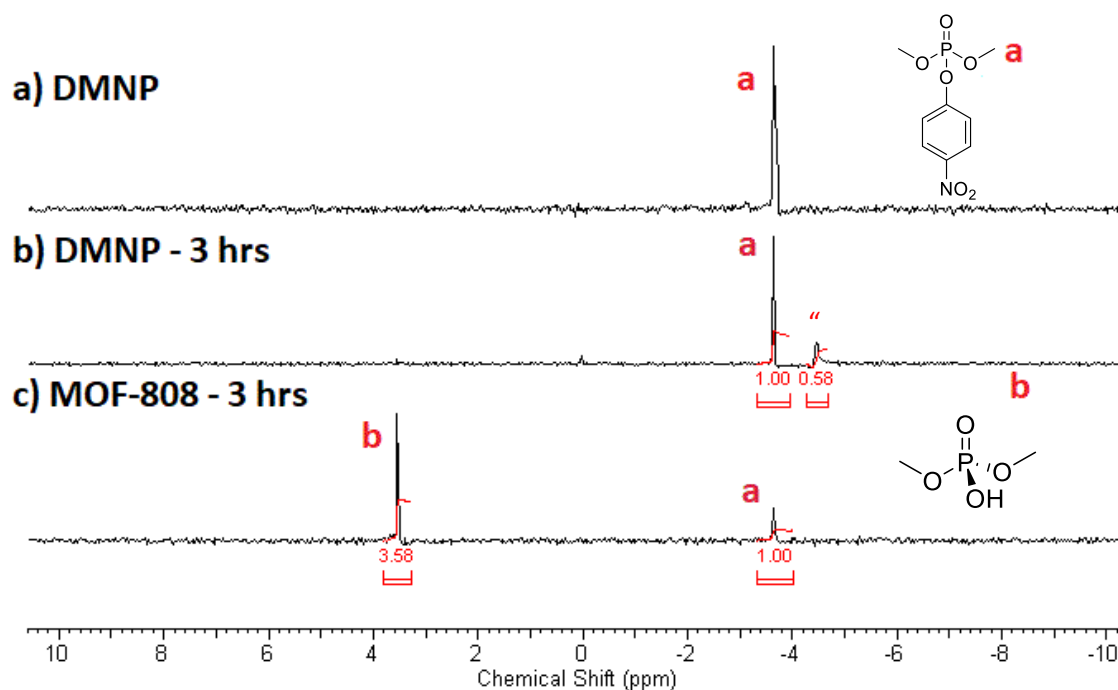


**Figure 2.17:** A  $^{31}\text{P}$  { $^1\text{H}$ } NMR in  $\text{D}_2\text{O}$  overlay. a) The top spectrum shows fresh DMNP in  $\text{D}_2\text{O}$ . b) a spectrum of DMNP in  $\text{D}_2\text{O}$  after 3 hours in the presence of 0.15 M NEM buffer c) A spectrum of DMNP in  $\text{D}_2\text{O}$  after 3 hours and in the presence of MOF-808 and 0.15 M NEM buffer. The reaction conditions are illustrated in Scheme 2.8. (“) represents an unknown peak.

Catalyst	Conditions	% DMNP Hydrolysed to DMP
Blank	0.15 M NEM Buffer, 3 hours	0 %
UiO-67-NH <sub>2</sub> -ML	0.15 M NEM Buffer, 3 hours	10 %
UiO-67-BiPy-ML	0.15 M NEM Buffer, 3 hours	12 %
Boron MOF	0.15 M NEM Buffer, 3 hours	4 %
<b>MOF-808</b>	0.15 M NEM Buffer, 3 hours	<b>78 %</b>
DUT-52	0.15 M NEM Buffer, 3 hours	10 %
DUT-84	0.15 M NEM Buffer, 3 hours	3 %

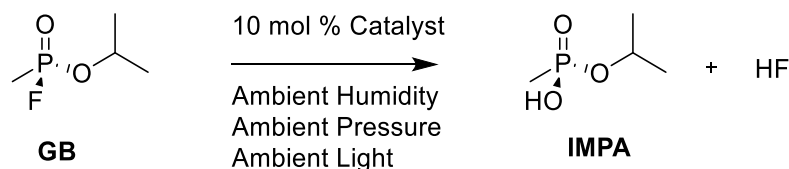
**Table 2.4:** A table showing the MOF catalysts which were screened as hydrolysis catalysts for the degradation of DMNP in the presence of aqueous 0.15 M NEM buffer over 3 hours. The % of DMNP which was hydrolysed to DMP is shown alongside each catalyst. Each measurement was performed once.

## 2.5 Preliminary OP CWA degradation using Nominated Catalysts

When obtaining results using simulants, it is vital to follow through with a study and validate any positive results using real CWAs. After performing numerous studies with a range of simulants and potential catalysts, a few of the more successful catalysts were nominated for further testing on live CWAs. All CWA testing was performed by DSTL in their Porton Down laboratories.

### 2.5.1 Preliminary GB Degradation using Oxidation Catalysts

For oxidation, Cu(TMEDA)Cl<sub>2</sub> and TiO<sub>2</sub> were nominated as potential oxidation catalysts for the degradation of Sarin (GB). Previously reported GB degradation studies involving Cu(TMEDA)Cl<sub>2</sub> were conducted in buffered aqueous solution, with a remarkable half-life ( $t_{1/2}$  0.5 mins) being achieved through an oxidative hydrolysis pathway.<sup>9</sup> It was therefore of interest to see whether the same catalyst would thrive under a neat degradation procedure, i.e no water. A catalyst loading of 10 mol % was selected for both Cu(TMEDA)Cl<sub>2</sub> and TiO<sub>2</sub>, the reaction conditions are outlined in Scheme 2.9 below.



**Scheme 2.9:** A reaction scheme outlining the conditions employed for the neat oxidative hydrolysis of GB into IMPA in the presence of TiO<sub>2</sub> and Cu(TMEDA)Cl<sub>2</sub>.

The <sup>31</sup>P [H] NMR overlay in Figure 2.18 shows the degree of GB conversion observed over the course of 24 hours in the presence of Cu(TMEDA)Cl<sub>2</sub> and TiO<sub>2</sub>. In <sup>31</sup>P [H] NMR, GB exists as a doublet centred around ~ 28.5 ppm, the doublet is the result of P-F bond coupling. Isopropyl methylphosphonic acid (IMPA), the GB degradation product, exists as a singlet around 33 ppm on the spectrum. Looking at the Cu(TMEDA)Cl<sub>2</sub> spectrum, two peaks are observed in a similar position to where one would expect to see un-degraded GB, there is however paramagnetic

signal broadening resulting from the  $\text{Cu}^{2+}$  species. No other peaks are present and so this is indicative of no degradation occurring over the course of the 24 hours. This is likely due to a much lower quantity of catalyst being used in this study compared to the literature study (10 mol % as opposed to 500 mol %). The reaction is also unbuffered and is conducted neat, as opposed to in aqueous medium. As for  $\text{TiO}_2$ , 18.4% conversion to IMPA is observed over 24 hours. The reaction was exposed to ambient light for the full 24 hours and so it is likely photo-oxidation is observed. Unfortunately no blank was supplied and GB is reported to slowly hydrolyse upon exposure to ambient humidity.<sup>72</sup> This makes the slow and partial  $\text{TiO}_2$  facilitated photo-oxidation quite unremarkable, it also negates the need for a catalyst unless rapid degradation is required.

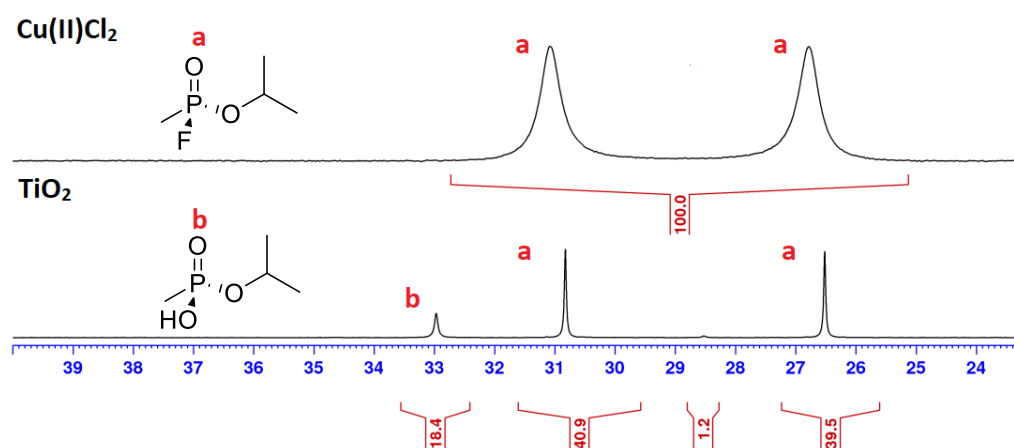
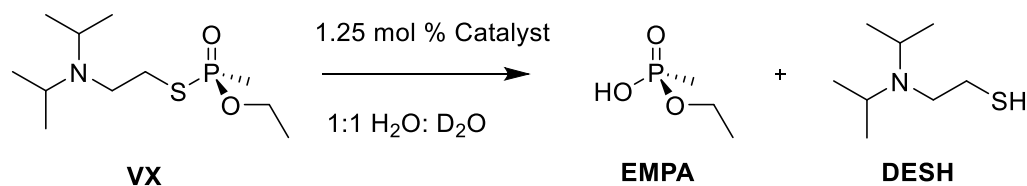


**Figure 2.18:** A  $^{31}\text{P}$  NMR overlay. The top spectrum shows GB in the presence of  $\text{Cu(TMEDA)Cl}_2$ , no degradation is observed after 24 hours. The bottom spectrum shows GB in the presence of  $\text{TiO}_2$ , a small amount of degradation to IMPA is shown after 24 hours. The conditions employed are outlined in Scheme 2.9.

## 2.5.2 Preliminary VX Degradation using Hydrolysis Catalysts

MOF-808, the most successful simulant hydrolysis catalyst, was then tested as a degradant for the decomposition of VX. At the time of screening, there existed only one previous example of MOF-facilitated VX degradation in unbuffered aqueous solution.<sup>11</sup> The MOF employed for this

was UiO-67-NMe<sub>2</sub>, a Zr MOF containing the basic 2-(dimethylamino)-[1,1'-biphenyl]-4,4'-dicarboxylate linker. Similar to DMNP, a basic buffer increases the exchange rate between zirconium node bound water molecules and the VX substrate, as well as functioning as a proximal base.<sup>71</sup> MOF-808 lacks a basic linker functionality, it was interesting to see if it would still degrade VX in unbuffered aqueous solution. The reaction scheme below outlines the conditions which were employed for the testing (Scheme 2.10).



**Scheme 2.10:** A reaction scheme outlining the conditions employed for the buffer-free aqueous hydrolysis of VX to EMPA in the presence of MOF-808.

Remarkably, 80% hydrolysis was observed after just 10 minutes (Figure 2.19). This unfortunately made it difficult to calculate the reaction order as over half of the substrate had been consumed by the time the first data point had been acquired. This was an unfortunate consequence of safety precautions which have to be followed when handling these toxic nerve agents. No repeat measurements were made. A total of 94% hydrolysis was then observed over 24 hours. It should be noted that only the EMPA degradation product was present as only P-S bond hydrolysis was occurring. This is highly beneficial as harsher catalysts/bases are capable of P-O bond cleavage which produces an equally harmful hydrolysis product. The reason that VX hydrolysis still occurs in the absence of a buffer is because the diisopropylaminoethanethiol (DESH) product is generated as one of the degradation products.<sup>71</sup> DESH contains a basic diisopropylamine moiety which buffers the remainder of the hydrolysis process. It has also been previously suggested that the diisopropylamine group in unhydrolysed VX is capable of producing a similar buffering effect.<sup>71</sup> Fortunately, this self-buffering effect carries over to the rest of the V-series, all of which produce a similar amine hydrolysis product.



contrast, the blank remained completely unreacted, this highlights how persistent VX remains in an ambient environment after deployment. Despite the hydrolysis being rather slow, the low catalyst loading combined with the high ambient stability of VX adds value to the efficacy of the process.

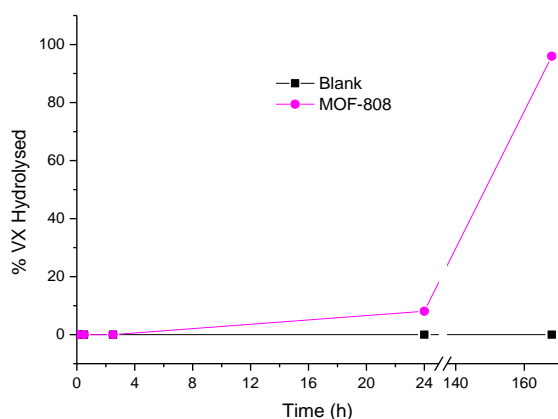
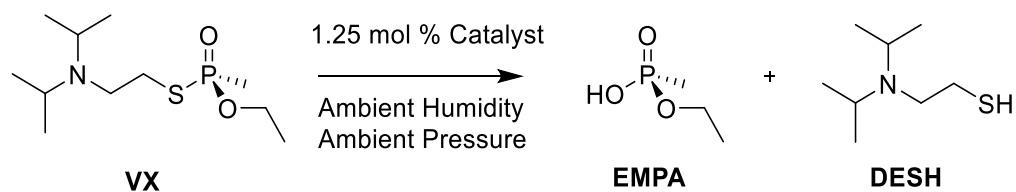


**Figure 2.20.** A degradation plot showing the hydrolysis of VX to EMPA over time in the presence of stoichiometric quantities of water along with MOF-808 and a blank. The conditions employed are outlined in Scheme 2.11.

Although using a stoichiometric quantity of water was slow, full hydrolysis was still observed therefore decided to conduct one final study with MOF-808 and VX. Neat reaction conditions were employed, no water was added and so the degradation was completely limited to ambient humidity. Reaction Scheme 2.12 outlines the exact conditions which were employed.



**Scheme 2.12:** A reaction scheme outlining the conditions employed for the buffer-free hydrolysis of VX to EMPA in the presence of MOF-808 and ambient humidity and pressure.

The first data point was collected after 24 hours at which point 8% hydrolysis was observed, roughly no slower than when a stoichiometric quantity of water was present. Full hydrolysis

was observed after 7 days (Figure 2.21). There is therefore little difference between adding stoichiometric H<sub>2</sub>O to the reaction mixture and simply leaving it to ambient humidity, this is in contrast to when a large excess of H<sub>2</sub>O is present. VX is sparingly soluble in water and so when small quantities of H<sub>2</sub>O are introduced to neat VX, there is likely very slow diffusion of the H<sub>2</sub>O to the catalytic Zr<sub>6</sub> nodes through the VX medium. Ambient hydration of the Zr<sub>6</sub> nodes is therefore the rate limiting step for neat hydrolysis to occur. For a more effective process, improved compatibility is required between H<sub>2</sub>O and VX. This can be achieved by embedding MOF-808 in an appropriate polymer membrane, this is discussed in detail throughout chapter 5. Despite the challenges that lay ahead, a catalyst has been identified, capable of fully degrading VX under neat conditions and in the absence of any buffer or reagent.

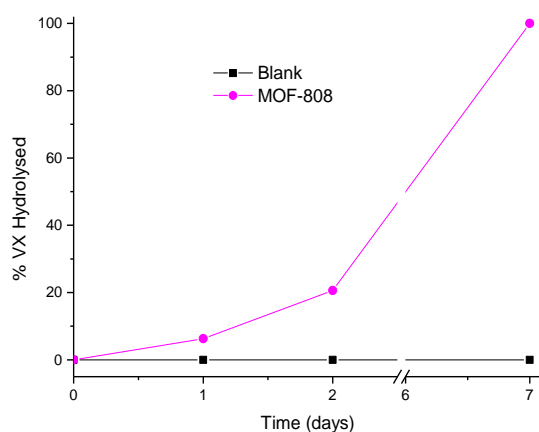


**Figure 2.21.** A degradation plot showing the hydrolysis of VX to EMPA over time in the presence of MOF-808 and a blank. The conditions employed are outlined in Scheme 2.12.

In an attempt to quantify the hydration of the MOF-808 nodes, a short study was conducted to determine the maximum quantity of H<sub>2</sub>O that MOF-808 could ‘ambiently’ adsorb. Samples of MOF-808 was vacuum dried at 70 °C for 72 hours and then immediately exposed to two different environments, one with a relative humidity (RH) of 30 % and another of 65 %. The weight change of each sample was then closely monitored. The plot below (Figure 2.22) shows the weight gain of each sample as a percentage of the dry mass of the MOF-808.

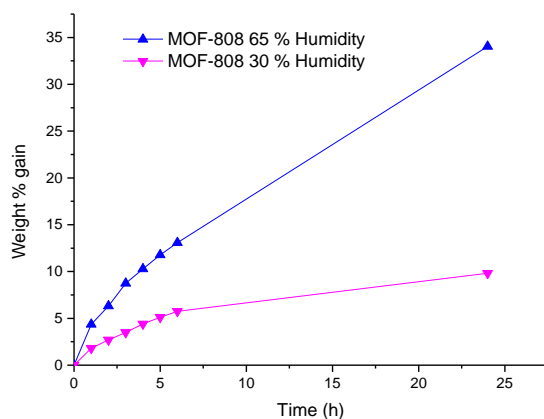


**Figure 2.22.** A plot showing the % weight gain of MOF-808 over time in the presence of two different humidities.

At the lower humidity of 30 %, a 10 weight % gain by mass is observed over the course of 24 hours. At the higher humidity of 65 %, a 32 weight % gain by mass is observed over 24 hours. This can be expressed as an efficiency of 0.32 ml per gram of MOF-808 over 24 hours. This demonstrates that MOF-808 has a high affinity for ambient H<sub>2</sub>O and therefore reinforces our decision to use this framework as a degradant for neat V-series agent. In the following chapter, an attempt is made to elucidate any subtle structural changes which may be occurring upon hydration of the MOF-808 nodes through the use of solid-state photoluminescence spectroscopy.

## 2.6 Summary and Conclusion

The ultimate aim of this chapter was to identify a degradation catalyst capable of degrading OP CWAs under neat conditions, i.e. no solvent, no additional reagent. A range of materials were explored as potential catalysts for the degradation of OP CWAs. First, a number of commercial MONPs were screened as potential oxidation catalysts, under ambient conditions, only TiO<sub>2</sub> was found to be effective at oxidising TPP to TPPO. TiO<sub>2</sub> was also able to slightly speed up the photo-oxidative hydrolysis of GB under neat conditions. As the final aim of this project would be to embed a degradation catalyst in a 3D swellable polymer matrix, varying degrees of polymer opacity would make the use of a photocatalysts obsolete. P-H bond oxidation in DEP using Cu<sup>2+</sup> species was also explored. There was, however, little carryover to live CWAs. Simulant selection was also an important aspect of this study, and the literature was surveyed for a number of simulants which have been used to mimic the degradation of OP CWAs. Tests were conducted with DCP but it was found that the lability of the P-Cl bond under ambient conditions made it a poor compound for simulating neat degradation. Finally, DMNP was tested as a hydrolysis simulant. In the presence of NEM buffer, hydrolysis of DMNP closely mimicked the aqueous hydrolysis of V-series agents. A variety of Zr MOFs were synthesised and screened, some of which had been previously reported as hydrolysis catalysts and some of which were believed to exhibit similar properties. These Zr MOFs were then tested on the DMNP simulant. It was found that MOF-808, a 6-connected Zr MOF containing 6 coordination vacancies per Zr<sub>6</sub> SBU, to be the most effective hydrolysis catalyst. Building on the principles that made MOF-808 an effective catalyst, a novel zirconium MOF (Zr-Boron MOF) was synthesised. Unfortunately, Zr-Boron MOF proved ineffective and a potential explanation is offered in chapter 4 as to why this framework makes an unsuitable catalyst.

Following on from the successful simulant tests in the presence of MOF-808, MOF-808 was tested on the V-series agent VX. Remarkably, MOF-808 was able to rapidly degrade VX in aqueous medium ( $t_{1/2} < 5$  minutes) in the absence of a buffer. Following on, a neat screening

procedure was utilised and showed that MOF-808 was capable of fully degrading VX under neat conditions, relying solely on ambient humidity. This degradation was significantly slower with full hydrolysis being observed after 7 full days. A hydrolysis catalyst capable of hydrolysing V-series agents under neat conditions has therefore been identified and the ultimate aim of this chapter has been fulfilled. To further enhance this hydrolysis process, the effect of hydration upon the  $Zr_6$  cluster is explored. In chapter 3, solid state photoluminescence spectroscopy is utilised in an attempt to differentiate between any potential hydration states. In chapter 4, a novel activation procedure is reported where microwave irradiation is used to remove bound modulator from the  $Zr_6$  cluster and replace it with  $H_2O$ .

## 2.7 Bibliography

- 1 1925 Geneva Protocol – UNODA, <https://www.un.org/disarmament/wmd/bio/1925-geneva-protocol/>, (accessed 3 September 2018).
- 2 Z. Moshaver, *Int. Aff.*, 1994, **70**, 590–591.
- 3 S. L. Bartelt-Hunt, D. R. U. Knappe and M. A. Barlaz, *Crit. Rev. Environ. Sci. Technol.*, 2008, **38**, 112–136.
- 4 M. J. Katz, J. E. Mondloch, R. K. Totten, J. K. Park, S. T. Nguyen, O. K. Farha and J. T. Hupp, *Angew. Chem. Int. Ed.*, 2014, **126**, 507–511.
- 5 M. J. Katz, S.-Y. Moon, J. E. Mondloch, M. H. Beyzavi, C. J. Stephenson, J. T. Hupp and O. K. Farha, *Chem. Sci.*, 2015, **6**, 2286–2291.
- 6 Y. Liu, S.-Y. Moon, J. T. Hupp and O. K. Farha, *ACS Nano*, 2015, **9**, 12358–12364.
- 7 P. K. Gutch, A. Mazumder and G. Raviraju, *RSC Adv.*, 2016, **6**, 2295–2301.
- 8 Y. Zhou, S. Yin, Y. Gao, Y. Zhao, M. Goto and L.-B. Han, *Angew. Chem. Int. Ed.*, 2010, **49**, 6852–6855.
- 9 R. C. Courtney, R. L. Gustafson, S. J. Westerback, H. Hyytiainen, S. C. Chaberek and A. E. Martell, *J. Am. Chem. Soc.*, 1957, **79**, 3030–3036.
- 10 H. Rasoulnezhad, G. Kavei, K. Ahmadi and M. R. Rahimipour, *J. Mater. Sci. Mater. Electron.*, 2017, **28**, 18337–18347.
- 11 S.-Y. Moon, G. W. Wagner, J. E. Mondloch, G. W. Peterson, J. B. DeCoste, J. T. Hupp and O. K. Farha, *Inorg. Chem.*, 2015, **54**, 10829–10833.
- 12 H. Furukawa, F. Gándara, Y.-B. Zhang, J. Jiang, W. L. Queen, M. R. Hudson and O. M. Yaghi, *J. Am. Chem. Soc.*, 2014, **136**, 4369–4381.
- 13 J. Jiang, F. Gándara, Y.-B. Zhang, K. Na, O. M. Yaghi and W. G. Klemperer, *J. Am. Chem. Soc.*, 2014, **136**, 12844–12847.
- 14 W. Liang, H. Chevreau, F. Ragon, P. D. Southon, V. K. Peterson and D. M. D’Alessandro, *CrystEngComm*, 2014, **16**, 6530–6533.
- 15 S. L. Bartelt-Hunt, D. R. U. Knappe and M. A. Barlaz, *Crit. Rev. Environ. Sci. Technol.*, 2008, **38**, 112–136.
- 16 J. Lavoie, S. Srinivasan and R. Nagarajan, *J. Hazard. Mater.*, 2011, **194**, 85–91.
- 17 M. R. Sambrook, J. R. Hiscock, A. Cook, A. C. Green, I. Holden, J. C. Vincent and P. A. Gale, *Chem. Commun.*, 2012, **48**, 5605–5607.
- 18 R. Kaiser, A. Kulczyk, D. Rich, R. J. Willey, J. Minicucci and B. MacIver, *Ind. Eng. Chem. Res.*, 2007, **46**, 6126–6132.
- 19 J. R. Hiscock, F. Piana, M. R. Sambrook, N. J. Wells, A. J. Clark, J. C. Vincent, N. Busschaert, R. C. D. Brown and P. A. Gale, *Chem. Commun.*, 2013, **49**, 9119–9121.
- 20 D. R. Goud, D. Pardasani, V. Tak and D. K. Dubey, *RSC Adv.*, 2014, **4**, 24645–48.
- 21 I. Candel, M. D. Marcos, R. Martínez-Mañez, F. Sancenón, A. M. Costero, M. Parra, S. Gil, C. Guillem, F. Pérez-Plá and P. Amorós, *Microporous Mesoporous Mater.*, 2015, **217**, 30–38.

- 22 J. R. Hiscock, M. R. Sambrook, N. J. Wells and P. A. Gale, *Chem. Sci.*, 2015, **6**, 5680–5684.
- 23 M. B. Pushkarsky, M. E. Webber, T. Macdonald and C. K. N. Patel, *Appl. Phys. Lett.*, 2006, **88**, 044103.
- 24 A. B. Kanu, P. E. Haigh and H. H. Hill, *Anal. Chim. Acta*, 2005, **553**, 148–159.
- 25 M. E. Webber, M. B. Pushkarsky and C. K. N. Patel, *J. Appl. Phys.*, 2005, **97**, 113101.
- 26 V. B. Raj, H. Singh, A. T. Nimal, M. Tomar, M. U. Sharma and V. Gupta, *Sensors Actuators B Chem.*, 2015, **207**, 375–382.
- 27 Y. Wang, Z. Yang, Z. Hou, D. Xu, L. Wei, E. S.-W. Kong and Y. Zhang, *Sensors Actuators B Chem.*, 2010, **150**, 708–714.
- 28 A. Komano, T. Hirakawa, K. Sato, S. Kishi, C. K. Nishimoto, N. Mera, M. Kugishima, T. Sano, N. Negishi, H. Ichinose, Y. Seto and K. Takeuchi, *Appl. Catal. B Environ.*, 2013, **134–135**, 19–25.
- 29 Y. Sagatelian, D. Sharabi and Y. Paz, *J. Photochem. Photobiol. A Chem.*, 2005, **174**, 253–260.
- 30 E. López-Maya, C. Montoro, L. M. Rodríguez-Albelo, S. D. Aznar Cervantes, A. A. Lozano-Pérez, J. L. Cenís, E. Barea and J. A. R. Navarro, *Angew. Chem. Int. Ed.*, 2015, **54**, 6790–6794.
- 31 C. Montoro, F. Linares, E. Quartapelle Procopio, I. Senkovska, S. Kaskel, S. Galli, N. Masciocchi, E. Barea and J. A. R. Navarro, *J. Am. Chem. Soc.*, 2011, **133**, 11888–11891.
- 32 R. Ramaseshan and S. Ramakrishna, *J. Am. Ceram. Soc.*, 2007, **90**, 1836–1842.
- 33 J. E. Mondloch, M. J. Katz, W. C. Isley III, P. Ghosh, P. Liao, W. Bury, G. W. Wagner, M. G. Hall, J. B. DeCoste, G. W. Peterson, R. Q. Snurr, C. J. Cramer, J. T. Hupp and O. K. Farha, *Nat. Mater.*, 2015, **14**, 512–516.
- 34 G. W. Wagner, *Main Gr. Chem.*, 2010, **9**, 257–263.
- 35 Y.-C. Yang, *Acc. Chem. Res.*, 1998, **32**, 109–115.
- 36 J. Epstein, V. E. Bauer, M. Saxe and M. M. Demek, *J. Am. Chem. Soc.*, 1956, **78**, 4068–4071.
- 37 P. Janoš, J. Henych, O. Pelant, V. Pilařová, L. Vrtoch, M. Kormunda, K. Mazanec and V. Štengl, *J. Hazard. Mater.*, 2016, **304**, 259–268.
- 38 G. W. Wagner, Q. Chen and Y. Wu, *J. Phys. Chem. C*, 2008, **112**, 11901–11906.
- 39 U. R. Pillai and S. Deevi, *Appl. Catal. B Environ.*, 2006, **64**, 146–151.
- 40 Z. G. and K. L. Hohn, *Ind. Eng. Chem. Res.*, 2003, **43**, 30–35.
- 41 P. Amigues and S. J. Teichner, *Discuss. Faraday Soc.*, 1966, **41**, 362.
- 42 A. A. Mirzaei, H. R. Shaterian, S. H. Taylor and G. J. Hutchings, *Catal. Letters*, 2003, **87**, 103–108.
- 43 S.-Y. Moon, Y. Liu, J. T. Hupp and O. K. Farha, *Angew. Chem. Int. Ed.*, 2015, **54**, 6795–6799.
- 44 X. Ma, L. Zhang, M. Xia, X. Zhang and Y. Zhang, *J. Hazard. Mater.*, 2018, **355**, 65–73.
- 45 M. J. Katz, S.-Y. Moon, J. E. Mondloch, M. H. Beyzavi, C. J. Stephenson, J. T. Hupp and O. K. Farha, *Chem. Sci.*, 2015, **6**, 2286–2291.

- 46 M. Kaposi, M. Cokoja, C. H. Hutterer, S. A. Hauser, T. Kaposi, F. Klappenberger, A. Pöthig, J. V. Barth, W. A. Herrmann and F. E. Kühn, *Dalton. Trans.*, 2015, **44**, 15976–15983.
- 47 M. A. Gotthardt, S. Grosjean, T. S. Brunner, J. Kotzel, A. M. Gänzler, S. Wolf, S. Bräse and W. Kleist, *Dalton. Trans.*, 2015, **44**, 16802–16809.
- 48 R. S. Kularatne, P. Sista, H. D. Magurudeniya, J. Hao, H. Q. Nguyen, M. C. Biewer and M. C. Stefan, *J. Polym. Sci. Part A Polym. Chem.*, 2015, **53**, 1617–1622.
- 49 S. Yamaguchi, T. Shirasaka and K. Tamao, *Org. Lett.*, 2000, **2**, 4129–32.
- 50 B. A. Blight, R. Guillet-Nicolas, F. Kleitz, R.-Y. Wang and S. Wang, *Inorg. Chem.*, 2013, **52**, 1673–1675.
- 51 G. Margraf, J. W. Bats, M. Wagner and H.-W. Lerner, *Inorganica Chim. Acta*, 2005, **358**, 1193–1203.
- 52 V. Bon, I. Senkovska, M. S. Weiss and S. Kaskel, *CrystEngComm*, 2013, **15**, 9572–9577.
- 53 H. Fei and S. M. Cohen, *Chem. Commun.*, 2014, **50**, 4810–4812.
- 54 S. Øien, D. Wragg, H. Reinsch, S. Svelle, S. Bordiga, C. Lamberti and K. P. Lillerud, *Cryst. Growth Des.*, 2014, **14**, 5370–5372.
- 55 S. M. Chavan, G. C. Shearer, S. Svelle, U. Olsbye, F. Bonino, J. Ethiraj, K. P. Lillerud and S. Bordiga, *Inorg. Chem.*, 2014, **53**, 9509–9515.
- 56 P. Kuran, P. Janos, M. Kormunda, V. Stengl, T. M. Grygar, M. Dosek, M. Stastny, J. Ederer, V. Pilarova and L. Vrtoch, *J. RARE EARTHS*, 2014, **32**, 360.
- 57 J. Henych, V. Štengl, M. Slušná, T. Matys Grygar, P. Janoš, P. Kuráň and M. Štastný, *Appl. Surf. Sci.*, 2015, **344**, 9–16.
- 58 R. Gao, D. G. Ho, T. Dong, D. Khuu, N. Franco, O. Sezer and M. Selke, *Org. Lett.*, 2001, **3**, 3719–3722.
- 59 S. Yamaguchi, T. Shirasaka and K. Tamao, *Org. Lett.*, 2000, **2**, 4129–32.
- 60 G. P. Jose, S. Santra, S. K. Mandal and T. K. Sengupta, *J. Nanobiotechnology*, 2011, **9**, 9.
- 61 Y. Xie, S. Heo, S. Yoo, G. Ali and S. Cho, *Nanoscale Res. Lett.*, 2009, **5**, 603–7.
- 62 H. J. Foroudian, N. D. Gillitt and C. A. Bunton, *J. Colloid Interface Sci.*, 2002, **250**, 230–237.
- 63 J. Zhang, S. Ohara, M. Umetsu, T. Naka, Y. Hatakeyama and T. Adschiri, *Adv. Mater.*, 2007, **19**, 203–206.
- 64 P. Janoš, J. Henych, O. Pelant, V. Pilařová, L. Vrtoch, M. Kormunda, K. Mazanec and V. Štengl, *J. Hazard. Mater.*, 2016, **304**, 259–268.
- 65 P. Ji, J. Zhang, F. Chen and M. Anpo, *J. Phys. Chem. C*, 2008, **112**, 17809–17813.
- 66 J. H. Cavka, S. Jakobsen, U. Olsbye, N. Guillou, C. Lamberti, S. Bordiga and K. P. Lillerud, *J. Am. Chem. Soc.*, 2008, **130**, 13850–13851.
- 67 G. W. Peterson, S.-Y. Moon, G. W. Wagner, M. G. Hall, J. B. DeCoste, J. T. Hupp and O. K. Farha, *Inorg. Chem.*, 2015, **54**, 9684–9686.
- 68 A. M. Rasero-Almansa, A. Corma, M. Iglesias and F. Sánchez, *ChemCatChem*, 2014, **6**, 3426–3433.

- 69 Y. Liu, R. C. Klet, J. T. Hupp and O. Farha, *Chem. Commun.*, 2016, **52**, 7806–7809.
- 70 M. J. Katz, R. C. Klet, S.-Y. Moon, J. E. Mondloch, J. T. Hupp and O. K. Farha, *ACS Catal.*, 2015, **5**, 4637–4642.
- 71 M. C. de Koning, M. van Grol and T. Breijaert, *Inorg. Chem.*, 2017, **56**, 11804–11809.
- 72 T. C. Marrs, R. L. Maynard, F. R. Sidell and Wiley InterScience, *Chemical warfare agents : toxicology and treatment*, Wiley, 2007, pp. 67-88.

## Chapter 3. Photoluminescence as a Probe for Screening the Functional Properties of MOFs

The work described in this chapter was previously published in the following journals:

Z. H. Fard, Y. Kalinovsky, D. M. Spasyuk, B. A. Blight and G. K. H. Shimizu, *Chem. Commun.*, 2016, **52**, 12865–12868.

R. J. Marshall, Y. Kalinovsky, S. L. Griffin, C. Wilson, B. A. Blight and R. S. Forgan, *J. Am. Chem. Soc.*, 2017, **139**, 6253–6260.

The synthesis and characterization of H<sub>6</sub>L, MOF-1 (Ba) and MOF-2 (Ba) were all performed by Z. Fard, D. Spasyuk and G. Shimizu at the University of Calgary. The synthesis and characterization of L1, L2, L5, L6, and L7 along with Zr-L1, Zr-L2, Zr-L5, Zr-L6 and Zr-L7, were all performed by R. Marshall, S. Griffin, C. Wilson and R. Forgan at the University of Glasgow. All solid-state fluorometry analysis of the aforementioned materials was conducted by the author of this thesis, as were some PXRD and contact angle measurements.

### 3.1 Introduction

MOFs are a group of chemically diverse, porous and crystalline hybrid materials. There exist a number of techniques for evaluating the functional properties of MOFs. Porosimetry<sup>1-3</sup> is a widely accepted method for determining the porosity of MOFs and assessing their suitability for applications in gas sorption and carbon sequestration. PXRD<sup>4-7</sup> and TGA<sup>8-10</sup> can be used to confirm the stability and structural integrity of frameworks. Single-crystal X-ray diffraction (SCXRD)<sup>11-13</sup> analysis is another technique which is commonly used to probe subtle host-guest interactions in single-crystalline frameworks. Another common feature of the majority of frameworks is that they are composed of organic linkers.<sup>14</sup> The conjugated nature of these bridging ligands lends them chromophoric properties and as a result, there are numerous reports of ligand based emission in the MOF literature.<sup>15-18</sup> The coordination of these linkers to various metal/cluster centres perturbs the solid-state emissive profile of these linkers by

providing alternative relaxation pathways. Additionally, interactions between guest molecules and the nodes and/or linkers can further alter the emission profiles of these materials.<sup>19–21</sup> All of these intricate changes can be monitored using solid-state photoluminescence (ssPL) spectroscopy.<sup>22–24</sup> This chapter shows that ssPL is a quick and efficient technique for the rapid screening a wide array of materials upon exposure to a range of liquid and gaseous analytes. This is demonstrated by the use of ssPL as a probe for screening the functional properties of a number of novel MOF materials.

Water sensing has a number of important applications in processes that include environmental surveying, food processing and pharmaceutical manufacturing.<sup>15,25</sup> These applications include the detection of water in both the liquid and gaseous phase. MOFs that exhibit a hydration-dependent emission upon exposure to liquid water/water vapour can be employed as potential water sensors. When designing MOF sensors, the vast array of building blocks and synthetic strategies present a seemingly endless amount of possibilities for assembling chemically versatile structures. Stability can often be a compromising factor when designing new frameworks; there are numerous reports of MOFs with poor ambient and aqueous stability.<sup>26–28</sup>

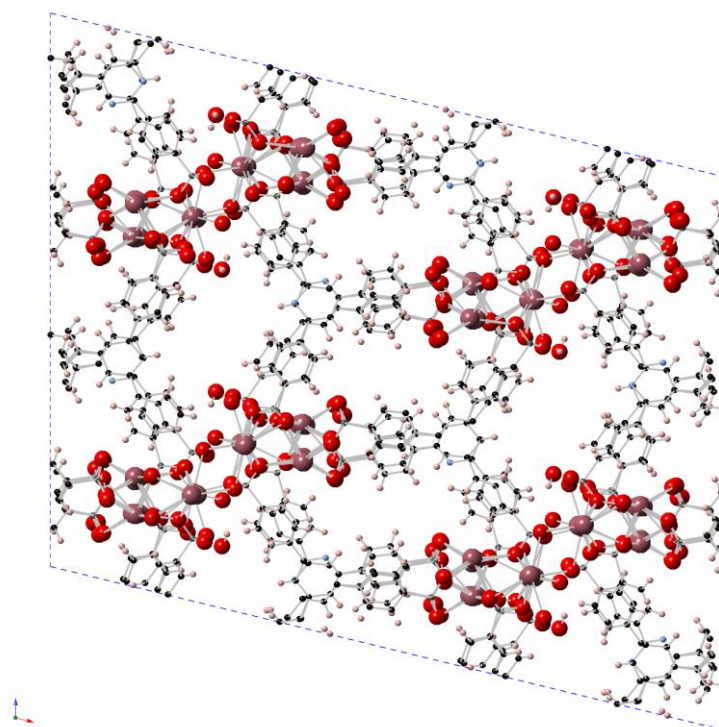
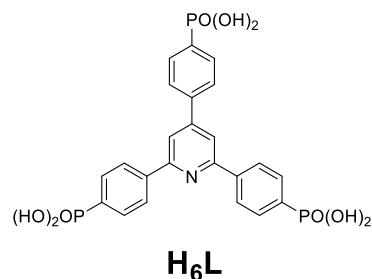
Alkaline earth (AE) MOFs are an emergent group of materials which have attracted considerable interest over the last few years. AE MOFs possess a malleable coordination environment due largely in part to their highly ionic character.<sup>29–31</sup> The unpredictability of their coordination environments makes it difficult to rationally control their structure and dimensionality but their ionic character still offers a number of advantages. The higher charge density of the AE ions allows for the formation of very strong interactions between the metal and the linker, which significantly increases the stability of these materials.<sup>32,33</sup> The ionic nature of these frameworks also enables these frameworks to be used in proton-conducting applications.<sup>33,34</sup> The vast majority of MOFs are assembled using carboxylate linkers, but phosphonate ligands are an alternative building block strategy for the formation of MOFs.<sup>35–37</sup>

Phosphonates linkers possess several ligation modes and thus form less predictable structures. However, they form stronger interactions than carboxylate and thus enhanced thermal stability can be achieved.<sup>38</sup> The low solubility of phosphonate linkers also improves the chemical stability of phosphonate-based MOFs.<sup>34</sup> Additionally, Zirconium MOFs have received significant coverage due in part to their robustness.<sup>10,13,39</sup> The high valence nature of the Zr metal increases the electrostatic attraction between metal and ligand and results in a highly stable coordination bond.<sup>3</sup> This stability makes Zr MOFs another ideal candidate for application as a functional solid-state sensor.

In the previous chapter, hydrolysis was chosen as the desired technique for CWA hydrolysis. A range of Zr MOFs were screened as potential catalysts and MOF-808 was identified as the most effective zirconium-MOF catalyst. Additionally, it was interesting to learn whether the propensity of a framework towards hydration would affect its effectiveness as a hydrolysis catalyst. It was postulated that understanding the different states of hydration and the interactions between water and the  $Zr_6$  node could provide further insight into the hydrolysis mechanism. A brief study was conducted to look at how hydration would affect the solid state PL properties of these MOFs.

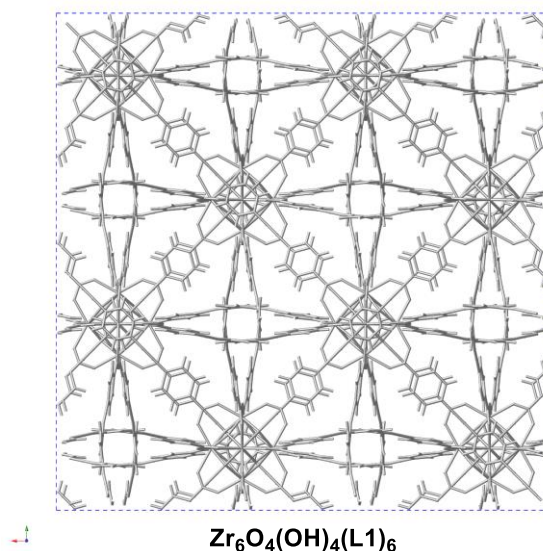
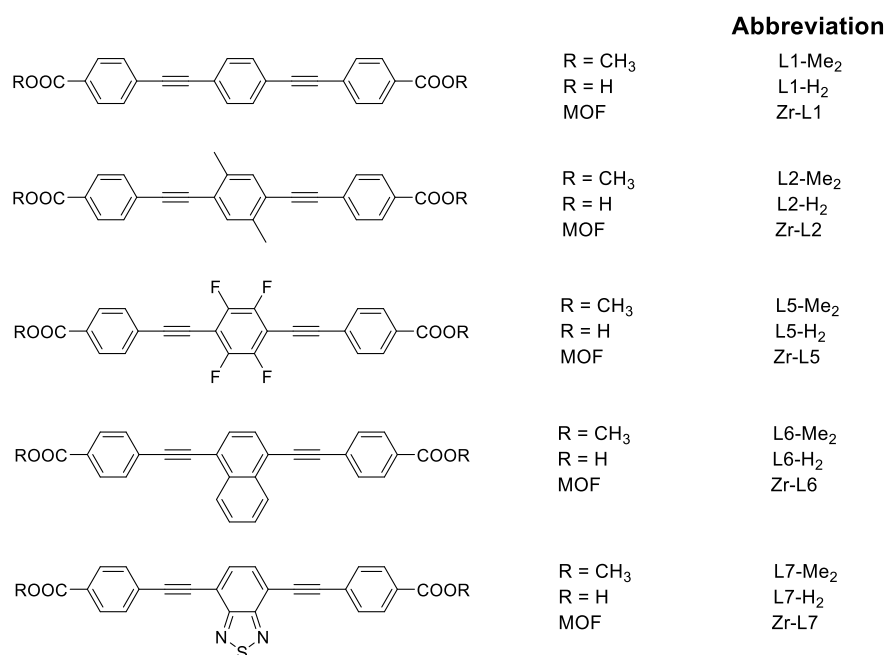
There has been some interest in the photoluminescent properties of AE MOFs upon exposure to water. MJ Manos et al.<sup>15</sup> reported a  $Mg^{2+}$  AE MOF capable of red-shifted emission in the presence of trace quantities of water (0.05 - 5 % v/v) in various organic solvents. A partnership was established in conjunction with the Shimizu group, at the University of Calgary, Canada, who had synthesised two novel, isostructural, phosphonate ligand-based AE MOFs.<sup>40</sup> The frameworks were assembled using a 2,4,6-tris(4-phosphonophenyl)pyridine linker ( $H_6L$ ) and either  $BaBr_2$  or  $SrBr_2$  to yield  $Ba_4(H_2L)_2(H_2O)_x$  (MOF-1 (Ba)) and  $Sr_4(H_2L)_2(H_2O)_x$  (MOF-2 (Sr)). The illustration on the next page shows the unit formulae of the AE MOFs along with a structural representation of the MOF-1 (Ba) unit cell. Subsequently, the hydration-dependent emission

profiles of MOF-1 (Ba) and MOF-2 (Sr) are studied, as is the sensitivity and reversibility of these emission processes.



The strong fluorescence ( $\Phi_F = 91\%$ ) and absorption of 4,4'-[1,4-phenylene-bis(ethyne-2,1-diyl)]-dibenzoate ( $\text{peb}^{2-}$ ) in the UV region has been previously documented.<sup>41</sup> A zirconium MOF composed of the  $\text{peb}^{2-}$  linker,  $\text{Zr}_6\text{O}_4(\text{OH})_4(\text{peb}^{2-})_6$ , has also been noted for the ability to photocatalytically degrade organic dyes in solution.<sup>42</sup> A second collaboration was opened with the Forgan Group at the University of Glasgow, Scotland, who had synthesised a range of novel interpenetrated, 12-connected Zr MOFs. The frameworks were composed of various modified  $\text{peb}^{2-}$  ligands. Due to the inherent fluorescence of the  $\text{peb}^{2-}$  linker, the frameworks were analysed and their potential was gauged for possible applications as solid-state sensors.<sup>43</sup> The illustration on the next page shows the range of MOFs which were synthesised in this study.  $\text{LX-Me}_2$  denotes the dimethyl ester of the corresponding  $\text{peb}^{2-}$  linker,  $\text{LX-H}_2$  refers to the

carboxylic acid and Zr-LX refers to the resulting zirconate framework. The numerous modifications of the  $\text{peb}^{2-}$  ligand with naphthyl, dimethyl, fluoro and benzothiadiazolyl functionalities, did not affect the topology of the frameworks. The PL properties of the Zr MOFs is screened using ssPL in a wide array of environments including water, various solvents and several gasses.



ssPL is shown to be an effective analytical technique for rapidly screening novel materials under a variety of conditions. Additionally, ssPL is shown to act as a useful tool for probing potential functional properties in these solid materials.

## 3.2 Experimental Methods

### Emission Measurements

The fluorescence emission measurements were carried out using an Edinburgh Instruments FS5 Fluorescence Spectrometer. An SC-10 Front Face Sample Holder was used along with a solid-state cuvette. Solid-state quantum yield (QY) and lifetime measurements were also performed with the FS5 instrument, equipped with a standard xenon lamp (150W) and a standard PMT detector (R928P, Hamamatsu). Spectral and lifetime measurements were performed using SC-10 Front Face holder for Powders. QY measurements were performed using SC-30 Integrating Sphere module. An example of a QY measurement for MOF-1 (Ba) is shown below (Figure 3.1).

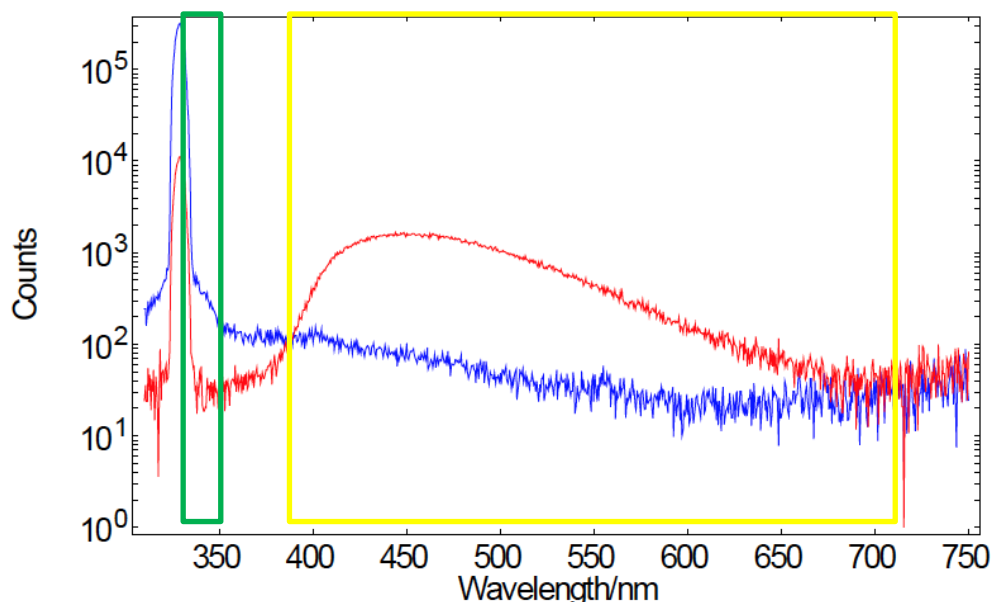


**Figure 3.1.** Example measurement of QY evaluation for the initially dry MOF-1 (Ba). The blue spectrum corresponds to data obtained during a blank measurement. The red spectrum corresponds to the data obtained during a measurement in the presence of MOF-1 (Ba). The green rectangle represents the scatter range and the yellow rectangle shows the emission range.

The humidity exposure experiments were performed using a custom-made humidity chamber. Beakers containing saturated salt solutions were used to vary the humidity in the chamber. The chamber was equilibrated to the appropriate humidity for 24 hours prior to sample

exposure. Samples were exposed to the respective humidity for an additional 24 hours prior to analysis. It should be noted that temperature fluctuations between 22 °C and 24 °C were observed during each 24 hour humidity chamber cycle. All samples were excited at their respective dry excitation wavelength. Unless otherwise stated, dry samples of MOF-1 (Ba), MOF-2 (Sr), Zr-L1, Zr-L2, Zr-L5, Zr-L6 and Zr-L7 were prepared by drying in a vacuum oven at reduced pressure at 80 °C for 1 hour. This procedure was established based upon the conditions which were required to reverse MOF-1 (Ba) and MOF-2 (Sr) from a wet (fluorescent yellow) colour to a dry (light yellow) colour. The 100 % humidity samples were prepared by wetting the samples directly with deionised water. For the wet/dry cycling of MOF-1 (Ba) and MOF-2 (Sr), the dry emission of each MOF was first analysed, this was followed by the liquid wetting of the dry sample and further emission analysis. The wet samples were then dried in a vacuum oven at 80 °C for 24 hours, the consecutive wet/dry cycle was conducted a total of three times. For solid state emission measurements in the presence of solvent analytes, dry MOF powders were directly wetted with the liquid solvent and their emission profiles were immediately recorded using their respective dry excitation wavelength. Solid powders of dimethyl esters of MOF linkers were analysed using the same procedures described above. UiO-67-NH<sub>2</sub>, UiO-67 BiPy, DUT-52, DUT-84, MOF-808 and Boron MOF were all vacuum dried for 24 hours at 80 °C before recording any fluorescence spectra.

### **PXRD Measurements**

PXRD patterns were collected on a silicon zero-background sample holder using a Rigaku Miniflex 600 desktop XRD and a Copper K- $\alpha$  (1.5406 Å) source. Measurements were taken in the 3 – 45 ° 2 $\theta$  range with a step size of 0.02 ° 2 $\theta$  and a scan speed of 1 ° 2 $\theta$  min<sup>-1</sup>.

### **Contact Angle Measurements**

Contact angle measurements were performed using an Attension-Theta optical tensiometer (Biolin Scientific), at room temperature. Using a glass microscope slide with a thin recess,

powdered sample was loaded into the recess and packed flat until level with the slide. Analysis was performed using the One-Attension software package.

#### **PL Measurements under N<sub>2</sub> and CO<sub>2</sub> environments**

N<sub>2</sub> or CO<sub>2</sub> gas was fed into a sealed quartz tube containing the MOF analyte. The gas feed was then removed and the quartz tube was immediately placed in a fluorometer and analysed as usual.

#### **PL Measurements under H<sub>2</sub>S environment**

Hydrogen sulfide measurements were conducted by dropping 4M HCl onto Na<sub>2</sub>S to generate H<sub>2</sub>S gas. This gas was fed into a sealed quartz tube containing the MOF analyte. The gas feed was then removed and the quartz tube was immediately placed in a fluorometer and analysed as usual. The outlet from this system was fed into a closed bubbler containing concentrated bleach solution to neutralize any excess H<sub>2</sub>S, the outlet from the bleach bubbler fed into a saturated solution of CuSO<sub>4</sub>.

#### **Wet/Dry Cycling of MOF-1 (Ba) and MOF-2 (Sr)**

For the wet/dry cycling of MOF-1 (Ba) and MOF-2 (Sr), each MOF powder was wetted directly with liquid water, analysed using ssPL, dried at 80 °C for 1 hour, and then analysed using ssPL and PXRD. This process was repeated twice more to yield ssPL and PXRD data for 3 subsequent cycles.

#### **Synthesis of UiO-67-NH<sub>2</sub>-ML, UiO-67 BiPy-ML, DUT-52, DUT-84, MOF-808 and Boron MOF**

UiO-67-NH<sub>2</sub>-ML, UiO-67 BiPy-ML, DUT-52, DUT-84, MOF-808 and Boron MOF were all synthesised using a solvothermal reaction procedure. The exact method and characterization is shown in the experimental section of chapter 2. The frameworks were all vacuum dried for 24 hours at 80 °C before recording any fluorescence spectra. No further characterization was conducted.

### **Synthesis of 2,3,6-tris(4-phosphonophenyl)pyridine ligand (H<sub>6</sub>L) (Performed by Z. H. Fard)**

2,4,6-tris(4-bromophenyl)pyridine was synthesised and characterised by Zoreh H. Fard at the University of Calgary. The linker was synthesised via phosphorylation of 2,4,6-tris(4-bromophenyl)pyridine via the Michaelis-Arbuzov reaction. The exact procedure, along with <sup>1</sup>H, <sup>13</sup>C, <sup>31</sup>P NMR and mass spectrometry characterization data may be found in reference 40.

### **Synthesis and characterization of MOF-1 (Ba) and MOF-2 (Sr) (Performed by Z. H. Fard)**

MOF-1 (Ba) and MOF-2 (Sr) were both synthesised and characterised by Zoreh H. Fard at the University of Calgary, the exact procedure may be found in reference 40. MOF-1 (Ba) was synthesised via the solvothermal reaction of H<sub>6</sub>L with BaBr<sub>2</sub> in DMF/H<sub>2</sub>O, single crystals were obtained using this methodology. MOF-2 (Sr) was synthesised using a similar procedure via the solvothermal reaction of H<sub>6</sub>L with Sr(OH)<sub>2</sub> in DMF/H<sub>2</sub>O. No single crystals were obtained using this methodology but PXRD patterns of bulk MOF-1 (Ba) and MOF-2 (Sr) matched the simulated PXRD pattern obtained from the single crystal data of MOF-1 (Ba). Both MOFs were additionally characterized using thermal analysis, elemental analysis and gas adsorption analysis, this characterization data can be found in reference 40.

### **Synthesis of L1, L2, L5, L6 and L7 ligands (Performed by R. J. Marshall)**

L1, L2, L5, L6 and L7 were all synthesised and characterized by Ross J Marshall of the Forgan Group at the University of Glasgow using the procedure outlined in reference 43. In brief the ligands were synthesised through the palladium cross-coupling of commercially available aryl bis-halides and methyl 4-ethylbenzoate to form the corresponding dimethyl ester. The dimethyl esters were then saponified to yield the corresponding dicarboxylic acid ligand. The exact procedure, along with <sup>1</sup>H, <sup>13</sup>C, and mass spectrometry characterization data may be found in reference 43.

**Synthesis and characterization of Zr-L1, Zr-L2, Zr-L5, Zr-L6 and Zr-L7 (Performed by R. J. Marshall)**

The iso-structural Zr-L1, Zr-L2, Zr-L5, Zr-L6 and Zr-L7 were all synthesised and characterized by Ross J Marshall of the Forgan Group at the University of Glasgow using a procedure outlined in reference 43. In brief, each MOF was synthesised in DMF using solvothermal reaction conditions, L-proline was used to modulate all bulk syntheses with the exception of Zr-L5 for which benzoic acid was used. The bulk crystalline phase of the material was analysed using PXRD (Figure 3.2). Single crystals were obtained using slightly modified procedures for each corresponding MOF. Each MOF was subsequently characterized using single crystal XRD, good agreement was shown between simulated PXRD data and the PXRD data for the bulk material (Figure 3.3). All of the MOFs were additionally characterized using thermal analysis and gas adsorption analysis, this characterization data can be found in reference 43.

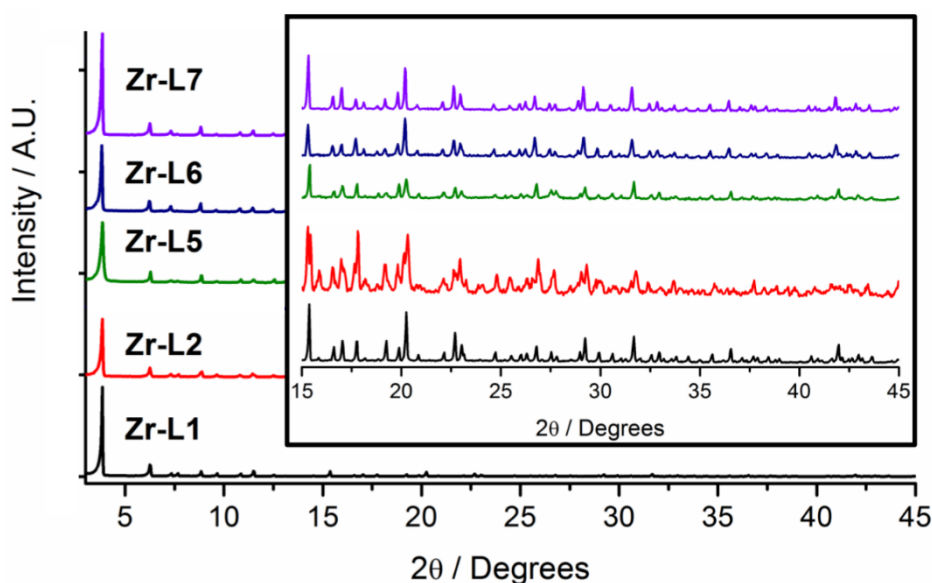


**Figure 3.2.** PXRD comparison of the Zr MOFs synthesised during this study. The inset is an expanded region of the high angle data.

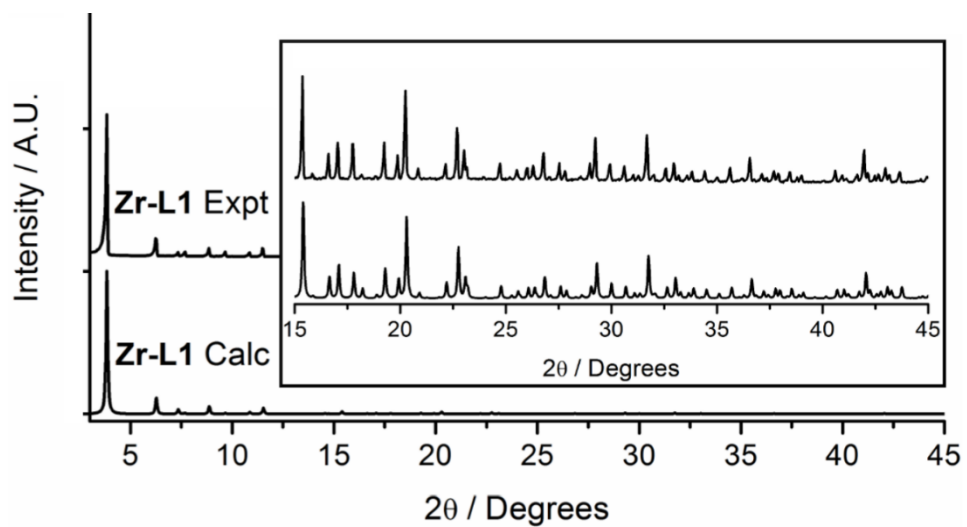


**Figure 3.3.** Comparison of the calculated and experimental PXRD patterns of Zr-L1. The inset is an expanded region of the high angle data.

### 3.3 Solid State Photoluminescence of Zirconium MOF CWA Catalyst Candidates

The hydrolysis of CWAs relies on H<sub>2</sub>O to facilitate the degradation. The previous chapter looked at a number of Zirconium MOFs as potential hydrolysis catalysts for CWA degradation. The availability of uncoordinated Zr<sup>4+</sup> sites is the key to effectively catalysing phosphoester hydrolysis. MOF-808, a 6-connected framework, was found to be the most potent catalyst for hydrolysing both the simulant DMNP and the nerve agent VX. MOFs are generally composed of linkers which possess some degree of conjugation thus bestowing upon them a photoluminescent profile. The water absorption properties of zirconium MOFs<sup>13</sup> has been previously noted and there have also been several reports of hydration dependant fluorescence in MOFs.<sup>15,25,44</sup> It was therefore of interest to see if the propensity of a zirconium MOF to become hydrated could be monitored using ssPL spectroscopy, and if such a change could be correlated to the frameworks effectiveness as a hydrolysis catalyst.

UiO-67-NH<sub>2</sub>-ML, UiO-67 BiPy-ML, DUT-52, DUT-84, MOF-808 and Boron MOF were all synthesised using a solvothermal reaction procedure described in the experimental section of chapter 2. These frameworks were then all vacuum dried for 24 hours at 80 °C. ssPL emission spectra were then recorded for each dry MOF. The normalised ssPL emission spectra are shown in Figure 3.4. The frameworks all showed a  $\lambda_{\text{max}}$  emission profile in the purple-blue region. Upon wetting with liquid water, the emission spectrum of each framework was recorded using their corresponding dry  $\lambda_{\text{ex}}$  wavelength. No measureable change was observed in the emission  $\lambda_{\text{max}}$  upon wetting. It can therefore be assumed that hydration of the Zr<sub>6</sub> cluster produces no effect sufficient enough to perturb the relaxation pathway of the frameworks. MOF-808, DUT-52, and DUT-84 are all assembled from rigid organic linkers and so there is no possible ligand rotation which can arise from the presence of H<sub>2</sub>O in the framework pores. However, the large borane linker composing Boron MOF possesses some rotational freedom, the distance between the alternating linkers is however too great for any  $\pi$ -stacking interactions to occur. Any ligand rotation in Boron MOF is therefore insufficient enough to

offer any alternative relaxation pathways. UiO-67-NH<sub>2</sub>-ML possesses an amine functionality and UiO-67 BiPy-ML contains imine groups, both can form hydrogen-bonding interactions with water, it is therefore surprising that no measurable change in emission  $\lambda_{\text{max}}$  is observed upon wetting.

No measurable hydration-dependant fluorescence response was detected for the zirconium MOFs which were tested. The final part of this chapter explores an alternative series of Alkaline Earth MOFs and interpenetrated zirconium MOFs composed of flexible ditopic linkers.

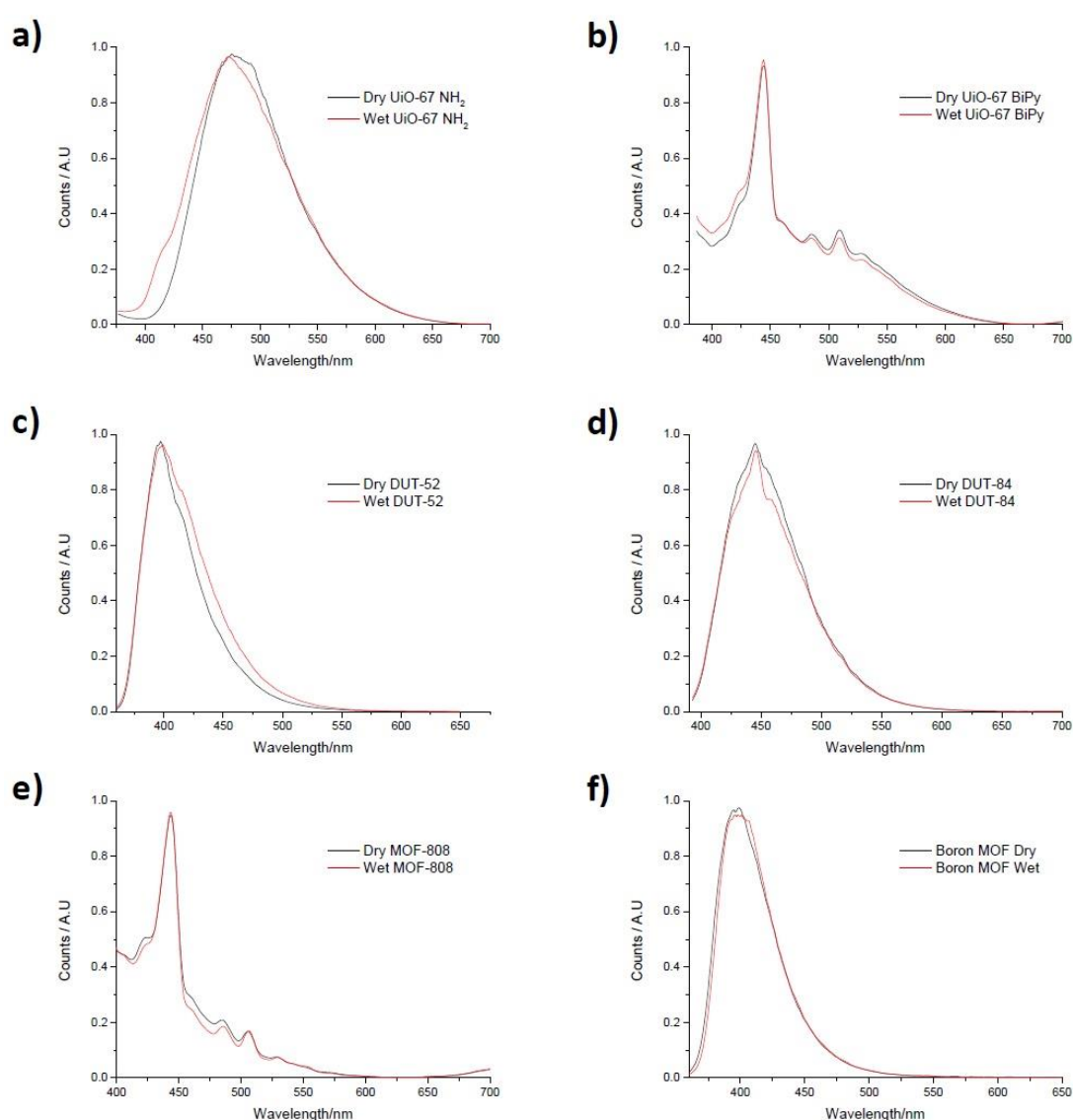


**Figure 3.4.** Normalised solid-state fluorescence emission spectra of a) UiO-67 NH<sub>2</sub>-ML ( $\lambda_{\text{ex}} = 361$  nm), b) UiO-67 BiPy-ML ( $\lambda_{\text{ex}} = 372$  nm), c) DUT-52 ( $\lambda_{\text{ex}} = 345$  nm), d) DUT-84 ( $\lambda_{\text{ex}} = 378$  nm), e) MOF-808 ( $\lambda_{\text{ex}} = 370$  nm) and f) Boron MOF ( $\lambda_{\text{ex}} = 345$  nm) under wet and dry conditions.

### 3.4 Solid-State Photoluminescence in Alkaline Earth MOFs

Two novel AE MOFs were synthesised by Zoreh H. Ford of the George K. H. Shimizu Group at the University of Calgary. Both MOFs were synthesised from 2,4,6-tris(4-phosphonophenyl)pyridine ligand ( $H_6L$ ) and either  $BaBr_2$  or  $Sr(OH)_2$  via solvothermal reaction. MOF-1 (Ba) contained Barium, MOF-2 (Sr) contained Strontium. Despite containing two different AE metal centres, both frameworks were iso-structural and can be described by the general formula  $M_4(H_2L)_2(H_2O)_x$  where  $M = Ba^{2+}$  or  $Sr^{2+}$ . Upon synthesis of these materials, it was noted that they possessed obvious emissive properties. There has been some interest in the photoluminescent properties of AE MOFs upon exposure to water. MJ Manos et al.<sup>15</sup> reported a  $Mg^{2+}$  AE MOF capable of red-shifted emission in the presence of trace quantities of water (0.05-5 % v/v) in various organic solvents. At the time of writing, only a single report existed of a MOF which demonstrates a gradual emissive shift upon exposure to increasing degrees of relative humidity.<sup>12</sup> Towards the end of this chapter, another example of such an effect is presented. Drawing upon the interesting AE MOF photoluminescent properties described in previous studies, MOF-1 (Ba) and MOF-2 (Sr) were thoroughly probed over a series of studies.

#### 3.4.1 Hydration

The study was initiated by examining the solid-state emission of MOF-1 (Ba), MOF-2 (Sr) and  $H_6L$  under dry conditions. Figure 3.5 shows the respective overlapped excitation and emission spectra of MOF-1 (Ba), MOF-2 (Sr) and  $H_6L$ . The dry linker exhibited a fluorescent emission centred on  $\lambda_{em} = 421$  nm ( $\lambda_{ex} = 371$  nm). The emission of the  $H_6L$  ligand falls within the typical range observed for  $\pi \rightarrow \pi^*$  ( $\lambda = 200 - 400$  nm) and  $n \rightarrow \pi^*$  ( $\lambda = 400 - 700$  nm) transitions and so it is highly likely that the emission is derived from these electronic transitions. Dry, as synthesised MOF-1 (Ba) ( $\lambda_{ex} = 330$  nm,  $\lambda_{em} = 446$  nm) and MOF-2 (Sr) ( $\lambda_{ex} = 330$  nm,  $\lambda_{em} = 500$  nm) both exhibited a red shifted emission when compared to the  $H_6L$  linker (Figure 3.5), along with a slightly increased quantum yield ( $\Phi_f$ ) (Table 3.1). The red-shifted emission of the AE

MOFs in relation to the dry H<sub>6</sub>L can be attributed to the electron withdrawing effects of the AE metals upon the linker. The greater red-shift of MOF-2 over that of MOF-1 can be attributed to the higher charge density of the Sr<sup>2+</sup> ion.<sup>15</sup> For  $\pi$ -stacking to occur, the distance between the conjugated systems layers must be no larger than 4.2 Å. The distance between the H<sub>6</sub>L is greater than this physical limit and this therefore rules out inter-ligand charge transfer. For metal-ligand charge (MLCT) transfer to occur, transient oxidation of the AE metal would have to occur due to the partial transfer of electrons from metal to ligand. In MOF-1 and MOF-2, the respective Ba and Sr are already in the maximum oxidation state of +2, this precludes MLCT as no further oxidation is possible. Reduction of an AE metal from the +2 to +1 oxidation is also not feasible due to their extremely negative reduction potential; this excludes ligand-metal charge transfer (LMCT) as an electronic transition.<sup>45</sup> It can therefore be assumed that the red-shifted emission of both MOF-1 and MOF-2 can be attributed to metal perturbed intra-ligand charge transfer. This is confirmed through a number of conditional assessments that were performed throughout the study.

**Table 3.1.** Solid-state QY measurements of both MOF-1 (Ba) and MOF-2 (Sr) in representative states of hydration ( $\lambda_{\text{ex}} = 330$  nm). Reported values are based on triple independent measurements with all values showing less than 0.7% variance ( $\sigma^2$ ).

	MOF-1 (Ba)			MOF-2 (Sr)			Ligand
	Dry	Wet	Redried	Dry	Wet	Redried	
Mean QY %	9.9	16.1	7.1	8.7	14.3	6.4	7.2

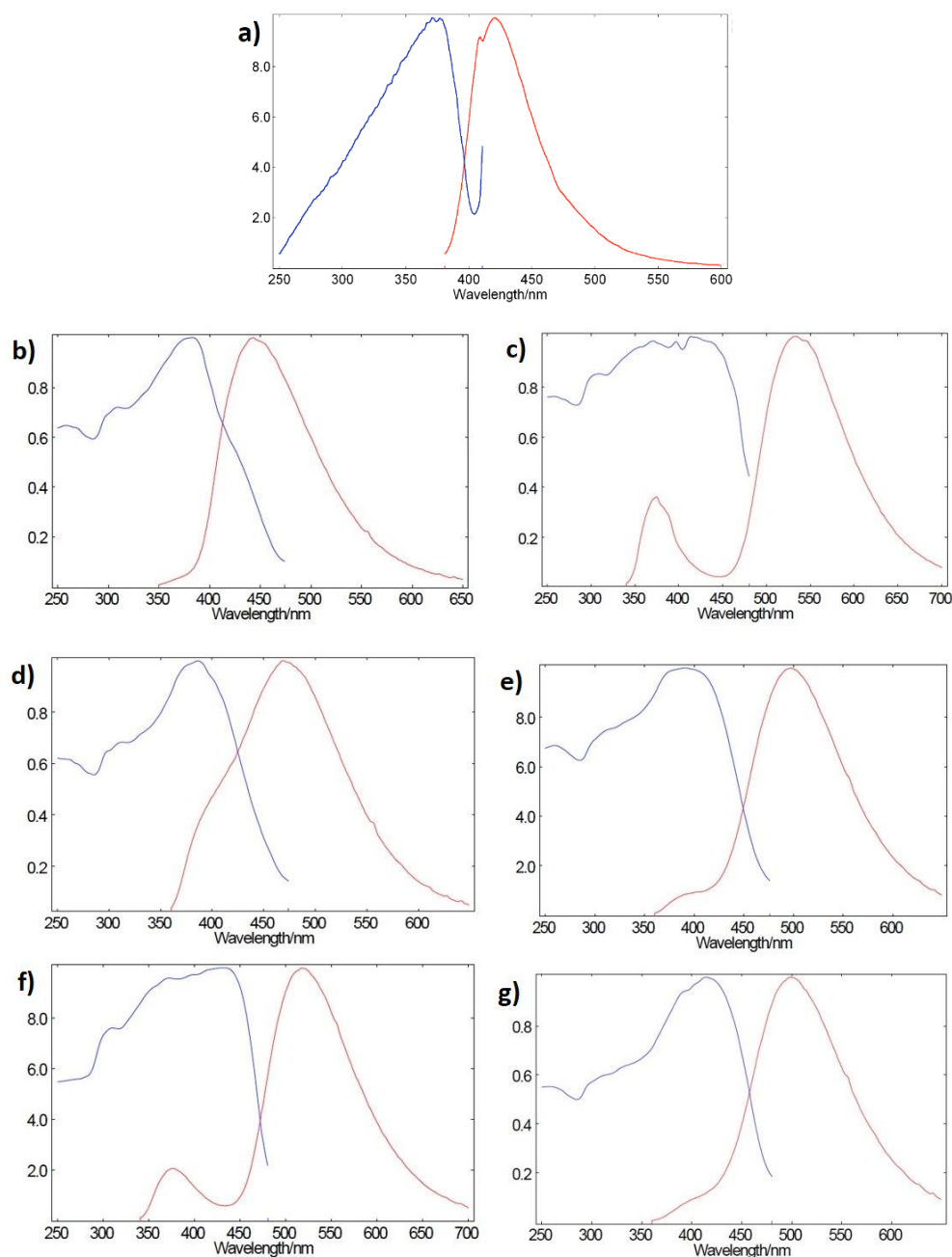


**Figure 3.5.** Normalized excitation (blue) and emission (red) spectra of a) powdered *dry* H<sub>6</sub>L ( $\lambda_{\text{ex}} = 371$  nm,  $\lambda_{\text{em}} = 421$  nm), b) powdered *dry* (prior to treatment with H<sub>2</sub>O) MOF-1 (Ba) ( $\lambda_{\text{ex}} = 330$  nm,  $\lambda_{\text{em}} = 446$  nm), c) powdered *wet* (with H<sub>2</sub>O) MOF-1 (Ba) ( $\lambda_{\text{ex}} = 330$  nm,  $\lambda_{\text{em}} = 500$  nm), d) powdered *re-dried* MOF-1 (Ba) ( $\lambda_{\text{ex}} = 330$  nm,  $\lambda_{\text{em}} = 500$  nm), e) powdered *dry* (prior to treatment with H<sub>2</sub>O) MOF-2 (Sr) ( $\lambda_{\text{ex}} = 330$  nm,  $\lambda_{\text{em}} = 500$  nm), f) powdered *wet* (with H<sub>2</sub>O) MOF-2 (Sr) ( $\lambda_{\text{ex}} = 330$  nm,  $\lambda_{\text{em}} = 500$  nm), g) powdered *re-dried* (H<sub>2</sub>O removed in vacuum oven) MOF-2 (Sr) ( $\lambda_{\text{ex}} = 330$  nm,  $\lambda_{\text{em}} = 500$  nm).

Upon wetting with liquid water, both MOFs exhibited a visible colour change from pale-yellow to bright-yellow. The solid state emissive properties of these materials were then investigated in their ‘hydrated’ states. Figure 3.6 shows the difference in emission between dry and

hydrated MOF-1 and MOF-2. Both materials exhibited sharp excitation peaks at 408 nm during excitation measurements. To allow for a more direct comparison between samples under various conditions, a mutual excitation wavelength ( $\lambda_{\text{ex}} = 408 \text{ nm}$ ) was chosen. Upon direct wetting with liquid water, both frameworks experience a red-shift in emission into the green region with a  $\lambda_{\text{max}}$  of 522 nm and 504 nm for MOF-1 and MOF-2 respectively. The change in  $\lambda_{\text{max}}$  upon hydration is significantly more drastic in MOF-1 in comparison to MOF-2. It should also be noted that the quantum yields were recorded for the dry and hydrated materials (Table 3.1) both materials exhibited a significant increase in quantum yield upon hydration, thus reinforcing their utility as sensors for the detection of water. Interestingly enough, it was also noted that upon drying both hydrated MOFs at 80 °C under reduced pressure, they exhibited a near full reversion in emission to that of the dry state.

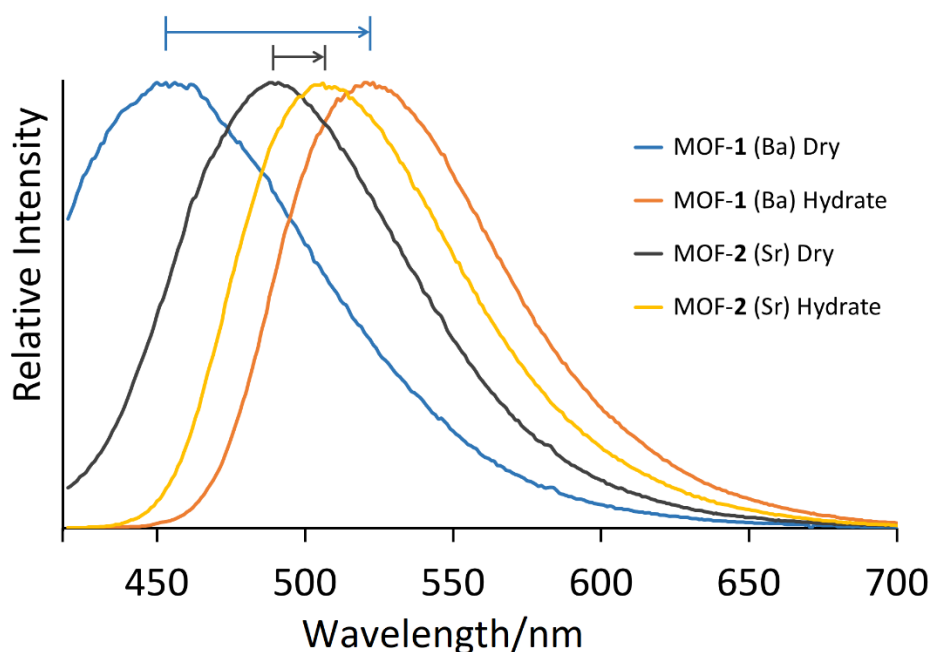


**Figure 3.6.** Normalized solid state emission spectra ( $\lambda_{\text{ex}} = 408 \text{ nm}$ ) of dry MOF-1 (Sr) and MOF-2 (Sr) along with their hydrated counterparts after exposure to liquid water.

### 3.4.2 Detection Limit – A Humidity Study

To further demonstrate the utility of the AE MOFs as functional hydration sensors, the sensitivity of their response was investigated. First, a variety of gasses were trialed to see if they would elicit a change in emission. The materials were subjected to environments of CO<sub>2</sub>, N<sub>2</sub> and H<sub>2</sub>S but no change in  $\lambda_{\text{max}}$  was observed. Both MOFs were also subjected to a polar protic solvent and a polar aprotic solvent in the form of MeOH and DMSO. Again, no change in  $\lambda_{\text{max}}$  was observed. The hydration detection limit was then measured for each framework. With the help of a range of saturated salt solutions, the MOFs were subjected to varying degrees of relative humidity (% RH). The RH values were chosen based upon the availability of the salts which could be used to achieve them. A temperature variation from 22 °C to 24 °C was observed throughout the study. Before a measurement was taken, each MOF was subjected to the chosen humidity for 24 hours. A remarkable observation was made in the case of MOF-2; the incremental increases in RH (from 29 % RH onwards) exhibited a gradual red shift in the emission  $\lambda_{\text{max}}$  (Figure 3.7). At the time that the study was performed, there existed only one other example of a MOF which exhibited a spectral change upon exposure to increasing degrees of RH.<sup>12</sup>

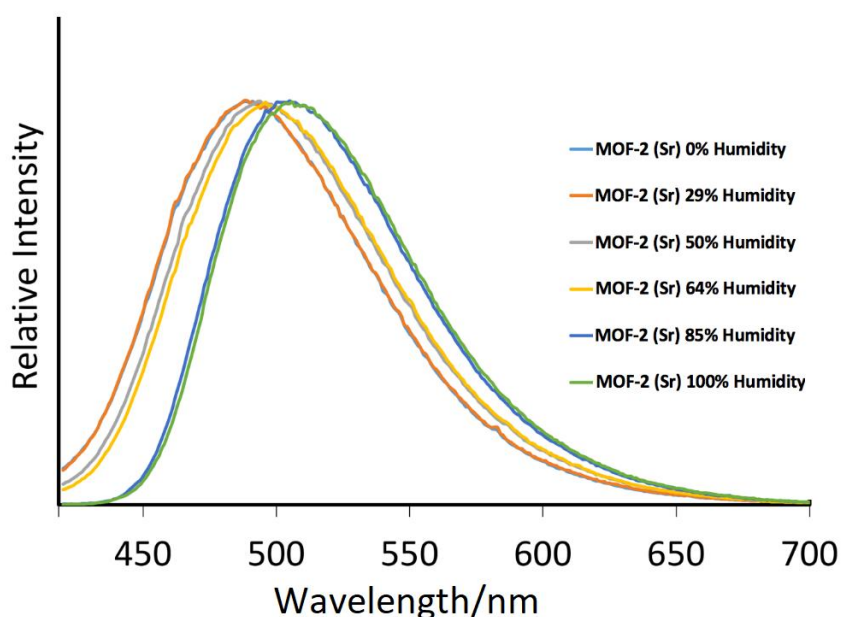


**Figure 3.7.** Normalized emission of powdered MOF-2 (Sr) exposed to different degrees of humidity showing a gradual red shift in  $\lambda_{\text{max}}$  with increasing humidity ( $\lambda_{\text{ex}} = 408 \text{ nm}$ ).

For the case of MOF-1, no change in emission  $\lambda_{\max}$  was observed upon increasing the RH. A small change was observed at 85 % RH. However, upon reaching 100 % RH, a drastic red-shift in emission is observed (Figure 3.8). Given more time, it would be interesting to investigate just how sensitive the hydration-dependant emissive response is between 85 – 100 % RH. Consequently, two materials have been investigated which both function as water sensors but which differ drastically in the emissive response that they elicit. MOF-1 acts as a binary sensor with a high detection (85 % RH) threshold whereas MOF-2 possesses a lower detection limit (29 % RH) and provokes an analogue response to varying degrees of hydration stimuli.

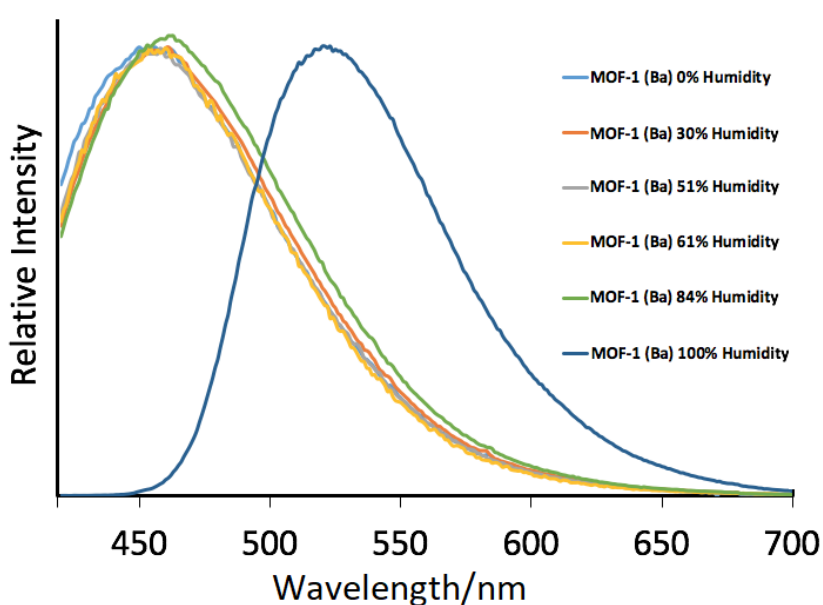
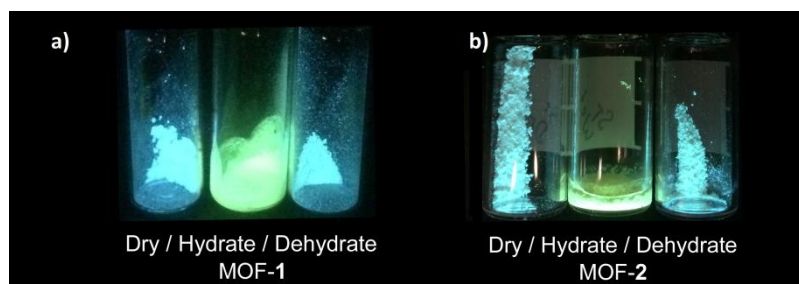


**Figure 3.8.** Normalized emission of powdered MOF-1 (Ba) exposed to different degrees of humidity showing a sharp red shift in  $\lambda_{\max}$  during complete hydration ( $\lambda_{\text{ex}} = 408 \text{ nm}$ ).

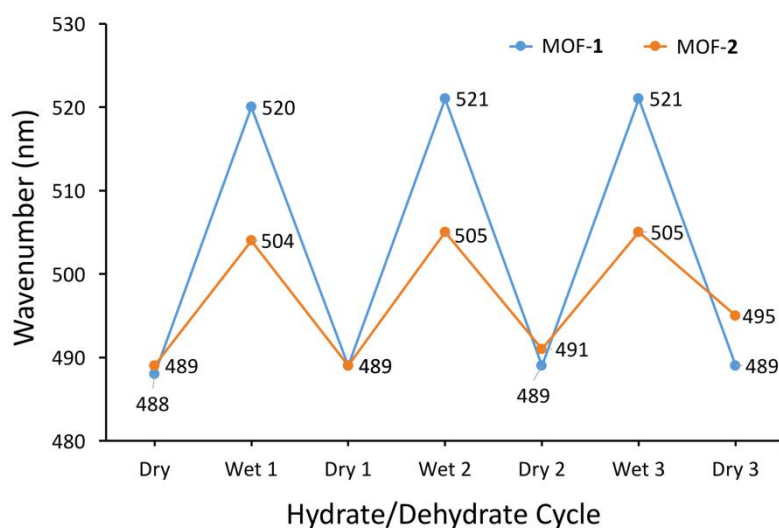
### 3.4.2 Reversibility of Hydration

Figure 3.9 shows a visual representation of both MOF-1 and MOF-2 upon liquid wetting and dehydration, a change in colour is observed for both frameworks which can clearly be distinguished by eye. Three wet/dry cycles were performed to investigate the reversibility of the emission along with the reusability of the material. The  $\lambda_{\max}$  was noted during each wet and dry state and can be seen in Figure 3.10. There appeared to be little change in the emission  $\lambda_{\max}$  for MOF-1 with a slight change in the  $\lambda_{\max}$  in MOF-2 after the 3<sup>rd</sup> drying cycle. Three cycles

were deemed sufficient to demonstrate the reversibility of the hydration-dependent emission process.



**Figure 3.9.** a) The colour change of MOF-1 in response to hydration. b) The colour change of MOF-2 in response to hydration.



**Figure 3.10.** A graph demonstrating the reversible emission response upon hydration and dehydration of MOF-1 and MOF-2.

It should be noted that during the cycling studies, the  $\lambda_{\max \text{ dry}}$  of MOF-1 (Ba) does not match the earlier  $\lambda_{\max \text{ dry}}$  of MOF-1 (Ba) when wet/dry (Section 3.4.1) and humidity studies (Section 3.4.2) were performed. The cycling studies were performed more than 6 months after the wet/dry and humidity studies described earlier in this chapter. It is therefore possible that some structural change may have occurred over this time period. Unfortunately, this discrepancy was not noted at the time and was not investigated further. The long-term storage stability of both materials requires further examination.

During each wet/dry cycle of MOF-1 and MOF-2, PXRD analysis was performed to more closely examine any changes in crystallinity upon wetting and drying of the materials. With each cycle, both MOF-1 and MOF-2 showed a gradual shift towards amorphization (Figure 3.11), evident by the increased broadening present on the diffractograms after each subsequent cycle. If a simultaneous inference is to be made from the PXRD and emission data after each cycle, it can be assumed that long range order has little impact on the emissive properties of both materials as there is little change in the  $\lambda_{\max}$  despite a loss in crystallinity. It is however interesting that these frameworks degrade after exposure to H<sub>2</sub>O despite the fact that they're synthesised in a mixture of H<sub>2</sub>O/DMF. This is likely the result of the malleability of the AE metal coordination spheres.<sup>29-31</sup> After a wetting cycle, the fast dehydration of these frameworks at a temperature of 80 °C and reduced pressure leads to the rapid desolvation of the AE coordination sphere. This subsequently leads to the formation of a less ordered dehydrated phase. An additional tentative explanation is that upon hydration, the increased pliability of the AE coordination arc allows the H<sub>6</sub>L linker to engage in disordered  $\pi$ -stacking interactions. This would explain the prominent colour change of both materials along with the red-shift in the emission  $\lambda_{\max}$  upon hydration. This is also supported by the greater difference between the  $\lambda_{\max \text{ wet}}$  and  $\lambda_{\max \text{ dry}}$  in MOF-1; the larger coordination sphere of Ba<sup>2+</sup> results in a more flexible ligand configuration which is able to form stronger and more proximal  $\pi$ -stacking interactions. For completion, it was also noted that the solid-state emission of H<sub>6</sub>L was unaffected by wetting with liquid water. The sensing response of these materials is therefore facilitated by the hydration of the AE coordination sphere and due to the loss of crystallinity, relies solely on the short range structure of the frameworks. This is a notable example in MOF research which often places significant emphasis on the retention of structural order when evaluating the value of a functional property.

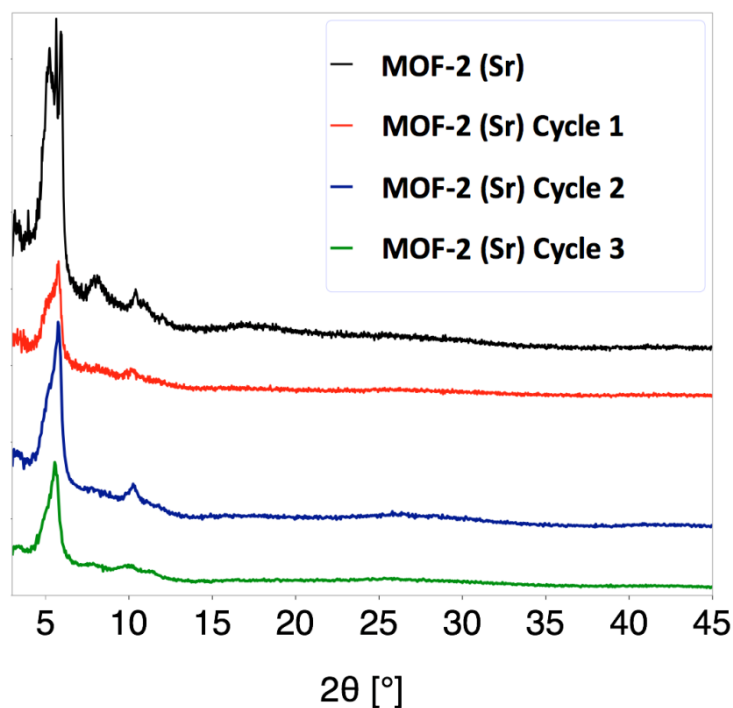
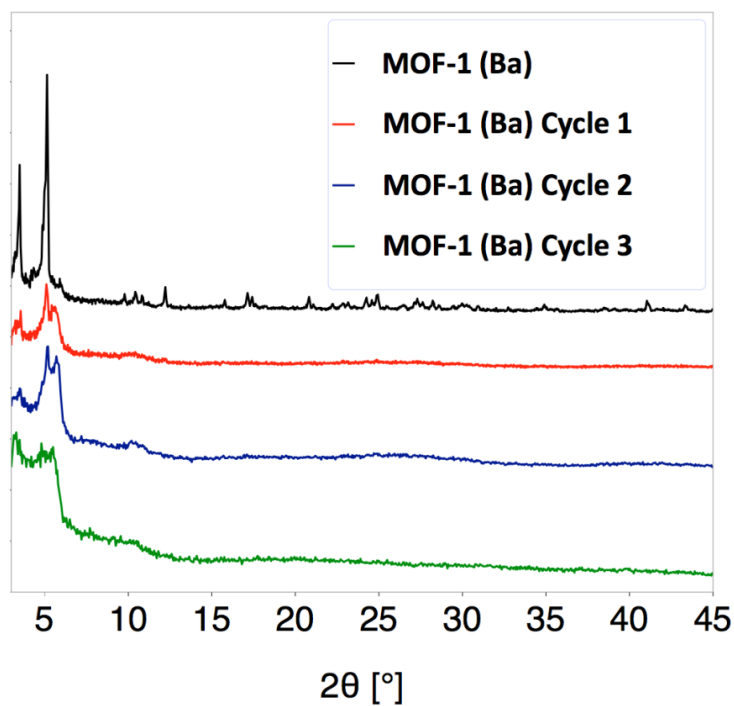


**Figure 3.11.** PXRD pattern overlay of MOF-1 (Ba) and MOF-2 (Sr) after subsequent Wet/Dry cycles showing a decrease in crystallinity after each hydration. The broadening/loss of intensities of the lower angle ( $3 - 15^\circ 2\theta$ ) diffraction peaks indicates a deterioration of long range order. The black diffractograms represent the as-synthesised materials.

In summary, two new AE MOFs have been synthesised and their functional properties were characterized. Their interesting hydration-dependent emissive properties were noted and probed further with solid-state fluorescence. Based on the MOFs different emissive response to varying degrees of hydration, the difference in their utility as potential water sensors was highlighted. Finally, the origin of the emission was de-convoluted further by examining the decline in crystallinity upon exposure to subsequent wet/dry cycles despite the hydration-dependent fluorescence being reversible. Due to discrepancies in later emission measurements, the long term storage stability of these materials need to be further investigated.

### 3.5 Solid State Photoluminescence in a series of Iso-Structural Zirconium MOFs

When designing MOF sensors, the vast array of building blocks and synthetic strategies present a seemingly endless amount of possibilities for assembling chemically versatile structures. Stability can often be a compromising factor when designing new frameworks; there are numerous reports of MOFs with poor ambient and aqueous stability.<sup>26–28</sup> Fortunately, Zirconium MOFs have received significant coverage due in part to their robustness.<sup>10,13,39</sup> The high valence nature of the Zr metal increases the electrostatic attraction between metal and ligand and results in a highly stable coordination bond.<sup>3</sup> This stability makes Zr MOFs ideal candidates for application as functional solid-state sensors.

In this next section, a range of iso-structural Zr MOFs are investigated and ssPL is shown to be a very simple yet powerful tool for examining their functional properties. A series of studies were conducted on a novel series of Zr MOFs which were synthesised and characterized by Ross J. Marshall of the Forgan Group at the University of Glasgow. The aforementioned Zr MOFs are composed of the chromophoric  $\text{peb}^{2-}$  linker<sup>41</sup> with various substitutions present on the central aromatic ring. Due to the length and dimensionality of the linker, all the resulting frameworks were 12-connected and interpenetrated. Based on a previously reported procedure, single crystals of each framework were obtained by modulating the MOF syntheses with L-proline.<sup>11</sup>

#### 3.5.1 Hydration

The excitation pathway of Zr MOFs composed of conjugated linkers has been studied and has been shown to best follow a Ligand-Cluster Charge-Transfer (LCCT) transition mechanism with photo-absorption occurring on the linker followed by charge transfer onto the  $\text{Zr}_6$  cluster.<sup>46</sup> The optical properties of Zr-L1 were previously reported by Kordova et al.<sup>42</sup> The high aqueous stability of the MOF, coupled with the strong light absorption in the visible region, led to an enhanced application of Zr-L1 as a photo-catalyst for the photodegradation of waste organic dyes in aqueous medium. Studies have also been performed to determine the origin of the

emissive properties of the L1-H<sub>2</sub> ligand which are derived from the high degree of  $\pi$ -conjugation present in the ligand. This conclusion is based on DFT calculations which have confirmed that increasing the number of aromatic and alkyne units in a chromophore would naturally enrich the photo-absorption properties by enhancing the degree of conjugation.<sup>42</sup> It was postulated that the introduction of various functionalities to the central aromatic unit of the peb backbone could result in some slightly altered photo-properties.

Earlier in this chapter, the hydration-dependent emission profiles of some AE MOFs were studied, it was therefore of interest to see how the emissive profiles of each Zr-LX MOF differed upon wetting with liquid water. To have a better insight into the origin of these photoluminescent properties, the study of the peb Zr MOFs was initiated by examining the wet and dry solid-state emissive properties of the LX-Me<sub>2</sub> molecules and Zr-LX MOFs. A direct comparison was made between the wet and dry ssPL properties of each Zr-MOF and the corresponding dimethyl-ester (Figure 3.12). L1-Me<sub>2</sub> ( $\lambda_{\text{ex}} = 367$  nm) exhibited an emission  $\lambda_{\text{max}}$  of 450 nm, in contrast to Zr-L1 ( $\lambda_{\text{ex}} = 367$  nm) which exhibited a similar emission profile with a blue shifted  $\lambda_{\text{max}}$  of 407 nm. Similar emission profiles were also observed for L2, L6 and L7 methyl esters and the corresponding MOFs. The MOFs all exhibited a blue shifted  $\lambda_{\text{max}}$  when compared to their LX-Me<sub>2</sub> counterparts. This is to be expected as the incorporation of the ligands into a framework acts to separate them and removes their ability to form  $\pi$ -stacking interactions and eliminates inter-ligand charge transfer in favour of the LCCT transition. The only exception was L5, a tetra-fluorinated analogue of -L1. This could be tentatively explained by the opposing quadrupole moment of a C-F substituted ring compared to a C-H, which would form arene-perfluoroarene  $\pi$ -stacking interactions in the solid-state of the methyl ester linker.<sup>47</sup> However, there were no changes in the solid state emission  $\lambda_{\text{max dry}}$  and  $\lambda_{\text{max wet}}$  of the LX-Me<sub>2</sub> linkers, which is unsurprising as the ligands are insoluble in water. This is in contrast to the Zr-LX MOFs (with the exception of Zr-L5) which all exhibited a hydration-dependent emission, this implied that the substituents involved in the LCCT transition were sensitive towards hydration.

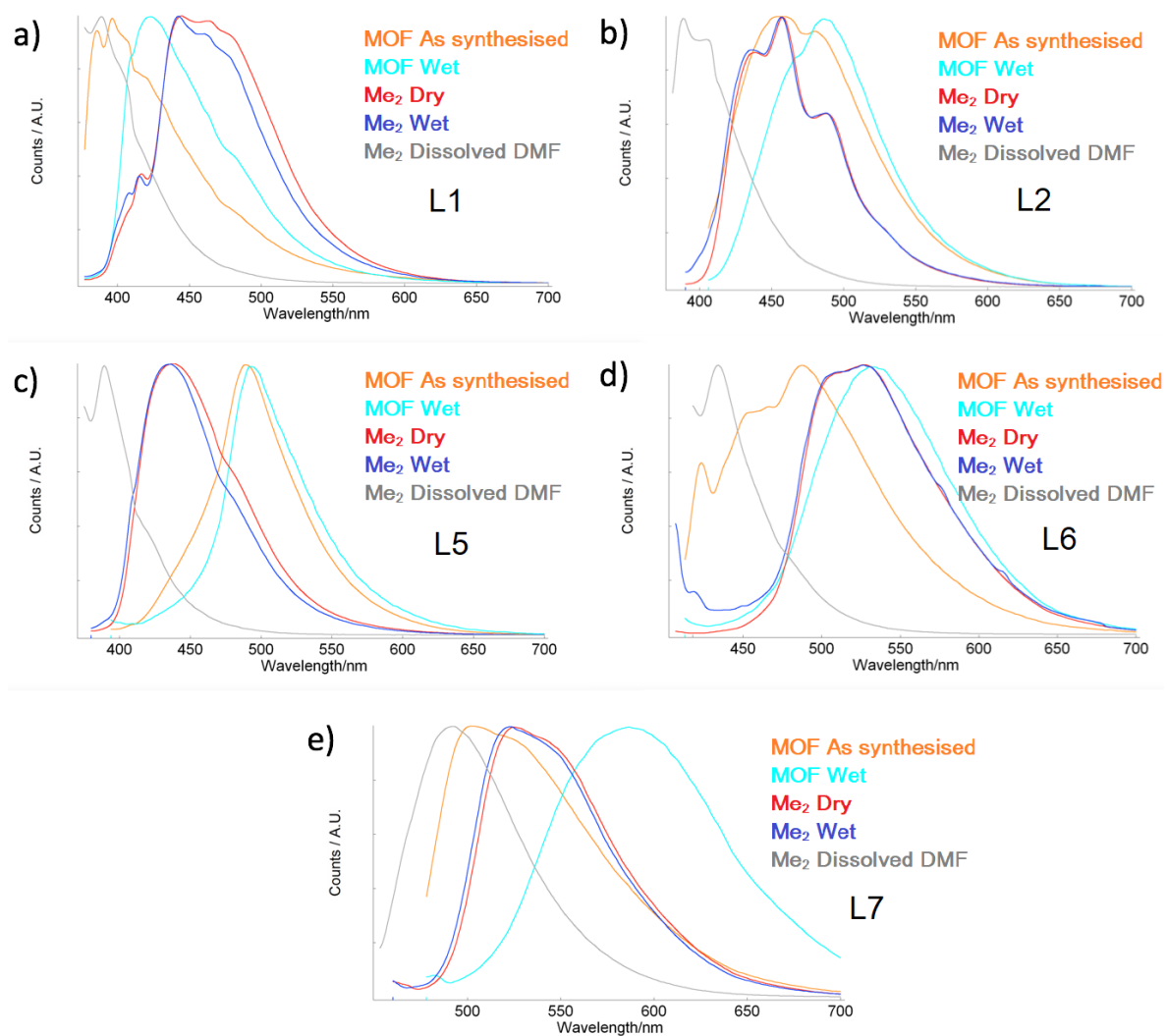


**Figure 3.12.** Normalised solid-state and solution state fluorescence emission spectra of:

a) Zr-L1 Solid State As synthesised and Wet ( $\lambda_{\text{ex}} = 367$  nm), L1-Me<sub>2</sub> Solid State Dry and Wet ( $\lambda_{\text{ex}} = 367$  nm), L1-Me<sub>2</sub> dissolved in DMF ( $10^{-5}$  M;  $\lambda_{\text{ex}} = 367$  nm); b) Zr-L2 Solid State As synthesised and Wet ( $\lambda_{\text{ex}} = 396$  nm), L2-Me<sub>2</sub> Solid State Dry and Wet ( $\lambda_{\text{ex}} = 380$  nm), L2-Me<sub>2</sub> dissolved in DMF ( $10^{-5}$  M;  $\lambda_{\text{ex}} = 376$  nm); c) Zr-L5 Solid State As synthesised and Wet ( $\lambda_{\text{ex}} = 384$  nm), L5-Me<sub>2</sub> Solid State Dry and Wet ( $\lambda_{\text{ex}} = 370$  nm), L5-Me<sub>2</sub> dissolved in DMF ( $10^{-5}$  M;  $\lambda_{\text{ex}} = 365$  nm); d) Zr-L6 Solid State As synthesised and Wet ( $\lambda_{\text{ex}} = 403$  nm), L6-Me<sub>2</sub> Solid State Dry and Wet ( $\lambda_{\text{ex}} = 397$  nm), L6-Me<sub>2</sub> dissolved in DMF ( $10^{-5}$  M;  $\lambda_{\text{ex}} = 408$  nm); e) Zr-L7 Solid State As synthesised and Wet ( $\lambda_{\text{ex}} = 468$  nm), L7-Me<sub>2</sub> Solid State Dry and Wet ( $\lambda_{\text{ex}} = 450$  nm), L7-Me<sub>2</sub> dissolved in DMF ( $10^{-5}$  M;  $\lambda_{\text{ex}} = 443$  nm)

For Zr-L1, a small red-shift in  $\lambda_{\max}$  from 407 nm to 423 nm was observed upon wetting with liquid water. Also, a drop in quantum yield was observed from 17.3 down to 12.3 %  $\Phi_F$  (Table 3.2).

**Table 3.2.** Values of solid-state fluorescence quantum efficiencies collected for wet and dry samples of the listed MOFs.

MOF	Dry			Wet		
	$\lambda_{\text{ex}}$ (nm)	$\lambda_{\text{max}}$ (nm)	$\Phi_F$ (%)	$\lambda_{\text{ex}}$ (nm)	$\lambda_{\text{max}}$ (nm)	$\Phi_F$ (%)
Zr-L1	367	409	17.3	367	421	12.3
Zr-L2	396	482	16.4	396	486	21.2
Zr-L5	384	491	9.1	384	492	9.0
Zr-L6	403	501	1.9	403	534	1.7
Zr-L7	468	500	1.6	468	586	1.7

As there is no change in emission upon wetting of the L1-Me<sub>2</sub> linker, the red-shift in emission of Zr-L1 is likely derived from the hydration of the Zr<sub>6</sub> cluster. This is further supported by a previous report of water forming hydrogen-bonding interactions with the –OH moieties of the Zr<sub>6</sub>O<sub>4</sub>(OH)<sub>4</sub><sup>12-</sup> cluster in UiO-67 type MOFs.<sup>48</sup> A similar trend of red-shifted emission  $\lambda_{\max}$  was observed for Zr-L2, Zr-L6 and Zr-L7 upon liquid wetting. Zr-L6 ( $\lambda_{\text{ex}} = 403$  nm) displayed a red-shifted emission from a  $\lambda_{\max \text{ dry}}$  of 501 nm to a  $\lambda_{\max \text{ wet}}$  534 nm. Zr-L7 ( $\lambda_{\text{ex}} = 468$  nm) exhibited an ever greater red-shift of 86 nm from a  $\lambda_{\max \text{ dry}}$  of 500 nm to a  $\lambda_{\max \text{ wet}}$  586 nm. It is believed that the hydration of the nodes, particularly for the highly conjugated Zr-L6 and Zr-L7, raises the HOMO levels for the LCCT transition. This change in band gap results in a red-shifted emission upon hydration. Figure 3.13 shows a visual representation of the more drastic colour change observed for Zr-L6 and Zr-L7 upon wetting. The decrease in the visual brightness of Zr-L1 should also be noted as this correlates with a drop in quantum yield (Table 3.2) upon wetting of the material. Both Zr-L6 and Zr-L7 possess a more conjugated linker backbone, the additional conjugation combined with the LCCT transitions produces a larger red-shift upon hydration of the Zr<sub>6</sub> node. The greater hydration dependant bathochromic shift of Zr-L7 over that of Zr-L6 can potentially be attributed to additional cooperative hydrogen bonding occurring on the L7 linker in the presence of water. This is further supported in section 3.5.2 when a red-shifted emission is observed in Zr-L7, but not Zr-L6, upon exposure to a polar-protic solvent.

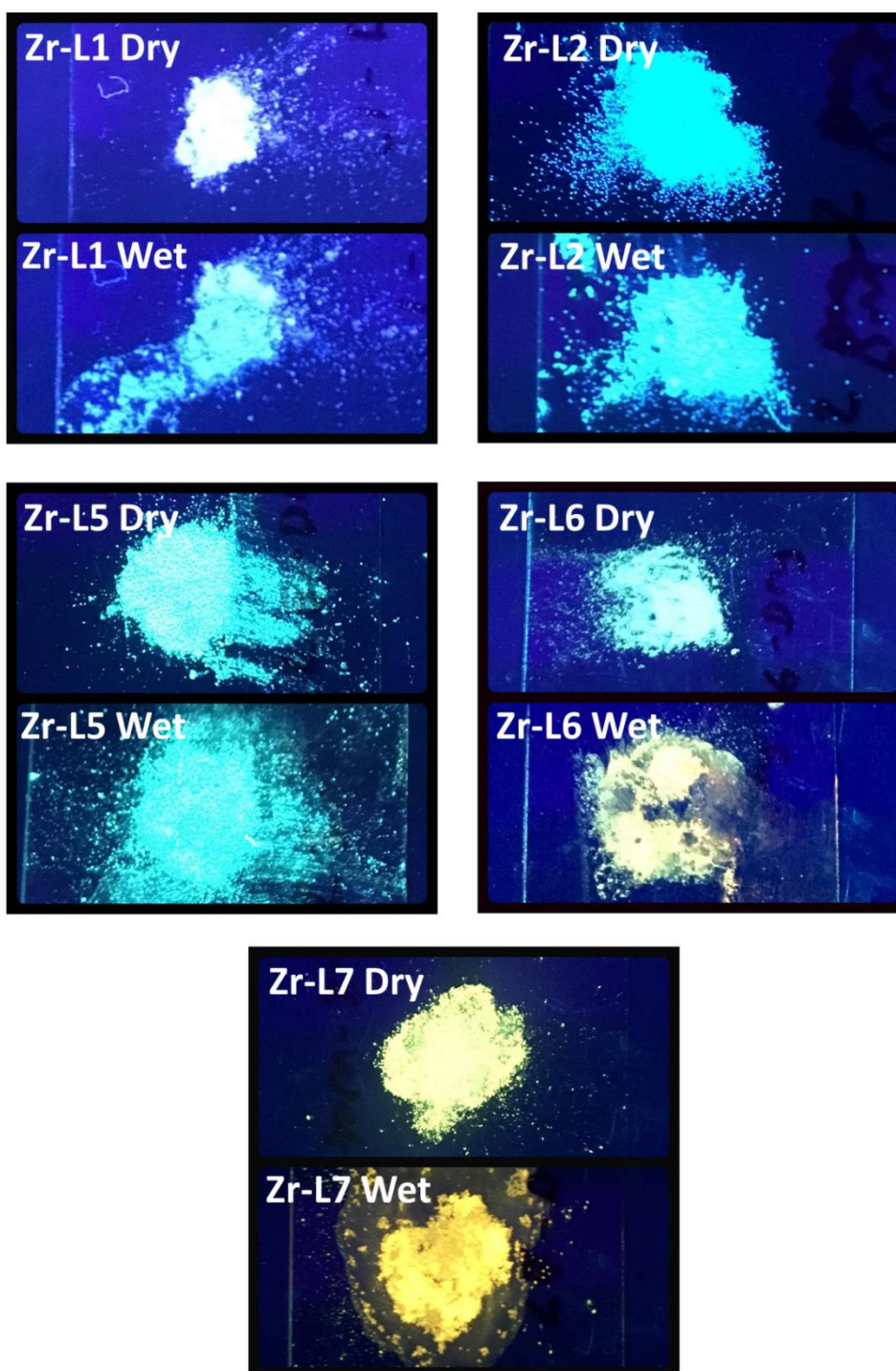


**Figure 3.13.** Dry (top images) and Wet (bottom images) Zr-L1 to Zr-L7 on exposure to a long wave UV lamp (365 nm).

In addition to water, ssPL measurements were also performed on the Zr-LX MOFs in the presence of CO<sub>2</sub>, N<sub>2</sub> and H<sub>2</sub>S. Small changes were observed in the emission  $\lambda_{\max}$  but none of the responses were large enough to be commendable (Figure 3.14).

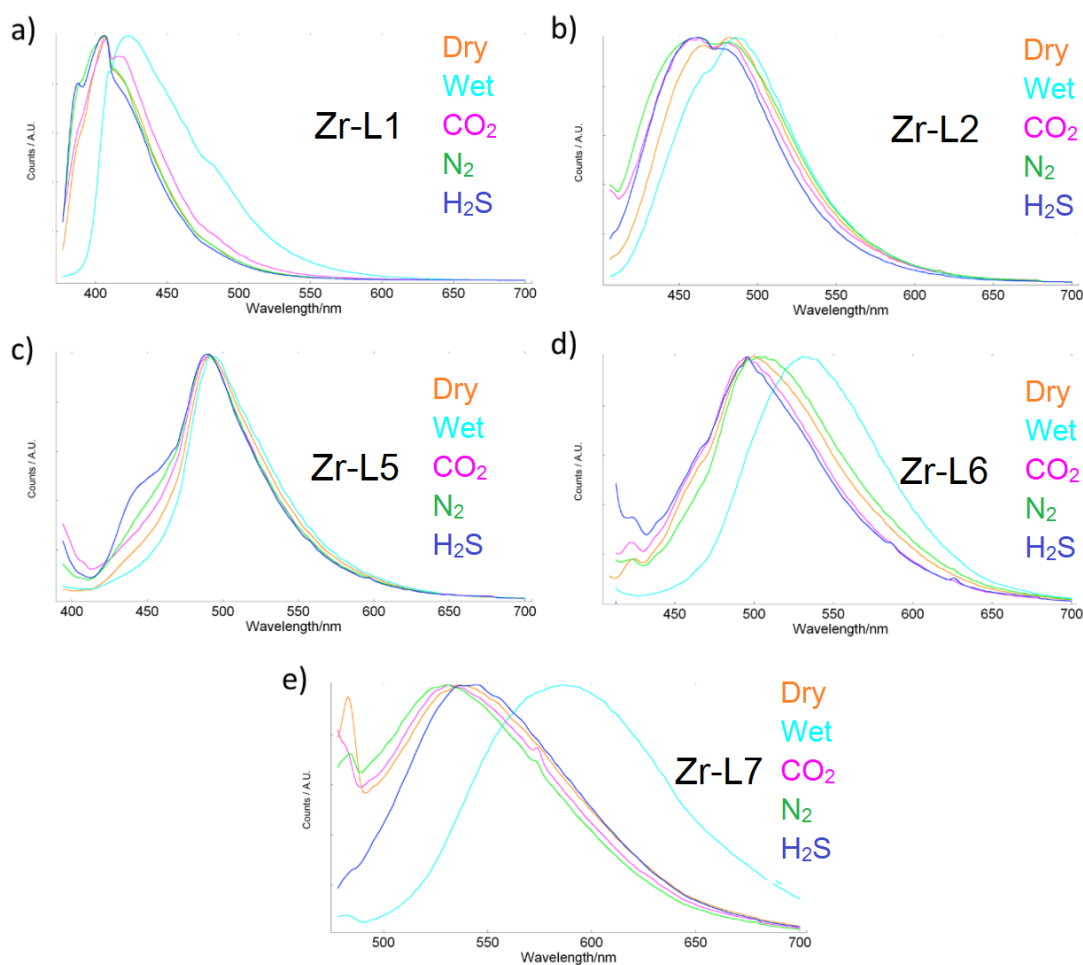


**Figure 3.14.** Normalised solid-state fluorescence emission spectra of a) Zr-L1 ( $\lambda_{ex} = 367$  nm), b) Zr-L2 ( $\lambda_{ex} = 396$  nm), c) Zr-L5 ( $\lambda_{ex} = 384$  nm), d) Zr-L6 ( $\lambda_{ex} = 403$  nm) and e) Zr-L7 ( $\lambda_{ex} = 468$  nm) under a variety of conditions including gas phase reagents.

However, seeing as several of the MOFs produced a large enough shift in  $\lambda_{max}$  on addition of water, a series of humidity experiments were conducted to probe their effectiveness as water sensors. For the AE MOFs, different saturated salt solutions were used to produce various relative humidities. The same methodology was used to probe the emission response of the Zr-LX MOFs. A temperature variation from 22 °C to 24 °C was observed throughout the study. Zr-L5 showed no change in emission over the gradual humidity increases. Fluorinated hydrocarbons have been documented for their hydrophobicity,<sup>49,50</sup> the lack of hydration-dependent emission in Zr-L5 is likely derived from the hydrophobicity of the L5 tetrafluorinated linker which repels water from accessing the MOF pores and hydrating the

zirconium cluster. For the case of Zr-L2, the emission shift upon wetting with liquid water was too small to make any discernible observations in the presence of increased RH. Zr-L1, Zr-L6 and Zr-L7 all showed varying degrees of change, as shown in Figure 3.15.

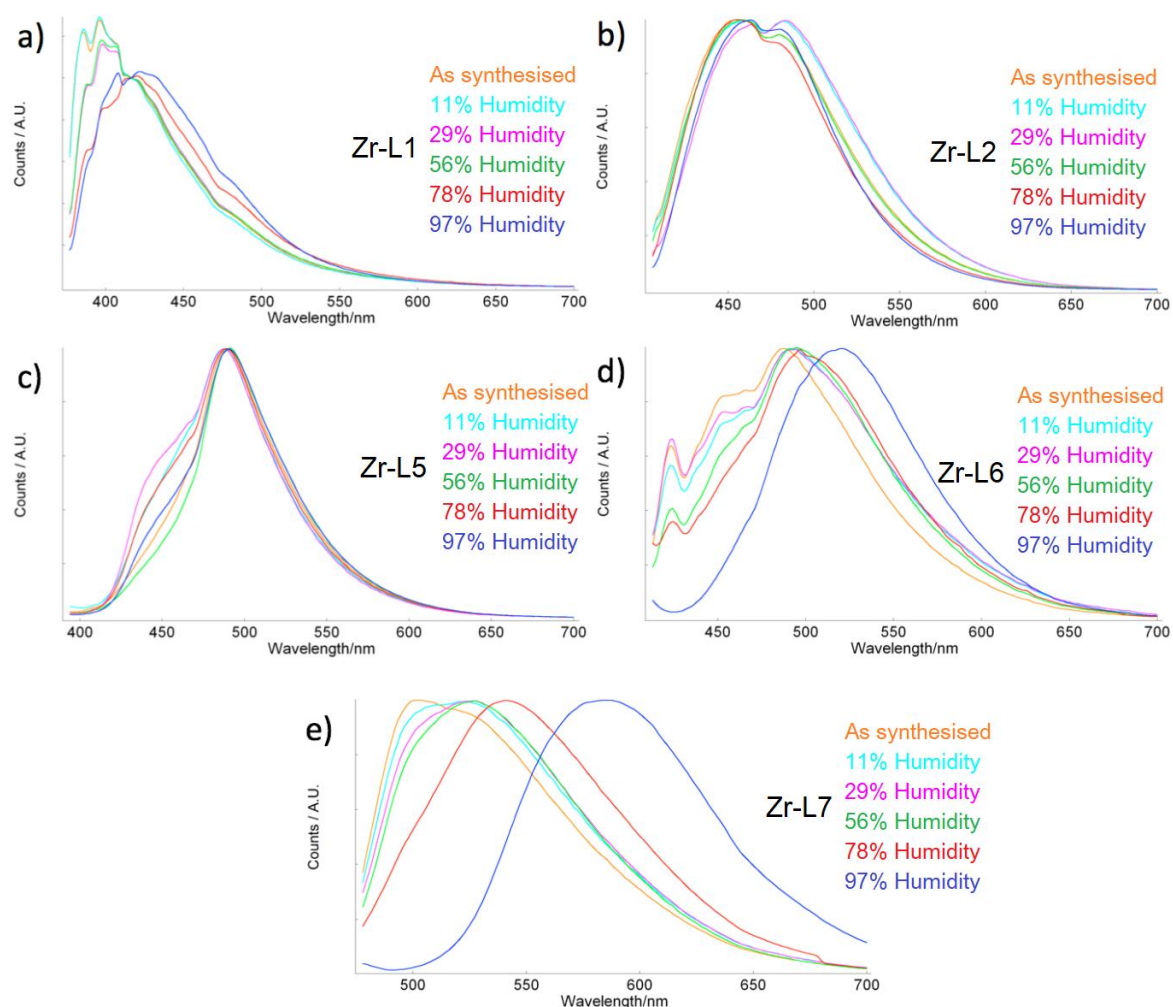


**Figure 3.15.** Normalised solid-state fluorescence emission spectra of a) Zr-L1 ( $\lambda_{\text{ex}} = 367$  nm), b) Zr-L2 ( $\lambda_{\text{ex}} = 396$  nm), c) Zr-L5 ( $\lambda_{\text{ex}} = 384$  nm), d) Zr-L6 ( $\lambda_{\text{ex}} = 403$  nm) and e) Zr-L7 ( $\lambda_{\text{ex}} = 468$  nm) after subjection to varying relative humidities.

Zr-L1 showed little change in  $\lambda_{\text{max}}$  until 78 % RH, at which point a red-shifted emission was observed. The shift was however not gradual. Given more time, it would have been interesting to have recorded the  $\Phi\text{F}$  to see if a gradual decrease was observed upon increasing the RH. With Zr-L6, there was a gradual decrease in intensity of the emission bands centred on 425 and 470 nm. There was also a relative increase and red-shift ( $\sim 10$  nm) in the band centred around 490 nm up to 78 % RH. Given more time, investigating additional increments between 78 and

97 % RH could show whether a more gradual hydration-dependent emission is observed in this humidity range. Upon full hydration (97 % RH), there was a sharp red-shifted emission to 534 nm. The emissive response upon full hydration was significant, but the change upon exposure to lower degrees of RH was not large enough to be accurately distinguishable. The most encouraging humidity-dependant change was observed for the case of Zr-L7 (Figure 3.16). An immediate humidity-dependent red-shift was observed at just 11 % RH with an increase in the emission intensity at the band centred around 520 nm compared to the 500 nm band. Between 11 – 56 % RH, there is a progressive disappearance of the 500 nm emission band. A further sharp change in  $\lambda_{\text{max}}$  was observed at 77 % RH followed by the maximum shift to 586 nm upon full hydration. The gradual humidity-dependent colour change can be summarised by the chromaticity diagram shown in Figure 3.16, there is a steady change in the emission from the deep green region to the yellow/orange. Upon full hydration, Zr-L7 was vacuum dried at 120°C, the emission was fully reversed and there was no deterioration in crystallinity, as shown by PXRD (Figure 3.17). Based on the sensitivity of the hydration-dependent emission, the reversibility of the process and the stability of the material, Zr-L7 shows great promise for potential applications in water sensing.

Varying degrees of hydration all elicited some form of emission response in the Zr-LX MOFs. The only exception was Zr-L5 which showed absolutely no hydration-dependent emission. This was of particular interest as there have been numerous reports of hydrophobicity upon fluorination of organic compounds. The hydrophobicity of Zr-L5 was investigated through the use of tensiometry.

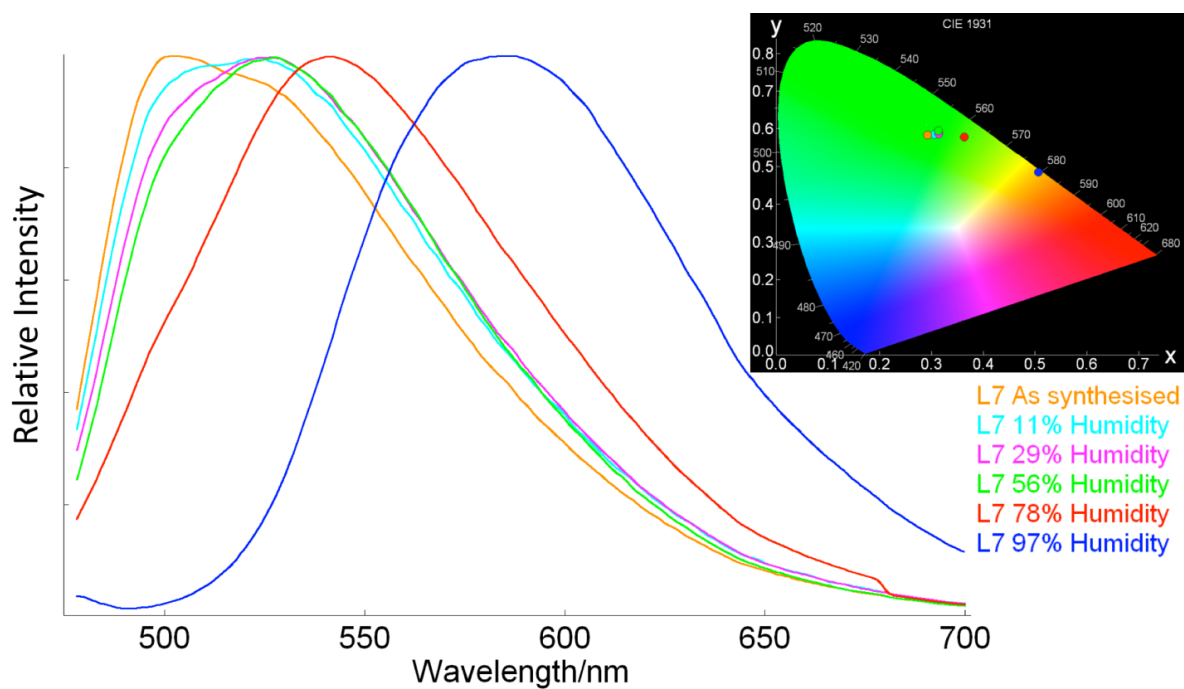


**Figure 3.16.** Normalised solid-state fluorescence emission spectra of Zr-L7 ( $\lambda_{\text{ex}} = 468 \text{ nm}$ ) in the presence of increasing relative humidity. Inset shows the chromaticity diagram of Zr-L7 in the presence of different relative humidities.

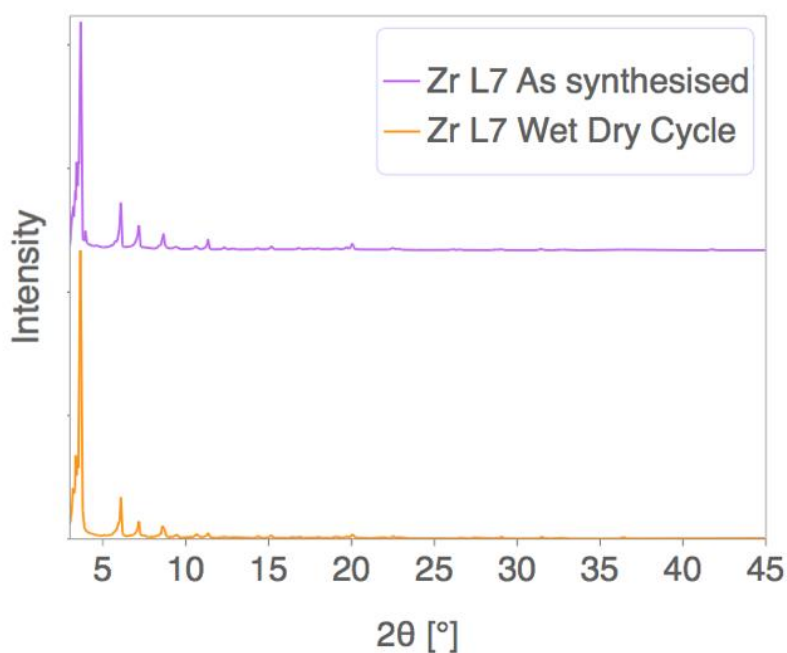


**Figure 3.17.** A PXR overlay showing as-synthesised Zr-L7 and Zr-L7 after wetting with liquid water followed by drying under vacuum at  $120 \text{ }^\circ\text{C}$  for 1 hour.

Tensiometry allows one to measure the surface tension of a liquid on a solid surface by recording the contact angle of the liquid on the surface.<sup>51</sup> With water as the liquid, a low contact angle demonstrates a propensity for ‘wetting’ and is indicative of a hydrophilic

material. A high contact angle suggests that there is a degree of 'repulsion' between the liquid and the surface and so indicates that the material is hydrophobic. Zr-L1 possesses the un-functionalised (non-fluorinated)  $\text{peb}^2$  linker and was therefore used for the first measurement to provide a point of comparison.

A contact angle of  $73.8^\circ$  was obtained (Figure 3.18), this falls within the range of a hydrophilic material.<sup>52</sup> This hydrophilicity likely permits the hydration of the zirconium node and explains why the Zr-L1 framework is able to produce a red-shifted LCCT emission upon liquid wetting. The same measurement was performed using Zr-L5, a contact angle of  $166.7^\circ$  was obtained. Figure 3.19 shows the water droplet on the surface of Zr-L5, the droplet appears to be almost spherical. The strong repulsion between the Zr-L5 surface and  $\text{H}_2\text{O}$  highlights just how hydrophobic the framework is. The hydrophobicity also explains why the emission  $\lambda_{\text{max}}$  of the framework remains completely unaffected upon wetting with water. It was also shown that using ssPL is a fast and cheap method for identifying the functional properties in a range of materials.

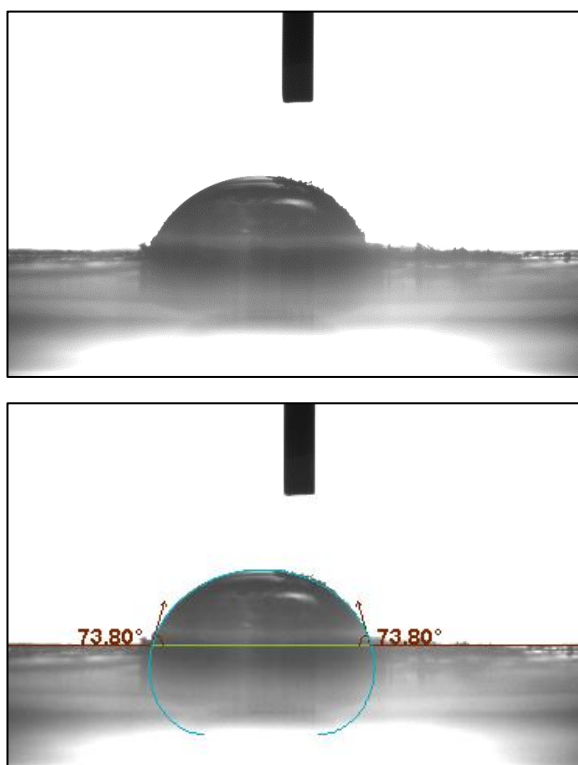


**Figure 3.18.** Contact angle measurements of water on a surface of packed Zr-L1, demonstrating a strong propensity for surface wetting.

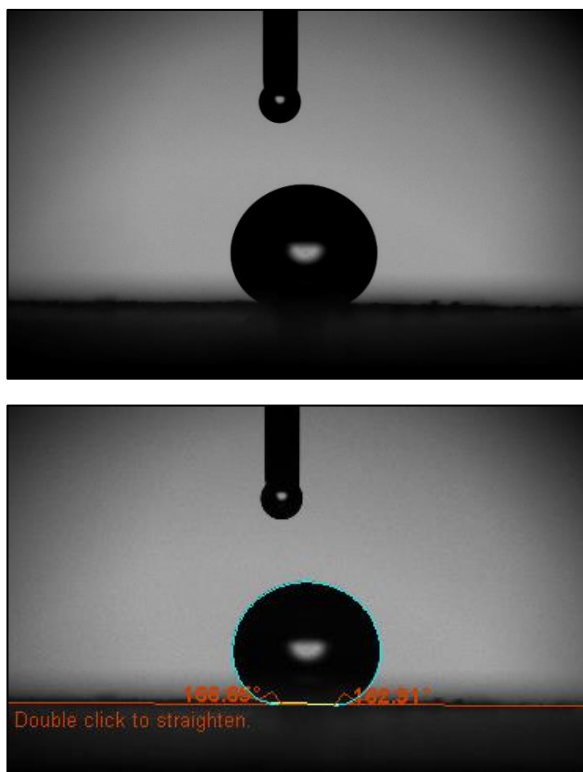


**Figure 3.19.** Contact angle measurements of water on a surface of packed Zr-L5, demonstrating little propensity for surface wetting.

### 3.5.2 Solvatochromism

Solvatochromism is the capacity of a material to change colour as a result of increasing or decreasing solvent polarity.<sup>53</sup> Upon completing a variety of humidity studies, the Zr-LX series of MOFs were also tested for their capacity to respond to a number of solvent environments. This study was again conducted using solid-state fluorometry by measuring any changes in the emission  $\lambda_{\max}$ . For completion, a wide range of polar-protic, polar aprotic and non-polar solvents were utilised (Figure 3.20). A variety of responses were observed for all of the frameworks, with the exception of Zr-L5 for which the emission  $\lambda_{\max}$  remained constant in the presence of all of the liquid analytes. Zr-L6 exhibited very little change also, with only EtOH perturbing the system enough to cause a blue-shift in emission  $\lambda_{\max}$  by increasing the intensity of a lower wavelength emission band. When Zr-L1 was tested, the most interesting change was in the presence of toluene which resulted in a red-shifted emission in  $\lambda_{\max}$ . This can potentially be attributed to toluene forming  $\pi$ -stacking interactions with the aromatic

backbone of the L1 linker in the Zr-L1 framework, this would permit a charge transfer transition between the L1 linker and the toluene. Utilising additional aromatic solvents in these studies, such as benzene, could be a useful way to confirm this effect. Whilst a number of other small solvent-dependent changes were noted for Zr-L1, there appeared to be very little order and so no overall trend was observed.

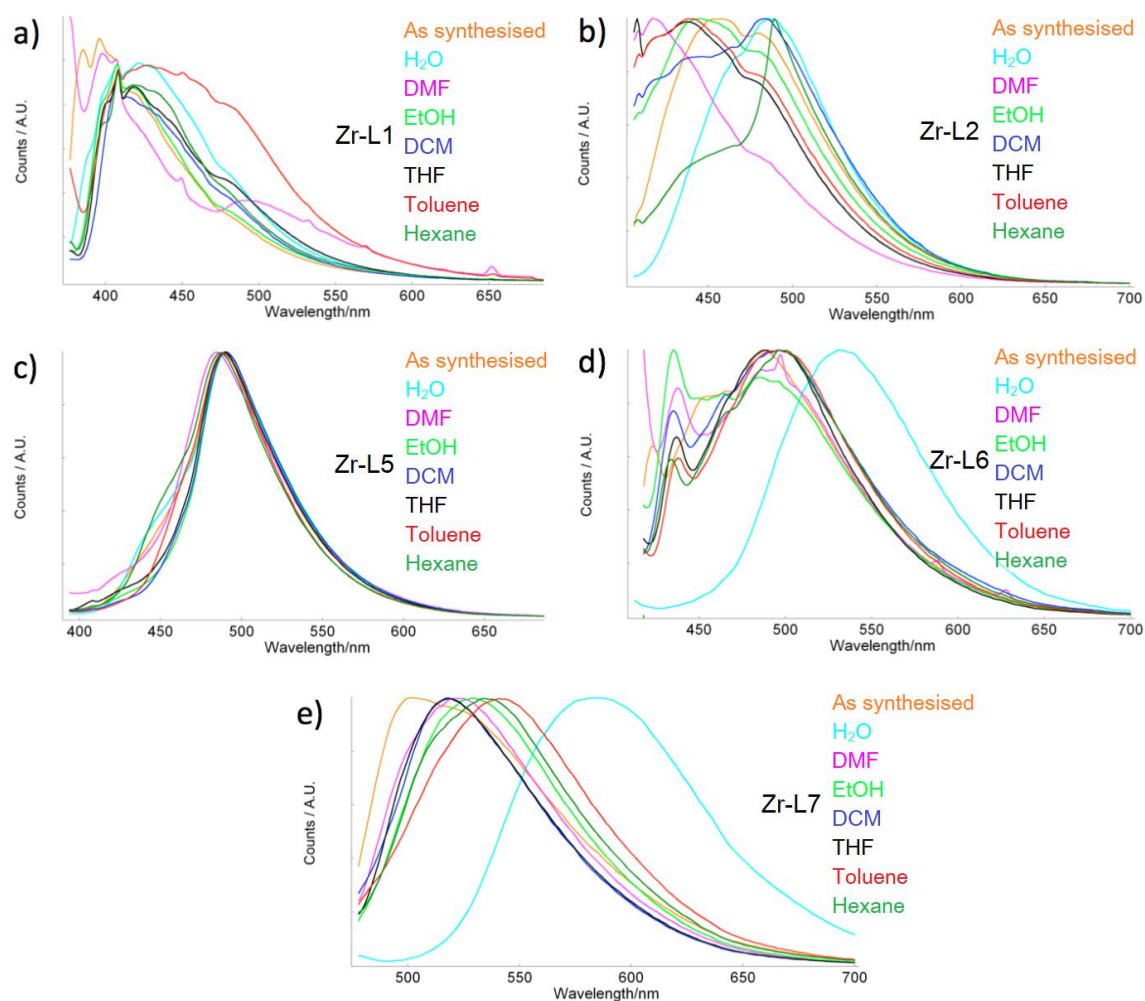


**Figure 3.20.** Normalised solid-state fluorescence emission spectra of a) Zr-L1 ( $\lambda_{\text{ex}} = 367$  nm), b) Zr-L2 ( $\lambda_{\text{ex}} = 396$  nm), c) Zr-L5 ( $\lambda_{\text{ex}} = 384$  nm), d) Zr-L6 ( $\lambda_{\text{ex}} = 403$  nm) and e) Zr-L7 ( $\lambda_{\text{ex}} = 468$  nm) in the presence of different solvents.

Zr-L7 produced a distinct and measurable change in emission  $\lambda_{\text{max}}$  in the presence of each solvent that was tested. The chromaticity diagram for Zr-L7 (Figure 3.21) illustrates the range of colours which were observed. The unique changes in  $\lambda_{\text{max}}$  highlight the sensitivity of the relaxation pathways in Zr-L7. It should also be noted that the solid-state emission profiles of L7-Me<sub>2</sub> were also measured and no change in  $\lambda_{\text{max}}$  was observed (Appendix Section 7.2). This

goes on to show the necessity of the LCCT transition which requires the framework topology to produce the observed solvent-dependent emission change. The most significant changes were witnessed when Zr-L2 was subjected to a range of solvents. A solvatochromic trend was observed where an increase in the solvent dipole moment resulted in a blue-shifted emission  $\lambda_{\text{max}}$ . The chromaticity diagram for Zr-L2 (Figure 3.22) illustrates the various colours which were observed.

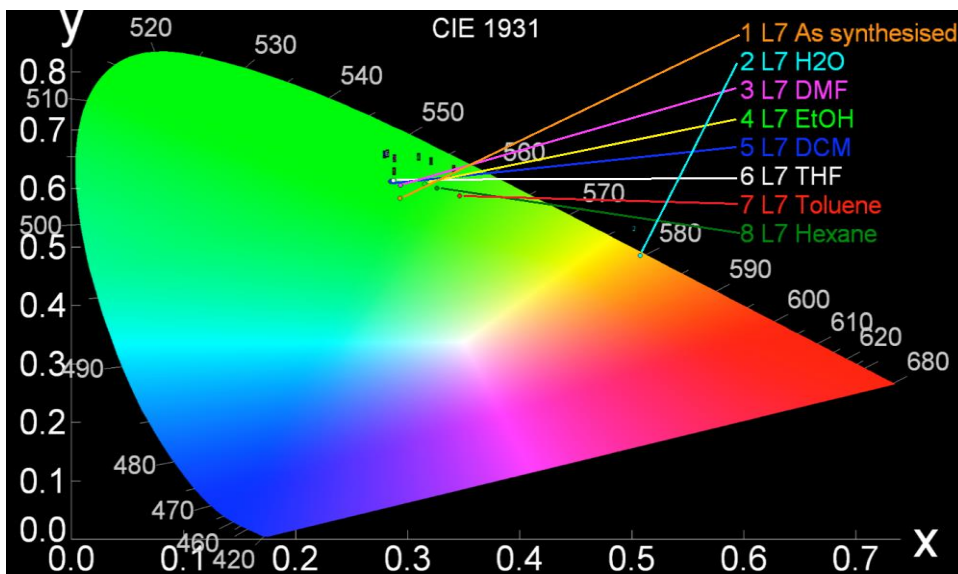


**Figure 3.21.** Chromaticity diagram of Zr-L7 ( $\lambda_{\text{ex}} = 468 \text{ nm}$ ) in the presence of various solvents.

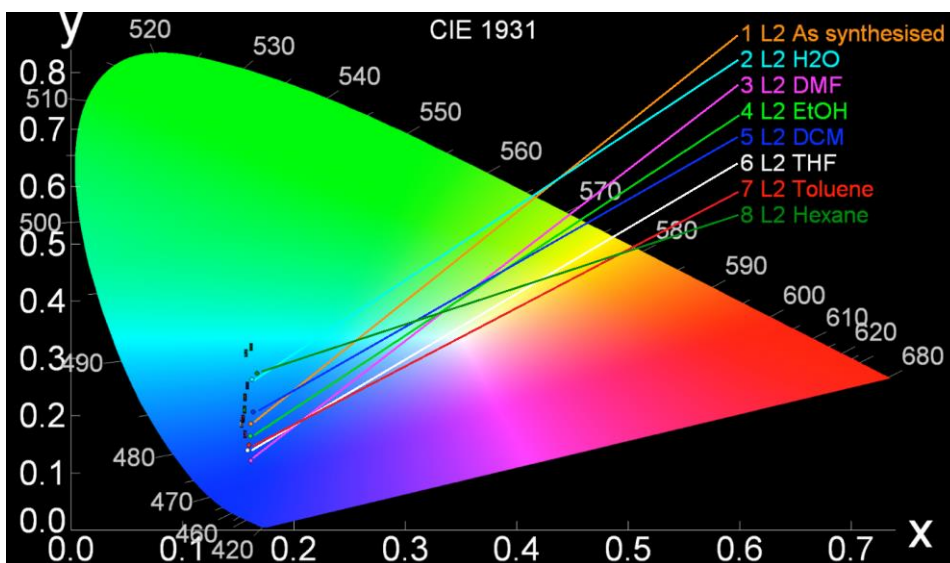


**Figure 3.22.** Chromaticity diagram of Zr-L2 ( $\lambda_{\text{ex}} = 396 \text{ nm}$ ) in the presence of various solvents.

To further probe this effect, Zr-L2 was additionally exposed to IPA, methanol and acetone (Figure 3.23). The emission  $\lambda_{\max}$  of Zr-L2 was still in good agreement with the dipole moment of these additional solvents. A moderate trend was therefore established between the emission  $\lambda_{\max}$  and the dipole moment of the liquid analytes with an  $R^2 = 0.78$ . Toluene participates in  $\pi$ -stacking interactions with the linker L2 linker and  $\text{H}_2\text{O}$  engages in node hydration, these two solvents were therefore treated as outliers and omitted from the trend. The subtle changes in emission are believed to derive from the rotational conformations of the bridging dimethylphenylene unit on the L2 ligand backbone. In fact, there appear to be two separate emission bands (468 nm and 482 nm) which are assumed to originate from the twisting of this ligand. It should again be noted that in the solid state, L2-Me<sub>2</sub> exhibited no change in emission  $\lambda_{\max}$  upon wetting with various solvents (Appendix Section 7.2), thus inferring the necessity of the hybrid MOF structure.

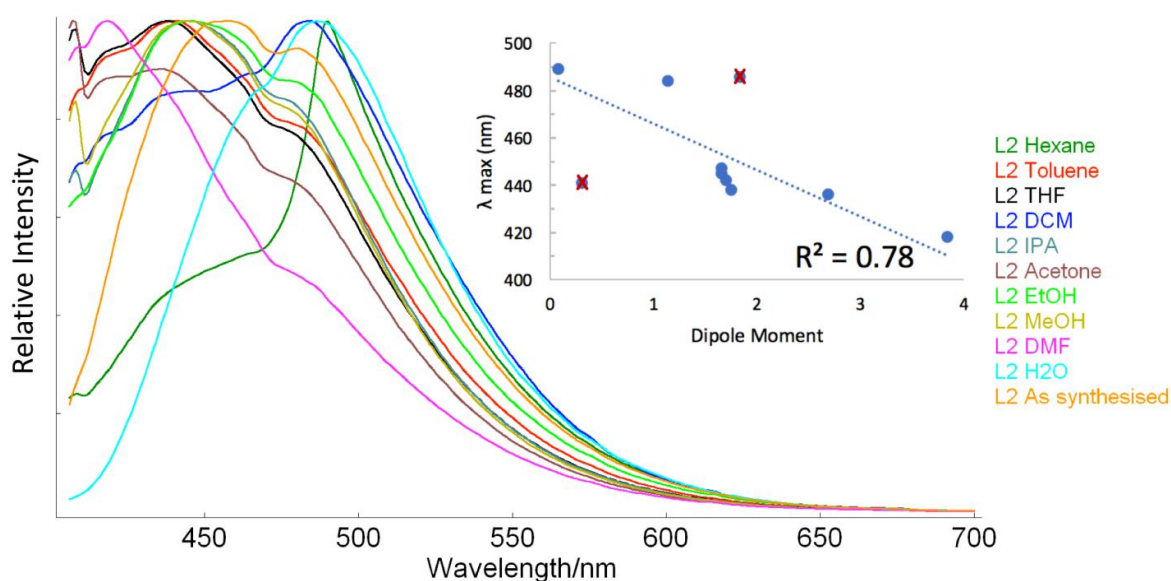


**Figure 3.23.** Normalised solid-state fluorescence emission spectra of Zr-L2 ( $\lambda_{\text{ex}} = 396$  nm) in the presence of a wide range of solvents. Inset is a plot of solvent Dipole Moment versus the corresponding Zr-L2 emission  $\lambda_{\max}$  achieved by solvent wetting.  $\text{H}_2\text{O}$  and Toluene are shown as outliers.

### 3.6 Summary and Conclusion

Using solid-state photoluminescence, a number of interesting properties have been investigated. Initial analysis of a number of Zirconium MOF catalyst candidates did not yield any information and no hydration dependant fluorescence was observed. Fortunately, upon analysing two novel AE MOFs, hydration-dependant fluorescence was observed. MOF-1 (Ba) exhibiting a sharp red-shifted emission upon liquid wetting/above 84 % RH. MOF-2 (Sr) displaying a gradual and more sensitive response to increases in relative humidity, up to 85 % RH. This was the first example of an AE MOF which was able to produce a gradual humidity-dependent emissive response. The hydration-dependent emissive shift is thought to be derived from the malleability of the AE metal coordination arc upon hydration of the framework which results in the formation of  $\pi$ -stacking in the hydrated state. These changes in emission were found to be reversible over a number of cycles, but each framework became increasingly amorphous after subsequent cycles. This was notable because of the emphasis that is often placed upon crystallinity when assessing a MOFs function. However, the long term storage stability of both materials requires further examination. All of these changes were probed using ssPL spectroscopy.

A series of novel interpenetrated Zr  $\text{peb}^{2-}$  based MOFs were also examined. The frameworks were iso-structural but possessed different functionalities on the central aromatic ring of the  $\text{peb}^{2-}$  linker. The functional properties of these frameworks were analysed using solid state photoluminescence spectroscopy and a variety of notable features were observed based on the different functionalities of the  $\text{peb}^{2-}$  linker. The dimethyl functionality in Zr-L2 resulted in a range of solvatochromic emission shifts based upon the dipole moment of different guest solvent molecules. Zr-L7 exhibited hydration dependant fluorescence which was sensitive to small variations in relative humidity. Finally, Zr-L5 which is composed of a tetrafluorinated linker was found to have no change in emission upon hydration. This prompted for the tensiometric analysis of Zr-L5. The framework was found to have the contact angle of a super

hydrophobic material. The study shows how small variations in linker functionality can lead to vastly different functional properties in MOFs.

This chapter has brought attention to the effectiveness of ssPL as an analytical tool for the characterization of MOFs. ssPL is a relatively cheap, fast and effective way for screening subtle changes in MOFs in the presence of various guest molecules, be they solvents or gasses. Using photoluminescence as a first point of protocol, to screen for various changes, further coupled with more in depth, application/property specific analysis is an effective way to probe the different functional properties which MOFs may exhibit. Photoluminescence is therefore an effective technique for probing functional properties in MOFs.

### 3.7 References

- 1 G. Giakisikli and A. N. Anthemidis, *Anal. Chim. Acta*, 2013, **789**, 1–16.
- 2 K. Seki and W. Mori, *J. Phys. Chem. B*, 2002, **106**, 1380–1385.
- 3 M. Bosch, M. Zhang and H.-C. Zhou, *Adv. Chem.*, 2014, **2014**, 1–8.
- 4 C. Atzori, G. C. Shearer, L. Maschio, B. Civalleri, F. Bonino, C. Lamberti, S. Svelle, K. P. Lillerud and S. Bordiga, *J. Phys. Chem. C*, 2017, **121**, 9312–9324.
- 5 A. J. Howarth, A. W. Peters, N. A. Vermeulen, T. C. Wang, J. T. Hupp and O. K. Farha, *Chem. Mater.*, 2017, **29**, 26–39.
- 6 C. Wang, Z. Xie, K. E. deKrafft and W. Lin, *J. Am. Chem. Soc.*, 2011, **133**, 13445–13454.
- 7 G. Wang, C. Sharp, A. M. Plonka, Q. Wang, A. I. Frenkel, W. Guo, C. Hill, C. Smith, J. Kollar, D. Troya and J. R. Morris, *J. Phys. Chem. C*, 2017, **121**, 11261–11272.
- 8 S. Devautour-Vinot, G. Maurin, F. Henn, C. Serre, T. Devic and G. Férey, *Chem. Commun.*, 2009, **0**, 2733.
- 9 N. Sahiner, K. Sel, O. F. Ozturk, S. Demirci and G. Terzi, *Appl. Surf. Sci.*, 2014, **314**, 663–669.
- 10 J. H. Cavka, S. Jakobsen, U. Olsbye, N. Guillou, C. Lamberti, S. Bordiga and K. P. Lillerud, *J. Am. Chem. Soc.*, 2008, **130**, 13850–13851.
- 11 R. J. Marshall, C. L. Hobday, C. F. Murphie, S. L. Griffin, C. A. Morrison, S. A. Moggach and R. S. Forgan, *J. Mater. Chem. A*, 2016, **4**, 6955–6963.
- 12 Y. Yu, X.-M. Zhang, J.-P. Ma, Q.-K. Liu, P. Wang and Y.-B. Dong, *Chem. Commun.*, 2014, **50**, 1444–1446.
- 13 H. Furukawa, F. Gándara, Y.-B. Zhang, J. Jiang, W. L. Queen, M. R. Hudson and O. M. Yaghi, *J. Am. Chem. Soc.*, 2014, **136**, 4369–4381.
- 14 Y. Cui, Y. Yue, G. Qian and B. Chen, *Chem. Rev.*, 2012, **112**, 1126–1162.
- 15 A. Douvali, A. C. Tshipis, S. V. Eliseeva, S. Petoud, G. S. Papaefstathiou, C. D. Malliakas, I. Papadas, G. S. Armatas, I. Margiolaki, M. G. Kanatzidis, T. Lazarides and M. J. Manos, *Angew. Chem Int. Ed.*, 2015, **127**, 1671–1676.
- 16 T. Mondal, S. Mondal, S. Bose, D. Sengupta, U. K. Ghorai and S. K. Saha, *J. Mater. Chem. C*, 2018, **6**, 614–621.
- 17 C. A. Bauer, T. V. Timofeeva, T. B. Settersten, B. D. Patterson, V. H. Liu, B. A. Simmons and M. D. Allendorf, *J. Am. Chem. Soc.*, 2007, **129**, 7136–7144.
- 18 J. D. Furman, A. Y. Warner, S. J. Teat, A. A. Mikhailovsky and A. K. Cheetham, *Chem. Mater.*, 2010, **22**, 2255–2260.
- 19 N. B. Shustova, B. D. McCarthy and M. Dincă, *J. Am. Chem. Soc.*, 2011, **133**, 20126–20129.
- 20 H. He, F. Sun, T. Borjigin, N. Zhao and G. Zhu, *Dalt. Trans.*, 2014, **43**, 3716–3721.
- 21 Y. Cui, R. Song, J. Yu, M. Liu, Z. Wang, C. Wu, Y. Yang, Z. Wang, B. Chen and G. Qian, *Adv. Mater.*, 2015, **27**, 1420–1425.
- 22 R. Lin, L. Shen, Z. Ren, W. Wu, Y. Tan, H. Fu, J. Zhang and L. Wu, *Chem. Commun.*, 2014,

- 50**, 8533-8535.
- 23 I.-H. Park, A. Chanthapally, H.-H. Lee, H. S. Quah, S. S. Lee and J. J. Vittal, *Chem. Commun.*, 2014, **50**, 3665-3667.
  - 24 M.-S. Wang, S.-P. Guo, Y. Li, L.-Z. Cai, J.-P. Zou, G. Xu, W.-W. Zhou, F.-K. Zheng and G.-C. Guo, *J. Am. Chem. Soc.*, 2009, **131**, 13572–13573.
  - 25 L. Chen, J.-W. Ye, H.-P. Wang, M. Pan, S.-Y. Yin, Z.-W. Wei, L.-Y. Zhang, K. Wu, Y.-N. Fan and C.-Y. Su, *Nat. Commun.*, 2017, **8**, 15985..
  - 26 M. De Toni, R. Jonchiere, P. Pullumbi, F.-X. Coudert and A. H. Fuchs, *ChemPhysChem*, 2012, **13**, 3497–3503.
  - 27 S. Wang, J. Wang, W. Cheng, X. Yang, Z. Zhang, Y. Xu, H. Liu, Y. Wu and M. Fang, *Dalton. Trans.*, 2015, **44**, 8049–8061.
  - 28 X.-W. Zhu, X.-P. Zhou and D. Li, *Chem. Commun.*, 2016, **52**, 6513–6516.
  - 29 A. E. Platero-Prats, M. Iglesias, N. Snejko, A. Monge and E. Gutiérrez-Puebla, *Cryst. Growth Des.*, 2011, **11**, 1750–1758.
  - 30 X.-Y. Dong, X.-P. Hu, H.-C. Yao, S.-Q. Zang, H.-W. Hou and T. C. W. Mak, *Inorg. Chem.*, 2014, **53**, 12050–12057.
  - 31 A. E. Platero-Prats, N. Snejko, M. Iglesias, Á. Monge and E. Gutiérrez-Puebla, *Chem. Eur. J.*, 2013, **19**, 15572–15582.
  - 32 L.-M. Yang, P. Ravindran, P. Vajeeston and M. Tilset, *Phys. Chem. Chem. Phys.*, 2012, **14**, 4713-4723.
  - 33 T. Kundu, S. C. Sahoo and R. Banerjee, *Chem. Commun.*, 2012, **48**, 4998-5000.
  - 34 P. Ramaswamy, N. E. Wong, B. S. Gelfand and G. K. H. Shimizu, *J. Am. Chem. Soc.*, 2015, **137**, 7640–7643.
  - 35 P. Deria, W. Bury, I. Hod, C.-W. Kung, O. Karagiari, J. T. Hupp and O. K. Farha, *Inorg. Chem.*, 2015, **54**, 2185–2192.
  - 36 J. M. Taylor, R. Vaidhyanathan, S. S. Iremonger and G. K. H. Shimizu, *J. Am. Chem. Soc.*, 2012, **134**, 14338–14340.
  - 37 K. J. Gagnon, H. P. Perry and A. Clearfield, *Chem. Rev.*, 2012, **112**, 1034–1054.
  - 38 F. Zhai, Q. Zheng, Z. Chen, Y. Ling, X. Liu, L. Weng and Y. Zhou, *CrystEngComm*, 2013, **15**, 2040–2043.
  - 39 A. Pankajakshan, M. Sinha, A. A. Ojha and S. Mandal, *ACS Omega*, 2018, **3**, 7832–7839.
  - 40 Z. H. Fard, Y. Kalinovsky, D. M. Spasyuk, B. A. Blight and G. K. H. Shimizu, *Chem. Commun*, 2016, **52**, 12865–12868.
  - 41 T. M. Fasina, J. C. Collings, J. M. Burke, A. S. Batsanov, R. M. Ward, D. Albesa-Jové, L. Porrès, A. Beeby, J. A. K. Howard, A. J. Scott, W. Clegg, S. W. Watt, C. Viney and T. B. Marder, *J. Mater. Chem.*, 2005, **15**, 690–697.
  - 42 T. L. H. Doan, H. L. Nguyen, H. Q. Pham, N.-N. Pham-Tran, T. N. Le and K. E. Cordova, *Chem. - An Asian J.*, 2015, **10**, 2660–2668.
  - 43 R. J. Marshall, Y. Kalinovsky, S. L. Griffin, C. Wilson, B. A. Blight and R. S. Forgan, *J. Am. Chem. Soc.*, 2017, **139**, 6253–6260.

- 44 Y.-Q. Chen, G.-R. Li, Z. Chang, Y.-K. Qu, Y.-H. Zhang and X.-H. Bu, *Chem. Sci.*, 2013, **4**, 3678-3682.
- 45 A. Ganguly, *Fundamentals of Physical Chemistry*, Pearson, 2011, pp. 9-42.
- 46 Y. Horiuchi, T. Toyao, M. Saito, K. Mochizuki, M. Iwata, H. Higashimura, M. Anpo and M. Matsuoka, *J. Phys. Chem. C*, 2012, **116**, 20848–20853.
- 47 B. W. Gung and J. C. Amicangelo, *J. Org. Chem.*, 2006, **71**, 9261–70.
- 48 N. Ko, J. Hong, S. Sung, K. E. Cordova, H. J. Park, J. K. Yang and J. Kim, *Dalton. Trans.*, 2015, **44**, 2047–2051.
- 49 V. H. Dalvi and P. J. Rossky, *Proc. Natl. Acad. Sci. U. S. A.*, 2010, **107**, 13603–7.
- 50 J. C. Biffinger, H. W. Kim and S. G. DiMugno, *ChemBioChem*, 2004, **5**, 622–627.
- 51 L. M. Lander, L. M. Siewierski, W. J. Brittain and E. A. Vogler, *Langmuir*, 1993, **9**, 2237–2239.
- 52 K.-Y. Law, *J. Phys. Chem. Lett.*, 2014, **5**, 686–688.
- 53 A. Marini, A. Muñoz-Losa, A. Biancardi and B. Mennucci, *J. Phys. Chem. B*, 2010, **114**, 17128–17135.

## Chapter 4. Activation through Hydration of Zirconium MOF

### Nodes

The work described in this chapter was previously published in the following journal:

Y. Kalinovsky, N. J. Cooper, M. J. Main, S. J. Holder and B. A. Blight, *Dalton Trans.*, 2017, **46**, 15704–15709.

MOF synthesis and characterization was all performed by the author of this thesis, as were all the hydrolysis studies involving DMNP. VM hydrolysis experiments were conducted at DSTL by N. Cooper and M. Main.

### 4.1 Introduction

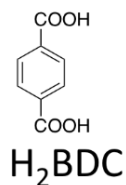
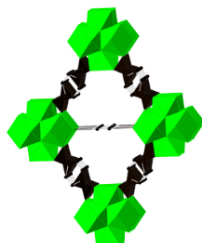
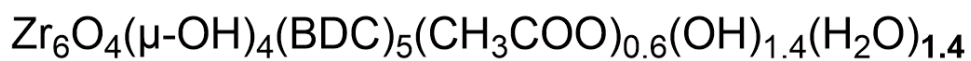
In Zirconium MOFs, missing linker defects/coordination vacancies facilitate lewis acid catalysed reactions.<sup>1</sup> These empty coordination sites should have an affinity for water. In the previous chapter, an unsuccessful attempt was made to measure the hydration of a series of zirconium MOF catalyst candidates using solid-state photoluminescence spectroscopy. An alternative approach to verifying hydration is taken in this chapter, one which ultimately leads to a modest enhancement in CWA simulant hydrolysis. This chapter describes a novel procedure for post-synthetic activation, achieved through the hydration of zirconium MOFs which were synthesised by modulation with acetic acid.<sup>2</sup>

A number of solvent free and mechanochemical routes have been reported for zirconium MOF assembly<sup>3,4</sup>; however, the vast majority of methods rely on solvothermal synthesis.<sup>5,6</sup> These hydrothermal techniques often employ high boiling point solvents such as dimethyl formamide (DMF) or dimethyl acetamide (DMA)<sup>7</sup> along with a monotopic acid modulator.<sup>8,9</sup> Benzoic acid, formic acid and acetic acid are some common examples of modulators. The modulator is essential for controlling the assembly of the structure and can readily influence the pore size, dimensionality and even the concentration of defects in the framework.<sup>8,10</sup> An interesting example is the PCN-222/MOF-545, PCN-223 and PCN-224 series of zirconium MOFs which are

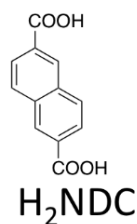
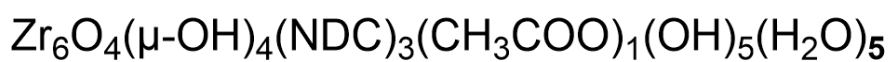
composed of the tetrakis(4-carboxyphenyl)porphyrin (TCPP) linker. Utilising dichloroacetic acid modulator results in the 8-connected PCN-222/MOF-545 framework, modulating the synthesis with acetic acid leads to the 12-connected PCN-223 framework, finally changing the modulator to benzoic acid will lead to PCN-224, a 6-connected zirconate MOF. Post synthesis, additional steps are required to 'activate' the MOF. Activation can simply refer to the desolvation of the MOF pores (i.e. removal of organic reaction solvent), it can also be used to describe the extraction of any free or bound modulator used during synthesis to create vacancies.<sup>10,11</sup> For clarity, in this chapter the meaning of activation will be taken to be both of these. Zirconium MOFs are typically desolvated by the use of solvent exchange techniques where the MOF is soaked in a low boiling point organic solvent, this solvent is then exchanged a number of times before subjecting the material to vacuum drying at high temperatures (200 – 300 °C). Supercritical CO<sub>2</sub> drying can also be employed for less structurally stable frameworks. Modulators can be removed either by high temperatures, which can compromise the structural integrity,<sup>12,13</sup> or by post-synthetic exchange (PSE) for an alternative moiety.<sup>14,15</sup> Herein, a novel, facile method is presented for the activation of three known zirconium MOFs; DUT-84 (6-connected),<sup>16</sup> MOF-808 (6-connected),<sup>17</sup> and defective UiO-66.<sup>10</sup> The structures of the 3 activated MOFs involved in this study are shown in Figure 4.1. The protocol utilises microwave irradiation and water to facilitate the removal of the acetic acid modulator from the Zr<sub>6</sub> SBU.

Zirconium MOFs with missing linker defects/coordination vacancies<sup>1</sup>, such as MOF-808,<sup>17,18</sup> NU-1000<sup>19</sup> and UiO-67-NH<sub>2</sub><sup>20</sup> have been shown to effectively catalyse the degradation of organophosphorus chemical warfare agents (CWAs). In the presence of N-ethylmorpholine (NEM) buffer, dimethyl 4-nitrophenyl phosphate (DMNP; a well-established hydrolysis simulant)<sup>21,22</sup> closely mimics the hydrolytic breakdown of V-series nerve agents such as VX and VM.<sup>20</sup> In a reaction medium containing UiO-67-NMe<sub>2</sub> and NEM buffer, a DMNP half-life (t<sub>1/2</sub>) of 2 minutes is observed, a VX t<sub>1/2</sub> of 1.8 minutes is witnessed using the same system.<sup>23</sup> It should be noted that the defect content of UiO-67-NMe<sub>2</sub> was not reported.

### UiO-66



### DUT-84



### MOF-808

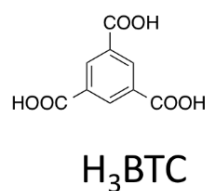
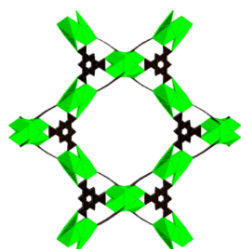
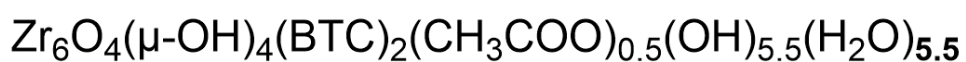


**Figure 4.1:** The structures of the 3 Zirconium MOFs involved in this study,  $\mu\text{-OH}$  denotes a bridging hydroxyl species in the  $\text{Zr}_6$  cluster.

The hydrolysis of the P-O bond in DMNP to form dimethylphosphate (DMP) simulates the severance of the P-S bond of VX to form ethyl methylphosphonate (EMPA) (Figure 4.2), thus both compounds exhibit similar degradation kinetics.

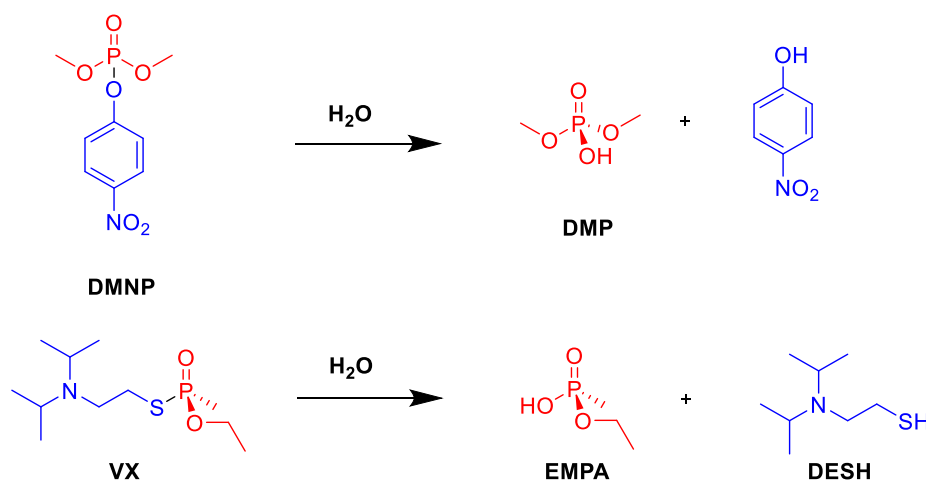


**Figure 4.2:** Stoichiometric hydrolysis reactions of: (Top) DMNP Simulant. (Bottom) VX Agent.

In this chapter, as-synthesised and activated MOF-808, DUT-84 and UiO-66 are employed for the hydrolysis of selected organophosphorus contaminants. An attempt is also made to activate Boron MOF (Chapter 2), which offers some insight into its underperformance as a hydrolysis catalyst. The NEM buffered DMNP hydrolysis system is used to probe the degradation rates of the activated catalysts and compare them to the degradation rates of their as-synthesised counterparts. The MOFs are also tested for their ability to degrade the V-series agent VM. When degrading V-series agents, P-S bond hydrolysis is highly desirable over that of P-O bond cleavage. P-O bond cleavage in V-series agents results in a degradation product of similar toxicity.<sup>24</sup> Unlike DMNP, the screening of VM was conducted in the absence of buffer as the minimisation of additional reagents is essential for enhancing the practical application of these catalysts.

## 4.2 Experimental methods

### Instrumentation

$^1\text{H}$  and  $^{31}\text{P}$  NMR spectroscopy was conducted at 298 K using a JEOL 400 MHz spectrometer with an auto-sampler. PXRD patterns were collected at 298 K on a silicon zero-background sample holder (a sample holder which presents no diffraction peaks) using a Rigaku Miniflex 600 desktop XRD and a Copper K- $\alpha$  (1.5406 Å) source. Measurements were taken in the  $3 - 45^\circ 2\theta$  range with a step size of  $0.02^\circ 2\theta$  and a scan speed of  $1^\circ 2\theta \text{ min}^{-1}$ . A Netzsch STA 409 PC25 instrument and an aluminium crucible was employed for all thermogravimetric analyses, heating rate:  $5^\circ\text{C min}^{-1}$  in  $\text{N}_2$ , 30 min isotherm at  $150^\circ\text{C}$ . A CEM Explorer Microwave Reactor with dynamic power cycling was used for all MOF activation steps.

### MOF-808 Synthesis and Characterization

MOF-808 was synthesised using a slightly modified procedure reported by Liang et al.<sup>18</sup> In a 250 ml vessel,  $\text{ZrCl}_4$ , (1281 mg, 5.5 mmol) was dissolved in 60 ml of N,N dimethylformamide and sonicated for 10 minutes. 1,3,5 benzenetricarboxylic acid ( $\text{H}_3\text{BTC}$ ), (1115 mg, 5.5 mol) was then added and the solution was sonicated for a further 10 minutes. Finally, (31 ml, 54mmol) acetic acid was added to the solution which was sonicated for another 10 minutes. The solution was sealed in a 250 ml glass vial and placed in a preheated oven where it was heated at  $130^\circ\text{C}$  for 24 hours. The vial was removed from the oven and allowed to cool to room temperature over the course of an hour. A white solid was observed. The solid was vacuum filtered, washed with DMF (3 x 20 ml) and acetone (3 x 20 ml). The filtrate was dried under vacuum for 24 hours to yield a white microcrystalline powder of nMOF-808. The bulk phase of the as-synthesised MOF-808 was confirmed by PXRD by comparing against a simulated pattern of MOF-808 (Figure 4.3).

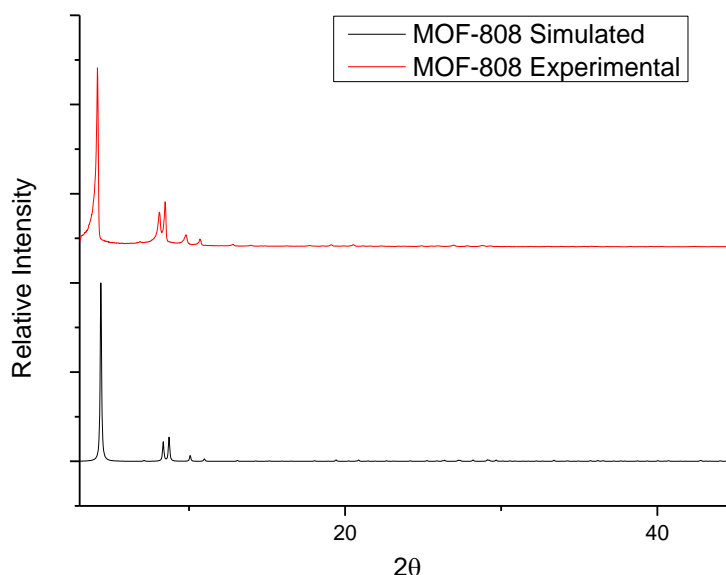


**Figure 4.3:** A PXRD overlay showing a simulated pattern for MOF-808 obtained from reference 18 and a PXRD of the as-synthesised material (nMOF-808).

200 mg of as synthesised nMOF-808 was suspended in 7 ml of distilled water in an 11 ml microwave vessel. The vessel was placed in a microwave reactor where it was activated at 150°C for 20 minutes with heavy stirring. After cooling to room temperature, the MOF was vacuum filtered, washed with H<sub>2</sub>O (3 x 10 ml) and acetone (3 x 10 ml) and dried under vacuum for 24 hours to yield the white microcrystalline powder of aMOF-808.

Assumed Formula:  $Zr_6O_4(\mu-OH)_4(BTC)_2(CH_3COO)_{0.5}(OH)_{5.5}(H_2O)_{5.5} \cdot xH_2O, x(CH_3)_2CO$

CHN analysis Calculated: C, 17.34; H, 2.15 N, 0.00 Found: C, 18.75; H, 2.03; N, 0.00.

nMOF-808 and aMOF-808 were digested in a mixture of D<sub>2</sub>SO<sub>4</sub>/DMSO. A <sup>1</sup>H NMR spectrum was obtained of both materials to investigate the ratio of acetic acid that remained after the activation procedure. This is shown in Section 4.3.2.

For TGA analysis, each sample was annealed at 100 °C for 24 hours before analysis.

#### **DUT-84 Synthesis and Characterization**

DUT-84 was synthesised using a slightly modified procedure reported by Bon et al.<sup>16</sup> In a 250 ml vessel, ZrCl<sub>4</sub>, (570 mg, 3.05 mmol) was dissolved in 120 ml of N,N dimethylformamide and sonicated for 10 minutes. 2,6 naphthalenedicarboxylic acid (H<sub>2</sub>NDC), (500 mg, 2.78 mmol) was

then added and the solution was sonicated for a further 10 minutes. Finally, acetic acid, (50 ml, 794 mmol) was added to the solution which was sonicated for another 10 minutes. The solution was sealed in a 250 ml glass vial and placed in a preheated oven where it was heated at 120 °C for 24 hours. The vial was removed from the oven and allowed to cool to room temperature over 1 hour. A white solid was observed. The solid was vacuum filtered, washed with DMF (3 x 20 ml) and acetone (3 x 20 ml). The filtrate was dried under vacuum for 24 hours to yield a white microcrystalline powder of nDUT-84. The bulk phase of the as-synthesised DUT-84 was confirmed by PXRD by comparing against a simulated pattern of DUT-84 (Figure 4.4).

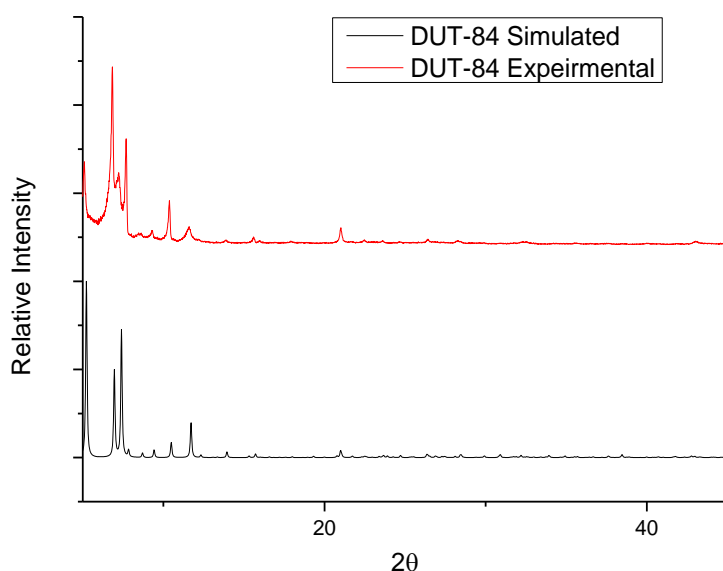


**Figure 4.4:** A PXRD overlay showing a simulated pattern for DUT-84 obtained from reference 16 and a PXRD of the as-synthesised material (nDUT-84).

200 mg of nDUT-84 was suspended in 7 ml of distilled water in an 11 ml microwave vessel. The vessel was placed in a microwave reactor where it was activated at 150 °C for 20 minutes with heavy stirring. After cooling to room temperature, the MOF was vacuum filtered, washed with H<sub>2</sub>O (3 x 10 ml) and acetone (3 x 10 ml) and dried under vacuum for 24 hour to yield the white microcrystalline powder of aDUT-84.

Assumed Formula:  $Zr_6O_4(\mu-OH)_4(NDC)_3(CH_3COO)_1(OH)_5(H_2O)_5 \cdot xH_2O, x(CH_3)_2CO$

CHN analysis: Calculated C, 31.11; H, 2.13; N, 0.00 Found C, 35.49; H, 2.87; N 0.00. The error in calculated CHN composition is possibly derived from the unknown quantity of adsorbed H<sub>2</sub>O and acetone in the aDUT-84 pores.

nDUT-84 and aDUT-84 were digested in a mixture of D<sub>2</sub>SO<sub>4</sub>/DMSO. A <sup>1</sup>H NMR spectrum was obtained of both materials to investigate the ratio of acetic acid that remained after the activation procedure. This is shown in Section 4.3.3.

For TGA analysis, each sample was annealed at 100 °C for 24 hours before analysis.

### **UiO-66 Synthesis and Characterization**

Defective UiO-66 was synthesised using a slightly modified procedure reported by Shearer et al.<sup>10</sup> In a 250 ml vessel, ZrCl<sub>4</sub>, (862 mg, 4.62mmol) was dissolved in 100 ml of N,N dimethylformamide and sonicated for 10 minutes. 1,4 benzenedicarboxylic acid (H<sub>2</sub>BDC), (615mg, 3.70 mmol) was then added and the solution was sonicated for a further 10 minutes. Finally, acetic acid, (22 ml, 349.4 mmol) and conc. HCl, (0.2 ml, 2.3 mmol) was added to the solution which was sonicated for another 10 minutes. The solution was sealed in a 250 ml glass vial and placed in a preheated oven where it was heated at 120 °C for 24 hours. The vial was removed from the oven and allowed to cool to room temperature over 1 hour. A white solid was observed. The solid was vacuum filtered, washed with DMF (3 x 20 ml) and acetone (3 x 20 ml). The filtrate was dried under vacuum for 24 hours to yield a white microcrystalline powder of nUiO-66. The bulk phase of the as-synthesised UiO-66 was confirmed by PXRD by comparing against a simulated pattern of UiO-66 (Figure 4.5).

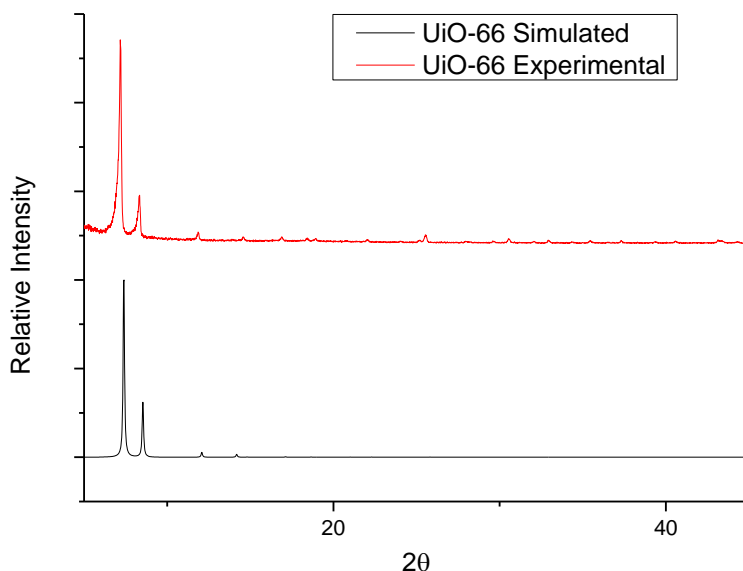


**Figure 4.5:** A PXRD overlay showing a simulated pattern for UiO-66 obtained from reference 10 and a PXRD of the as-synthesised material (nUiO-66).

200 mg of nUiO-66 was suspended in 7 ml of distilled water in an 11 ml microwave vessel. The vessel was placed in a microwave reactor where it was activated at 150 °C for 20 minutes with heavy stirring. After cooling to room temperature, the MOF was vacuum filtered, washed with H<sub>2</sub>O (3 x 10 ml) and acetone (3 x 10 ml) and dried under vacuum for 24 hour to yield the white microcrystalline powder of aUiO-66.

Assumed Formula:  $Zr_6O_4(\mu-OH)_4(BDC)_5(CH_3COO)_{0.6}(OH)_{1.4}(H_2O)_{1.4} \cdot xH_2O, x(CH_3)_2CO$

CHN analysis: Calculated C, 31.23; H, 1.91; N, 0.00 Found C, 24.68; H 3.13; N 0.00. The error in calculated CHN composition is possibly derived from the unknown quantity of adsorbed H<sub>2</sub>O and acetone in the aUiO-66 pores.

nUiO-66 and aUiO-66 were digested in a mixture of D<sub>2</sub>SO<sub>4</sub>/DMSO. A <sup>1</sup>H NMR spectrum was obtained of both materials to investigate the ratio of acetic acid that remained after the activation procedure. This is shown in Section 4.3.3.

For TGA analysis, each sample was annealed at 100 °C for 24 hours before analysis.

### Benzoic acid modulated UiO-66 (Benzoic acid) Synthesis and Characterization

Benzoic acid modulated UiO-66, termed UiO-66 (Benzoic acid) was synthesised using the following procedure. In a 250 ml vessel,  $ZrCl_4$ , (1165 mg, 6.24 mmol) was dissolved in 90 ml of N,N dimethylformamide and sonicated for 10 minutes. 1,4 benzenedicarboxylic acid ( $H_2BDC$ ), (830 mg, 5.0 mmol) was then added and the solution was sonicated for a further 10 minutes. Finally, benzoic acid, (2.44 g, 19.9 mmol) and conc. HCl, (0.8 ml, 9.2 mmol) was added to the solution which was sonicated for another 10 minutes. The solution was sealed in a 250 ml glass vial and placed in a preheated oven where it was heated at 120 °C for 48 hours. The vial was removed from the oven and allowed to cool to room temperature over 1 hour. A white solid was observed. The solid was vacuum filtered, washed with DMF (3 x 20 ml) and acetone (3 x 20 ml). The filtrate was dried under vacuum for 24 hours to yield a white microcrystalline powder of UiO-66 (Benz). The bulk phase of the as-synthesised UiO-66 (Benz) was confirmed by PXRD by comparing against a simulated pattern of UiO-66 (Figure 4.6)

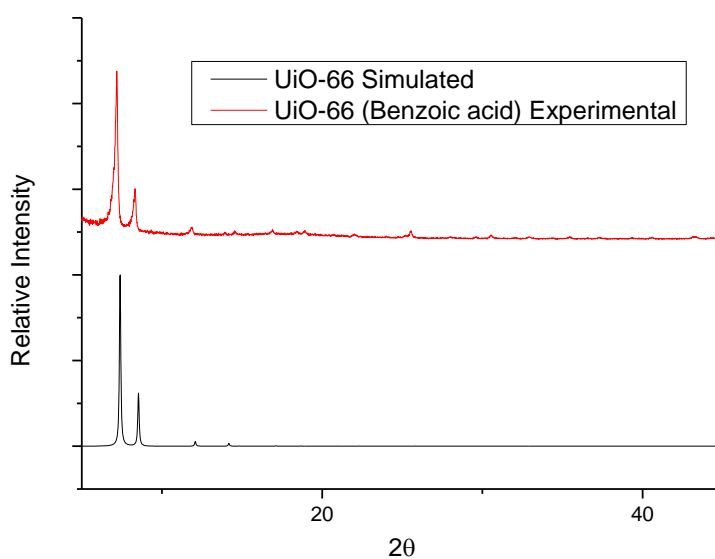


**Figure 4.6:** A PXRD overlay showing a simulated pattern for UiO-66 obtained from reference 10 and a PXRD of the as-synthesised benzoic acid modulated UiO-66 (Benzoic acid).

UiO-66 (Benzoic acid) was digested in a mixture of  $D_2SO_4$ /DMSO. A  $^1H$  NMR spectrum was obtained to investigate the ratio of benzoic acid that remained after the activation procedure. This is discussed in Section 4.3.3.

### **Boron MOF Synthesis and Characterization**

Boron MOF was synthesised and characterised using the procedure outlined in chapter 2.

Boron MOF was digested in a mixture of  $D_2SO_4$ /DMSO. A  $^1H$  NMR spectrum was obtained to investigate the ratio of acetic acid that remained after the activation procedure. This is discussed in Section 4.3.3.

### **DMNP and VM hydrolysis procedure**

The following procedure was used to probe the hydrolysis rates of the as-synthesised MOFs and their activated counterparts. An NMR tube was charged with DMNP, (20  $\mu$ L, 0.09 mmol). The MOF catalyst (0.11  $\mu$ mol, 1.25 mol % relative to DMNP) was then added to the tube. 0.1 ml of  $D_2O$  along with 0.6 ml of 0.1 M *N*-ethyl morpholine (NEM) buffer was then added to the tube. The tube was inverted 3 times and immediately loaded into an NMR auto-sampler and the first  $^{31}P$  NMR (161.83 MHz) spectrum was obtained within 3 minutes of the reaction commencing. The instrument temperature was set to 298 K throughout. The sample was then cycled on the auto-sampler for 3 hours, subsequent data points were collected every 6.5 minutes for the first hour and every half an hour after the first hour. VM testing was carried out at Porton Down (DSTL) by Marcus J. Cooper. For VM, the same procedure and the same ratios were used, the only difference was that the testing was conducted in the absence of any buffer.

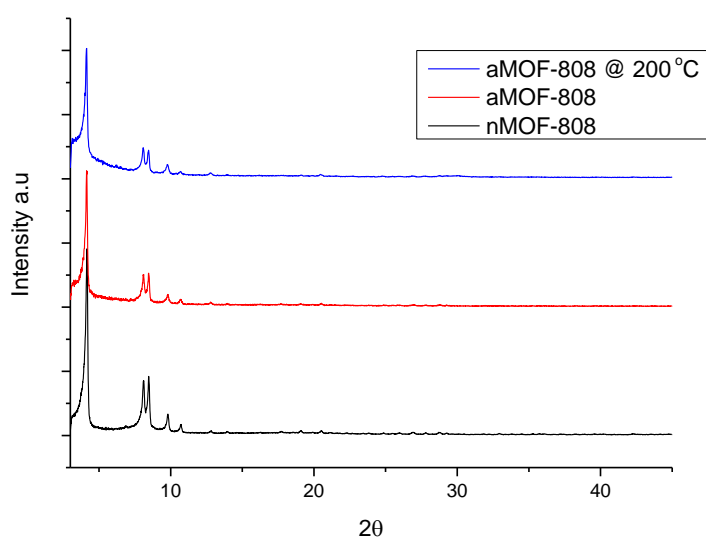
## 4.3 Results and Discussion

### 4.3.1 Synthesis of nMOFs

The as-synthesised MOFs (henceforth termed non-activated (n); i.e. nMOF-808) nMOF-808, nDUT-84, nUiO-66 and nBoron MOF were all synthesised solvothermally in DMF, their assembly was modulated with acetic acid. A control, nUiO-66 (Benzoic acid), was synthesised solvothermally but the synthesis was modulated using benzoic acid. Bulk phase properties were then confirmed using PXRD analysis (Figure 4.3, 4.4, 4.5, and 4.6).

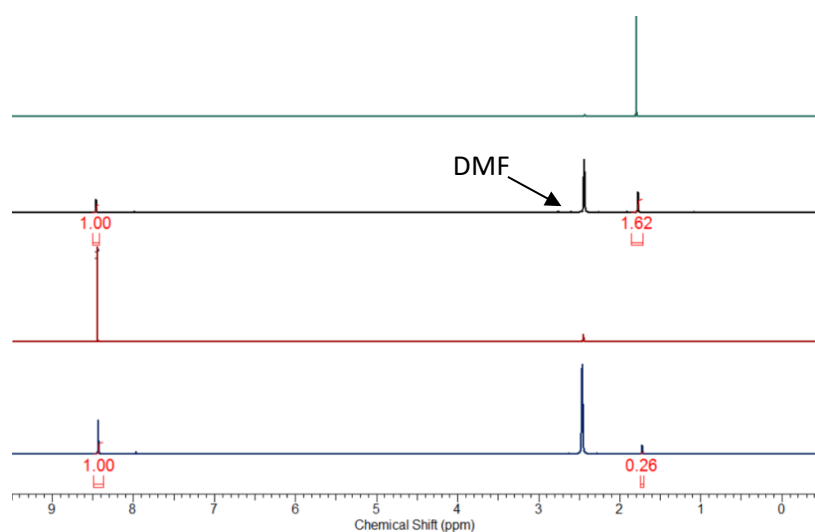
### 4.3.2 Microwave activation of MOF-808 and Optimisation

Upon exploring alternative methods for activating modulator bound Zr MOFs, the utility of microwave irradiation for this application was discovered. nMOF-808 was suspended in distilled water and sealed in a glass microwave reaction vessel. The vessel was then placed in a microwave reactor and subjected to microwave irradiation for 20 minutes at a temperature of 150 °C. The MOF powder was then filtered from solution, washed with acetone and vacuum dried to yield aMOF-808. To ensure that crystallinity had been retained, aMOF-808 was analysed using PXRD and the pattern was compared to that of nMOF-808. (Figure 4.7)



**Figure 4.7.** A PXRD overlay showing nMOF-808 (black), aMOF-808 (red), and aMOF-808 @ 200°C (blue).

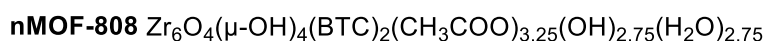
Upon confirming the retention of crystallinity, a procedure was required to analyse the composition of aMOF-808 and thus determine the ratio of acetate modulator to 1,3,5-benzene tricarboxylate linker in the framework. Digesting/chemically degrading MOFs with strong acids can yield their ligand composition to analysis. Using a strong acid, such as  $\text{H}_2\text{SO}_4$ , will strip away any linkers which are bound to the  $\text{Zr}_6\text{O}_4(\text{OH})_4^{12-}$  node, thus effectively degrading and solubilising the heterogeneous material and allowing the ligand ratio to be determined through NMR. Acid digestion was therefore chosen as a suitable technique for analysing the ligand composition of the frameworks. aMOF-808 was suspended in deuterated DMSO and several drops of  $\text{D}_2\text{SO}_4$  were added, the mixture was then heated with the aid of a heat gun until the MOF was fully dissolved. The resulting solution was then analysed using proton NMR. For a point of comparison, the same digestion procedure was utilised for nMOF-808, the composition of which was also analysed using proton NMR (Figure 4.8).



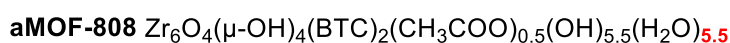
**Figure 4.8.** A proton NMR (in DMSO/ $\text{D}_2\text{SO}_4$ ) overlay showing acetic acid (green), as-synthesised (washed with  $\text{H}_2\text{O}$ ) digested nMOF 808 (black), free  $\text{H}_3\text{BTC}$  ligand (red) and the digested *activated* aMOF-808 (blue).

Figure 4.8 shows the digested  $^1\text{H}$  spectra of nMOF-808 and aMOF-808. By integrating the peaks representative of the  $\text{H}_3\text{BTC}$  linker and acetic acid, their ratio can be determined. MOF-808 possesses a 6-connected structure, this means that each  $\text{Zr}_6$  node has a linker connectivity

of 6. Each node therefore forms 6 linkages with 6 individual BTC<sup>3-</sup> linkers, this makes the average formula unit of pristine MOF-808 to be Zr<sub>6</sub>O<sub>4</sub>(OH)<sub>4</sub>(BTC)<sub>2</sub>(CH<sub>3</sub>COO)<sub>6</sub>.<sup>18</sup> For charge balance to occur, it is assumed that each vacancy which is not occupied by linker or modulator molecules, is instead occupied by a hydroxyl and a water molecule. This has been previously reported for zirconium MOFs with missing linker/modulator vacancies.<sup>25-27</sup> The formula of nMOF-808 was determined to be Zr<sub>6</sub>O<sub>4</sub>(μ-OH)<sub>4</sub>(BTC)<sub>2</sub>(CH<sub>3</sub>COO)<sub>3.25</sub>(OH)<sub>2.75</sub>(H<sub>2</sub>O)<sub>2.75</sub>, thus inferring that there are on average, 2.75 acetate free sites per formula unit. The formula of aMOF-808 was determined to be Zr<sub>6</sub>O<sub>4</sub>(μ-OH)<sub>4</sub>(BTC)<sub>2</sub>(CH<sub>3</sub>COO)<sub>0.5</sub>(OH)<sub>5.5</sub>(H<sub>2</sub>O)<sub>5.5</sub> with 5.5 acetate-free sites/coordination vacancies which are occupied by water from the activation procedure.



**2.75 acetate-free sites**



**5.5 acetate-free sites**

**Scheme 4.1.** A scheme showing the difference in acetate composition between nMOF-808 and aMOF-808, as determined by NMR (Figure 4.8).

The optimum microwave temperature for the activation to occur was found to be 150 °C, reinforced by the observation of PXRD data which showed that there was no loss of crystallinity after the activation procedure. When MOF-808 was subjected to an activation temperature of 200 °C, mild amorphization was observed by PXRD (aMOF-808 @ 200°C Figure 4.7). At a lower activation temperature of 120 and 140 °C, a higher ratio of acetate:linker was present post activation, as determined by NMR digestion. The same was found to be true for decreasing the duration of the activation, when MOF-808 was activated for 5 minutes at 150 °C there was a reduction in the acetate:linker ratio, as shown by NMR digestion (Figure 4.9). It should also be noted that activating at 150 °C and above results in the removal of residual DMF solvent from the MOF pores, this roughly coincides with the boiling point of DMF which is 153 °C. As a result of these observations, all future activations were performed at 150 °C for 20 minutes.

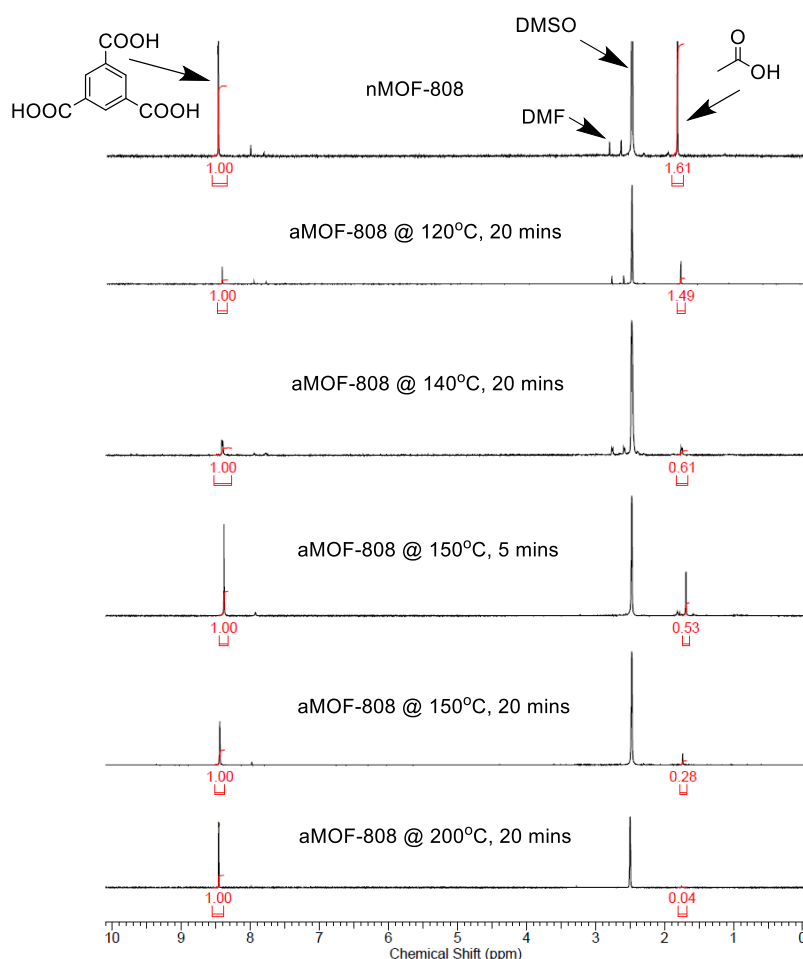


**Figure 4.9.** A proton NMR (in DMSO/D<sub>2</sub>SO<sub>4</sub>) overlay showing from (from top to bottom), as-synthesised (washed with H<sub>2</sub>O) digested nMOF-808, the digested *activated* aMOF-808 [120 °C for 20 minutes], the digested *activated* aMOF-808 [140 °C for 20 minutes], the digested *activated* aMOF-808 [150 °C for 5 minutes], the digested *activated* aMOF-808 [150 °C for 20 minutes] and the digested *activated* aMOF-808 [200 °C for 20 minutes].

### 4.3.3 Microwave activation of Acetate-Modulated MOFs

Upon realising a successful activation procedure for modifying nMOF-808 to form aMOF-808, the same activation technique was used to modify nDUT-84 and nUiO-66. nDUT-84 was subjected to the same activation procedure which involved microwave irradiation in H<sub>2</sub>O for 20 minutes at a temperature of 150 °C to yield aDUT-84. aDUT-84 was analysed using PXRD and compared to nDUT-84 (Figure 4.10).

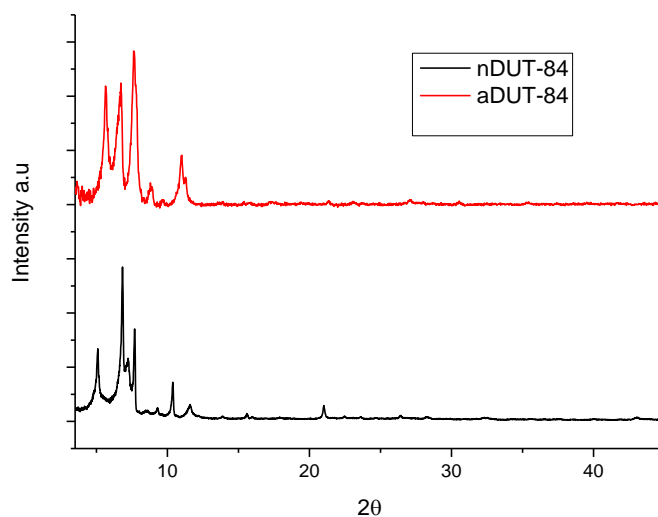


**Figure 4.10.** A PXRD overlay showing nDUT-84 (black) and aDUT-84 (red).

The activation of DUT-84 resulted in a transition to a ‘desolvated’ phase which was observed by the original authors upon utilising their own activation procedure.<sup>16</sup> However, this phase has not been formally characterized and so it is not possible to say whether the structure has changed considerably. Upon activation, aDUT-84 and nDUT-84 were both digested using deuterated DMSO/D<sub>2</sub>SO<sub>4</sub> and the resulting solutions were analysed using proton NMR to elucidate their ligand compositions.

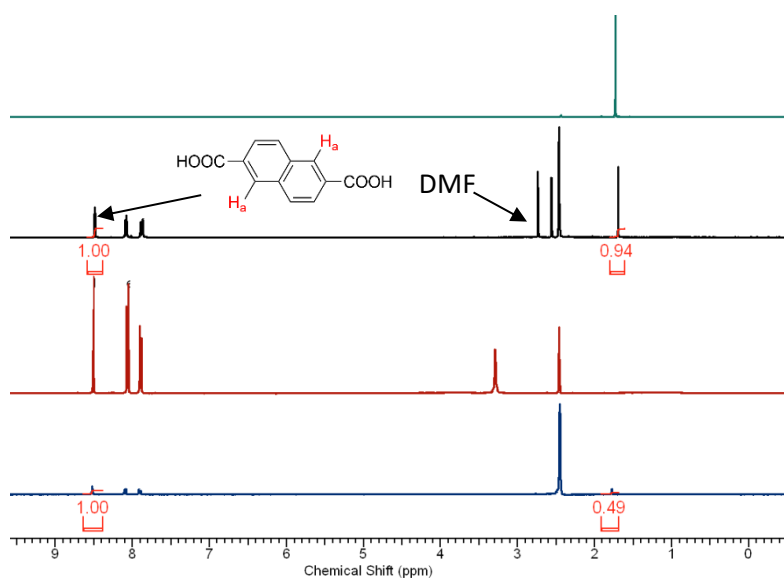


**Figure 4.11.** A proton NMR (in DMSO/D<sub>2</sub>SO<sub>4</sub>) overlay showing acetic acid (green), as-synthesised (washed with H<sub>2</sub>O) digested nDUT-84 (black), free H<sub>2</sub>NDC (red) and the digested *activated* aDUT-84 (blue).

Figure 4.11 shows the digested  $^1\text{H}$  spectra of nDUT-84 and aDUT-84. By integrating the peaks representative of the NDC linker and acetic acid, their ratio can be determined, DUT-84 has a ligand connectivity of 6.<sup>16</sup> The formula of nDUT-84 was therefore determined to be  $\text{Zr}_6\text{O}_4(\mu\text{-OH})_4(\text{NDC})_3(\text{CH}_3\text{COO})_{1.9}(\text{OH})_{4.1}(\text{H}_2\text{O})_{4.1}$ , thus inferring that there are on average, 4.1 acetate free sites per formula unit. The formula of aDUT-84 was assumed to be  $\text{Zr}_6\text{O}_4(\mu\text{-OH})_4(\text{NDC})_3(\text{CH}_3\text{COO})_1(\text{OH})_5(\text{H}_2\text{O})_5$  with 5 acetate-free sites/coordination vacancies which are occupied by water from the activation procedure. It should be noted that the formula for aDUT-84 is an approximation due to the fact that the phase change which occurs upon activation (Figure 4.10) is not structurally characterized.

**nDUT-84**  $\text{Zr}_6\text{O}_4(\mu\text{-OH})_4(\text{NDC})_3(\text{CH}_3\text{COO})_{1.9}(\text{OH})_{4.1}(\text{H}_2\text{O})_{1.9}$

**4.1 acetate-free sites**

**aDUT-84**  $\text{Zr}_6\text{O}_4(\mu\text{-OH})_4(\text{NDC})_3(\text{CH}_3\text{COO})_1(\text{OH})_5(\text{H}_2\text{O})_5$

**5 acetate-free sites**

**Scheme 4.2.** A scheme showing the difference in acetate composition between nDUT-84 and aDUT-84, as determined by NMR (Figure 4.11).

After the activation of DUT-84, nUiO-66 was activated using the same procedure which involved suspending the framework in water and subjecting it to microwave irradiation at 150 °C for 20 minutes. This yielded aUiO-66. aUiO-66 was then analysed using PXRD and compared to that of nUiO-66 (Figure 4.12), the activated framework retained its crystallinity.

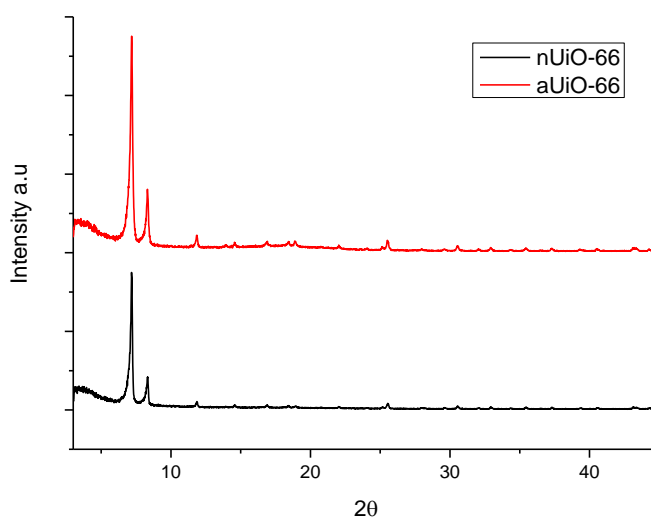


**Figure 4.12.** A PXRD overlay showing nUiO-66 (black) and aUiO-66 (red).

Upon activation, aUiO-66 and nUiO-66 were both digested using a mixture of deuterated DMSO/D<sub>2</sub>SO<sub>4</sub>, the resulting solutions were analysed using proton NMR.

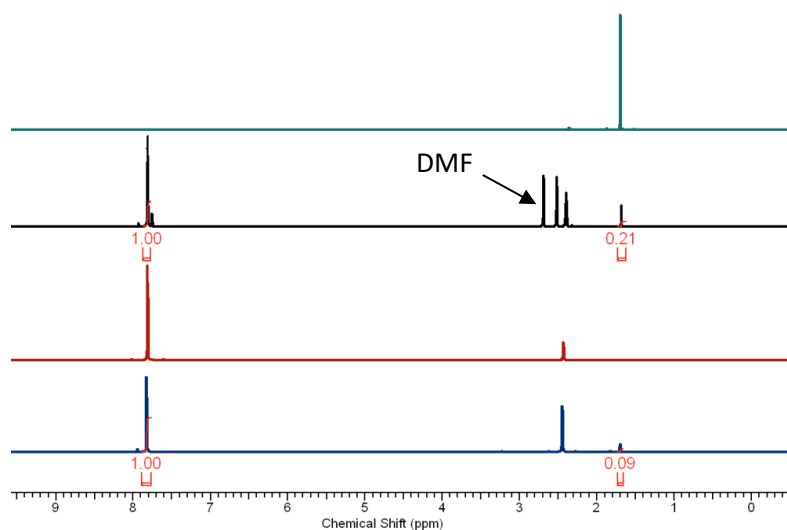
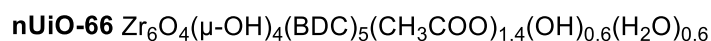
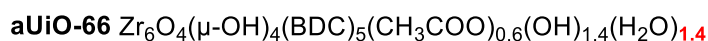


**Figure 4.13.** A proton NMR (in DMSO/D<sub>2</sub>SO<sub>4</sub>) overlay showing acetic acid (green), as-synthesised (washed with H<sub>2</sub>O) digested nUiO-66 (black), free H<sub>2</sub>BDC (red) and the digested *activated* aUiO-66 (blue).

Figure 4.13 shows the digested <sup>1</sup>H spectra of aUiO-66 and nUiO-66. By integrating the peaks representative of the BDC linker and acetic acid, their ratio can be determined, defective UiO-66 has ligand connectivity of 10.<sup>10</sup> The formula of nUiO-66 was therefore determined to be Zr<sub>6</sub>O<sub>4</sub>(μ-OH)<sub>4</sub>(BDC)<sub>5</sub>(CH<sub>3</sub>COO)<sub>1.4</sub>(OH)<sub>0.6</sub>(H<sub>2</sub>O)<sub>0.6</sub>, thus inferring that there are on average, 0.6 acetate free sites per formula unit. The formula of aUiO-66 was determined to be Zr<sub>6</sub>O<sub>4</sub>(μ-OH)<sub>4</sub>(BDC)<sub>5</sub>(CH<sub>3</sub>COO)<sub>0.6</sub>(OH)<sub>1.4</sub>(H<sub>2</sub>O)<sub>1.4</sub> with 1.4 acetate-free sites/coordination vacancies which are occupied by water from the activation procedure.



**0.6 acetate-free sites**



**1.4 acetate-free sites**

**Scheme 4.3.** A scheme showing the difference in acetate composition between nUiO-66 and aUiO-66, as determined by NMR (Figure 4.13).

In summary, partial removal of the acetate modulator was achieved for all activated MOFs. The complete extraction of residual DMF used in synthesis was also observed for all activated samples, showing that the activation procedure was also effective for DMF solvent evacuation. Each Zr<sub>6</sub>SBU can coordinate a total maximum of 12 carboxylate moieties. Table 4.1 summarises the degree of activation which was observed for each MOF. The most efficient exchange was achieved for MOF-808<sup>17</sup> (Figure 4.8) which has a linker connectivity of 6, with 2.75 acetate ligands removed per unit, leaving 5.5 free coordination sites. DUT-84 also has a linker connectivity of 6,<sup>16</sup> but only 0.9 acetates per formula unit were removed (Figure 4.11) resulting in 5 unmodulated sites. This is because the non-activated material possesses just 2 acetate modulated sites. aUiO-66 had the lowest quantity of acetate removed (Figure 4.13) per unit owing to its higher strut connectivity requiring 10 coordination sites,<sup>10</sup> this meant that there were fewer modulated vacancies. In summary, this activation method offers a quicker alternative for activation when compared to thermally activating at 200-300 °C under dynamic vacuum, a commonly reported activation method.<sup>4,13,28</sup>

**Table 4.1.** A comparison of the degree of activation achieved for each MOF based on the ratio of acetate to ligand, as calculated from <sup>1</sup>H NMR integrals.

	<b>uMOF-808</b>	<b>aMOF-808</b>	<b>uDUT-84</b>	<b>aDUT-84</b>	<b>uUiO-66</b>	<b>aUiO-66</b>
<b>Acetate:Ligand ratio</b>	1.62	0.26	0.6	0.33	0.22	0.07
<b>Acetate per unit</b>	3.25	0.5	1.9	1	1.4	0.6
<b>Exchange Efficiency</b>	-	<b>84.60%</b>	-	<b>47.30%</b>	-	<b>57.10%</b>
<b>Acetate removed</b>	-	<b>2.75</b>	-	<b>0.9</b>	-	<b>0.8</b>
<b>Acetate-free sites<sup>a</sup></b>	-	<b>5.5</b>	-	<b>5</b>	-	<b>1.4</b>

<sup>a</sup>The number of coordination sites per formula unit that are free of modulator This only applies to the activated counterpart of each MOF.

SEM micrographs were also obtained for each MOF before and after activation as shown in Figure 4.14. No visual change in particle size or morphology was observed post activation. Interestingly, the DUT-84 particles appear to be significantly larger than the particles of UiO-66

and MOF-808. The original reported procedure for the synthesis of DUT-84<sup>16</sup> requires 243 equivalents of acetic acid modulator relative to  $ZrCl_4$ . The large excess of modulator results in a slower, more controlled nucleation of DUT-84 crystals, thus leading to a larger particle size.

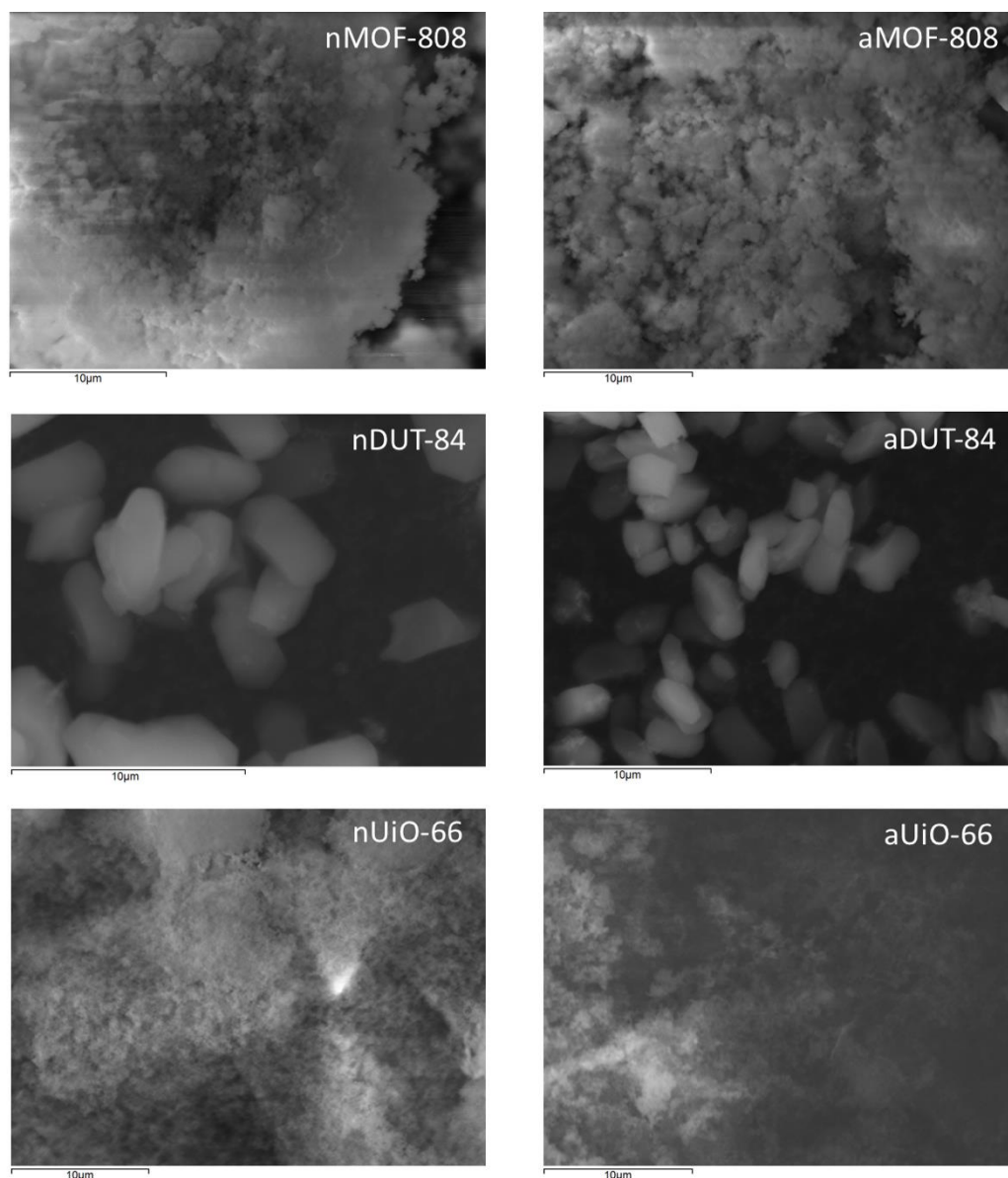


**Figure 4.14.** Scanning electron microscope (SEM) images of MOF-808, DUT-84 and UiO-66 before and after activation.

It should be noted that there were several MOFs which were not susceptible to activation using the microwave activation procedure. As a control, nUiO-66 (Benzoic acid) was synthesised using benzoic acid ( $pK_a = 4.20$ ) as a modulator. Upon subjecting this variant of UiO-66 to the microwave activation procedure, no change in ligand composition was observed

upon digestion of the framework. (Figure 4.15). This could be the result of a number of factors, acetic acid ( $pK_a = 4.76$ ) has a higher  $pK_a$  than benzoic acid and thus forms weaker coordination interaction with the the  $Zr^{4+}$  nodes.<sup>29</sup> Compared to acetic acid, benzoic acid also possesses a significantly lower solubility in  $H_2O$  at room temperature, thus making the exchange process less thermodynamically viable.

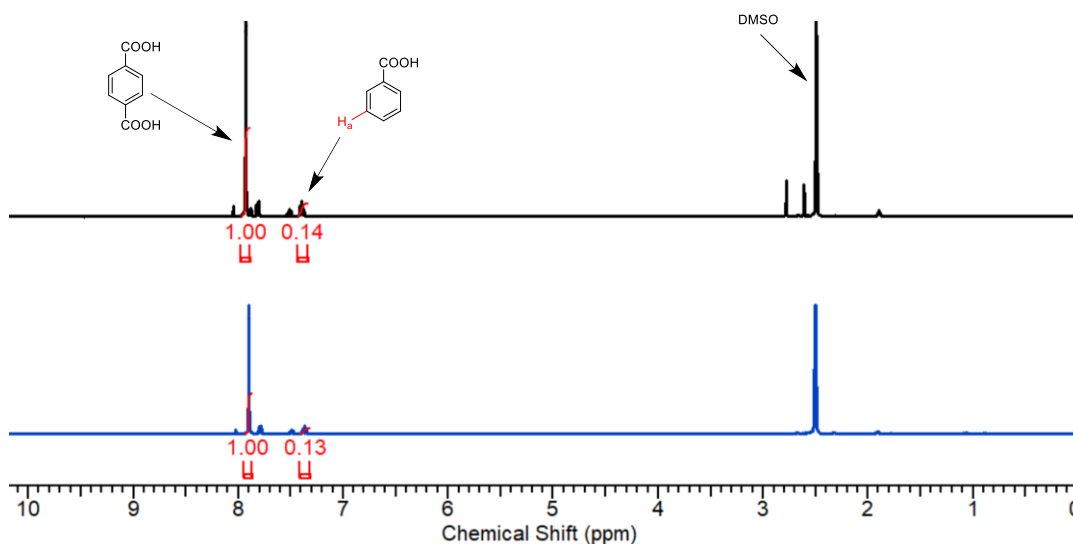


**Figure 4.15.** A proton NMR (in DMSO/ $D_2SO_4$ ) overlay showing as-synthesised (washed with  $H_2O$ ) digested nUiO-66 (Benzoic acid) (black) and the digested *activated* aUiO-66 (Benzoic acid) (blue).

In chapter 2, a 6-connected Zr-MOF was synthesised which was composed of a tritopic borane centred linker (Boron MOF). For the synthesis of Boron MOF, acetic acid was used to modulate the assembly, in a similar fashion to that of MOF-808. An attempt was made to activate this framework using the microwave procedure but upon digestion, there appeared to be minimal change in the ratio of acetic present (Figure 4.16). The increased electron-withdrawing effect provided by the borane linker on the  $Zr_6$  SBU would act to increase the lewis acidity of the uncoordinated  $Zr^{4+}$  nodes. This could potentially increase the stability of the bound acetate and therefore make it unsusceptible to activation using the procedure in this study. In chapter 2, NEM buffered hydrolysis experiments were conducted on the DMNP simulant in the presence of Boron MOF. A 6-connected Zr MOF would be expected to function as a potent

hydrolysis catalyst. It is possible that because Boron MOF is not prone to activation using the microwave procedure, the coordination strength of the bound acetate modulator is too great to be displaced by the DMNP substrate. This enhanced modulated node stability is therefore believed to make the catalytic  $Zr^{4+}$  inaccessible to the substrate. It would be of interest to see whether other MOF modulators, such as formic acid, propionic acid or L-proline could be removed using the microwave activation procedure described in this chapter.

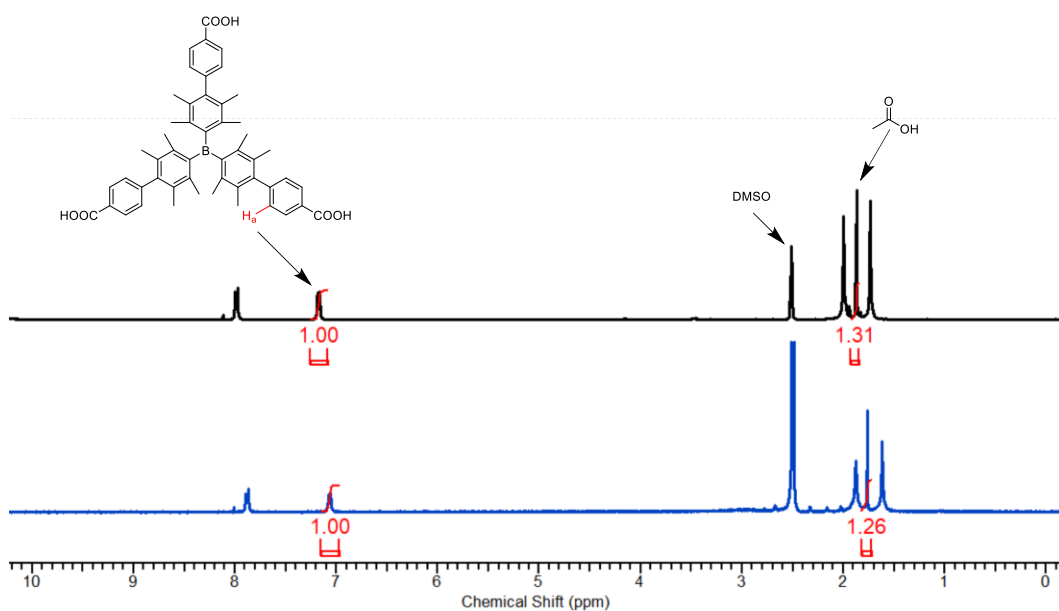


**Figure 4.16.** A proton NMR (in DMSO/ $D_2SO_4$ ) overlay showing as-synthesised (washed with  $H_2O$ ) digested nBoron MOF (black) and the digested *activated* aBoron MOF (blue).

#### 4.3.4 Thermal Analysis of Activated MOFs

Upon activating MOF-808, DUT-84, UiO-66 and characterising the degree of acetate removed using NMR, thermal data was then obtained for the as-synthesised and activated counterpart of each framework. Each activated and non-activated framework was annealed at  $100\text{ }^\circ\text{C}$  for 24 hours before analysis. For the TGA analysis, a heating rate of  $5\text{ }^\circ\text{C min}^{-1}$  in  $N_2$  was used. Each sample was also subjected to a 30 minute isotherm at  $150\text{ }^\circ\text{C}$ , this was to ensure the complete removal of any residual DMF/ $H_2O$  species which were not coordinated to the  $Zr_6$  nodes. The mass % remaining was noted for each sample at the end of the isotherm, this mass % was assumed to represent a guest-free MOF with empty pores. Post-isotherm, a second heating

ramp was employed and each sample was heated to 500 °C. The % mass loss was then determined between weight % at the start of the second ramp and at the end of the ramp. This was termed the 'Mass % Loss after 2<sup>nd</sup> ramp'. The mass % loss after 2<sup>nd</sup> ramp was meant to function as an indicator of linker and modulator loss upon heating. The TGA trace for nMOF-808 and aMOF-808 is shown in Figure 4.17. The TGA trace for nDUT-84 and aDUT-84 is shown in Figure 4.18. The TGA trace for nUiO-66 and aUiO-66 is shown in Figure 4.19.

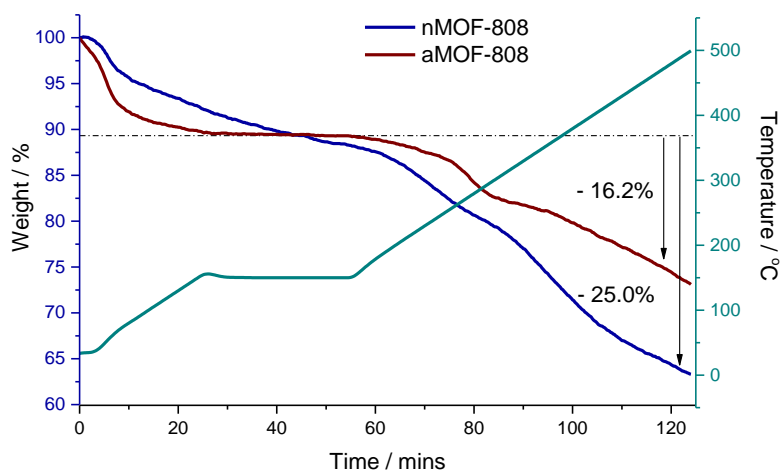


**Figure 4.17.** TGA trace for nMOF-808 and aMOF-808. Heating rate: 5 °C min<sup>-1</sup> in N<sub>2</sub>, 30 min isotherm at 150 °C followed by a ramp to 500 °C. A value for the Mass % Loss post isotherm until end of the final ramp is shown on the TGA trace for each material.

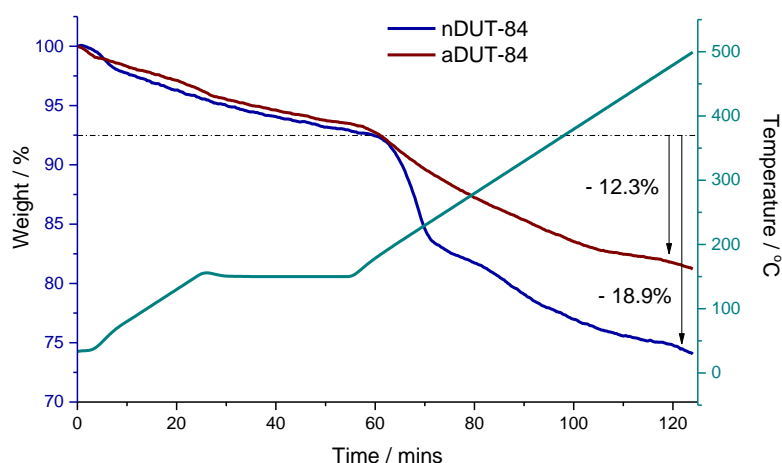


**Figure 4.18.** TGA trace for nDUT-84 and aDUT-84. Heating rate: 5 °C min<sup>-1</sup> in N<sub>2</sub>, 30 min isotherm at 150 °C followed by a ramp to 500 °C. A value for the Mass % Loss post isotherm until end of the final ramp is shown on the TGA trace for each material.

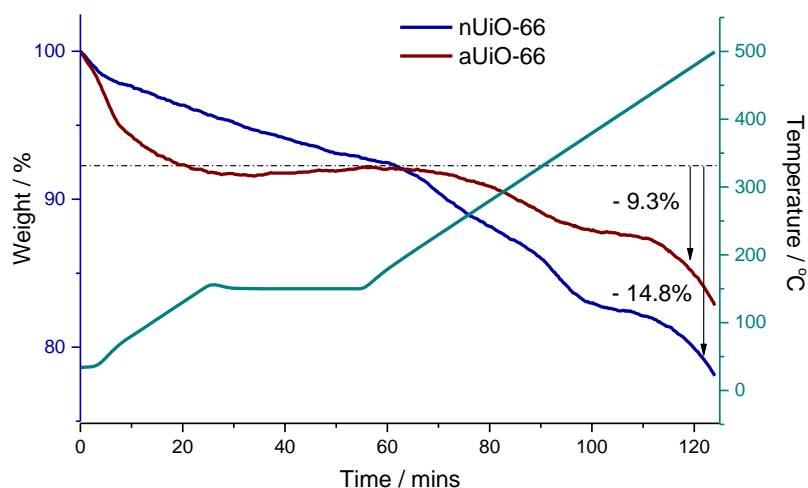


**Figure 4.19.** TGA trace for nUiO-66 and aUiO-66. Heating rate:  $5\text{ }^{\circ}\text{C min}^{-1}$  in  $\text{N}_2$ , 30 min isotherm at  $150\text{ }^{\circ}\text{C}$  followed by a ramp to  $500\text{ }^{\circ}\text{C}$ . A value for the Mass % Loss post isotherm until end of the final ramp is shown on the TGA trace for each material.

The mass % loss after 2<sup>nd</sup> ramp for each framework is summarised in Table 4.2. nMOF-808 and aMOF-808 showed the greatest mass % Loss after 2<sup>nd</sup> ramp. The large mass % loss for nMOF-808 can be attributed to the framework having the largest amount of bound acetate (Table 4.1). The second largest mass loss was observed for the DUT-84 variants. The UiO-66 variants showed the smallest reduction in mass % loss after 2<sup>nd</sup> ramp, this is likely due to the framework having the smallest number of bound acetate per unit cell. Particularly interesting was the greater thermal stability of all activated MOFs after the second ramp (Figure 4.17, 4.18, 4.19) which corresponded with each activated framework having less bound acetate. A 'Rel. Mass % Loss' was then calculated for each MOF (Table 4.2), this was to discount any mass % loss which occurred before the second ramp. The difference in rel. mass % loss between each activated and as-synthesised material was then calculated, this was denoted as 'Mass % Loss difference'. The mass % loss difference was used to highlight that a smaller mass % loss was observed for each activated MOF over that of the as-synthesised counterpart, as each activated MOF would contain less structurally-bound acetate. MOF-808 showed the greatest Mass % Loss difference (Table 4.2). This value can be ascribed to the activation process

removing approximately 2.75 equivalents of acetate from each formula unit of the MOF (Table 4.1), and the largest quantity of the three MOFs. This was followed by DUT-84 and then UiO-66, respectively. The thermal Mass % Loss difference for each of the analysed MOFs was in agreement with the quantity of acetate removed, as determined by NMR. Each activated MOF also displayed enhanced thermal stability post activation. It was not possible to determine any information regarding the composition of each MOF from the thermal data. This is because BTC, NDC and BDC linker decomposition all occur at different temperatures and so a specific thermal ramp sequence would be required for each MOF.

**Table 4.2.** A comparison of the weight loss observed during TGA analysis for the non-activated and activated MOFs.

	<b>nMOF-808</b>	<b>aMOF-808</b>	<b>nDUT-84</b>	<b>aDUT-84</b>	<b>nUiO-66</b>	<b>aUiO-66</b>
<b>Mass % Remaining after 150 °C isotherm<sup>a</sup></b>	88.30%	89.30%	93.00%	93.50%	92.90%	92.10%
<b>Mass % Loss after 2<sup>nd</sup> ramp<sup>b</sup></b>	25.00%	16.20%	18.90%	12.30%	14.80%	9.30%
<b>Rel. Mass % Loss<sup>c</sup></b>	28.30%	18.10%	20.30%	13.20%	15.90%	10.10%
<b>Mass % Loss difference<sup>d</sup></b>		<b>- 10.20%</b>		<b>- 7.10%</b>		<b>- 5.80%</b>

<sup>a</sup>Mass % Remaining after maintaining a 150 °C isotherm. <sup>b</sup>Mass % Loss after second ramp. <sup>c</sup>Relative Mass % Loss observed (b/a)\*100. <sup>d</sup>Difference in relative Mass % Loss between the activated and non-activated materials.

#### 4.4 DMNP Hydrolysis Enhancement

After determining the degree of activation using NMR, and inferring the loss of modulator using TGA, the hydrolytic capabilities of the activated MOFs were investigated and compared to their non-activated counterparts. Zirconium MOFs, particularly those with coordination defects, have been shown as highly effective hydrolysis catalysts for the degradation of organophosphate V- and G-series nerve agents along with the CWA simulant, DMNP.<sup>19,22</sup> A zirconium node-facilitated degradation mechanism has been previously proposed and is illustrated in Figure 4.20. First, a molecule of DMNP replaces a substitutionally labile water ligand on a Lewis acidic Zr site. The phosphoryl oxygen atom (P=O) then forms a strong interaction with a Zr atom. Upon this interaction forming, a hydroxyl anion from solution is able to attack the phosphorus atom which leads to the p-nitrophenoxide anion being released from the phosphorus species. The product is then desorbed from the Zr atom, thus regenerating the catalytic site.

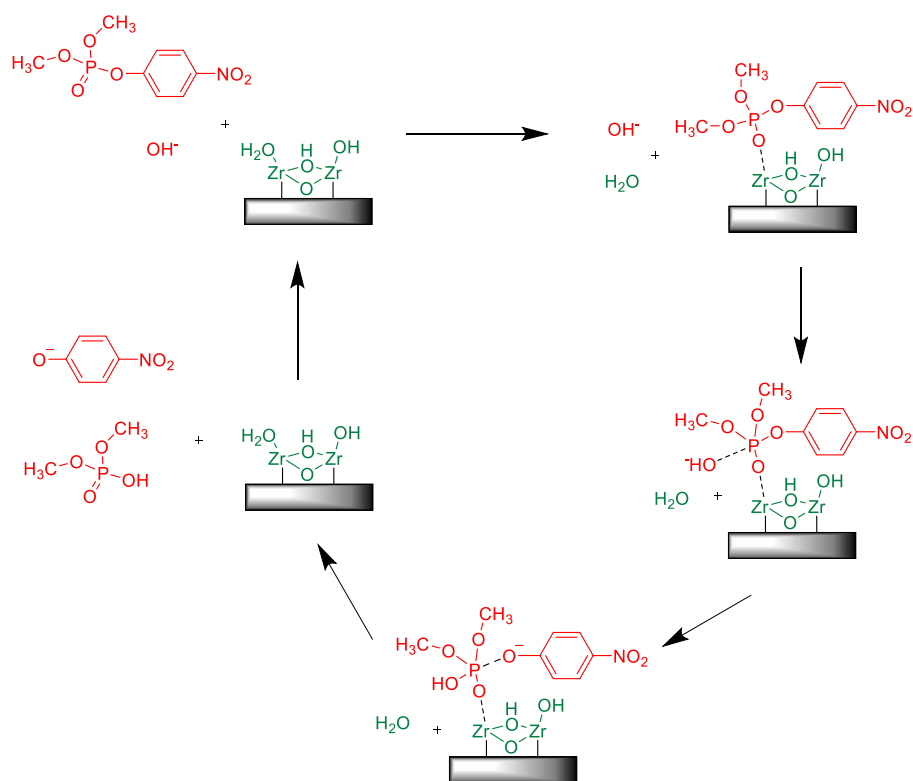
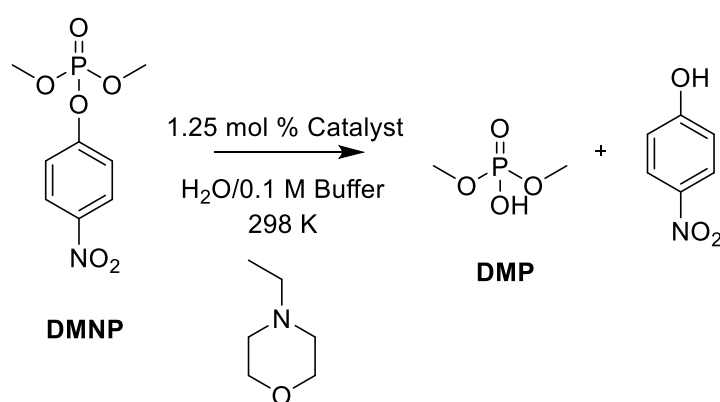


**Figure 4.20:** A reaction scheme illustrating the catalytic cycle of a DMNP molecule on the surface of a Zr<sub>6</sub> node.

In previous studies, DMNP, buffered with an aqueous solution of NEM, was established as good simulant system for mimicking the hydrolysis of VX (diisopropylaminoethyl O-ethyl methylphosphonothioate) in solution, with good agreement in the degradation rates. In a previously reported study, MOF-808, modulated with formic acid and with a catalytic loading of 5 mol % (relative to DMNP) was found to degrade DMNP in 0.4 M NEM buffer with a half-life of just 0.5 mins. A higher dilution buffer solution than convention (0.1 M vs 0.4 M) was therefore used in these studies along with a lower catalytic loading (1.25 mol % vs 5 mol %). Scheme 4.4 illustrates the DMNP hydrolysis conditions which were employed in this study.



**Scheme 4.4:** An illustration of the DMNP hydrolysis conditions which were employed in this study.

To summarise the hydrolysis procedure, an NMR tube was charged with DMNP followed by the addition of 1.25 mol % (relative to DMNP) of a corresponding as-synthesised or activated MOF catalyst. 0.1 M NEM buffer was then added to the tube along with a small amount of D<sub>2</sub>O, the tube was inverted 3 times and immediately placed in an NMR auto-sampler and analysed using <sup>31</sup>P NMR spectroscopy. The MOF-reaction suspension remained undisturbed for the remainder of the reaction. The probe temperature was set to 298 K throughout each experiment. The first measurement was obtained within 3 minutes of the reaction commencing. Subsequent measurements were obtained for a total of 3 hours. <sup>31</sup>P NMR spectroscopy was used to monitor the presence of peaks corresponding to DMNP and DMP. An example spectral overlay is shown in Figure 4.21. The peaks corresponding to DMNP and DMP were integrated, the

integrals were used to determine the % of DMNP which had been hydrolysed to DMP at each time interval. The reaction was followed by  $^{31}\text{P}$  NMR spectroscopy instead of fluorescence spectroscopy because later hydrolysis experiments involving V-series agents were monitored using NMR also.

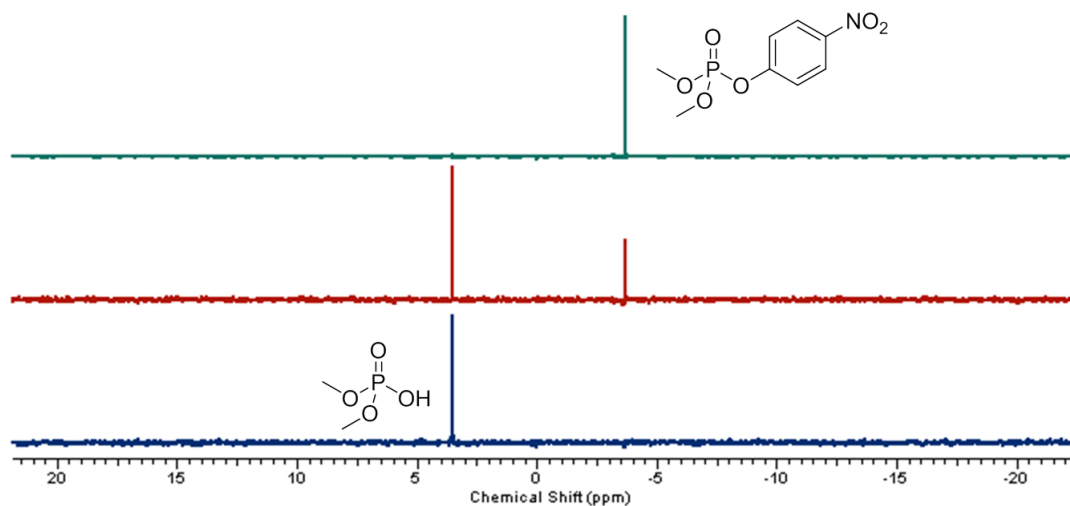


**Figure 4.21.** A  $^{31}\text{P}$  NMR overlay showing the different stages of DMNP hydrolysis that were observed before catalyst addition (green), 30 mins after the addition of 1.25 mol % aMOF-808 relative to substrate in 0.1 M NEM buffer (red), 24 hours after the addition of 1.25 mol % aMOF-808 relative to substrate in 0.1 M NEM buffer (blue).

The hydrolysis procedure was repeated in triplicate in the presence of the activated and non-activated counterpart of each MOF. All of the frameworks were able to hydrolyse DMNP to DMP to some degree over the course of the 3 hour reaction period. Unsurprisingly, nMOF-808 and aMOF-808 showed the greatest performance, this was followed by the DUT-84 counterparts and then the UiO-66 counterparts. Figure 4.22 summarises the results and shows the percent conversion of DMNP to DMP in the presence of the activated and non-activated catalysts in NEM buffer. It should also be noted that when the reaction was conducted using the same procedure but in the absence of a MOF catalyst, the background reaction rate was found to be negligible.

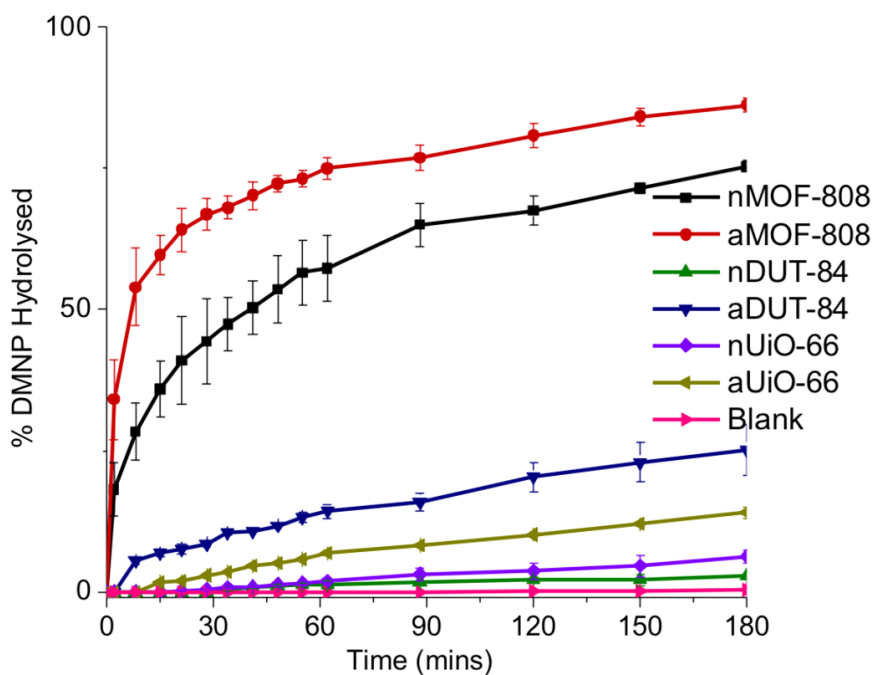


**Figure 4.22:** a plot showing the hydrolysis of DMNP over time in the presence of the various MOF catalysts. Each set of data was obtained in triplicate and is shown with standard deviation error bars.

The reaction rate of each reaction,  $k$ , was then calculated for each data set. This was performed by plotting the natural logarithm of DMNP concentration over time (Figure 4.23). Throughout the reaction, the concentration of MOF catalyst (regenerated as shown in Figure 4.20) and  $H_2O$  (present in excess) and the pH (buffered using NEM buffer) are assumed to remain constant. As the reaction progresses, only the concentration of DMNP changes, the degradation of DMNP would therefore be expected to follow pseudo first order kinetics with respect to the concentration of the DMNP substrate. For a first order/pseudo first order process, the slope of a line ( $m$ ), corresponds to  $k$  such that  $m = -k$ . A linear fit was obtained through the initial (15 – 63 minutes) data points of each MOF catalyst. The gradient of each linear fit therefore corresponded to the reaction rate  $k$  ( $s^{-1}$ ) of each MOF catalysed degradation.

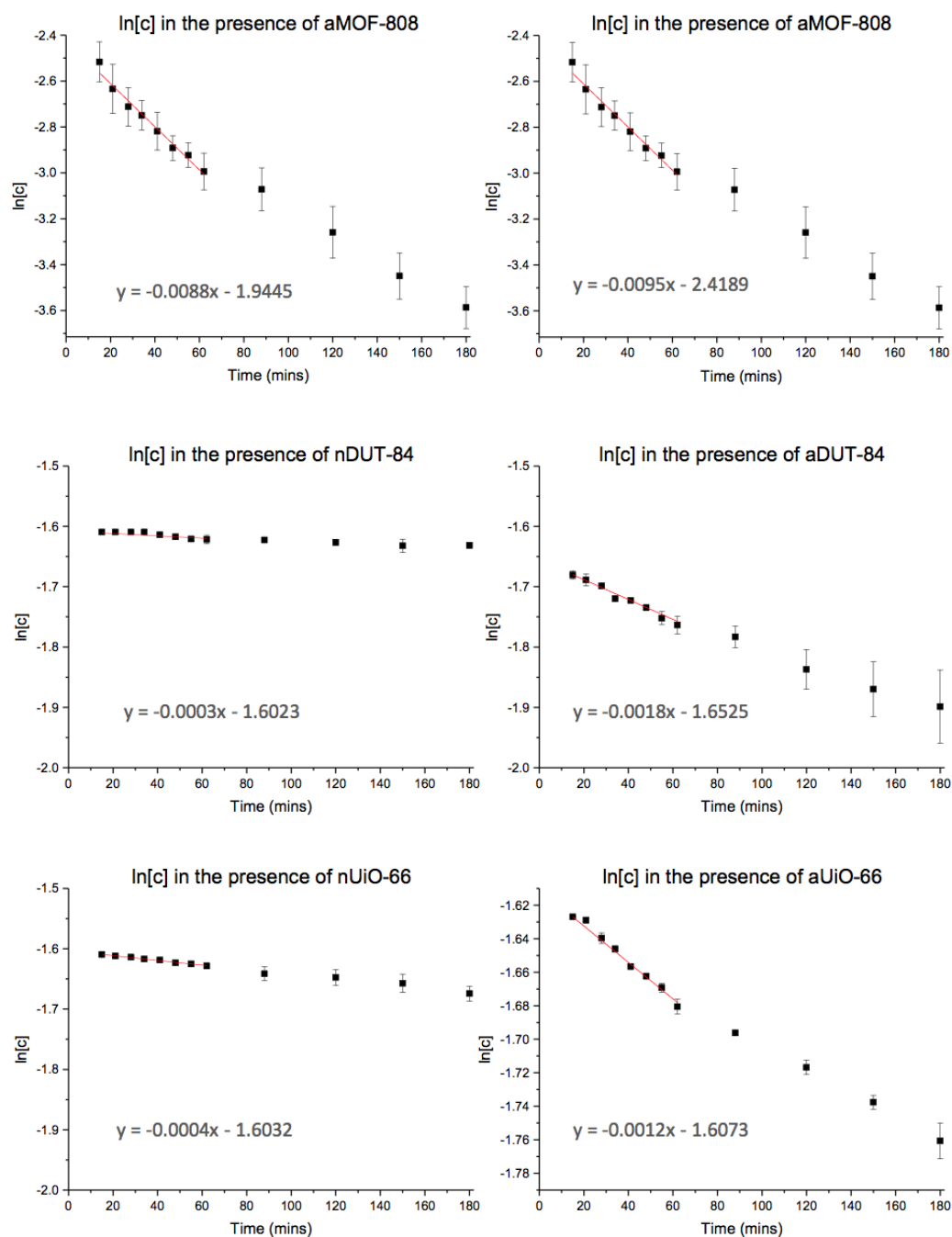


**Figure 4.23.** Natural logarithms of concentrations corresponding to DMNP residues in the presence of the as-synthesised and activated MOF catalysts. The first order rate constants were calculated using a linear fit (in Microsoft Excel) through the initial 8 data points for each catalyst to give a line with the equation  $y = mx + c$  where the slope,  $m$ , is the rate constant. The formulae for calculating  $m$  and  $c$  are shown below.

$$m = \frac{n\sum(xy) - \sum x\sum y}{n\sum x^2 - (\sum x)^2} \qquad c = \frac{\sum y - m\sum x}{n}$$

Table 4.3 shows the calculated degradation rates ( $s^{-1}$ ) of DMNP in the presence of each MOF catalyst. The table also states literature values for the limiting pore diameter ( $\text{\AA}$ ) and BET surface area ( $\text{m}^2 \text{g}^{-1}$ ) of each as-synthesised MOF. aMOF-808 was the most effective degradation catalyst ( $k = 9.5 \times 10^{-3} \text{ s}^{-1}$ ), closely followed by nMOF-808 ( $k = 8.8 \times 10^{-3} \text{ s}^{-1}$ ). This can be explained by the 6-connected nature of aMOF-808 along with the 5.5 acetate-free coordination sites (Table 4.1). These catalytic sites are Lewis acidic and are able to facilitate the hydrolysis of the substrate in the presence of  $\text{H}_2\text{O}$ . nMOF-808 performed slower in the initial stage of the reaction but still performed relatively well compared to the other tested materials. This performance can be attributed to nMOF-808 framework possessing, on average, 2.75 vacancies per  $\text{Zr}_6$  SBU. Both MOF-808 variants have a pore limiting diameter of ca.  $10 \text{ \AA}$  which is the largest of all the MOFs investigated here, and large enough to facilitate some access of DMNP ( $11 \times 4.5 \text{ \AA}$ ).

**Table 4.3.** A table showing the first order rate constants with respect to DMNP in the presence of the MOF catalysts. Literature values for the limiting pore diameter and BET surface area are also shown for comparison.

	$k \text{ (s}^{-1}\text{)}$	$k \text{ standard error}$	Limiting pore diameter ( $\text{\AA}$ )	BET ( $\text{m}^2 \text{g}^{-1}$ )
<b>nMOF-808</b>	0.0088	$3.8 \times 10^{-4}$	<b>10<sup>a</sup></b>	<b>1606<sup>a</sup></b>
<b>aMOF-808</b>	0.0095	$5.7 \times 10^{-4}$		
<b>nDUT-84</b>	0.0003	$2 \times 10^{-5}$	<b>7.57<sup>b</sup></b>	<b>637<sup>b</sup></b>
<b>aDUT-84</b>	0.0018	$1.5 \times 10^{-4}$		
<b>nUiO-66</b>	0.0004	$1 \times 10^{-5}$	<b>5<sup>c</sup></b>	<b>1525<sup>c</sup></b>
<b>aUiO-66</b>	0.0012	$4 \times 10^{-5}$		

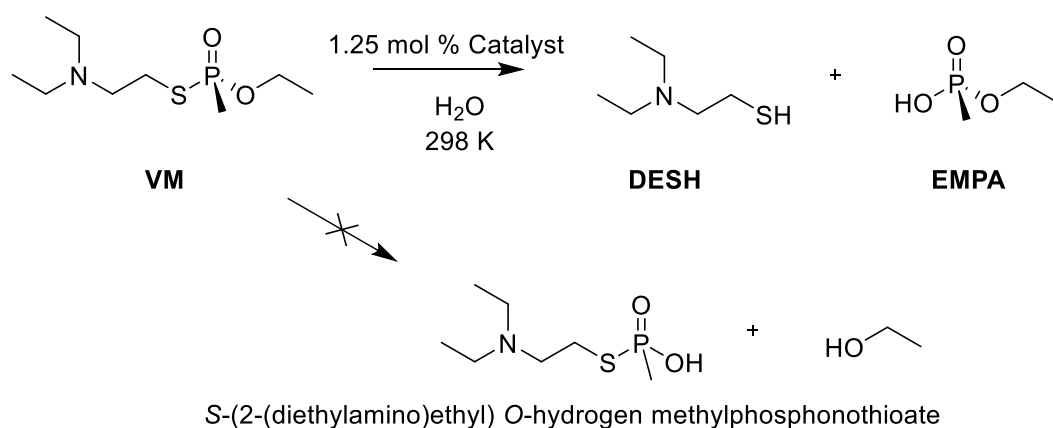
<sup>a</sup>Values obtained from reference 18. <sup>b</sup>Values obtained from reference 16. <sup>c</sup>Values obtained from reference 10.

DUT-84 is a 6-connected framework and so the hydrolysis rate was expected to be somewhat similar to that of MOF-808. The degradation was however significantly slower. A possible explanation for this is the difference in particle size as shown by SEM in Figure 4.14. The superior surface area/volume ratio of MOF-808 enhances the population of active surface sites. This diminishes the amount of catalysis occurring in the MOF voids which is less

kinetically favourable. This could suggest that the catalysis occurs primarily on the surface of the MOF. Despite the degradation being rather slow, the degradation rate for aDUT-84 was significantly enhanced ( $k = 1.8 \times 10^{-3} \text{ s}^{-1}$ ) over that of nDUT-84 ( $k = 3 \times 10^{-4} \text{ s}^{-1}$ ), simply through the activation protocol. UiO-66 was the worst performer of the group. This was expected as aUiO-66 ( $k = 1.2 \times 10^{-3} \text{ s}^{-1}$ ) has the smallest amount of acetate free sites compared to the other MOFs. The average pore limiting diameter in UiO-66 is ca.  $5 \text{ \AA}$ ,<sup>30</sup> which is smaller than the molecular size of DMNP. The catalytic activity is therefore restricted to just the surface of the framework, significantly reducing the number of accessible active sites.<sup>31</sup> Among the 3 MOFs tested, a general trend was observed where a higher pore limiting diameter correlated with a higher rate constant  $k$  for DMNP hydrolysis (Table 4.3). The MOF-808 and DUT-84 variants were selected for further testing on the V-series agent VM.

## 4.5 Zirconium MOFs as Hydrolysis Catalysts for live CWA Hydrolysis

After screening the three MOF catalysts with the DMNP simulant, MOF-808 and DUT-84 were selected for testing on the V-series agent VM, a diethyl analogue of VX, which was readily available at the time of testing. To further showcase the true applicability of the zirconium MOF-808 as a degradation catalyst, it was decided that the studies would be conducted in the absence of buffer (Scheme 4.5).



**Scheme 4.5:** An illustration of the VM hydrolysis conditions which were employed in this study.

Testing and data processing was conducted at Porton Down (DSTL) by Nicholas J. Cooper and James T. Jones. In brief, an NMR tube was charged with VM followed by the addition of 1.25 mol % (relative to DMNP) of a corresponding as-synthesised or activated MOF-808/DUT-84 variant. H<sub>2</sub>O then added to the tube along with a small amount of D<sub>2</sub>O, the tube was inverted 3 times and immediately placed in an NMR auto-sampler and analysed using <sup>31</sup>P NMR spectroscopy. The probe temperature was set to 298 K throughout each experiment. The first measurement was obtained within 12 minutes of the reaction commencing. Subsequent measurements were obtained for a total of 12 hours. <sup>31</sup>P NMR spectroscopy was used to monitor the presence of peaks corresponding to VM and EMPA. Diethyl dimethyldisphosphonate (DEM DP) was also formed during the reaction, presumably by the condensation of EMPA. An example spectral overlay is shown in Figure 4.24. This was used to determine the % of VX which had been hydrolysed to EMPA and DEM DP at each time interval.

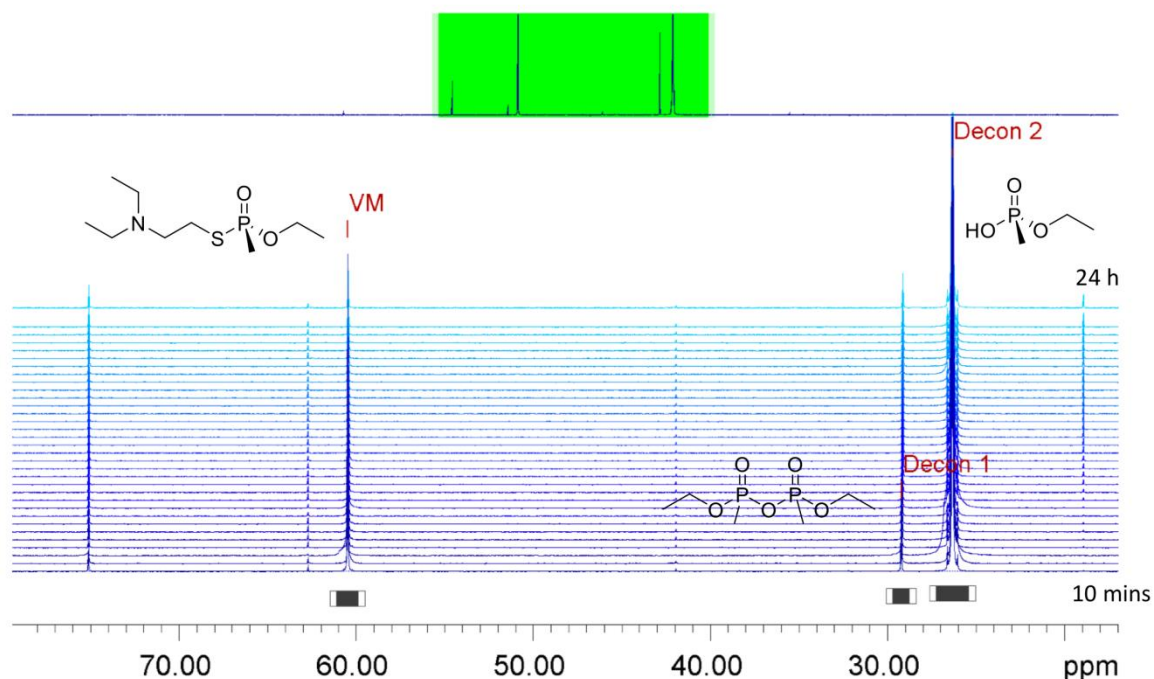


**Figure 4.24.** A  $^{31}\text{P}$  NMR overlay showing the different stages of VM hydrolysis in  $\text{H}_2\text{O}$  that were observed over 24 hours in the presence of 1.25 mol % nMOF-808 relative to VM.

Excellent results were obtained for both nMOF-808 and aMOF-808 (Figure 4.25). There was little discernible difference between the two catalysts because the first measurement could only be acquired 12 minutes after the reaction had commenced, at which point most of the VM had been hydrolysed. This was an unfortunate safety limitation of the experimental procedure. The first DUT-84 was also successful at hydrolysing VM, albeit, at a slower rate. As postulated, aDUT-84 significantly outperformed nDUT-84, and parallels with the simulant hydrolysis study. It should be noted that when the zirconium MOFs were used, only P–S bond cleavage of the VM occurred. A small amount of S-(2-(diethylamino)ethyl) O-hydrogen methylphosphonothioate ( $\delta$  - 42 ppm<sup>29</sup>) was present in the VM as a synthetic impurity, a small peak can be observed in Figure 4.24. However, this peak does not evolve throughout the course of the experiment which indicates that no P–O bond cleavage is occurring. The selective hydrolysis is highly desirable as the hydrolysis product formed from P–O bond cleavage of a V-series agent results in a product which maintains its toxicity.<sup>24</sup> For instance, hydrolysis with a

strong base such as NaOH which results in the competitive cleavage of both P–O and P–S bonds.<sup>32</sup> The above experiment further highlights the utility of these Zirconium MOFs for rapid and selective hydrolysis of V-series agents in the presence of only water (i.e. no buffer).

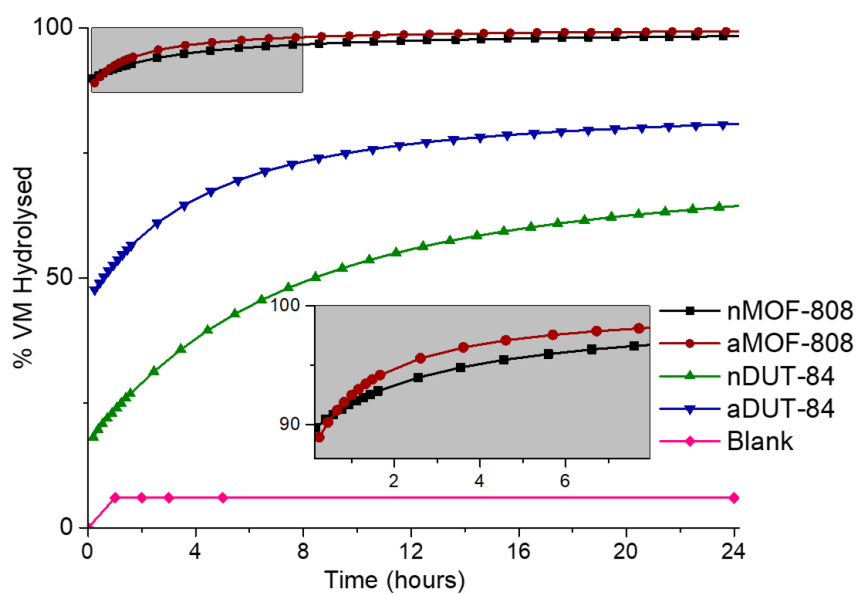


**Figure 4.25.** A degradation plot showing the hydrolysis of VM over time in the presence of the MOF catalysts. Inset: highlight of the slight difference between nMOF-808 and aMOF-808.

## 4.6 Conclusion

Three acetic acid modulated zirconium MOFs were activated using a novel, highly facile technique which relied on the use of microwave irradiation. Microwave irradiation enables instant and evenly distributed heating above boiling temperature, something which is difficult to achieve with an autoclave vessel. This method offers a quicker alternative for activation when compared to thermally activating at 200 - 300 °C under dynamic vacuum, a commonly reported method. The extent of activation was determined using NMR with MOF-808 showing the greatest degree of activation. The activation was reinforced by thermal analysis, a lesser Mass % Loss was observed for the activated counterpart of each MOF due to the structures possessing less bound acetate. The activated MOFs, which possessed a higher proportion of hydrated nodes (as opposed to acetate bound nodes), were then employed in the catalytic hydrolysis of the CWA simulant DMNP. An enhancement in hydrolysis rates was observed in comparison to each MOFs non-activated counterpart. It is hypothesised that replacing the  $Zr_6$  node bound acetate with  $H_2O$  resulted in a more labile coordination interaction which could be readily displaced by the DMNP substrate. Finally, the degradation ability of nMOF-808, aMOF-808, nDUT-84 and aDUT-84 was tested for the ability to degrade the V-series agent, VM, in the absence of buffer. The rate of hydrolysis was too fast to discern a rate difference between nMOF-808 and aMOF-808, however, a significant enhancement was observed for the slower aDUT-84 over that of nDUT-84. The non-buffered hydrolysis highlighted the utility of Zirconium MOFs for CWA hydrolysis using minimal reagents. Combining the CWA hydrolysis results of this chapter along with that of chapter 2, MOF-808 has been shown as a potent and selective degradant for 2 V-series agents, VX and VM, in the absence of a buffering agent. Since all V-agents are structurally similar and possess a P-S functionality, it can be assumed that MOF-808 would be active for the remaining V-agents also. MOF-808 would therefore be a good choice of catalyst in the development of future materials for V-agent hydrolysis.

## 4.7 References

- 1 Y. Liu, R. C. Klet, J. T. Hupp and O. Farha, *Chem. Commun.*, 2016, **52**, 7806–7809.
- 2 Y. Kalinovsky, N. J. Cooper, M. J. Main, S. J. Holder and B. A. Blight, *Dalton Trans.*, 2017, **46**, 15704–15709.
- 3 K. Užarević, T. C. Wang, S.-Y. Moon, A. M. Fidelli, J. T. Hupp, O. K. Farha and T. Friščić, *Chem. Commun.*, 2016, **52**, 2133–2136.
- 4 Y.-H. Huang, W.-S. Lo, Y.-W. Kuo, W.-J. Chen, C.-H. Lin and F.-K. Shieh, *Chem. Commun.*, 2017, **53**, 5818–5821.
- 5 S. Biswas and P. Van Der Voort, *Eur. J. Inorg. Chem.*, 2013, **2013**, 2154–2160.
- 6 M. Miyamoto, K. Hori, T. Goshima, N. Takaya, Y. Oumi and S. Uemiya, *Eur. J. Inorg. Chem.*, 2017, **2017**, 2094–2099.
- 7 R. Seetharaj, P. V. Vandana, P. Arya and S. Mathew, *Arab. J. Chem.*, 2019, **12**, 295–315.
- 8 C. Atzori, G. C. Shearer, L. Maschio, B. Civalieri, F. Bonino, C. Lamberti, S. Svelle, K. P. Lillerud and S. Bordiga, *J. Phys. Chem. C*, 2017, **121**, 9312–9324.
- 9 R. J. Marshall, C. L. Hobday, C. F. Murphie, S. L. Griffin, C. A. Morrison, S. A. Moggach and R. S. Forgan, *J. Mater. Chem. A*, 2016, **4**, 6955–6963.
- 10 G. C. Shearer, S. Chavan, S. Bordiga, S. Svelle, U. Olsbye and K. P. Lillerud, *Chem. Mater.*, 2016, **28**, 3749–3761.
- 11 S. Yuan, Y.-P. Chen, J.-S. Qin, W. Lu, L. Zou, Q. Zhang, X. Wang, X. Sun and H.-C. Zhou, *J. Am. Chem. Soc.*, 2016, **138**, 8912–8919.
- 12 L. T. M. Hoang, L. H. Ngo, H. L. Nguyen, H. T. H. Nguyen, C. K. Nguyen, B. T. Nguyen, Q. T. Ton, H. K. D. Nguyen, K. E. Cordova and T. Truong, *Chem. Commun.*, 2015, **51**, 17132–17135.

- 13 G. C. Shearer, J. G. Vitillo, S. Bordiga, S. Svelle, U. Olsbye and K. P. Lillerud, *Chem. Mater.*, 2016, **28**, 7190–7193.
- 14 J. Jiang, F. Gándara, Y.-B. Zhang, K. Na, O. M. Yaghi and W. G. Klemperer, *J. Am. Chem. Soc.*, 2014, **136**, 12844–12847.
- 15 E. López-Maya, C. Montoro, L. M. Rodríguez-Albelo, S. D. Aznar Cervantes, A. A. Lozano-Pérez, J. L. Cenís, E. Barea and J. A. R. Navarro, *Angew. Chem. Int. Ed.*, 2015, **54**, 6790–6794.
- 16 V. Bon, I. Senkovska, M. S. Weiss and S. Kaskel, *CrystEngComm*, 2013, **15**, 9572–9577.
- 17 H. Furukawa, F. Gándara, Y.-B. Zhang, J. Jiang, W. L. Queen, M. R. Hudson and O. M. Yaghi, *J. Am. Chem. Soc.*, 2014, **136**, 4369–4381.
- 18 W. Liang, H. Chevreau, F. Ragon, P. D. Southon, V. K. Peterson and D. M. D’Alessandro, *CrystEngComm*, 2014, **16**, 6530–6533.
- 19 J. E. Mondloch, M. J. Katz, W. C. Isley III, P. Ghosh, P. Liao, W. Bury, G. W. Wagner, M. G. Hall, J. B. DeCoste, G. W. Peterson, R. Q. Snurr, C. J. Cramer, J. T. Hupp and O. K. Farha, *Nat. Mater.*, 2015, **14**, 512–516.
- 20 S.-Y. Moon, G. W. Wagner, J. E. Mondloch, G. W. Peterson, J. B. DeCoste, J. T. Hupp and O. K. Farha, *Inorg. Chem.*, 2015, **54**, 10829–10833.
- 21 G. Stork and D. E. Kahne, *J. Am. Chem. Soc.*, 1983, **105**, 1072–1073.
- 22 Y. Liu, S.-Y. Moon, J. T. Hupp and O. K. Farha, *ACS Nano*, 2015, **9**, 12358–12364.
- 23 S.-Y. Moon, G. W. Wagner, J. E. Mondloch, G. W. Peterson, J. B. DeCoste, J. T. Hupp and O. K. Farha, *Inorg. Chem.*, 2015, **54**, 10829–10833.
- 24 E. Ghanem, Y. Li, C. Xu and F. M. Raushel, *Biochemistry*, 2007, **46**, 9032–9040.
- 25 N. Planas, J. E. Mondloch, S. Tussupbayev, J. Borycz, L. Gagliardi, J. T. Hupp, O. K. Farha

- and C. J. Cramer, *J. Phys. Chem. Lett.*, 2014, **5**, 3716–3723.
- 26 T. C. Wang, N. A. Vermeulen, I. S. Kim, A. B. F. Martinson, J. F. Stoddart, J. T. Hupp and O. K. Farha, *Nat. Protoc.*, 2016, **11**, 149–162.
- 27 S.-Y. Moon, Y. Liu, J. T. Hupp and O. K. Farha, *Angew. Chem. Int. Ed.*, 2015, **54**, 6795–6799.
- 28 H. R. Abid, J. Shang, H.-M. Ang and S. Wang, *Int. J. Smart Nano Mater.*, 2013, **4**, 72–82.
- 29 P. Lu, Y. Wu, H. Kang, H. Wei, H. Liu and M. Fang, *J. Mater. Chem. A*, 2014, **2**, 16250–16267.
- 30 M. J. Katz, Z. J. Brown, Y. J. Colón, P. W. Siu, K. A. Scheidt, R. Q. Snurr, J. T. Hupp and O. K. Farha, *Chem. Commun.*, 2013, **49**, 9449–9451.
- 31 A. J. Howarth, Y. Liu, P. Li, Z. Li, T. C. Wang, J. T. Hupp and O. K. Farha, *Nat. Rev. Mater.*, 2016, **1**, 15018.
- 32 Y.-C. Yang, *Acc. Chem. Res.*, 1998, **32**, 109–115.

## Chapter 5. MOF/HIPE Composites for the Encapsulation and Degradation of VX

The work described in this chapter was part of an on-going collaboration with A. Wright, at the University of Kent. All polymer synthesis was conducted by A. Wright. Additionally, swelling studies, IR analysis, MAS NMR analysis and SEM analysis were all undertaken by A. Wright. All hydrolysis studies involving DMNP, along with MOF synthesis and PXRD analysis were conducted by the author of this thesis. All hydrolysis experiments involving the agent VX were completed by N. Cooper at DSTL.

### 5.1 Introduction

This penultimate chapter shall explore the marriage of two works. The end objective of this research is to develop a composite material able to both encapsulate and degrade organophosphorus nerve agents in the absence of excessive chemical reagents. In chapter 4, MOF-808 was identified as the most suitable zirconium MOF catalyst for the buffered hydrolysis of the OP CWA simulant DMNP. Additionally, MOF-808 was able to rapidly degrade the V-series agent VM in water without any buffering agents being present.<sup>1</sup> Over a longer timeframe, MOF-808 is also able to hydrolyse VX with sole reliance on atmospheric humidity (see chapter 2). MOF-808 was shown to be the most suitable candidate for incorporation into a composite material. This chapter describes a novel composite material for the encapsulation and degradation of neat VX in the absence of any excess chemical reagents.

A number of MOF-polymer composites have been reported for the degradation of OP CWAs. Zhao et al. reported the growth of UiO-66, UiO-66-NH<sub>2</sub> and UiO-67 on the surface of electrospun polymeric nanofibers of polyamide-6 (PA-6).<sup>2</sup> This study reported the first example of a MOF-polymer composite that was able to degrade OP CWAs. However, the degradation relied on the presence of a liquid buffering agent. Liang et al.<sup>3</sup> reported flexible, free-stranding ZrO<sub>2</sub> nanofiber mats functionalised with either UiO-66, UiO-67 or UiO-66-NH<sub>2</sub>. These

functionalised nanofiber mats exhibited enhanced DMNP hydrolysis performance when compared to the corresponding UiO-66, UiO-67 and UiO-66-NH<sub>2</sub> powders. However, the study was again conducted in the presence of a liquid buffering agent and no hydrolysis studies were performed on OP CWAs. The most compelling composite was documented by Moon et al.<sup>4</sup> who reported on the synthesis of a composite material featuring the MOF NU-1000 embedded in a polyethyleneimine (PEI) membrane (NU-1000/PEI). This composite could degrade DMNP without a solution buffer present, this was due to the presence of heterogeneous basic amine in the PEI framework. This composite was also able to facilitate the degradation of VX with a calculated TOF of 19.4 h<sup>-1</sup>. None of the above described composites have been shown to additionally swell OP CWAs, degrade CWAs in the absence of a stoichiometric buffering agent nor degrade neat OP CWAs.

PolyHIPEs are a category of porous polymers possessing a large internal volume.<sup>5</sup> A HIPE is defined as an emulsion with an internal phase greater than 74 % of the total volume.<sup>6</sup> For HIPE formation to occur, two immiscible liquid phases are required. For a water-in-oil HIPE, the internal phase is always water and the external phase is composed of an oil/organic liquid containing the monomers and initiators.<sup>7</sup> The emulsion is stabilised by the use of a surfactant and the polyHIPE is then formed through the polymerization of the external phase. Removal of the internal phase results in a highly porous and interconnected polymer structure characterized by a low bulk density (< 0.1 g cm<sup>-3</sup>).<sup>8-10</sup> PolyHIPEs have found a number of applications as solid supports and membranes for chemical reactions,<sup>11-13</sup> absorptions<sup>8,14,15</sup> and separations.<sup>8,16,17</sup> The absorption properties of polyHIPEs make them ideal candidates as immobilization agents for the encapsulation of CWAs.

In parallel to the work carried out in this thesis, research performed by Alexander Wright has been focussed on identifying a suitable encapsulation agent. Previously reported styrenyl-monomer based ionic polymers were explored due to their high affinities and swelling capacities for a range of organic solvents.<sup>18</sup> Wright et al.<sup>19</sup> then reported on a styrenyl-HIPE,

crosslinked with divinyl benzene and possessing an internal phase greater than 95 % by volume, has shown remarkable swelling capacities (Q) for the uptake of CWAs. Swelling capacity (Q) can be defined as the following  $Q = (\text{weight of swollen polymer} - \text{weight of dry polymer}) / \text{weight of dry polymer}$ . Initial swelling experiments were conducted with the absorption simulant, methyl benzoate. Record high swelling values were then reported for VX (Q > 50) and HD (Q > 40), moderate swelling was reported for GB (Q > 20), although this swelling was still in line with other leading materials reported in the literature.<sup>20</sup> The initial uptake of the agent is facilitated through capillary forces which draw the liquid in. The compatibility between the agent and the internal phase results in further swelling of the polymer matrix, enabled by a low crosslinking-density.

Numerous reports have also been made of polyHIPEs that were assembled in the presence of nano-particulate sized heterogeneous materials, thus resulting in a composite structure.<sup>21-23</sup> Conveniently, nanoparticles can increase the stability of a HIPE emulsion thus making the synthesis of composite materials a highly facile procedure.<sup>24,25</sup> We can therefore surmise that it is possible to alternatively incorporate a heterogeneous catalyst into the HIPE polymer membrane. The resulting composite would function as a reactive, super-absorbent sponge capable of absorbing and reacting with the absorbate.

Two separate materials have been identified; the catalyst MOF-808 which is effective at 1.25 mol % for the degradation of V-series agents and a Polystyrene HIPE with VX swelling capacities exceeding 4000 weight % relative to the weight of the unswollen polymer. For a styrenyl pHIPE in VX, Q > 40 was achieved with methyl benzoate.<sup>19</sup> Both of the aforementioned materials fulfil the criteria of being effective at their respective application in low quantities. The focus of this chapter shall be the synthesis of a composite material which contains a dual functionality for the absorption and degradation of V-series agents.

In this chapter, the facile synthesis and characterization of a working, and readily scalable, MOF-HIPE prototype is reported. Preliminary NEM buffered hydrolysis tests are performed on

the simulant methyl-paraoxon (DMNP) and are shown to be successful. An improved rate of hydrolysis is observed with the composite material when compared to just MOF-808 alone. Swelling experiments were also conducted on methyl benzoate and no loss in swelling capacity was observed. The hydrolysis of phosphonate esters relies on H<sub>2</sub>O, and it is therefore imperative that water be able to enter the polymer matrix in which the MOF-808 catalyst is contained. It is demonstrated that by not removing the surfactant utilised during HIPE formation (MOF-HIPE-S; the S suffix indicates the surfactant), greatly improved water absorption properties are observed. Inspired by the previously reported NU-1000/PEI composite which houses a heterogeneous amine,<sup>4</sup> the tertiary amine, 4-vinylbenzyl piperidine<sup>26</sup> (4-VBPP) was selected as a suitable monomer for incorporation into a composite. The synthesis of a MOF-HIPE composite containing the 4-VBPP monomer (MOF-HIPE-VBPP-S) is then reported. When MOF-HIPE-VBPP-S was screened using a non-buffered DMNP hydrolysis system, a stoichiometric hydrolysis of DMNP relative to the quantity of 4-VBPP monomer is observed.

A number of hydrolysis tests were then conducted on the V-series agent VX. Degradation studies were performed on VX in the presence of the composites under neat conditions (ambient humidity, no buffer, no solvent) and alternatively in an aqueous mixture of H<sub>2</sub>O/THF. The collaborative effort was then concluded by reflecting on the strengths of the new composite material for the desired application when compared to existing technologies. The limitations of the work are also explored as are proposed improvements for enhancing the practical applicability of future composite materials.

## 5.2 Experimental Methods

### Instrumentation

$^1\text{H}$  and  $^{31}\text{P}$  NMR spectroscopy was conducted using a Bruker NEO 400 MHz spectrometer with an auto-sampler at 298 K and 16 scans per measurement.

PXRD patterns were collected on a silicon zero-background sample holder (a sample holder which presents no diffraction peaks) on a Rigaku Miniflex 600 desktop XRD using a Copper K- $\alpha$  (1.5406 Å) source. Measurements were taken in the 3 – 45 °  $2\theta$  range with a step size of 0.02 °  $2\theta$  and a scan speed of 1 °  $2\theta$  min $^{-1}$ .

Electron micrographs were gathered using a Hitachi S-3400 scanning electron microscope. The polymer samples were prepared for SEM by drying thoroughly and then cutting into thin slices with care taken to not disrupt or damage the surface of the sample.

Infra-red spectroscopy was carried out on a Shimadzu IRAffinity-1S, with an ATR gate, a sweep of 500 - 4000 cm $^{-1}$ , a resolution of 0.5 cm $^{-1}$  and 64 scans.

### $^1\text{H}$ MAS NMR Analysis

In solution-phase NMR, anisotropic effects are time-averaged by the random motion of the liquid analytes. However, in solid-state NMR, solid analytes exhibit anisotropic interactions which result in very broad spectra. MAS NMR is used for the analysis of solid or gel materials.

<sup>27</sup> The anisotropy of solid analytes can be negated by spinning an anisotropic sample at the magic angle (54.736 °) with respect to the magnetic field and at a high rotational frequency (5 to 35 kHz).  $^1\text{H}$  MAS NMR were acquired using a Bruker NEO 400 MHz spectrometer at 295 K. The samples were analysed using an HR-MAS semi-solids probe which utilised magic-angle spinning (54.736 °) at a frequency of 5000 Hz. The relaxation delay was set to 60 seconds.

### Synthesis of DUT-52

DUT-52 was synthesised and characterised using the same procedure as outlined in chapter 2.

### **Synthesis of MOF-808**

MOF-808 was synthesised and characterised using the same procedure as outlined in chapter 2.

### **Synthesis of 4-vinylbenzyl piperidine**

Piperidine (5.8 ml, 5 g, 85.15 g/mol, 0.06 mol) was dissolved in 50 ml MeCN. 4-vinylbenzyl chloride (8.5 ml, 9.15 g, 152.62 g/mol, 0.06 mol) was then added dropwise to the solution along with a flake of 4-tert-butylcatechol inhibitor. 4-tert-butylcatechol acts as a proton-donor, this effectively stabilises any free radicals and prevents the reaction of these radicals with the vinyl group. This was followed by the addition of potassium carbonate (16 g, 138.205 g/mol, 0.12 mmol). The mixture was refluxed at 120 °C for 2 hours. The mixture was subsequently allowed to ambiently cool to room temperature over half an hour and then chilled using an ice bowl and the resulting white precipitate was filtered off and washed with MeCN. Another flake of 4-tert-butylcatechol inhibitor was added to the filtrate. The filtrate was concentrated under reduced pressure to yield a pale-yellow oil which was filtered through an alumina column before use. (8.167 g, 201.30 g/mol, 39 mmol, 65 % yield)

$^1\text{H}$  NMR (400 MHz,  $\text{CDCl}_3$ ):  $\delta$  1.37-1.41 (m, 2H), 1.50-1.56 (m, 4H), 2.33 (m, 4H) 3.42 (s, 2H), 5.18 (d, 1H,  $J = 10.6$  Hz), 5.69 (d, 1H,  $J = 17.4$  Hz), 6.67 (dd, 1H,  $J = 10.9$  Hz, 17.4 Hz), 7.21-7.33 (m, 4H).  $^{13}\text{C}$  NMR (100.52 MHz,  $\text{CDCl}_3$ ):  $\delta$  24.4, 26.0, 54.5, 63.6, 113.3, 125.9, 129.4, 136.2, 136.7, 138.3.

### **General procedure for HIPE Formation (Performed by Alexander J. Wright)**

The following procedure outlines the general synthesis of a HIPE, the specific quantities for each formulation can be found in Table 5.1. The monomers, initiator (AIBN) and surfactant (span-80 (sorbitan monooleate)), were added into a 100 ml conical flask. The flask was stirred at 200 rpm with a 4 cm hemispherical PTFE overhead stirred paddle for 5 minutes to homogenize the oil phase. The aqueous phase was then prepared. Potassium sulfate was dissolved into deionized water. In the cases where a MOF was present, this was added into the

aqueous solution at a loading of 0.535 g (25 wt % [monomers]), after having been ground by hand to a fine powder. The aqueous phase was then vigorously mixed to suspend the MOF, but not sonicated. This agitation was continued throughout the addition of the aqueous phase to the organic to ensure good homogeneity of the MOF. The stirring speed of the organic mixture was increased to 750 rpm and the aqueous solution was dropped in at rate of around 1 drop per second. After all the aqueous phase was added, the stirring speed was increased further to 1000 rpm and left to homogenize for 5 minutes. The HIPE foam was transferred into a glass container, sealed and cured in an oven at 65 °C for 24 hours. After curing, the pHIFE monoliths were cooled and the vials destroyed to leave two samples of pHIFE. They were then dried under vacuum at 65 °C for 48 hours minimum. For HIPE and MOF-HIPE, surfactant was removed by soaking in ethanol for 24 hours followed by filtration and vacuum drying.

**Table 5.1:** A table outlining the masses of reagents used for the synthesis of each pHIFE discussed in this study.

Sample	Styrene	VBCI	VBPP	DVB	AIBN	SMO	Water/ K <sub>2</sub> SO <sub>4</sub>	MOF
HIPE	7.509g	0.579g	n/a	0.099	0.015g	1.65g	155ml/0.5g	n/a
DUT-HIPE	0.751g	0.058g	n/a	0.01	0.003g	0.17g	9.2ml/0.05g	0.205g
MOF-HIPE	1.344g	0.347g	n/a	0.020	0.006g	0.34g	32.5ml/0.1g	0.425g
MOF-HIPE-S	1.877g	0.145g	n/a	0.025g	0.004g	0.626g	38.9ml/0.13g	0.535g
HIPE-VBPP-S	1.778g	0.145g	0.191g	0.025g	0.004g	0.626g	39.8ml/0.13g	0.535g
MOF-HIPE-VBPP-S	1.778g	0.145g	0.191g	0.025g	0.004g	0.626g	39.8ml/0.13g	0.535g

VBCI – 4-vinylbenzyl chloride, VBPP - 4-vinylbenzyl piperidine, DVB – divinylbenzene, AIBN – azobisisobutyronitrile, SMO – sorbitan monooleate

### **Swelling with methyl benzoate procedure (performed by Alexander J Wright)**

A cube of chosen pHIPE composite of mass c. 150 mg submerged in methyl benzoate for 24 hours. The cube was then removed from the methyl benzoate, dabbed onto filter paper and re-weighed. The difference in weight was used to determine the degree of swelling.<sup>19</sup>

### **Buffered DMNP hydrolysis procedure**

The following procedure was used to probe the hydrolysis rates of the various MOF and polymer composite materials using a buffered simulant screening system. The HIPE containing MOF-808 (3.2 mg, 0.11  $\mu\text{mol}$ , 1.25 mol %) was sliced up into small pieces (1-2  $\text{mm}^3$ ), the pieces were then added to a single NMR tube along with DMNP, 20  $\mu\text{L}$  (0.09 mmol). A 0.6 ml mixture containing: 0.2 ml of  $\text{D}_2\text{O}$ , 0.2 THF and 0.2 ml of 1.45 M *N*-ethyl morpholine (NEM) aqueous buffer (effective concentration 0.45 M) was then added to the tube. The tube was inverted once and immediately loaded into an NMR auto-sampler and the first  $^{31}\text{P}$  NMR (161.83 MHz) spectrum was obtained within 8 minutes of the reaction commencing. The sample was then cycled on the auto-sampler to collect subsequent data points. Each measurement was performed in triplicate.

For the THF-free experiments, the same procedure was followed with the exception of the 0.2 ml of THF being replaced with an additional 0.2 ml of  $\text{H}_2\text{O}$ .

### **DMNP hydrolysis throughout sections of MOF-HIPE**

The following procedure was used to observe the difference in hydrolysis between different sections of MOF-HIPE. DMNP 120  $\mu\text{L}$  (0.54 mmol) was dissolved in a solution of 2.4 ml of  $\text{D}_2\text{O}$ , 2.4 ml THF and 2.4ml of 1.45 M NEM aqueous buffer (effective concentration 0.45 M), the solution was transferred to a petri dish. A single circular chunk of MOF-HIPE 200 mg (40 mg, 1.37  $\mu\text{mol}$ , 2.5 mol %) was placed in the centre of the dish with roughly half of the polymer being above the solution level. The reaction was covered with a watch glass and left for 3 hours. After 3 hours, the polymer was removed from the dish, a circular segment was then cut from the central half (half by radius) of the HIPE thus also leaving a circular outer half. The

contents of the central half were vacuum filtered and analysed using  $^{31}\text{P}$  NMR (161.83 MHz) spectroscopy. The contents of the outer half were also vacuum filtered and analysed using  $^{31}\text{P}$  NMR spectroscopy. Finally, an aliquot was taken from the remaining reaction mixture and analysed using  $^{31}\text{P}$  NMR spectroscopy.

### **MOF-HIPE-S Hydrolysis Cycling**

The following procedure was used to test the hydrolytic effectiveness of MOF-HIPE-S over 3 cycles. The HIPE containing MOF-808 (3.2 mg, 0.11  $\mu\text{mol}$ , 1.25 mol %) was sliced up into small chunks (1-2  $\text{mm}^3$ ) then added to the tube along with 0.6 ml mixture containing: 0.2 ml of  $\text{D}_2\text{O}$ , 0.2 THF and 0.2 ml of 1.45 M *N*-ethyl morpholine (NEM) aqueous buffer (effective concentration 0.45M). The tube was inverted once and left to stand for 24 hours. After 24 hours, the tube was analysed using  $^{31}\text{P}$  NMR (161.83 MHz) spectroscopy. The HIPE was then removed from the tube, washed 5 times with THF and re-used in the same manner as described above. This was repeated two more times to give a total of 3 cycles.

### **Non-Buffered DMNP hydrolysis procedure**

The following procedure was used to probe the hydrolysis rates of the MOF-HIPE-VBPP-S polymer composite material using a non-buffered simulant screening system. 5 NMR tubes were each charged with DMNP, 5  $\mu\text{L}$  (0.02 mmol). HIPEs were all sliced up into small chunks (1-2  $\text{mm}^3$ ). Various quantities of MOF-HIPE-VBPP-S were used (32.5mg, 16.5 mg and 8 mg) along with MOF-HIPE-S (32.5 mg) and MOF-808 (5.2 mg). MOF-HIPE-VBPP-S (32.5 mg) contained MOF-808 (5.2 mg, 0.18  $\mu\text{mol}$ , 14.5 mol %) and 4-vinylbenzyl piperidine. MOF-HIPE-VBPP-S (16.5 mg) contained MOF-808 (2.7 mg, 0.09  $\mu\text{mol}$ , 7.3 %) and 4-vinylbenzyl piperidine. MOF-HIPE-VBPP-S (8 mg) contained MOF-808 (1.3 mg, 0.04  $\mu\text{mol}$ , 3.6 mol %) and 4-vinylbenzyl piperidine. For controls, MOF-HIPE-S (32.5 mg) was used, which contained MOF-808 (5.2 mg, 0.18  $\mu\text{mol}$ , 14.5 mol %), and powdered MOF-808 (5.2 mg, 0.18  $\mu\text{mol}$ , 14.5 mol %). Each quantity of HIPE was sliced up into small chunks (1-2  $\text{mm}^3$ ) s then added to the corresponding tube along with 0.2 ml of  $\text{D}_2\text{O}$ , 0.2 THF and 0.2 ml of  $\text{H}_2\text{O}$ . The tubes were inverted once and

left to react for 20 hours. After 20 hours, the content of each tube was analysed using solution phase  $^{31}\text{P}$  NMR (161.83 MHz) spectroscopy, the solids were not filtered before spectral acquisition.

#### **VX hydrolysis procedure in the presence of Water/THF (performed by Nicholas J. Cooper)**

The following procedure was used to probe the hydrolysis rates of the various MOF and polymer composite materials for the degradation of VX in a mixture of THF and water. The HIPE containing MOF-808 (3.2 mg, 0.11  $\mu\text{mol}$ , 1.25 mol %) was sliced up into small chunks (1-2  $\text{mm}^3$ ) then added to an NMR tube along with VX, 24  $\mu\text{L}$  (0.09 mmol). A 0.6 ml mixture containing: 0.15 ml of  $\text{D}_2\text{O}$ , 0.3 ml of THF and 0.15 ml of  $\text{H}_2$  was then added. The tube was inverted once and immediately loaded into an NMR auto-sampler and the first  $^{31}\text{P}$  NMR (161.83 MHz) spectrum was obtained within 8 minutes of the reaction commencing. The sample was then cycled on the auto-sampler to collect subsequent data points. Each measurement was performed once.

#### **Neat VX hydrolysis procedure (performed by Nicholas J. Cooper)**

The following procedure was used to probe the hydrolysis rates of the various MOF and polymer composite materials for the degradation of neat VX in absence of solvent and buffer. A vial was charged with VX (267.37 g/mol, 250  $\mu\text{L}$ , 1.14 mmol) and the HIPE (10mg) containing MOF-808 (2 mg, 0.15 mol %), the ambient humidity was recorded (50 RH %). A small aliquot was taken after 4d, 7d, 11d and 14d and analysed using  $^{31}\text{P}$  NMR (161.83 MHz) spectroscopy. Each measurement was performed in duplicate.

## 5.3 Results and Discussion

### 5.3.1 Swelling studies

Swelling studies were performed by Alexander Joseph Wright, and conducted with methyl benzoate ( $\rho = 1.084 \text{ g/cm}^3$ ) which was previously identified as a V-agent (VX,  $\rho = 1 \pm 0.1 \text{ g/cm}^3$  swelling simulant).<sup>19</sup> For each HIPE, the studies were conducted in triplicate. The following equation was used for calculating Q, the swelling capacity:

$$Q = \frac{(\text{Mass of swollen polymer} - \text{mass of dry polymer})}{\text{Mass of dry polymer}}$$

Where the HIPE contained additional material such as MOF or surfactant, a modified equation was used for calculating the Q value. This was to offset the additional weight which did not contribute to the swelling. The following modified equation was used.

$$Q_{mod} = \left( \frac{Q}{M_p} \right) * (M_p + M_e)$$

$M_p$  represents the total % mass of the polymer and surfactant, and  $M_e$  represents the % mass of the extra components. For example, in MOF-HIPE-VBPP-S  $M_e$  is 35 (25 % MOF and 10 % extra surfactant).

## 5.3.2 Prototyping

The initial aim of this chapter was to successfully create a prototype composite material which would be composed of a zirconium MOF embedded in a styrenyl-HIPE polymer. The composite material would need to retain the functionality of the individual materials. The styrene HIPE is responsible for swelling in the presence of the substrate; the swelling is reliant on the maintenance of a consistent and high volume internal phase throughout the polymer matrix. The role of the zirconium MOF is to degrade the substrate. For the hydrolysis to occur, the  $Zr_6$  nodes must be maintained and so crystallinity is a useful indicator of this structural integrity. Last of all, it is imperative that water, is able to access the polymer matrix within which the catalyst is housed.

### 5.3.2.1 DUT/HIPE

As an initial proof of concept, a readily available zirconium MOF, DUT-52, was taken and an attempt was made to embed it in a styrene HIPE polymer. As a starting point, a previously reported method was utilised for making a styrene HIPE polymer (92 % Internal Phase) and the zirconium MOF was simply added to the reaction mixture. Fortunately, this initial attempt was successful as the addition of a MOF did nothing to interfere with the formation of an emulsion during the synthesis. The standard procedure was followed through and DUT/HIPE was synthesised by Alexander J Wright. After synthesising this first composite prototype, it was important to ensure that it retained both functional properties. To confirm that the high volume internal phase was still intact, the swelling of the prototype was investigated and compared to that of a HIPE polymer (92 % Internal Phase). When synthesising the composite, the loading of DUT-52 was 20 % wt of the total polymer weight. 20 % of the polymers weight was therefore omitted when calculating the degree of swelling,  $Q$ , this was to account for the fractional weight of DUT-52 in the polymer which does not contribute to the swelling. Unsurprisingly, the  $Q$  value achieved with the DUT-HIPE prototype was comparable to that of the unfunctionalised HIPE polymer, with  $Q$  values of 32 and 37 being observed for each

respective polymer in the presence of methyl benzoate. The similar Q values were a good indicator that the high internal phase remained unperturbed by the presence of DUT-52. An attempt was then made to investigate the crystallinity of the embedded DUT-52, PXRD patterns were obtained of DUT-52 (Figure 5.1), the un-functionalised HIPE polymer and the DUT-HIPE composite. The diffraction pattern for the unfunctionalised HIPE shows the broad diffraction of the non-crystalline polymer. The diffraction pattern of the DUT-HIPE suggests that the DUT-52 MOF is still present due to the match with the more dominant DUT-52 diffraction peaks.

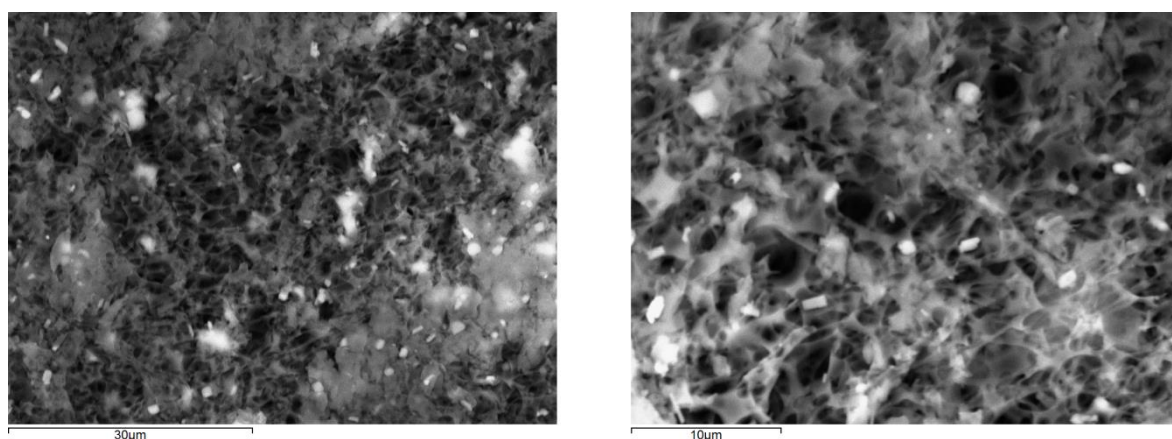
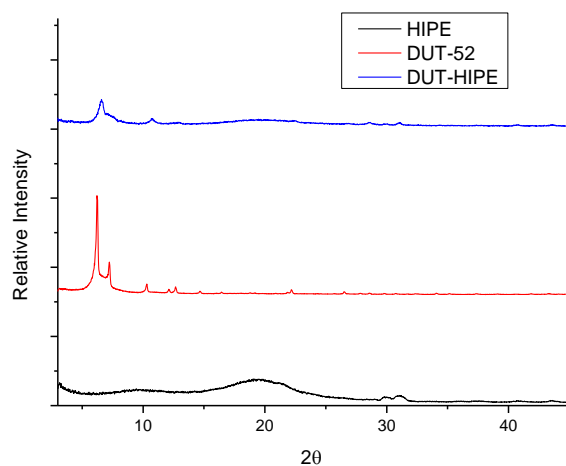


**Figure 5.1.** (Top) A PXRD overlay showing HIPE (black), DUT-52 (red) and DUT-HIPE (blue) (Bottom) SEM images showing the porous structure of the HIPE membrane and DUT-52 particles embedded in the membrane.

Finally, SEM analysis was conducted to investigate the porosity of the internal phase and to visually inspect the dispersion of the MOF throughout the matrix. Two slices were taken at different cross-sections of DUT-HIPE. Visually (Figure 5.1), a high internal phase was observed along with a good dispersion of the zirconium MOF throughout the polymer without excessive clumping.

To summarise, a proof of concept model material was synthesised. The material retained a high internal phase which is essential for the function of swelling. The zirconium MOF housed in the polymer maintained its crystallinity and was evenly dispersed through the polymer matrix. It was hypothesised that the catalytic activity of a zirconium MOF catalyst would therefore remain intact and the good dispersion would result in equal hydrolysis throughout the material.

## 5.4 Working Prototypes

### 5.4.1 MOF-HIPE, a working prototype

Inspired by the above successes, the same methodology was utilised to incorporate MOF-808, a catalyst which was previously shown to be catalytically active for OP hydrolysis, into a HIPE polymer (95 % Internal Phase). Following the same procedure, an emulsion was readily formed and MOF-808/HIPE was synthesised by Alexander J Wright. It should be noted that the MOF-808 which features in this chapter was not activated post-synthesis. The swelling was then investigated in the presence of methyl benzoate, whilst accounting for 20 % wt of MOF-808 which does not contribute to the swelling. The obtained Q values were again comparable to that of the unfunctionalised HIPE with Q values of 55 and 52 being observed for each respective polymer. PXRD and SEM were also conducted (Figure 5.2).

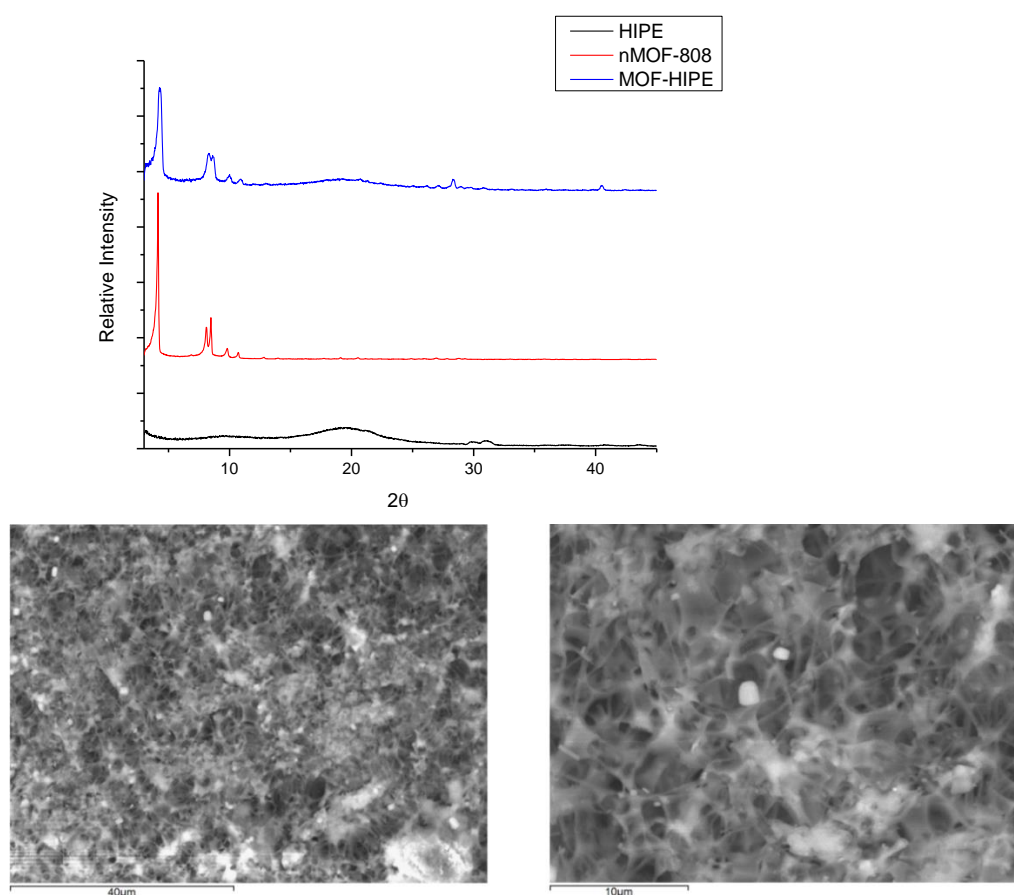


**Figure 5.2.** (Top) A PXRD overlay showing HIPE (black), MOF-808 (red) and MOF-HIPE (blue); (Bottom) SEM images showing the porous structure of the HIPE membrane and MOF-808 particles embedded in the membrane.

PXRD analysis (Figure 5.2) confirmed that the phases of MOF-808 were present in the bulk of the composite material therefore establishing that the crystallinity of MOF-808 remained intact along with catalytic activity. It should be noted that 2 additional diffraction peaks ( $28^\circ$   $2\theta$  and  $40^\circ$   $2\theta$ ) are present in the diffractogram of MOF-HIPE. These are postulated to arise from a synthetic salt impurity derived from the  $K_2SO_4$  salt used during HIPE synthesis.

A number of experiments were then performed to probe the hydrolytic capabilities of the new composite. A previously reported literature hydrolysis procedure was utilised, involving the hydrolysis of DMNP in water and in the presence of 0.45 M NEM Buffer.<sup>28,29</sup> The main difference being that a 50:50 mixture of  $H_2O$ :THF was used as the reaction medium as opposed to just  $H_2O$ . The polystyrene HIPE membrane readily swells in THF but not in  $H_2O$  and so this adjustment was made to improve the compatibility between the reaction mixture and the HIPE membrane in which MOF-808 was embedded.

The DMNP hydrolysis procedure utilised in this study is discussed in greater detail in Section 5.6, as are the derivations of the rate constants. As a starting point, the hydrolysis of DMNP was screened in the presence of MOF/HIPE and MOF-808 using the modified screening procedure. In brief, the procedure involved charging an NMR tube with DMNP followed by the addition of a diced HIPE polymer containing 1.25 mol % (relative to DMNP) of MOF-808. A solution containing THF,  $H_2O$ ,  $D_2O$  and NEM buffer was then added and immediately placed in an NMR auto-sampler and analysed using  $^{31}P$  NMR spectroscopy. More details are provided in Section 5.6. The unfunctionalised HIPE served as a blank. The hydrolysis rate of MOF-HIPE ( $k = 0.0267\ s^{-1}$ ) was significantly enhanced over that of MOF-808 ( $k = 0.0034\ s^{-1}$ ) with minimal hydrolysis occurring in the presence of the HIPE blank (Figure 5.3). 95 % hydrolysis was achieved by MOF-HIPE after 6 hours when compared to 80% which was achieved by MOF-808 after 24 hours. This enhancement can be attributed to the superior dispersion of the MOF-808 catalyst which is provided by the HIPE (Figure 5.4). It should be noted that previous literature examples of DMNP hydrolysis in the presence of MOF-808 involved the formation of MOF-808

suspension in the reaction medium.<sup>30</sup> In this study, the powdered MOF was left undisturbed throughout the reaction period.

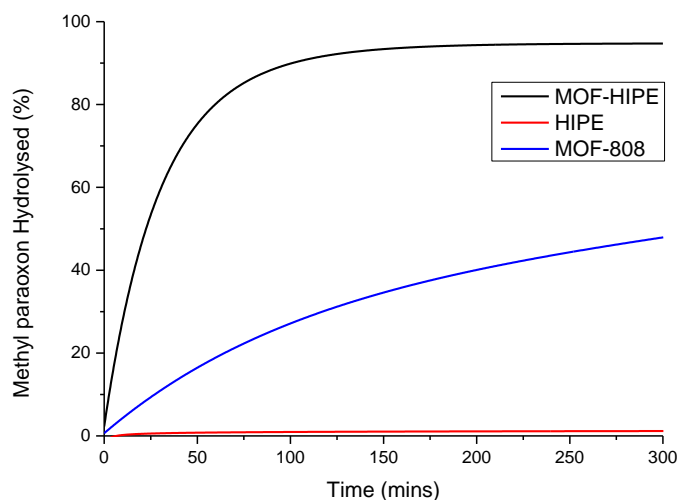


**Figure 5.3.** a) A plot showing the hydrolysis of DMNP over time in the presence of MOF-808 and MOF-HIPE in 0.45 M NEM buffer, THF and H<sub>2</sub>O, as determined by <sup>31</sup>P NMR. Each set of data was obtained in triplicate and an exponential fit was calculated for each set in a triplicate, each sample is represented as an average of the 3 exponential fits in a triplicate. Original data points are shown in the appendix (section 7.3).



**Figure 5.4.** An image highlighting the difference in dispersion of MOF-808. Both tube a) and c) contain the same quantity of MOF. Tube b) contains no MOF-808. Tube a) shows the superior dispersion provided by the HIPE polymer matrix.

A small study was performed to validate that the hydrolysis of DMNP was occurring throughout the polymer matrix and not simply being restricted to MOF-808 embedded in the surface of the HIPE. First, a qualitative swelling study was performed on MOF-HIPE using a 25:75 mixture of DMNP:THF. The MOF-HIPE readily swelled the total volume of the mixture of the two components. The swelling was conclusive enough to show that methyl-paraoxon is compatible with the internal phase of the HIPE. Second, an experiment was performed to determine the degree of hydrolysis occurring throughout different sections of the material after a period of 3 hours. This involved placing a chunk of MOF-HIPE into a H<sub>2</sub>O:THF solution containing NEM buffer and DMNP. Figure 5.5 highlights the different sections of the HIPE that were sampled. After 3 hours, the sections were physically separated by cutting and their contents were vacuum filtered, the filtrate was then analysed using <sup>31</sup>P NMR and the % of the dimethyl phosphate (DMP) product was determined.

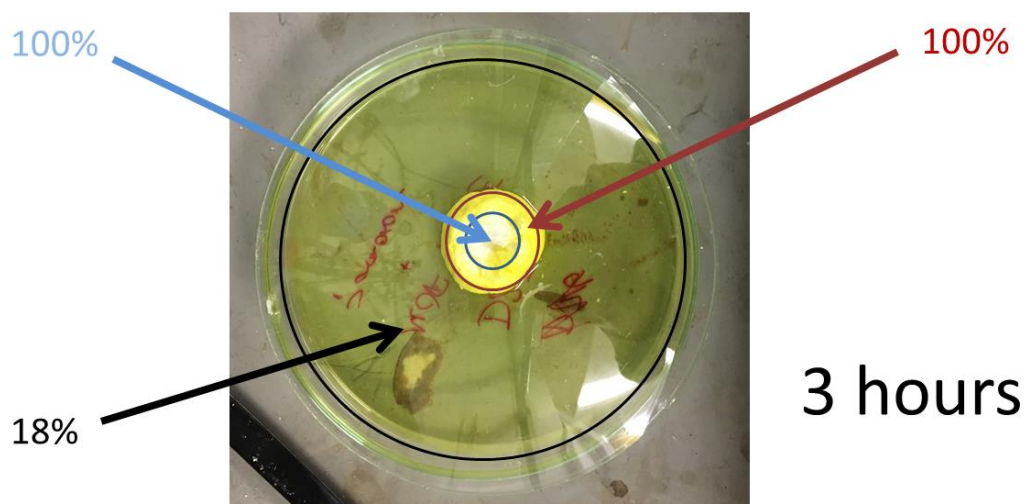


**Figure 5.5:** An image showing a DMNP degradation mixture containing MOF-HIPE, 2 different sections of the composite were analysed for their degradant composition after 3 hours, both sections exhibited 100 % hydrolysis. Only 18 % hydrolysis was observed in the supernatant.

There was no difference in the amount of hydrolysis observed between the inner and the outer section with full degradation occurring and only the DMP product being present. There was however only 18 % hydrolysis occurring in the supernatant. The lack of a difference in

hydrolysis between the two sections suggests that the hydrolysis takes place evenly throughout the polymer matrix and is not simply restricted to the surface of the polymer. This also validates that H<sub>2</sub>O and NEM buffer are able to access the catalytic Zr<sub>6</sub> nodes throughout the whole material.

#### **5.4.2 MOF-HIPE-S, Enhancing Aqueous Compatibility**

If the composite material is to degrade neat V-series agent in the presence of only ambient humidity, water would need to be compatible with the HIPE membrane. A new HIPE, MOF-HIPE-S was synthesised by Alexander Wright using the same procedure as MOF-HIPE, the only exception being that the surfactant content was increased from 20 to 30 wt % to be consistent with MOF-HIPE-VBPP-S (Section 5.4.3). Swelling studies were performed with methyl benzoate and an adjusted Q value of 63 was observed. MOF crystallinity and HIPE porosity were also confirmed using PXRD and SEM (Figure 5.6). Contact angle measurements (Figure 5.7) were then performed by Alexander Joseph Wright which visually confirmed the water absorption properties of HIPE before and after removal of surfactant. A hydrolysis study was conducted on DMNP in the presence of a surfactant free MOF-HIPE (removed by soaking in EtOH overnight) with a slight alteration to the previous procedure. The composition of the reaction mixture was altered so that THF was replaced with H<sub>2</sub>O. This was to more accurately mimic a hydrolysis environment where only water and agent are present. For MOF-HIPE, a slow degradation of DMNP was achieved ( $k = 0.0038 \text{ s}^{-1}$ ). MOF-HIPE-S (30 % surfactant) was then screened for the hydrolysis of DMNP using the same buffered, THF free procedure described above. MOF-HIPE-S ( $k = 0.0093 \text{ s}^{-1}$ ) exhibited a notable hydrolysis enhancement over that of the surfactant free MOF-HIPE ( $k = 0.0038 \text{ s}^{-1}$ ), this is shown in more detail in Section 5.6 of this chapter. We posit that the hydrophilic head of the sorbitan monooleate surfactant was therefore facilitating enhanced absorption of H<sub>2</sub>O into the polymer matrix of the HIPE.

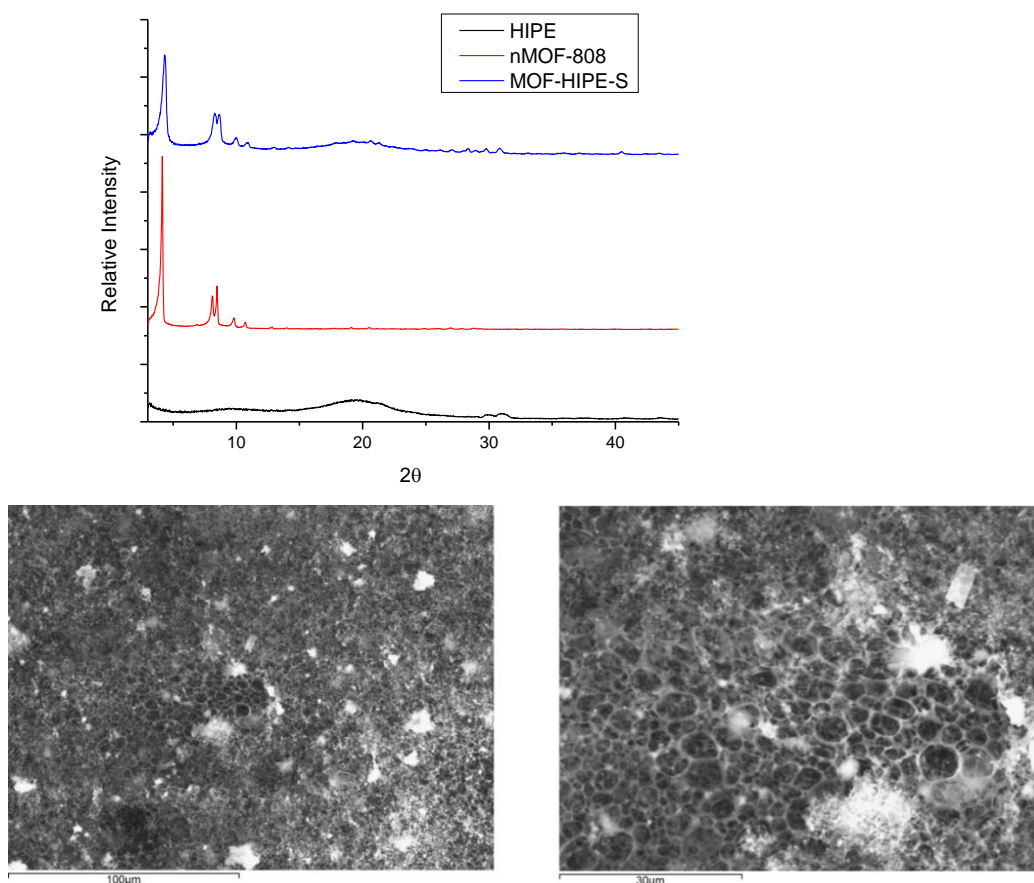


**Figure 5.6.** (Top) A PXR D overlay showing HIPE (black), MOF-808 (red) and MOF-HIPE-S (blue) (Bottom) SEM images showing the porous structure of the HIPE membrane and MOF-808 particles embedded in the membrane.

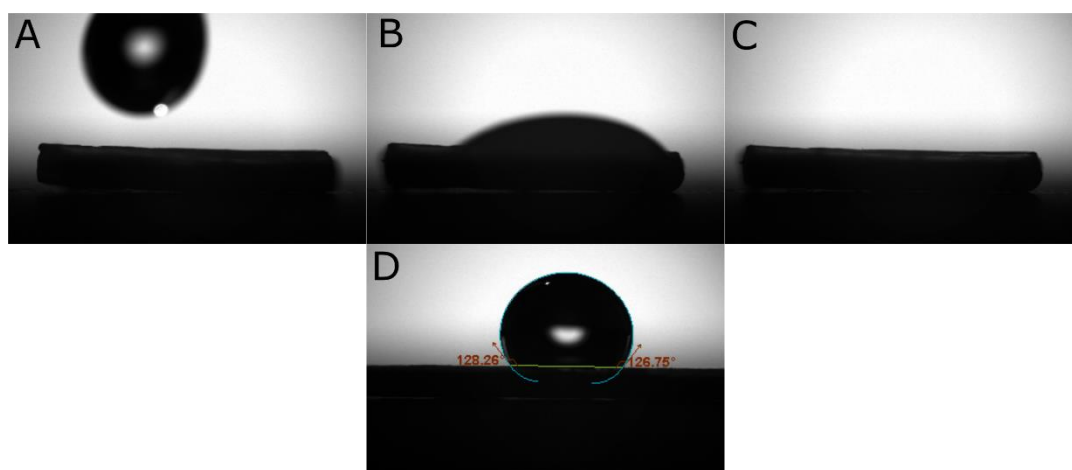


**Figure 5.7.** A composite image showing contact angle measurements recorded at 14 frames per second. A, B and C show a water droplet falling onto the surface of HIPE-S, there is a difference of 2 frames between each image. Image D shows a water droplet on a surfactant free HIPE, no absorption is observed and a hydrophobic contact angle<sup>31</sup> is recorded.

This result established that not removing surfactant from the HIPEs post synthesis is beneficial for enhancing the compatibility between the composite and H<sub>2</sub>O. All future composites were therefore not purged of their remaining surfactant post-synthesis.

To summarise, in synthesising MOF-HIPE, the utility of a working prototype was demonstrated. It was shown that the MOF-HIPE internal phase is compatible with DMNP, the simulant of choice. Hydrolysis testing revealed a dispersion-aided enhanced rate of hydrolysis in the presence of the composite when compared to just MOF-808. It was also confirmed that the hydrolysis of DMNP occurs uniformly throughout the polymer matrix and not just the on surface of the composite. Finally, after learning of the beneficial role of the surfactant in our material, the synthesis was optimised to maximise the compatibility of the polymer membrane with water; the fuel for hydrolysis.

#### **5.4.3 MOF-HIPE-VBPP-S; Heterogeneous Amine**

MOF-HIPE-S shows great promise as an encapsulation and degradation agent for organophosphorus contaminants. It has a high swelling capacity for V-series agents. The catalyst housed in the HIPE polymer, MOF-808 is able to slowly degrade neat V-series and the polymer membrane is compatible with water, the hydrolytic fuel. The remaining issue is that the hydrolysis of methyl-paraoxon requires buffer. Inspired by a PEI polymer housing MOF NU-1000 which degrades methyl-paraoxon without a solution buffer,<sup>4</sup> it was decided that a heterogeneous buffer would be incorporated into the HIPE polymer backbone. The heterogeneous buffer would come in the form of a basic, tertiary amine monomer. To degrade DMNP, a stoichiometric quantity of buffer would be required; altering the polymer composition with a large proportion of basic amine would have a drastic effect on the internal phase and would thus impact the swelling. However, it was hypothesized that having a small proportion of basic amine would be enough to buffer the initial hydrolysis of a pure V-series agent. The initial hydrolysis would generate diisopropylaminoethanethiol (DESH), a tertiary amine degradation product which would buffer further degradation. The continuous

generation of the tertiary amine by-product makes the hydrolytic degradation of V-series agents a self-buffering system.<sup>32</sup>

A previously reported amine monomer,<sup>33</sup> vinyl-benzyl-piperidine (vinyl-benzyl-piperidinium, pKa = 10.08), was selected for incorporation into the composite material. After synthesising the monomer, several attempts were made to incorporate it into a HIPE polymer. A composition of 5 wt % VBPP relative to styrene was selected. Initial attempts followed the previous synthetic procedure used for the formation of MOF-HIPE. This proved unsuccessful. Having a basic amine moiety in the reaction mixture alters the pH and thus interferes with the formation and stabilisation of the HIPE. Several other attempts were made with differing concentrations of ammonium chloride but the quality of the emulsions formed were low. Fortunately upon consulting the work of Joel M. Williams,<sup>34,35</sup> simply changing the quantity of the surfactant sorbitan monooleate, from 20 wt % to 30 wt % (relative to the total weight of monomer), was enough to stabilise the emulsion and yield the amine functionalised HIPE polymer (MOF-HIPE-VBPP-S). This synthesis was conducted by Alexander J Wright. The new composite was then routinely examined for its swelling capacity and crystallinity. The swelling of MOF-HIPE-VBPP-S in methyl benzoate produced a Q of 33, this was significantly less than the Q of HIPE (95 % Internal Phase, Q of 55). PXRD analysis of the composite verified the presence of MOF-808 phases in the material, as shown in Figure 5.8. SEM analysis of several cross sections verified the dispersion of the MOF catalyst throughout the material although the porosity of the HIPE appeared less regular (Figure 5.8).

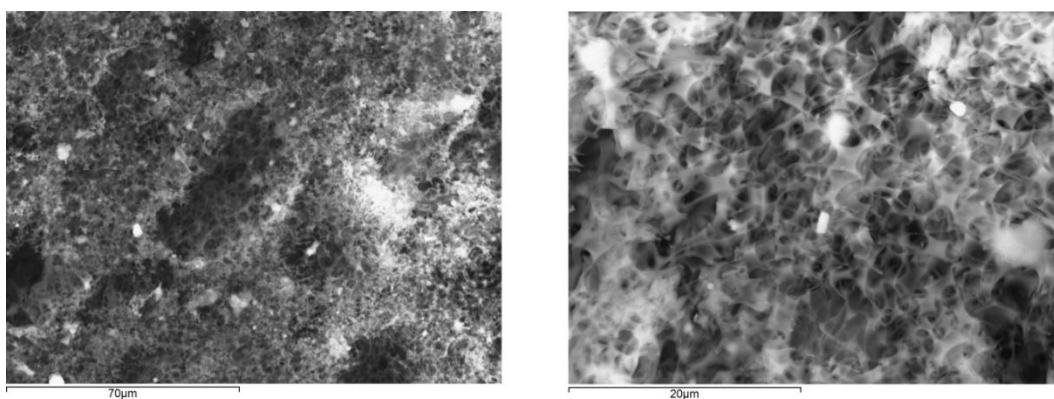
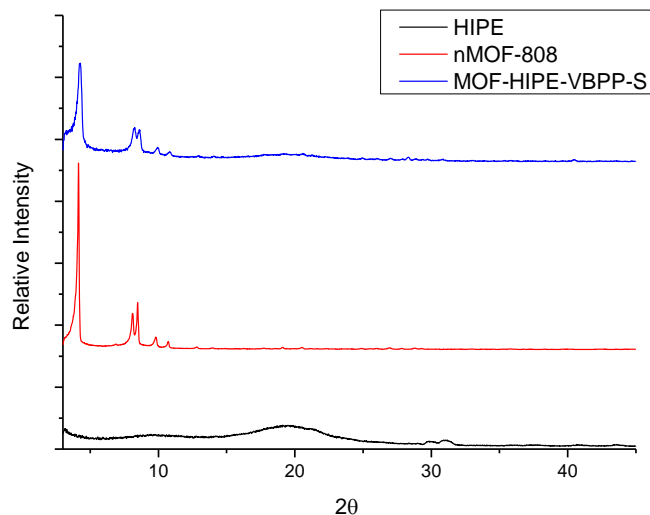


**Figure 5.8.** (Top) A PXR D overlay showing HIPE (black), MOF-808 (red) and MOF-HIPE –VBPP-S (blue) (Bottom) SEM images showing the porous structure of the HIPE membrane and MOF-808 particles embedded in the membrane.

Several attempts were also made to verify the presence of the VBPP amine in the composite structure. IR analysis was conducted on HIPE-VBPP-S to check for a C-N absorption band ( $1200\text{ cm}^{-1}$ ), the MOF free HIPE-VBPP-S was chosen to negate any additional IR absorptions arising from MOF-808. No such C-N band was observed (Figure 5.9). Ammonium HCl salts possess unique absorption bands in the  $2400\text{--}2700\text{ cm}^{-1}$  region with a piperidolate group showing a characteristic absorption at  $2560\text{ cm}^{-1}$ .<sup>36</sup> HIPE-VBPP-S was soaked in 2M HCl to protonate the piperidine groups and subsequently analysed again using IR spectroscopy but no new absorption bands were observed in the  $2400\text{--}2700\text{ cm}^{-1}$  region.

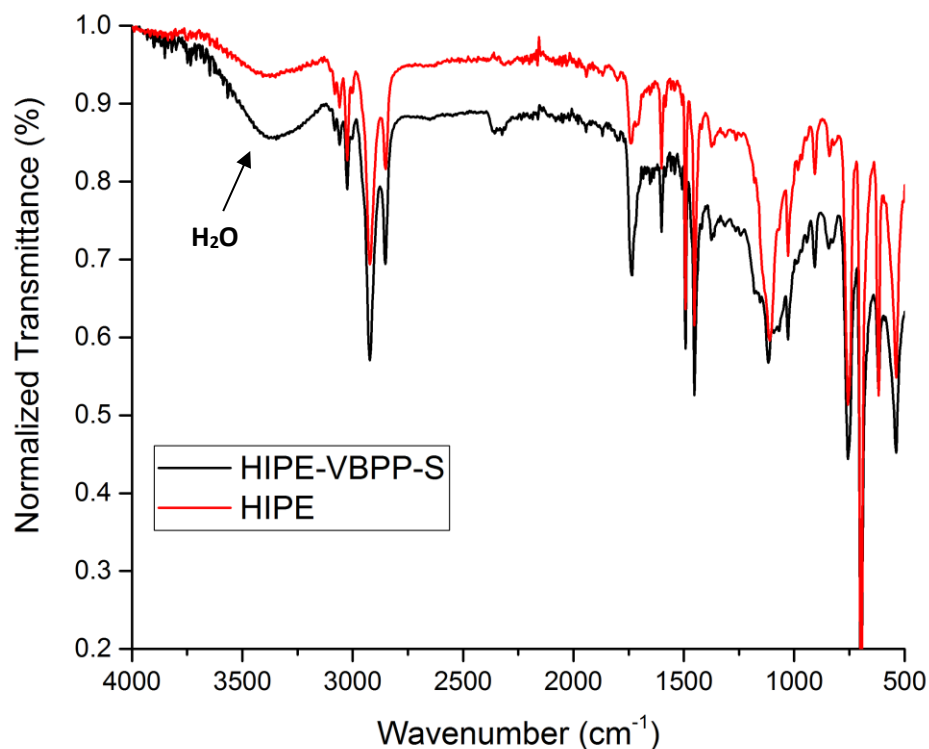


**Figure 5.9.** An overlay of the infrared spectra of VBPP-HIPE-S and HIPE.

A second attempt was made to characterise the presence of the VBPP monomer using magic angle spinning (MAS) NMR.<sup>27</sup> In solution-phase NMR, anisotropic effects are time-averaged by the random motion of the liquid analytes. However, in solid-state NMR, solid analytes exhibit anisotropic interactions which result in very broad spectra. MAS NMR is used for the analysis of solid or gel materials. The anisotropy of solid analytes can be negated by spinning an anisotropic sample at the magic angle ( $54.74^\circ$ ) with respect to the magnetic field and at a high rotational frequency (5 to 35 kHz). This was conducted by Alexander J. Wright. Figure 5.10 shows a  $^1\text{H}$  NMR overlay of the VBPP monomer, the sorbitan monooleate surfactant, as well as the  $^1\text{H}$  MAS NMR overlays of MOF-HIPE-VBPP-S and HIPE-S. Unfortunately, the piperidine ring protons were obstructed by the peaks arising from the polymer matrix. The N-CH<sub>2</sub> protons of the VBPP monomer were hidden beneath the surfactant peaks. Sadly, due to time constraints, it was not possible to perform any additional experiments/analyse additional nuclei ( $^{15}\text{N}$  and  $^{13}\text{C}$  MAS NMR) with the surfactant removed from the MOF-HIPE-VBPP-S and HIPE-S polymers.

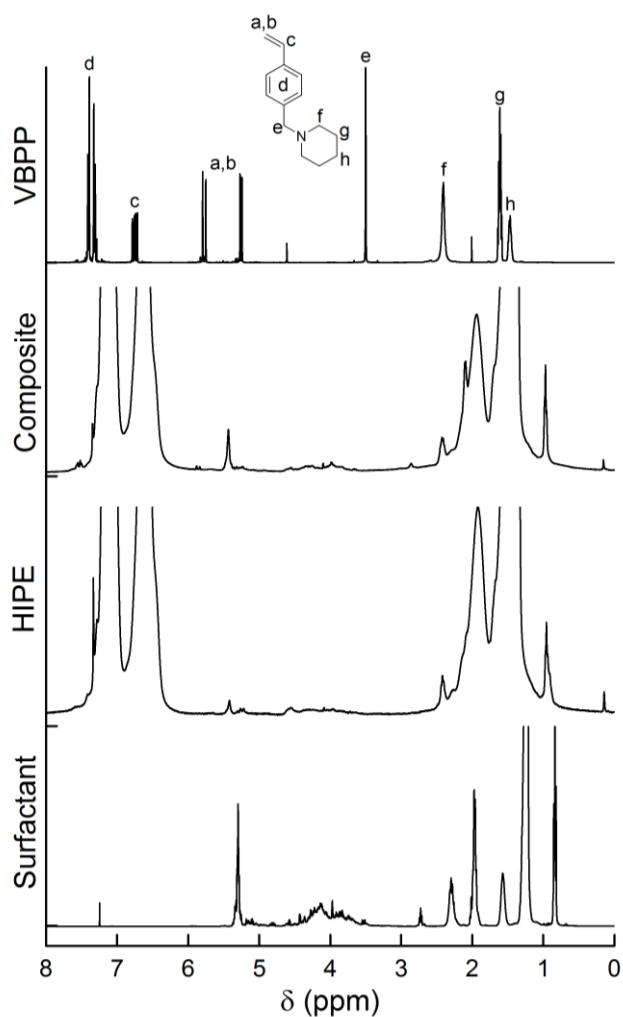


**Figure 5.10.**  $^1\text{H}$  NMR overlay (top to bottom) of VBPP monomer, MOF-HIPE-VBPP-S, MOF-HIPE-S and Sorbitan monooleate.  $^1\text{H}$  spectra of MOF-HIPE-VBPP-S and MOF-HIPE-S were acquired using MAS NMR.

After partially characterizing the newest composite, a number of hydrolysis studies were performed. To begin, the previous NEM buffered DMNP hydrolysis procedure was employed. A fast rate of hydrolysis was observed ( $k = 0.0261 \text{ s}^{-1}$ ) which was comparable to that of MOF-HIPE ( $k = 0.0267 \text{ s}^{-1}$ ). The new HIPE polymer was therefore hydrolytically active and the presence of the tertiary amine 4-VBPP monomer during the HIPE synthesis did not damage the MOF-808 catalyst. Next, a non-buffered degradation procedure was used to probe the effectiveness of the heterogeneous amine for the hydrolysis of DMNP. Since the loading of VBPP in MOF-HIPE-VBPP-S is only 5 %, a large excess of the composite was used in relation to the substrate. 3

different amounts of MOF-HIPE-VBPP-S were employed, each containing a different sub-equimolar quantity of VBPP relative to DMNP. The ratios of VBPP:DMNP that were achieved were 1:4, 1:8 and 1:16. The reactions were allowed to proceed for 24 hours in water, after which they were analysed using  $^{31}\text{P}$  NMR spectroscopy to determine the quantity of DMNP which had been degraded. Due to the lack of an excess of amine relative to the substrate, full hydrolysis was not achieved in any of the 3 reactions. Table 5.2 shows the different degrees of hydrolysis which were observed for each of the 3 reactions.

<b>Sample + Quantity</b>	<b>MOF-808 quantity</b>	<b>4-VBPP : DMNP Ratio</b>	<b>% Paraoxon Hydrolysed after 24 hours</b>
<b>MOF-HIPE-VBPP-S</b> 32.5 mg	4.9 mg	1:4	48.2 %
<b>MOF-HIPE-VBPP-S</b> 16 mg	2.4 mg	1:8	30.1 %
<b>MOF-HIPE-VBPP-S</b> 8 mg	1.2 mg	1:16	19.2 %
<b>MOF-HIPE-S</b> 32.5 mg	4.9 mg	No 4-VBPP	20.6 %
<b>MOF-808</b> 4.9 mg	4.9 mg	No 4-VBPP	24.0 %

**Table 5.2.** A table showing the various quantities of MOF-HIPE-VBPP-S that were screened on DMNP in the absence of any NEM buffer and the degree of hydrolysis that was observed.

MOF-HIPE-S and MOF-808 were included as blanks. 5  $\mu\text{L}$  of DMNP was used in all 5 studies.

Unsurprisingly, using more MOF-HIPE-VBPP-S relative to DMNP resulted in more hydrolysis occurring over the course of the reaction period. Partial buffer-free hydrolysis of DMNP had been achieved. It was therefore postulated that employing a catalytic quantity of MOF-HIPE-VBPP-S against neat VX would trigger a small quantity of sub-equimolar hydrolysis which would generate enough amine by product to make the remainder of the process self-buffering.

## 5.5 HIPE Swelling Summary

The swelling results are summarized in Figure 5.11. For DUT-HIPE, a Q value of 33 was achieved, whilst this may seem low in comparison to the other HIPEs, it is important to note that DUT-HIPE possessed a 92 % internal phase. When compared to previously reported Q values for a 92 % internal phase HIPE (Q = 37),<sup>19</sup> the swelling value can be considered relatively comparable. MOF-HIPE consisted of a 95 % internal phase and an adjusted Q value of 52 was observed, this is comparable to the swelling of the 95 % internal phase HIPE which produced a Q value of 55. MOF-HIPE-S contained additional surfactant and produced the highest adjusted Q value of 63. For the case of DUT-HIPE, MOF-HIPE and MOF-HIPE-S, it can be safely said that the incorporation of a MOF into the composite structure had a negligible negative impact on the swelling. The addition of the VBPP monomer reduced swelling capacity by roughly 50 % for both HIPE-VBPP-S (Q = 26) and MOF-HIPE-VBPP-S (Q = 32). This reduced performance is likely caused by the basic amine linker which inhibits the emulsion stability during HIPE formation. The perturbation of the emulsion leads to a less ordered internal phase, as seen by SEM (Figure 5.8), and therefore drastically affects the swelling. It should however be noted that the swelling MOF-HIPE-VBPP-S is higher than that of HIPE-VBPP-S, it can therefore be assumed that the presence of MOF-808 particles can partially stabilize the emulsion. A more effective synthetic method is therefore required to achieve a more stable and uniform internal phase during HIPE formation.

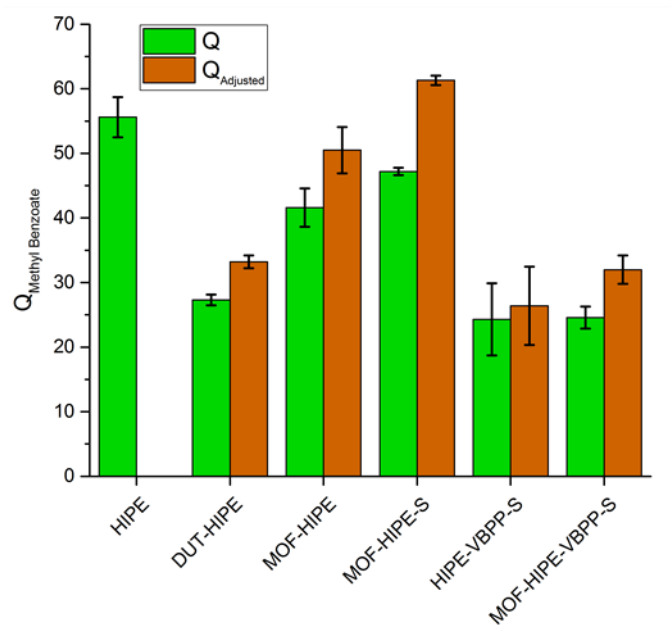
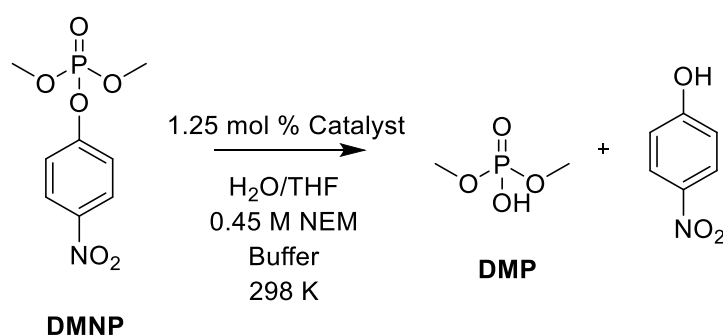


**Figure 5.11.** Graph showing the swelling degrees (Q) alongside the  $Q_{mod}$  for each of the samples presented in this work. HIPE does not have a  $Q_{mod}$  value associated for it as it does not contain any extra components outside of the basic synthesis.

## 5.6 Simulant Hydrolysis Summary

A number of HIPE polymers were synthesised to aid the development of the ultimate composite material for neat VX encapsulation and degradation. This next section will aim to draw a more direct comparison between all the simulant hydrolysis studies previously discussed in this chapter. All of these studies were conducted under standardised conditions in the presence of THF and 0.45 M aqueous NEM buffer and each material was studied in triplicate. The hydrolysis conditions are illustrated in Scheme 5.1.



**Scheme 5.1:** An illustration of the DMNP hydrolysis conditions which were employed in this study.

In brief, the procedure involved charging an NMR tube with DMNP followed by the addition of diced HIPE polymer containing a 1.25 % catalyst loading of MOF-808 (relative to DMNP). A solution containing THF, H<sub>2</sub>O, D<sub>2</sub>O and NEM buffer was then added and immediately placed in an NMR auto-sampler and analysed using <sup>31</sup>P NMR spectroscopy. The probe temperature was set to 298 K throughout each experiment. The first measurement was obtained within 8-9 minutes of the reaction commencing. Subsequent measurements were obtained for a total of 5 hours. <sup>31</sup>P NMR spectroscopy was used to monitor the presence of peaks corresponding to DMNP and DMP. An example spectral overlay is shown in Figure 5.12. This was used to determine the % of DMNP which had been hydrolysed to DMP at each time interval. An exponential fit was then derived for each data set in a triplicate and then an average curve was obtained from all 3 fits, the R<sup>2</sup> values for the derivations can be found in the Table 5.3.

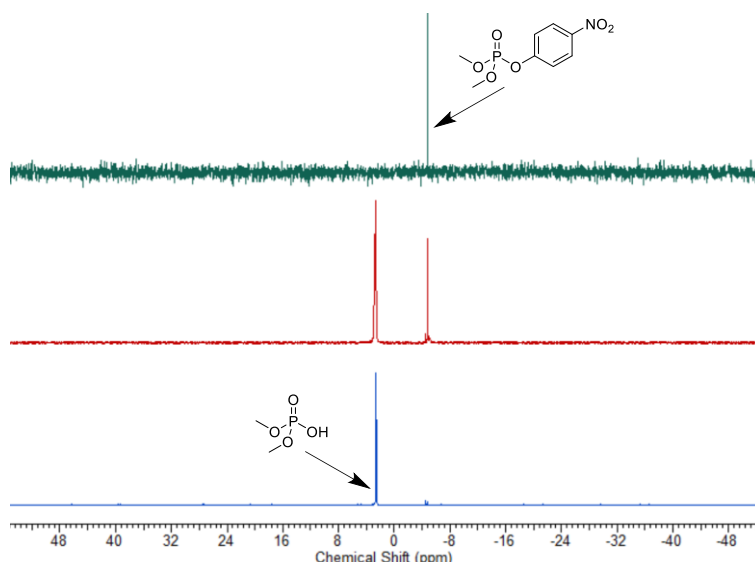


**Figure 5.12.** A  $^{31}\text{P}$  NMR in  $\text{D}_2\text{O}$  overlay showing the different stages of DMNP hydrolysis that were observed (green) fresh DMNP (red) DMNP 2 hours after the addition of MOF-HIPE containing 1.25 mol % MOF-808 relative to substrate in 0.45 M NEM buffer (blue) DMNP 20 hours after the addition MOF-HIPE containing 1.25 mol % MOF-808 relative to substrate in 0.45 M NEM.

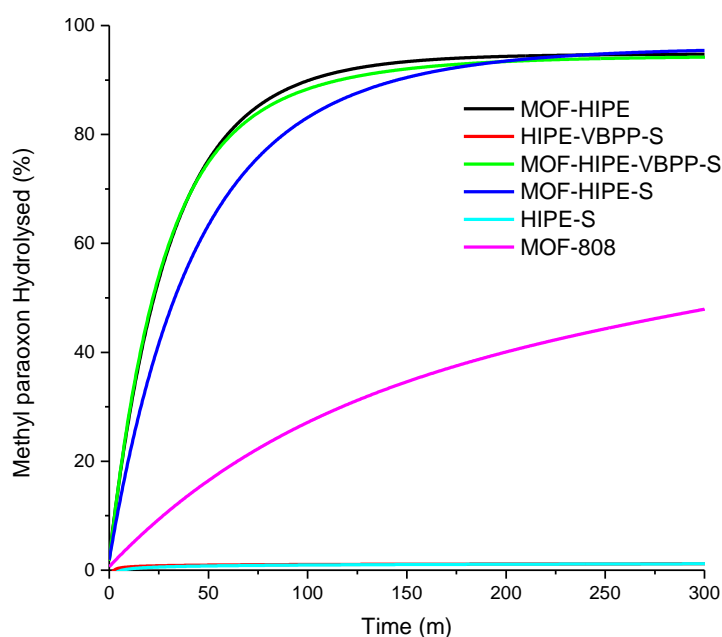
MOF-HIPE				MOF-808				MOF-HIPE-VBPP-S						
Model	Exponential			Model	Exponential			Model	Exponential					
Equation	$y = y_0 + A \cdot \exp(R_0 \cdot x)$			Equation	$y = y_0 + A \cdot \exp(R_0 \cdot x)$			Equation	$y = y_0 + A \cdot \exp(R_0 \cdot x)$					
Reduced Chi-Sqr	8.92269	9.17978	1.91953	Reduced Chi-Sqr	1.56097	0.86809	6.2778	Reduced Chi-Sqr	1.68922	0.72694	4.73275			
Adj. R-Square	0.99163	0.98326	0.99638	Adj. R-Square	0.99659	0.99708	0.98258	Adj. R-Square	0.99801	0.99904	0.99361			
		Value	Standard Error			Value	Standard Error			Value	Standard Error			
F1		y0	91.10245	1.87111	F1		y0	65.80617	1.20373	F1		y0	97.1793	0.48953
		A	-90.7499	3.44894			A	-65.36448	1.49938			A	-94.96783	1.01621
		R0	-0.02179	0.00211			R0	-0.00946	5.39242E-4			R0	-0.01379	3.52003E-4
D1		y0	97.49177	0.70387	D1		y0	59.90034	0.44896	D1		y0	98.10213	0.25056
		A	-92.2623	2.68818			A	-58.25925	0.64399			A	-96.45723	0.74627
		R0	-0.03358	0.00232			R0	-0.00814	2.39686E-4			R0	-0.0333	5.9508E-4
B		y0	95.72058	0.31201	B		y0	-27.20292	9.00165	B		y0	92.72348	0.74163
		A	-94.45781	1.26673			A	27.06111	8.09002			A	-90.83507	1.77064
		R0	-0.04362	0.00147			R0	0.00231	4.09677E-4			R0	-0.02086	9.38528E-4

MOF-HIPE-S				MOF-HIPE-S – NO THF				MOF-HIPE – NO THF						
Model	Exponential			Model	Exponential			Model	Exponential					
Equation	$y = y_0 + A \cdot \exp(R_0 \cdot x)$			Equation	$y = y_0 + A \cdot \exp(R_0 \cdot x)$			Equation	$y = y_0 + A \cdot \exp(R_0 \cdot x)$					
Reduced Chi-Sqr	6.16223	2.03069	2.72268	Reduced Chi-Sq	8.10425	6.21051	8.05736	Reduced Chi-Sq	3.44685	5.52629	1.93719			
Adj. R-Square	0.98968	0.99741	0.99608	Adj. R-Square	0.98713	0.98714	0.98664	Adj. R-Square	0.98936	0.97832	0.99011			
		Value	Standard Error			Value	Standard Error			Value	Standard Error			
F1		y0	86.38235	0.84034	D1		y0	83.04453	1.88062	F1		y0	66.18764	4.68412
		A	-80.74174	1.997			A	-80.68054	2.39682			A	-67.94228	4.19911
		R0	-0.01663	9.6448E-4			R0	-1.01242	0.08399			R0	-0.00764	0.00105
D1		y0	98.69998	0.39042	F1		y0	75.56857	2.15004	D1		y0	90.29788	24.63049
		A	-101.11973	1.29813			A	-71.81426	2.26213			A	-89.87636	23.76306
		R0	-0.04131	0.00128			R0	-0.83551	0.07695			R0	-0.00363	0.00141
B		y0	98.04732	0.44844	B		y0	86.41245	3.3906	B		y0	58.96722	4.9205
		A	-96.12797	1.51834			A	-81.08319	3.14777			A	-57.25173	4.48917
		R0	-0.04431	0.0017			R0	-0.48753	0.05297			R0	-0.00618	9.61091E-4

**Table 5.3:** A summary of the exponential fitting which was applied to the NMR kinetic data of each composite material. Each report shows the standard error which was derived from the exponential fit of each individual data set in a triplicate (generated using Origin 9.0).

Figure 5.13 shows the observed hydrolysis of DMNP in the presence of all the materials discussed in this chapter. Using the first hour of data for each sample, the reaction rate of each reaction,  $k$ , was then calculated for each data set. This was performed by plotting the natural logarithm of DMNP concentration over time and applying a linear fit through this data. The slope of the line ( $m$ ), corresponds to  $k$  such that  $m = -k$ . The first order residue plots are shown in Figure 5.14. Unsurprisingly, no DMNP hydrolysis was observed in the presence of HIPE-S and HIPE-VBPP-S due to the lack of any MOF-808, these materials therefore served as blank control samples. MOF-HIPE ( $k = 0.0267 \text{ s}^{-1}$ ), MOF-HIPE-S ( $k = 0.0192 \text{ s}^{-1}$ ) and MOF-HIPE-VBPP-S ( $k = 0.0261 \text{ s}^{-1}$ ) all performed faster than powdered MOF-808 consistent with the superior dispersion provided by the high volume HIPE scaffold. When comparing the composites, there was little discernible difference between the initial rate constants of MOF-HIPE and MOF-HIPE-VBPP-S. The initial rate of MOF-HIPE-S was somewhat slower but all 3 materials reached the same reaction end-point after 3 hours.



**Figure 5.13.** A plot showing the hydrolysis of DMNP over time in the presence of the various MOF/HIPE composites in of 0.45 M NEM buffer, THF and H<sub>2</sub>O. Each set of data was obtained in triplicate and an exponential fit was calculated for each set, each sample is represented as an average of the 3 exponential fits. Original data points are shown in the appendix (section 7.3).

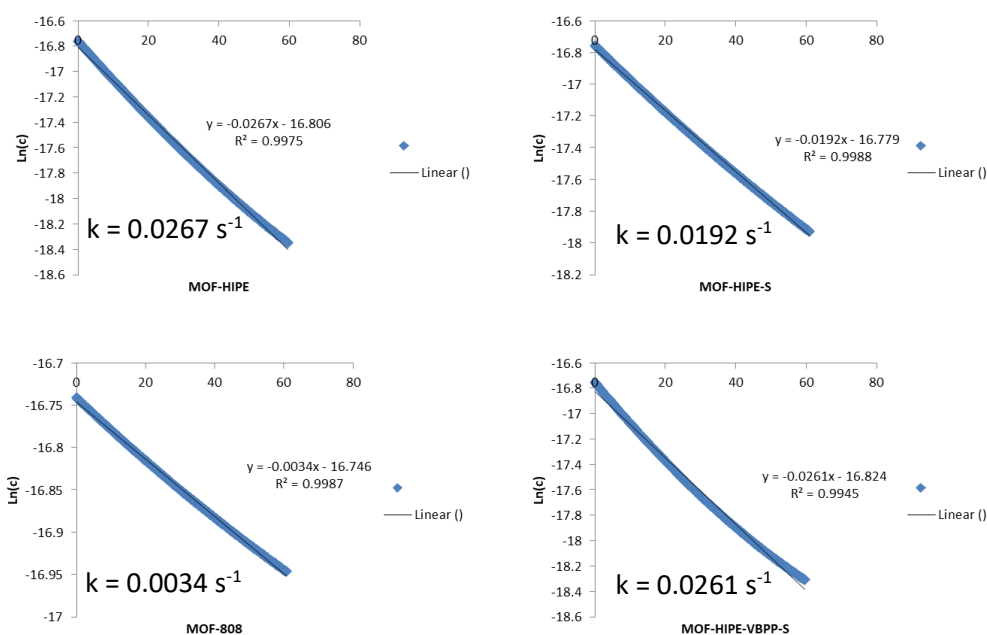


**Figure 5.14.** Natural logarithms of concentrations corresponding to DMNP residues in the presence of the various MOF/HIPE composites. The first order rate constants were calculated from a linear fit through the initial data points (first 60 minutes) for each composite.

Due to the similarity of the degradation rates amongst the composites, different reaction conditions were used to probe the effect of the subtle differences in composition of the various MOF HIPE composites. To demonstrate the effectiveness and the utility of the surfactant, the original degradation conditions were modified by replacing THF with  $\text{H}_2\text{O}$ . Figure 5.15 shows a comparison of the hydrolysis of DMNP in the presence of the surfactant free MOF-HIPE ( $k = 0.0038 \text{ s}^{-1}$ ) and MOF-HIPE-S ( $k = 0.0093 \text{ s}^{-1}$ ) and in the absence of THF. The first order residue plots are also shown. MOF-HIPE-S contains the surfactant Sorbitan monooleate (30 wt %) which enhances the uptake of  $\text{H}_2\text{O}$  into the polymer composite. The enhanced absorption provides superior transport of  $\text{H}_2\text{O}$  to the MOF-808 catalyst housed within the HIPE. It should however be noted that for MOF-HIPE-S,  $k = 0.0093 \text{ s}^{-1}$  in just  $\text{H}_2\text{O}$  whereas  $k = 0.0192 \text{ s}^{-1}$  in  $\text{H}_2\text{O}/\text{THF}$  (as shown in previous study). The reaction is therefore slower in the absence of a THF medium which aids with the swelling of the polymer.

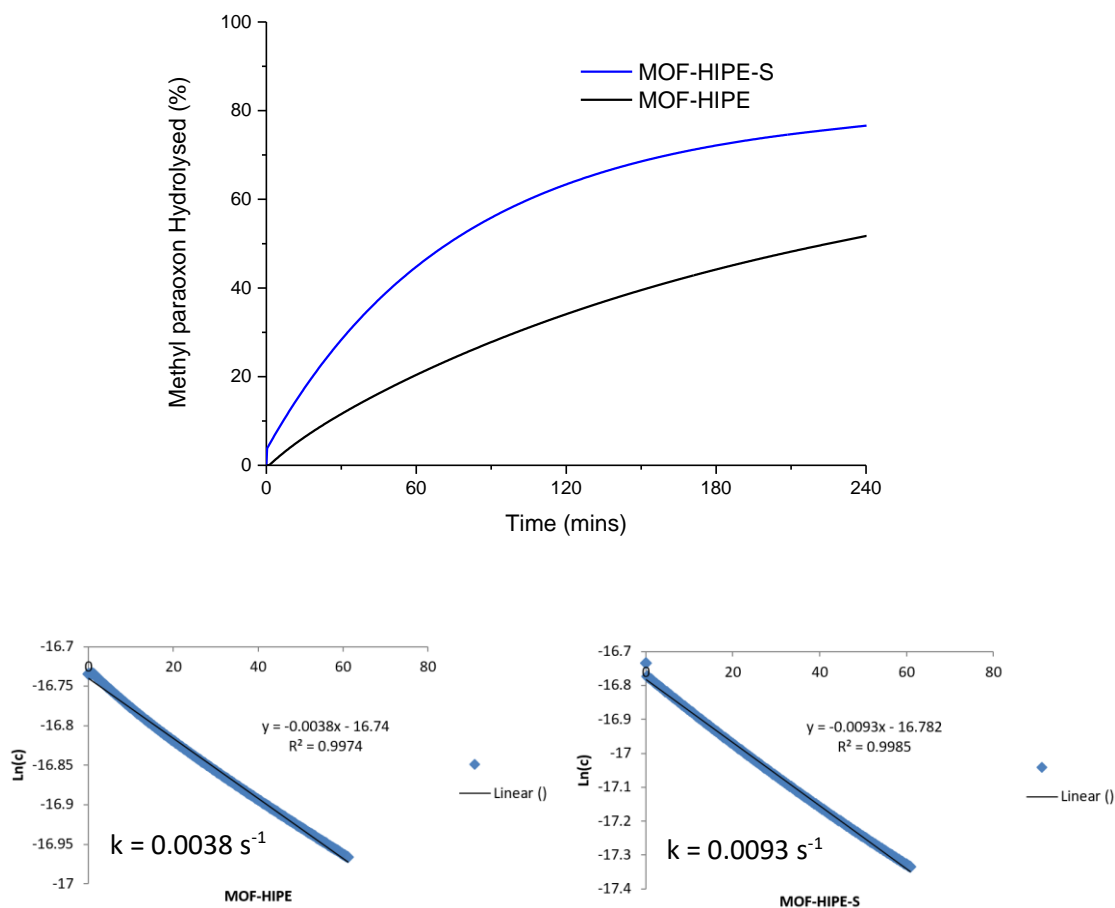
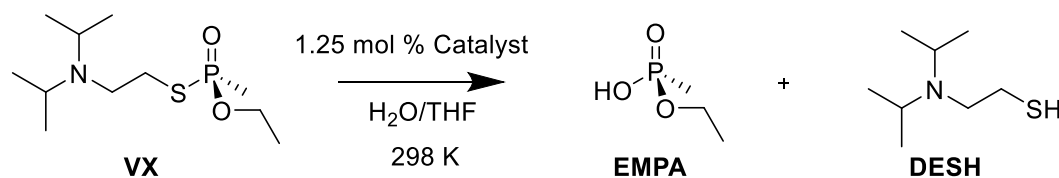


**Figure 5.15.** (top) A plot showing the hydrolysis of DMNP over time in the presence of MOF-HIPE and MOF-HIPE-S composites in 0.45 M NEM buffer and H<sub>2</sub>O. Each set of data was obtained in triplicate and an exponential fit was calculated for each set, each sample is represented as an average of the 3 exponential fits. Original data points are shown in the appendix (section 7.4). (bottom) Natural logarithms of concentrations corresponding to DMNP residues in the presence of MOF-HIPE and MOF-HIPE-S. The first order rate constants were calculated from a linear fit through the initial data points (first 60 minutes) for each composite.

## 5.7 Encapsulation and Degradation of V-series Agent

After synthesising, characterising and testing a number of HIPE composites as degradation materials for the hydrolysis of the simulant DMNP, the HIPE composites were sent to DSTL for testing. MOF-HIPE-S and MOF-HIPE-VBPP-S were the composites which were selected for further analysis, along with HIPE-VBPP-S, which would function as a blank. Testing was conducted on the Nerve Agent VX. Two different degradation studies were employed. The first VX degradation study was conducted in a very similar fashion to the THF/D<sub>2</sub>O experiments which were conducted with DMNP. The VX hydrolysis conditions are illustrated in Scheme 5.2.



**Scheme 5.2:** An illustration of the VX hydrolysis conditions which were employed in this study.

In brief, an NMR tube was charged with VX followed by the addition of a diced HIPE containing 1.25 mol % (relative to VX) MOF-808. A solution of H<sub>2</sub>O and THF was then then added to the tube along with a small amount of D<sub>2</sub>O, the tube was immediately placed in an NMR auto-sampler and analysed using <sup>31</sup>P NMR spectroscopy. The probe temperature was set to 298 K throughout each experiment. The first measurement was obtained within 15 minutes of the reaction commencing. Subsequent measurements were obtained for a total of 24 hours. <sup>31</sup>P NMR spectroscopy was used to monitor the presence of peaks corresponding to VX and EMPA. An example spectral overlay is shown in Figure 5.16. This was used to determine the % of VX which had been hydrolysed to EMPA at each time interval. It should be noted that no toxic EA-2192 by-product was formed, This is shown in Figure 5.16 where there is a distinct lack of a peak at approximately 40 ppm; the shift of EA-2192.<sup>37</sup>

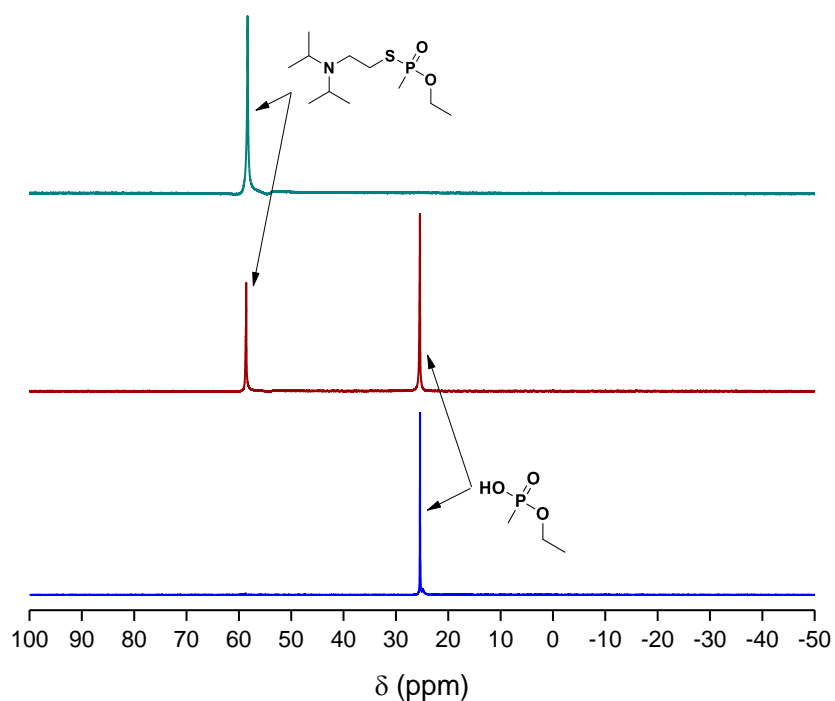


**Figure 5.16.** A  $^{31}\text{P}$  NMR in  $\text{D}_2\text{O}$  overlay showing the different stages of VX hydrolysis that were observed; (green) fresh VX; (red) VX 1.5 hours after the addition of MOF-HIPE-VBPP-S containing 1.25 mol % MOF-808 relative to substrate in THF/Water; (blue) VX 24 hours after the addition of MOF-HIPE-VBPP-S containing 1.25 mol % MOF-808 relative to substrate in THF/Water.

Figure 5.17 shows the degradation plots which were obtained for this particular experiment. Using the first hour of data for each sample, the reaction rate of each reaction,  $k$ , was then calculated for each material. This was performed by plotting the natural logarithm of VX concentration over time and applying a linear fit through this data. The slope of the line ( $m$ ), corresponds to  $k$  such that  $m = -k$ . The first order residue plots are shown in Figure 5.17.

Unsurprisingly, minimal VX hydrolysis was observed in the presence of HIPE-VBPP-S due to the lack of any MOF-808, this material therefore served as blank control sample. VX hydrolysis was observed in the presence of MOF-HIPE-S ( $k = 0.0044 \text{ s}^{-1}$ ) and MOF-HIPE-VBPP-S ( $k = 0.0059 \text{ s}^{-1}$ ), with only the EMPA product being formed. This was consistent with previous studies which

have been conducted regarding the aqueous, buffer-free hydrolysis of V-series agents in the presence of MOF-808.<sup>1,38</sup>

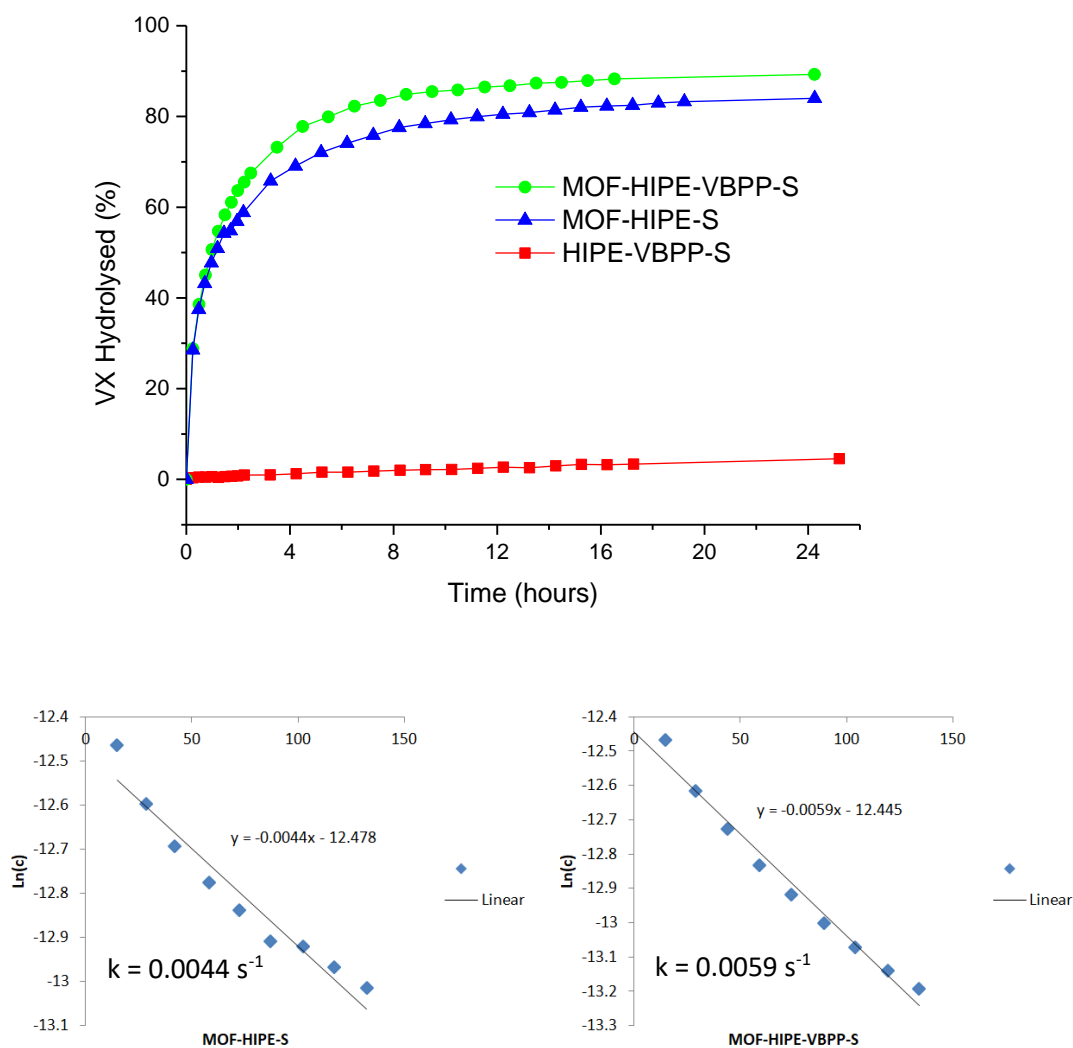


**Figure 5.17.** (top) A plot showing the hydrolysis of VX over time in the presence of MOF-HIPE-VBPP-S and MOF-HIPE-S composites in THF/H<sub>2</sub>O. Each set of data was obtained once (bottom) Natural logarithms of concentrations corresponding to VX residues in the presence of MOF-HIPE-VBPP-S and MOF-HIPE-S. The first order rate constants were calculated assuming a linear fit through the initial data points (first 120 minutes) for each composite.

These results were in agreement with the buffered hydrolysis testing that was conducted earlier on DMNP, where MOF-HIPE-VBPP-S slightly outperformed MOF-HIPE-S. These results also highlight how effective the MOF-containing composites are at degrading VX with an excess of one of the most readily available and abundant reagents, water. In fact, MOF-HIPE-VBPP-S results in a VX half-life of 1 hour with a catalytic loading of 1.25 %, which yields a calculated turn-over frequency (TOF) of  $40 \text{ h}^{-1}$ . The leading literature composite, NU-1000/PEI MW 2500,<sup>4</sup> results in a VX half-life of 15 mins but with a catalytic loading of 10.3%, this yields a calculated TOF of  $19.4 \text{ h}^{-1}$ . This makes MOF-HIPE-VBPP-S the leading material for the aqueous hydrolysis of VX, with the added benefit of being able to swell in VX ( $Q > 32$ ).

Moving on, the three HIPEs were then tested for their capacity to degrade neat VX in the presence of only ambient humidity (50 RH %). A catalyst loading of 1.25 mol % was used. After 7 days, it was not possible to extract an aliquot from any of the HIPEs due to the amount of VX used being well below the maximum swelling capacity of the HIPEs. No quantitative data was obtained but this case exemplifies that the HIPE membrane can retain absorbed nerve agent.

A second attempt was made at analysing the ability of HIPEs to degrade neat VX in the presence of ambient humidity (50 RH %). This time, the proportion of VX was adjusted to drive the HIPE swelling to  $Q > 25$ , this equated to a MOF-808 (2 mg,  $1.71 \mu\text{mol}$ ) catalyst loading of just 0.15 % relative to VX (250  $\mu\text{L}$ , 1.14 mmol). This ensured that there would be enough substrate to be extracted for analysis. Aliquots were taken at an interval of 4, 7, 11 and 14 days and analysed using  $^{31}\text{P}$  NMR in  $\text{CDCl}_3$ . The same peaks were monitored as shown in Figure 5.16. Figure 5.18 shows the results which were obtained over the course of 2 weeks. Minimal hydrolysis was observed after 4 days but after a week, 50 % hydrolysis was observed in the presence of MOF-HIPE-S with near full hydrolysis being achieved after 2 weeks in the presence of all the HIPEs, including HIPE-VBPP-S. There are several possible interpretations of these results. MOF-HIPE-S possesses far more consistent pore morphology than MOF-HIPE-VBPP-S, as demonstrated by the superior swelling values achieved. The superior swelling of MOF-HIPE-

S could therefore have enhanced the access of VX to the MOF catalyst housed within. As for HIPE-VBPP-S, there are two possibilities; the HIPE membrane facilitates the ambient uncatalysed hydrolysis of VX or the small quantity of VBPP is able to initiate the ambient hydrolysis of the agent. Unfortunately, neither of these possibilities can be verified due to the fact that HIPE-S did not feature in this study. This was due to a limited amount of V-agent available for testing. However, when comparing HIPE-VBPP-S to MOF-HIPE-VBPP-S, after 7 days, 22 % VX hydrolysis was observed in the presence of MOF-HIPE-VBPP-S compared to 8 % in the presence of HIPE-VBPP-S. This may only seem like a modest enhancement but the catalyst loading is 0.15 mol %, which makes it rather significant at such a low concentration.

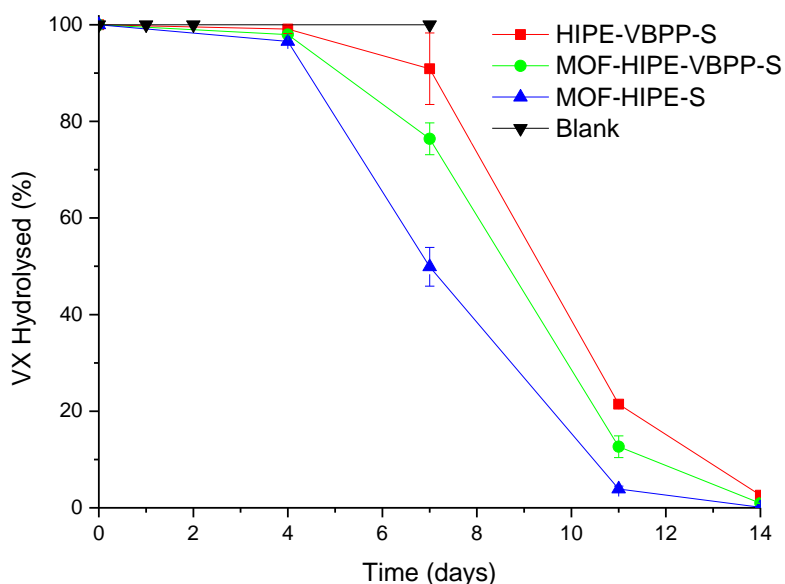


**Figure 5.18.** A graph showing the % degradation of VX over 14 days in the presence of HIPE-VBPP-S, MOF-HIPE-VBPP-S and MOF-HIPE-S. The error bars show the degree of error observed for the duplicate results.

## 5.8 Summary and Conclusion

A novel MOF-HIPE composite was synthesised from two materials; a pHIPE capable of swelling VX to  $Q > 50$  and a MOF which can facilitate the catalytic breakdown of V-series agents in the absence of a buffering agent. The composite, MOF-HIPE-S, retained both the swelling capacity and the degradation ability of the two counterparts, as shown through swelling studies and DMNP hydrolysis studies. The retention of surfactant in the HIPE structure was found to enable the absorption of water into the polymer matrix and a modest enhancement in hydrolysis was observed for MOF-HIPE-S over that of MOF-HIPE when an aqueous, THF-free, degradation procedure was used to probe DMNP hydrolysis. An additional HIPE, MOF-HIPE-VBPP-S, was then synthesised with a 5 % VBPP monomer loading. The characterization of the VBPP monomer in the MOF-HIPE-VBPP-S structure proved difficult and a lower Q value of 30 was achieved for the swelling of the methyl benzoate simulant due to a less regular internal phase. However, MOF-HIPE-VBPP-S proved just as potent a degradation material for the hydrolysis of the DMNP simulant. MOF-HIPE-VBPP-S was also able to facilitate the buffer-free hydrolysis of DMNP, with the quantity of hydrolysis being stoichiometrically linked to the quantity of VBPP present in the reaction mixture. Finally, MOF-HIPE-VBPP-S, MOF-HIPE-S and HIPE-VBPP-S were examined for their ability to degrade the nerve agent VX. MOF-HIPE-VBPP-S and MOF-HIPE-S were able to effectively hydrolyse the nerve agent VX in mixture of H<sub>2</sub>O/THF and in the absence of NEM buffer. The three composites were then employed for the degradation of neat VX (i.e, no solvent, no buffer, 50 RH %). MOF-HIPE-S proved to be the most successful degradation material for VX hydrolysis, followed by MOF-HIPE-VBPP-S and HIPE-VBPP-S. The presence of the VBPP units in MOF-HIPE-VBPP-S did not enhance the hydrolysis of VX, which is hypothesised to be the result of less regular polymer membrane when compared to that of MOF-HIPE-S. A possible future improvement would involve an alternative synthetic procedure which could enable the incorporation of the VBPP monomer into a HIPE without compromising the regularity of the polymer internal phase. However, the MOF-HIPE composite is still highly demonstrative. The composite is able to rapidly degrade VX

in the absence of buffer and in the presence of excess water, and rivals previously published work regarding aqueous VX hydrolysis in the presence of MOF composites (NU-1000/PEI 2500 MW). The MOF-HIPE composite also has the advantage of being able to swell in the presence of agent, something no other reported hydrolytic composite is capable of doing. The contents of this report is therefore highly novel and should facilitate the future development of degradation towards the catalytic breakdown of OP CWAs whilst negating the need for excess reagents.

## 5.9 References

- 1 Y. Kalinovsky, N. J. Cooper, M. J. Main, S. J. Holder and B. A. Blight, *Dalton. Trans.*, 2017, **46**, 15704–15709.
- 2 J. Zhao, D. T. Lee, R. W. Yaga, M. G. Hall, H. F. Barton, I. R. Woodward, C. J. Oldham, H. J. Walls, G. W. Peterson and G. N. Parsons, *Angew. Chem. Int. Ed.*, 2016, **55**, 13224–13228.
- 3 H. Liang, A. Yao, X. Jiao, C. Li and D. Chen, *ACS Appl. Mater. Interfaces*, 2018, **10**, 20396–20403.
- 4 S.-Y. Moon, E. Prousaloglou, G. W. Peterson, J. B. DeCoste, M. G. Hall, A. J. Howarth, J. T. Hupp and O. K. Farha, *Chem. Eur. J.*, 2016, **22**, 14864–14868.
- 5 M. S. Silverstein, *Polymer (Guildf.)*, 2014, **55**, 304–320.
- 6 M. S. Silverstein, *Prog. Polym. Sci.*, 2014, **39**, 199–234.
- 7 N. R. Cameron and D. C. Sherrington, 1996, pp. 163–214.
- 8 T. Zhang, Y. Wu, Z. Xu and Q. Guo, *Chem. Commun.*, 2014, **50**, 13821–13824.
- 9 A. Y. Sergienko, H. Tai, M. Narkis and M. S. Silverstein, *J. Appl. Polym. Sci.*, 2004, **94**, 2233–2239.
- 10 I. Gurevitch and M. S. Silverstein, *J. Polym. Sci. Part A Polym. Chem.*, 2010, **48**, 1516–1525.
- 11 S. Ungureanu, H. Deleuze, O. Babot, M.-F. Achard, C. Sanchez, M. I. Popa and R. Backov, *Appl. Catal. A Gen.*, 2010, **390**, 51–58.
- 12 S. Ungureanu, H. Deleuze, C. Sanchez, M. I. Popa and R. Backov, *Chem. Mater.*, 2008, **20**, 6494–6500.
- 13 N. Brun, P. Hesemann, G. Laurent, C. Sanchez, M. Birot, H. Deleuze and R. Backov, *New J. Chem.*, 2013, **37**, 157–168.
- 14 Y. Wu, T. Zhang, Z. Xu and Q. Guo, *J. Mater. Chem. A*, 2015, **3**, 1906–1909.
- 15 T. Zhang and Q. Guo, *Chem. Eng. J.*, 2017, **307**, 812–819.
- 16 M. Tebboth, A. Menner, A. Kogelbauer and A. Bismarck, *Curr. Opin. Chem. Eng.*, 2014, **4**, 114–120.
- 17 H.-Y. Luo, M. Zhang, N.-C. Si, M.-J. Meng, L. Yan, W.-J. Zhu and C.-X. Li, *Chinese Chem. Lett.*, 2015, **26**, 1036–1041.
- 18 T. Ono, T. Sugimoto, S. Shinkai and K. Sada, *Adv. Funct. Mater.*, 2008, **18**, 3936–3940.
- 19 A. J. Wright, M. J. Main, N. J. Cooper, B. A. Blight and S. J. Holder, *ACS Appl. Mater. Interfaces*, 2017, **9**, 31335–31339.
- 20 C. Wilson, M. J. Main, N. J. Cooper, M. E. Briggs, A. I. Cooper and D. J. Adams, *Polym. Chem.*, 2017, **8**, 1914–1922.
- 21 M. Wickenheisser, T. Paul and C. Janiak, *Microporous Mesoporous Mater.*, 2016, **220**, 258–269.
- 22 M. L. Pinto, S. Dias and J. Pires, *ACS Appl. Mater. Interfaces*, 2013, **5**, 2360–2363.
- 23 M. Claire Hermant, B. Klumperman and C. E. Koning, *Chem. Commun.*, 2009, **0**, 2738–

2740.

- 24 Y. Zhu, S. Zhang, Y. Hua, J. Chen and C. P. Hu, *Polymer (Guildf.)*, 2010, **51**, 3612–3617.
- 25 T. Li, H. Liu, L. Zeng, S. Yang, Z. Li, J. Zhang and X. Zhou, *J. Mater. Chem.*, 2011, **21**, 12865–12872.
- 26 A. R. Schultz, C. Jangu and T. E. Long, *Polym. Chem.*, 2014, **5**, 6003–6011.
- 27 T. Polenova, R. Gupta and A. Goldbourn, *Anal. Chem.*, 2015, **87**, 5458–69.
- 28 J. E. Mondloch, M. J. Katz, W. C. Isley III, P. Ghosh, P. Liao, W. Bury, G. W. Wagner, M. G. Hall, J. B. DeCoste, G. W. Peterson, R. Q. Snurr, C. J. Cramer, J. T. Hupp and O. K. Farha, *Nat. Mater.*, 2015, **14**, 512–516.
- 29 M. J. Katz, J. E. Mondloch, R. K. Totten, J. K. Park, S. T. Nguyen, O. K. Farha and J. T. Hupp, *Angew. Chem. Int. Ed.*, 2014, **126**, 507–511.
- 30 S.-Y. Moon, Y. Liu, J. T. Hupp and O. K. Farha, *Angew. Chem. Int. Ed.*, 2015, **54**, 6795–6799.
- 31 K.-Y. Law, *J. Phys. Chem. Lett.*, 2014, **5**, 686–688.
- 32 M. C. de Koning, M. van Grol and T. Breijaert, *Inorg. Chem.*, 2017, **56**, 11804–11809.
- 33 H. Miyamura, M. Morita, T. Inasaki and S. Kobayashi, *Bull. Chem. Soc. Jpn.*, 2011, **84**, 588–599.
- 34 J. M. Williams and D. A. Wroblewski, *Langmuir*, 1988, **4**, 656–662.
- 35 J. M. Williams, A. J. Gray and M. H. Wilkerson, *Langmuir*, 1990, **6**, 437–444.
- 36 W. E. Thompson, R. J. Warren, I. B. Eisdorfer and J. E. Zarembo, *J. Pharm. Sci.*, 1965, **54**, 1819–1821.
- 37 G. W. Wagner and R. Xega, *Ind. Eng. Chem. Res.*, 2012, **51**, 16146–16150.
- 38 S.-Y. Moon, G. W. Wagner, J. E. Mondloch, G. W. Peterson, J. B. DeCoste, J. T. Hupp and O. K. Farha, *Inorg. Chem.*, 2015, **54**, 10829–10833.

## Chapter 6. Thesis Summary and Conclusion

This thesis has covered a number of topics regarding Chemical Warfare Agent (CWA) hydrolysis and ligand-based photoluminescence in MOFs. The primary goal of the project described in this thesis was to develop a composite material capable of encapsulating and degrading organophosphorus (OP) CWAs; bulk degradation on the litre scale was the ultimate aim of the study. This thesis aimed to deal with the degradation aspect of the final composite material. A catalytic material was therefore required, one that would be capable of degrading neat V-series agents at low catalytic loading (< 5 % loading), in the absence of a buffer and any additional reagents.

### 6.1 Thesis Summary

Initially, the literature was surveyed to identify a number of systems that deal with the degradation of CWAs. Simulant systems were reviewed to identify and select simulant compounds which would mimic the degradation of OP CWAs. Phosphodiester compounds such as diethyl chlorophosphate, dimethyl methylphosphonate and methyl paraoxon (DMNP) were some of the commonly reported simulants. Metal oxide nanoparticles (MONPs) and Zirconium MOFs were then screened as catalysts for the oxidation/hydrolysis of a range of simulants. Compared to MONPs, Zirconium MOFs were found to function at lower catalytic loadings relative to their substrate. The DMNP simulant in aqueous buffer was also identified as the most appropriate OP CWA hydrolysis simulant. A selection of potential Zirconium MOF catalysts were then synthesised and tested for their ability to degrade the DMNP simulant. Frameworks lacking defects/empty coordination vacancies performed poorly as hydrolysis catalysts for the degradation of the DMNP simulant. MOF-808, a Zirconium MOF with a linker connectivity of six instead of the maximum of 12, was found to be the most effective material for degrading DMNP. The ability for the DMNP substrate to access linker-free coordination sites was therefore considered essential for facilitating phospho-ester hydrolysis. Following on, MOF-808 was selected for testing on the V-series agent VX. At a catalyst loading of 1.25 %,

MOF-808 was able to rapidly degrade VX in the presence of only water and in the absence of buffer. 80 % VX hydrolysis was observed after just 10 minutes in the presence of MOF-808. Buffer-free VX hydrolysis was thought to occur due to the stoichiometric generation of the basic diisopropylaminoethanethiol (DESH) by-product, thus making a VX hydrolysis reaction a self-buffering process. A follow-up MOF-808 degradation study was conducted on neat VX in the presence only 40 % Relative Humidity (RH %). However, this hydrolysis took 7 days and was therefore significantly slower. A natural interest was developed in how the propensity of zirconium MOFs to undergo hydration affected their function as a hydrolysis catalyst.

The hydration of a selection of Zirconium MOF catalyst candidates was analysed using solid-state photoluminescence spectroscopy (ssPL) but no interesting changes were noted upon hydration. However, through a collaborative effort, two novel alkaline earth (AE) MOFs, MOF-1 (Ba) and MOF-2 (Sr) were analysed for their hydration-dependent emission. Both frameworks exhibited reversible emissive profiles upon hydration and dehydration. MOF-2 (Sr) was found to exhibit a sensitive and gradual humidity-dependent emission from 29 % RH onwards. In contrast, MOF-1 (Ba) displayed a sharp red-shifted emission upon direct liquid wetting with no humidity-dependent emission until RH 84 %. Interestingly, both frameworks tended towards amorphization upon hydration and so the retention of long-range order was not essential to their function. Through a second collaboration, a series of novel Zirconium MOFs, composed of functionalised 4,4'-[1,4-phenylene-bis(ethyne-2,1-diyl)]-dibenzoate (peb) linkers, were analysed using ssPL for any hydration-dependant changes. Small changes in emission were observed for all of the frameworks, Zr-L7, a benzothiadiazolyl functionalised MOF was found to exhibit a humidity-dependent emission. Zr-L5, a MOF composed of a tetrafluorinated linker, did not display any hydration-dependent emission and contact angle measurements were used to highlight its super-hydrophobic properties. Finally, upon exposing the Zr MOFs to solvents with different dipole moment, Zr-L2, a MOF composed of a dimethyl functionalised peb linker, was found to exhibit solvatochromism. ssPL proved very valuable for screening solid materials under a variety of conditions, thus acting as a useful probe of functional properties in MOFs.

Also, hydration-dependent emission for water sensing applications remains an under-reported feature in photoluminescent MOFs. It is highly likely that there are many previously reported MOFs that exhibit hydration-dependent emission and simply have not yet been investigated.

Focusing on catalysis, three acetate modulated MOFs, MOF-808, DUT-84, and UiO-66, were activated using a novel microwave irradiation procedure in H<sub>2</sub>O. This activation procedure worked to remove excess acetate modulator which was bound to the Zr<sub>6</sub> node of each framework, thus exposing more catalytic coordination sites. The highest degree of acetate-removal was achieved in MOF-808. The activation procedure was also attempted on a benzoic acid modulated UiO-66 but no benzoic acid removal was observed. Further microwave activation and optimization tests are required with MOFs containing common carboxylate modulators such as formic acid, propionic acid and amino acids. As for the acetate-modulated MOFs, a modest enhancement in the buffered DMNP hydrolysis was observed in the presence of the activated frameworks when compared to their as-synthesised counterparts. DUT-84 and MOF-808 were then tested for their ability to degrade the V-series agent VM. A negligible difference was observed between the activated and non-activated MOF-808. However, a notable enhancement was noted in the presence of activated DUT-84 when compared to the as-synthesised counterpart. With both MOFs, VX hydrolysis occurred and in the absence of buffer, MOF-808 showed significantly enhanced activity over that of DUT-84. MOF-808 had therefore been shown to degrade VX and VM in aqueous medium in the absence of a buffering agent. MOF-808 was also shown to degrade neat VX in the presence of only ambient humidity. The effectiveness of MOF-808 as an OP hydrolysis catalyst, the low price and high availability of the constituent 1,3,5-benzene tricarboxylic acid (btc) linker precursor, along with the low formula weight of MOF-808 (in relation to other Zirconium frameworks), makes it the best candidate as a MOF hydrolysis catalyst.

MOF-808 was therefore selected for incorporation into a VX swelling HIPE polymer which had been developed by A. J. Wright. A MOF-HIPE composite was then formed which was capable of

swelling in methyl benzoate (a CWA swelling simulant) to  $Q > 50$  and hydrolysing DMNP in the presence of buffer. A vinyl benzyl piperidine functionalised MOF-HIPE (MOF-HIPE-VBPP-S) was then synthesised, and shown to be capable of partially hydrolysing DMNP in the absence of a buffering agent. The hydrolysis of DMNP occurred stoichiometrically in relation to the quantity of VBPP present. Upon conducting tests on VX, MOF-HIPE-VBPP-S and MOF-HIPE-S were capable of effectively hydrolysing VX in a solution of THF/H<sub>2</sub>O at a catalyst loading of 1.25 %. The performance of the MOF-HIPE composites for VX hydrolysis rivalled that of the leading reported composite material (NU-1000/PEI MW 2500). Additionally, the MOF-HIPE composites possessed the added advantage of being able to swell on adsorbing the VX agent. For the penultimate test, the composites were tested for the encapsulation and degradation of neat VX in the presence of only ambient humidity. To achieve a swelling degree of  $Q > 25$  the MOF-808 catalyst loading was taken to be 0.15 % relative to VX. MOF-HIPE-S was found to be the most effective degradation material for the neat hydrolysis of VX with a VX  $t_{1/2}$  of 7 days being observed. Slower degradation was achieved in the presence of MOF-HIPE-VBPP-S, but full degradation was observed after 2 weeks with both composites. The presence of the VBPP monomer during HIPE synthesis was believed to have affected the consistency of the polymer membrane, thus hindering the absorption of VX throughout the HIPE matrix.

## 6.2. Thesis Conclusion

The aim of this thesis was to develop a composite material for the bulk encapsulation and catalytic degradation of neat OP CWAs. MOF-808 was identified as the most promising OP CWA catalyst and was found to be very effective for the hydrolysis of V-series agents in aqueous medium. MOF-808 is also superior to other Zirconium MOF hydrolysis catalysts in terms of cost, scalability and weight factor, whilst rivalling their performance. However, the MOF-808 facilitated hydrolysis of VX was significantly slower in the presence of only ambient humidity. A time of 7 days was required for complete neutralization which was not ideal. The

diffusion of ambient water appeared to be the rate limiting determinant for enabling hydrolysis. There appeared to be no way around this, apart from simply adding water.

Upon incorporating MOF-808 into a polyHIPE to form the MOF-HIPE composite, the hydrolytic capability of the resulting material was not diminished. The incorporation of a VBPP monomer into the MOF-HIPE composite was then attempted. It was hoped that the basic VBPP units would help to kick-start the initial hydrolysis of VX and lead to a faster hydrolysis overall. No net increase in DMNP simulant hydrolysis was noted for MOF-HIPE-VBPP-S vs. MOF-HIPE-S, however an equivalent quantity of MOF-HIPE-VBPP-S was able to hydrolyse a greater quantity of DMNP in the absence of buffer. MOF-HIPE-VBPP-S was also able to hydrolyse VX in a THF/H<sub>2</sub>O mixture at a slightly faster rate than MOF-HIPE-S, this enhancement could very well have been due to the presence of the basic amine monomer unit. In terms of TOF, both HIPE composites rival the most effective literature composites for the aqueous, buffer-free hydrolysis of VX, with the added advantage of possessing a high swelling capacity for VX. Despite this advantage, the aim of the thesis was to hydrolyse neat agent.

Upon testing both composites for the neat hydrolysis of VX, MOF-HIPE-S significantly outperformed MOF-HIPE-VBPP-S. Without further improvements and optimizations, MOF-HIPE-S would appear to be the superior material for V-agent encapsulation and degradation. Further alterations to the synthesis of MOF-HIPE-VBPP-S could still potentially yield an enhanced material. The VX hydrolysis in the presence of MOF-HIPE-S was still rather slow, taking ~ 11 days, however, the catalyst loading of MOF-808 was a mere 0.15 %. A slow hydrolysis can still be considered significant at such a low loading. Furthermore, the HIPE scaffold adds the benefit of agent retention; once the V-agent has been absorbed into the HIPE membrane, it becomes very difficult and unsafe to extract it again. Slow hydrolysis of neat agent under ambient conditions is therefore not an issue because once the agent has been absorbed, it is rendered inaccessible and can therefore be allowed to degrade slowly.

Reflecting on the ultimate goal of this thesis, the objective was met. A composite material has been developed which possesses a swelling functionality along with a degradation ability. The material is able to rapidly swell neat VX followed by a steady, selective breakdown of VX to the non-toxic EMPA product. With an effective MOF-808 catalyst loading of only 0.15 %, the hydrolysis proceeds slowly. A timeframe of just under 2 weeks is required for full hydrolysis, but the HIPE sponge effectively immobilizes the agent, thus making speed less of a concern. The whole process also occurs in the complete absence of any additional/excess reagents, only ambient humidity is required to fuel the hydrolysis.

### **6.3 Future Work**

For future work, a few possible strategies exist for enhancing or further demonstrating the utility of the MOF-HIPE composite. MOF-HIPE-VBPP-S synthesis can be optimised to ensure the retention of a more ordered internal phase in the presence of the VBPP monomer. This could potentially allow for a higher VBPP monomer loading (i.e 10 % vs 5 %), thus increasing the abundance of heterogeneous amine to kickstart VX hydrolysis. Second, the hydrolysis of VX proceeds rapidly in the presence of the MOF-HIPE composites and an excess of water, regardless of whether VBPP monomer is present. The transport of water into the HIPE membrane containing MOF-808 catalyst is therefore the rate limiting step for facilitating V-agent hydrolysis. Thus, any alterations to the composite or the components that lead to an increase in the hygroscopicity of the material would likely positively affect the hydrolytic properties for V-series agent hydrolysis. This could be achieved by partially incorporating a more hygroscopic monomer unit into the HIPE scaffold but this would have to be carefully balanced with internal phase stability and swelling ability. Finally, it would be interesting to determine just how selectively the HIPE composites are capable of swelling the V-series agents. This could be achieved by attempting to swell with multi-component solutions containing methyl benzoate along with a less swelling liquid component, such as ethanol or

water. This would demonstrate whether the composite would be able to absorb and degrade V-agents in more dilute concentrations, such as contaminated water sources.

To conclude this project, the work described in this thesis is highly applied. Through a collaborative effort with Alex Wright and DSTL, a novel composite material has been developed. The composite material can swell to a high degree ( $Q > 50$ ) in the presence of V-series agents. The composite, containing a MOF-808 catalyst loading of just 1.25 % relative to substrate, is also able to facilitate the hydrolysis of VX in the presence of an excess of water. Additionally, the composite (with a MOF-808 catalyst loading of 0.15 %) is able to facilitate the encapsulation and complete degradation of neat VX over 2 weeks, and in the presence of only ambient humidity. If faster hydrolysis is required, all that is necessary is the addition of water, one of the most readily available reagents. The studies described in this work should therefore aid in the future development of composite materials for the bulk degradation and encapsulation of highly toxic OP CWAs. This work should also help to advance the field of reactive polymer composites which possess both a substrate-swelling membrane and a reactive heterogeneous catalyst.

## Chapter 7. Appendix

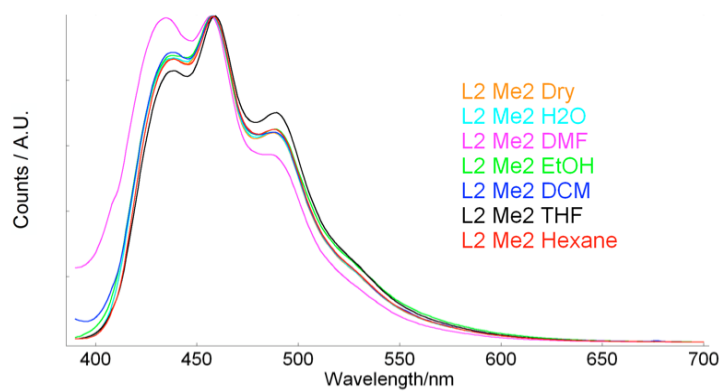
### 7.1 Boron MOF Single Crystal Data (performed by Helena J. Shepherd)

A suitable crystal of Boron MOF was selected and mounted on a glass fiber with inert oil on a 'Bruker APEX-II CCD' diffractometer at the ALS station 11.3.1. The crystal was kept at 100 K during data collection. Using Olex2, the structure was solved with the XS structure solution program using Direct Methods and refined with the ShelXL refinement package using Least Squares minimisation. The structure requires further refinement. The crystal data and structural refinement details are shown below:

Empirical formula	C <sub>60</sub> H <sub>60</sub> B <sub>2</sub> O <sub>10</sub> Zr
Formula weight	1053.92
Temperature/K	100
Crystal system	monoclinic
Space group	P2 <sub>1</sub> /m
a/Å	13.4322(18)
b/Å	45.670(6)
c/Å	13.956(2)
α/°	90
β/°	116.443(4)
γ/°	90
Volume/Å <sup>3</sup>	7665.8(18)
Z	6
ρ <sub>calc</sub> /cm <sup>3</sup>	1.370
μ/mm <sup>-1</sup>	0.277
F(000)	3300.0
Crystal size/mm <sup>3</sup>	0.01 × 0.01 × 0.005
Radiation/ Å	CuKα (λ = 0.71073)
2θ range for data collection/°	3.38 to 41.63
Index ranges	-13 ≤ h ≤ 13, -45 ≤ k ≤ 45, -13 ≤ l ≤ 13
Reflections collected	37968
Independent reflections	8144 [R <sub>int</sub> = 0.0895, R <sub>sigma</sub> = 0.0681]
Data/restraints/parameters	8144/1/711
Goodness-of-fit on F <sup>2</sup>	2.566
Final R indexes [I ≥ 2σ (I)]	R <sub>1</sub> = 0.1474, wR <sub>2</sub> = 0.3783
Final R indexes [all data]	R <sub>1</sub> = 0.1841, wR <sub>2</sub> = 0.3921
Largest diff. peak/hole / e Å <sup>-3</sup>	2.94/-4.05

## 7.2 ssPL Emission Spectra of L2-Me<sub>2</sub> and L7-Me<sub>2</sub> in the Presence of Various Solvents

a)



b)

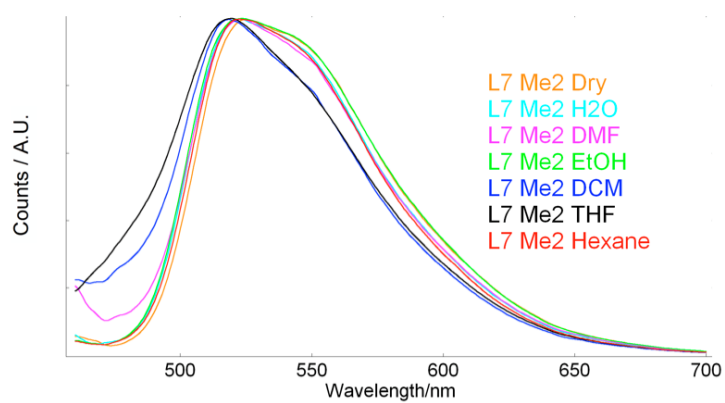


**Figure 7.1.** Normalised solid-state fluorescence emission spectra of a) L2-Me<sub>2</sub> ( $\lambda_{\text{ex}} = 380$  nm), and b) L7-Me<sub>2</sub> ( $\lambda_{\text{ex}} = 450$  nm) in the presence of a wide array solvents.

### 7.3 Buffered DMNP hydrolysis in the presence of MOF-HIPE composites and THF/H<sub>2</sub>O

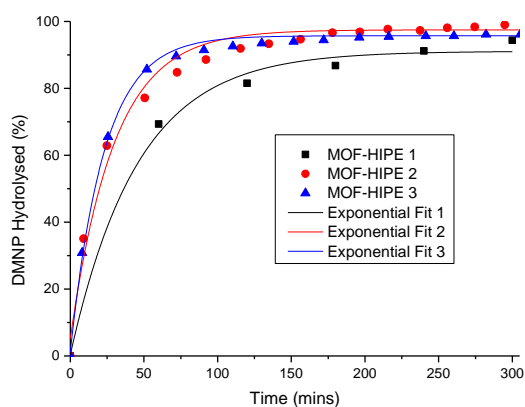


**Figure 7.2.** A plot showing the hydrolysis of DMNP over time in the presence of MOF-HIPE in of 0.45 M NEM buffer, THF and H<sub>2</sub>O. The individual data points for each data set in a triplicate are shown, along with the exponential fit that was derived from each data set.

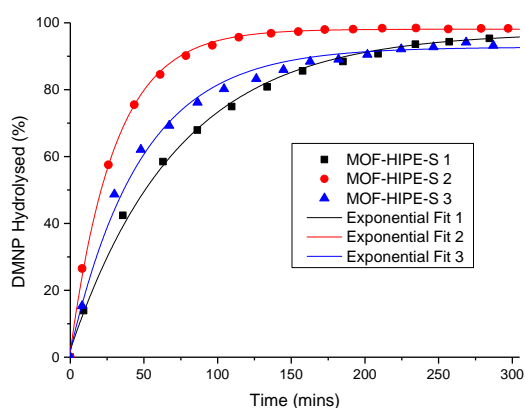


**Figure 7.3.** A plot showing the hydrolysis of DMNP over time in the presence of MOF-HIPE-S in of 0.45 M NEM buffer, THF and H<sub>2</sub>O. The individual data points for each data set in a triplicate are shown, along with the exponential fit that was derived from each data set.

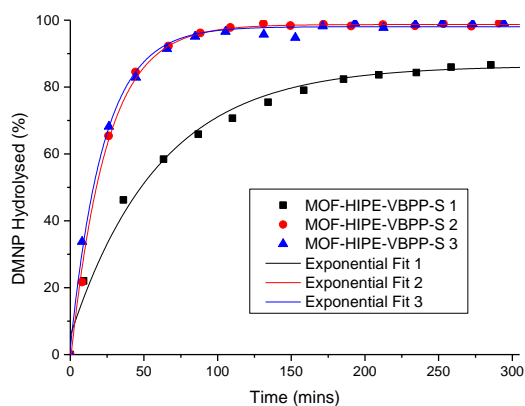


**Figure 7.4.** A plot showing the hydrolysis of DMNP over time in the presence of MOF-HIPE-VBPP-S in of 0.45 M NEM buffer, THF and H<sub>2</sub>O. The individual data points for each data set in a triplicate are shown, along with the exponential fit that was derived from each data set.

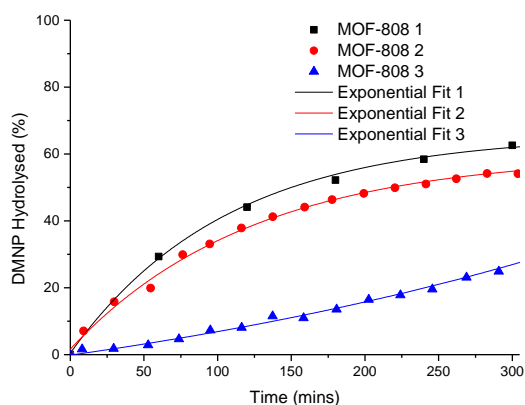


**Figure 7.5.** A plot showing the hydrolysis of DMNP over time in the presence of MOF-808 in of 0.45 M NEM buffer, THF and H<sub>2</sub>O. The individual data points for each data set in a triplicate are shown, along with the exponential fit that was derived from each data set.

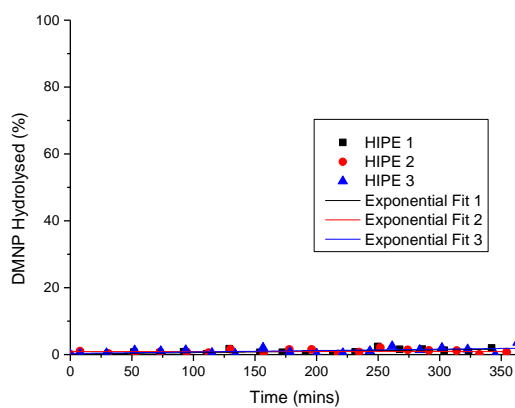


**Figure 7.6.** A plot showing the hydrolysis of DMNP over time in the presence of HIPE in of 0.45 M NEM buffer, THF and H<sub>2</sub>O. The individual data points for each data set in a triplicate are shown, along with the exponential fit that was derived from each data set.

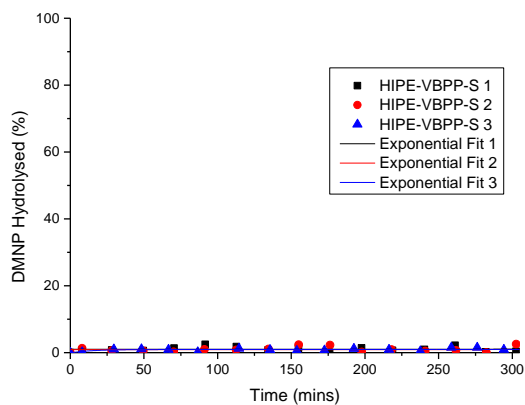


**Figure 7.7.** A plot showing the hydrolysis of DMNP over time in the presence of MOF-HIPE-VBPP-S in of 0.45 M NEM buffer, THF and H<sub>2</sub>O. The individual data points for each data set in a triplicate are shown, along with the exponential fit that was derived from each data set.

## 7.4 Buffered DMNP hydrolysis in the presence of MOF-HIPE composites and

H<sub>2</sub>O

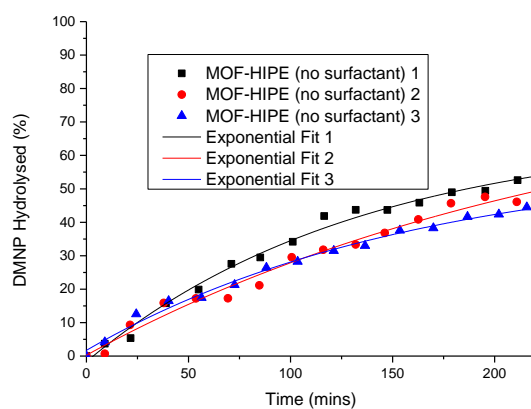


**Figure 7.8.** A plot showing the hydrolysis of DMNP over time in the presence of MOF-HIPE (no surfactant) in of 0.45 M NEM buffer H<sub>2</sub>O. The individual data points for each data set in a triplicate are shown, along with the exponential fit that was derived from each data set.

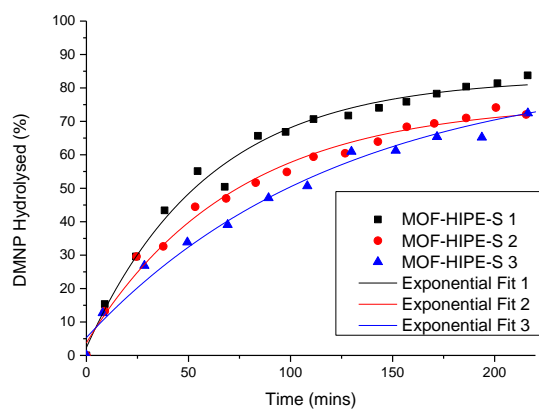


**Figure 7.9.** A plot showing the hydrolysis of DMNP over time in the presence of MOF-HIPE-S in of 0.45 M NEM buffer H<sub>2</sub>O. The individual data points for each data set in a triplicate are shown, along with the exponential fit that was derived from each data set.

## 7.5 MOF-HIPE-S Hydrolysis Cycling

The following procedure was used to test the hydrolytic effectiveness of MOF-HIPE-S over 3 cycles. The HIPE containing MOF-808 (3.2 mg, 0.11  $\mu\text{mol}$ , 1.25 mol %) was sliced up into small chunks (1-2  $\text{mm}^3$ ) then added to the tube along with 0.6 ml mixture containing: 0.2 ml of  $\text{D}_2\text{O}$ , 0.2 THF and 0.2 ml of 1.45 M *N*-ethyl morpholine (NEM) aqueous buffer (effective concentration 0.45M). The tube was inverted once and left to stand for 24 hours at room temperature (298 K). After 24 hours, the tube was analysed using  $^{31}\text{P}$  NMR (161.83 MHz) spectroscopy. The HIPE was then removed from the tube, washed 5 times with THF and re-used in the same manner as described above. This was repeated two more times to give a total of 3 cycles.

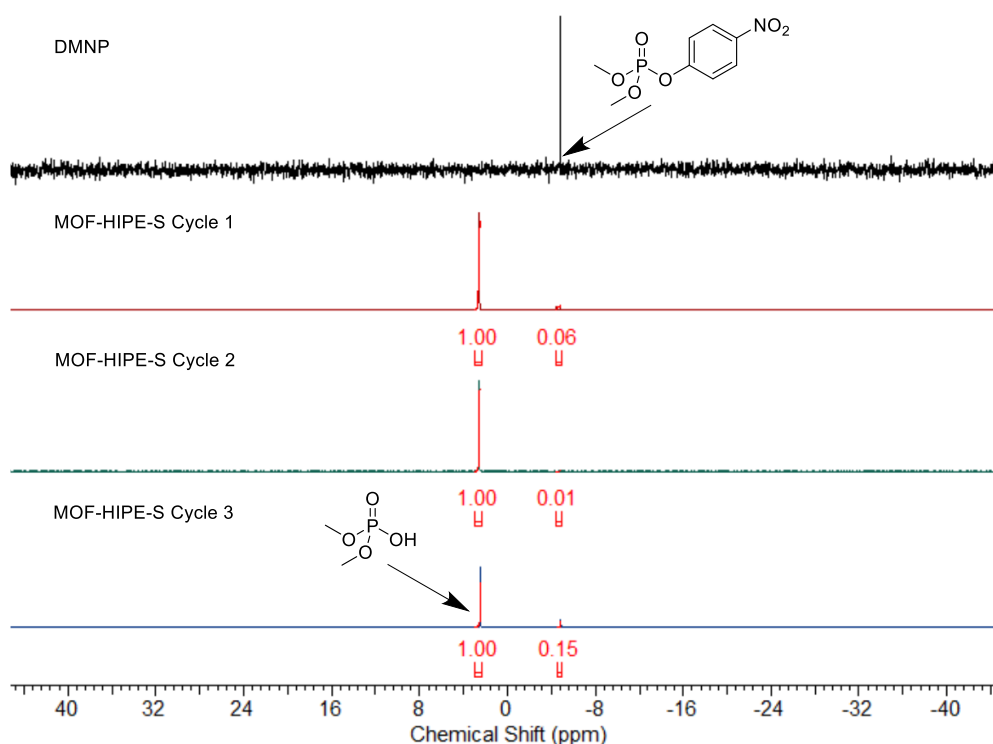


**Figure 7.10.** A  $^{31}\text{P}$  NMR in  $\text{D}_2\text{O}$  overlay showing (black) fresh DMNP (red) DMNP 24 hours after the addition of MOF-HIPE-S containing 1.25 mol % MOF-808 relative to substrate in 0.45 M NEM buffer (green) DMNP 24 hours after the addition of the same MOF-HIPE-S containing 1.25 mol % MOF-808 relative to substrate in 0.45 M NEM buffer (red) DMNP 24 hours after the addition of the same MOF-HIPE-S containing 1.25 mol % MOF-808 relative to substrate in 0.45 M NEM buffer.